Modelling, Design and Characterisation of Terahertz Photoconductive Antennas

by

Neda Khiabani

Submitted in accordance with the requirements for the award of the degree of Doctor of Philosophy of the University of Liverpool

September 2013

Copyright

To my darling husband, Saeed, and my parents

Abstract

The area of Terahertz (THz) is one of the fastest growing research fields in recent years. THz antennas based upon photoconduction techniques are the most common devices in THz systems. However, the radiated THz power from these devices and the efficiency are very low. Also, different antenna excitation and current generation process in THz antennas, as compared to microwave antennas, requires new analyses approaches. Therefore, the motivation of this thesis is to theoretically establish why the THz antenna is inefficient; from which, general methods to improve the performance of such antennas are explored and validated. These investigations are essential to gain a better understanding of THz photoconductive antenna performance.

In this research a new equation for the source conductance of a THz antenna is firstly developed. This is a prerequisite for further antenna radiated power analysis. Next, a new equivalent circuit, modelling the underlying physical behaviour of the device through the use of a lumped-element network, is developed. Through this model, various factors which affect the radiated power and efficiency of the THz photoconductive antenna are examined and compared with measurement results. This model can be applied to maximize the optical-to-THz conversion efficiency. Also, temporal voltage behaviour of the antenna can be predicted more realistically. Furthermore, a computational simulation procedure, solving both optoelectronic and electromagnetic problems, is proposed and validated by measurement results. This approach facilitates prediction of THz photoconductive antenna performance before antenna fabrication.

In addition, considering the requirement of high THz power and good SNR devices for various THz applications, a new top loaded THz antenna embedded on a conical horn with the trapezoidal photomixer is proposed. The generation of THz photocurrent, impedance matching and coupling of the THz wave to air (the necessary factors for power enhancement) are improved. Moreover, the new trapezoidal photomixer is examined and the measurement results show that it has better radiated THz power and SNR than the bare gap and rectangular photomixers.

Acknowledgements

First and foremost, I would like to thank my supervisor Professor Yi Huang, who has provided me this, both academically and personally, life changing opportunity. I am sincerely grateful for his advice, continuous and generous support and trust on my capabilities. I would also like to thank Dr. Yaochun Shen for his invaluable guidance and patience in numerous and long discussions throughout the period of my PhD research. Financially, I gratefully acknowledge the support from the Engineering and Physical Sciences Research Council (EPSRC).

I am earnestly indebted to Professor Luis Enrique Garcia-Muñoz and Alejandro Rivera-Lavado, at the Universidad Carlos III de Madrid for my antenna fabrication and measurements.

At the Wireless Engineering group, I would also like to express my gratitude to the past and present members; to Dr. Stephen Boyes for all fruitful discussions and proof readings of my work, to Ping Cao and Rula Alrawashdeh for all inspiring and life-related talks and a good time we had in our office, to Lei Xing and Qian Xu for their work-related inspiring suggestions.

Thanks to my great friend, Elham who inspired me to step forward for a new life experience abroad. I am very grateful for all her support and effort to cheer me up. In the department, it is a great pleasure to thank my friend, Waqar, for boosting my morale and for his full support especially in the very crucial moments of my studies.

I would like to offer my personal and special thanks to my family who have encouraged me over the years. Primarily this must be my father and mother, who have believed in me and surrounded me with their love and blessing. I never forget their sacrifices that have made my life a lot easier. I must also thank my brothers, Mehdi and Navid, for making me cheerful all the time.

Finally, I should thank my husband, Saeed, who has endured the inevitable long-distance life due to my studies. I am very thankful for his patience on all my stresses during our acquaintances time and after marriage. He truly motivates me, and I am genuinely grateful for his constant support and love.

List of Publications

1. **N. Khiabani**, Y. Huang, Y. Shen, S. J Boyes, “Theoretical Modeling of a Terahertz Photoconductive Antenna in a Pulsed System”, *IEEE Transaction on Antenna and Propagation*, vol. 61, no. 4, pp. 1538-1546, April 2013.
2. **N. Khiabani**, Y. Huang, Y. Shen, L. E. Garcia-Muñoz, A. Rivera-Lavado, “A Novel THz Photomixer with Nano-Trapezoidal Electrodes”, submitted to *IEEE Transactions on Terahertz Science and Technology.*
3. **N. Khiabani**, Y. Huang, Y. Shen, A. Abu Bakar Sajak, “Photoconductive THz Antennas”, accepted for *LAPC 2013.*
4. **N. Khiabani**, Y. Huang, Y. Shen, S. J Boyes, Q. Xu, “A Novel Simulation Method for THz Photoconductive Antenna Characterization”, *Proceeding of the 7th EuCAP*, Sweden, April 2013.
5. S. Boyes, Y. Huang, P. J. Soh, G. A. E. Vandenbosch, **N. Khiabani**, “Measurement and Performance of Textile Antenna Efficiency on a Human Body in a Reverberation Chamber”, *IEEE Transaction on Antenna and Propagation*, vol 61, no. 2, pp 871-880, February 2013.
6. S. Boyes, P. J. Soh, Y. Huang, G. A. E. Vandenbosch, **N. Khiabani**, “On-body Performance of Dual-band Textile Antennas”, *IET Microwaves, Antennas & Propagation*, vol. 6, no. 15 , pp. 1696-1703, December 2012.
7. **N. Khiabani**, Y. Huang, Y. Shen, S. J Boyes, “Efficiency Calculation of THz Photoconductive Antennas in a Pulsed System”, *Proceeding of the 6th EuCAP*, pp. 3250-3254, Czech republic, March 2012.
8. **N. Khiabani**, Y. Huang, Y. Shen, S. J Boyes, “THz Photoconductive Antennas in Pulsed Systems and CW Systems”, *Proceeding of the iWAT 2012*, pp. 181-184, USA, March 2012.
9. **N. Khiabani**, Y. Huang, Y. Shen, S. J Boyes, “Time Varying Source Conductance in THz Photoconductive Antennas”, *4th China-Europe Workshop on Millimetre waves and Terahertz*

Technologies, September 2011.

10. **N. Khiabani**, Y. Huang, Y. Shen, S. J Boyes "Time Variant source Resistance in the THz Photoconductive Antenna", *LAPC 2011*, UK, November 2011.
11. **N. Khiabani**, Y. Huang, Y. Shen, "Comparison of ultra-wideband THz generation and detection systems", *Proceeding of the 5th EuCAP*, pp. 457-461, April 2011.
12. **N. Khiabani**, Y. Huang, Y. Shen, "Discussions on the Main Parameters of THz Photoconductive Antennas as Emitters", *Proceeding of the 5th EuCAP*, pp. 462-466, April 2011.
13. Y. Huang, **N. Khiabani**, Y. Shen, D. Li, "Terahertz Photoconductive Antenna Efficiency ", *Proceeding of the iWAT 2011*, pp. 152-156, Hong Kong, March 2011.
14. **N. Khiabani**, Y. Huang, Y. C. Shen, D. Li, S. Boyes, "Substrate Effects on the Performance of Photoconductive Antennas", *3rd China-Europe Workshop on Millimetre waves and Terahertz Technologies*, September 2010.
15. D. Li, Y. Huang, Y. C. Shen, **N. Khiabani**, "Effects of Substrate on the Performance of Photoconductive THz Antennas", *Proceeding of the iWAT 2010*, Portugal, March 2010.

Contents

Chapter 1. Introduction 1

- 1.1. The Terahertz Spectrum 1
- 1.2. THz Sources 2
  - 1.2.1. THz Sources from RF/MW Side 2
  - 1.2.2. THz Sources from Optical Side 4
  - 1.2.3. THz Sources Combining RF/MW and Optical Techniques 5
- 1.3. THz Detectors 7
- 1.4. The THz Wave Properties and Applications 9
  - 1.4.1. Atmospheric Characteristics of THz Waves 10
  - 1.4.2. Applications of THz Radiation 11
- 1.5. Research Motivations and Objectives 15
- 1.6. Thesis Overview 17

Chapter 2. THz Generation and Detection Systems Based upon the Antenna 20

- 2.1. Introduction 20
- 2.2. The Laser Pulses 21
- 2.3. The EO Crystal 22
- 2.4. The THz Photoconductive Antenna 24
  - 2.4.1. Working Principle of a THz Photoconductive Antenna as an Emitter 26
  - 2.4.2. Working Principle of a THz Photoconductive Antenna as a Detector 29
- 2.5. The THz Pulsed Systems 30
  - 2.5.1. Characterisation of THz Pulsed Systems 31
  - 2.5.2. Comparison of Ultra-Wideband THz Systems 36
- 2.6. The THz CW Systems 42
- 2.7. Summary 44

Chapter 3. THz Antennas 46

- 3.1. Introduction 46
- 3.2. Necessity of Having a THz Antenna in a THz System 47
- 3.3. Comparison of THz Antennas with RF/MW Antennas 47
  - 3.3.1. Excitation Source, Feeding and Biasing 48
  - 3.3.2. Substrate Material 49
  - 3.3.3. Antenna Electrode Material 54
  - 3.3.4. Type of Current 55
  - 3.3.5. Fabrication and Measurement 55
  - 3.3.6. Computer Aided Design 57
- 3.4. Problems of THz Antennas 58
  - 3.4.1. Problems Related to THz Photoconductive Antennas 60
  - 3.4.2. Problems Related to THz Photomixer Antennas 62
- 3.5. Requirements for High Power and Efficient THz Antennas 63
  - 3.5.1. Improvements in Time-Varying Transient Photocurrent 65
  - 3.5.2. Improvement in Antenna Impedance Matching 75
  - 3.5.3. Improvement in Coupling of THz Wave to Air 76
  - 3.5.4. Other Methods for Improving the THz Radiated Power 77
- 3.6. THz Antennas for Various Applications 78
- 3.7. Summary 79

Chapter 4. Source Conductance in THz Antennas 81

- 4.1. Introduction 81
- 4.2. Source Conductance of THz Photoconductive Antennas 82
  - 4.2.1. Derivation of the New Source Conductance Equation 83
  - 4.2.2. Parameter Analysis 88
- 4.3. Source Conductance of THz Photomixer Antennas 94

4.3.1. Parameter Analysis 97

4.4. Comparison of Source Conductance of THz Antennas 101

4.5. Summary 104

Chapter 5. Theoretical Modelling of a Photoconductive Antenna in a Terahertz Pulsed System 106

5.1. Introduction 106

5.2. Generation of THz Wave from a THz Photoconductive Antenna 107

5.3. Antenna Equivalent Circuit Analysis 109

5.4. Antenna Radiated Power and Efficiency Analysis 117

5.5. Summary 125

Chapter 6. Further Investigation of THz Antennas from Substrate Effect and CAD Analysis Perspectives 127

6.1. Introduction 127

6.2. Effect of Substrate Thickness on Performance of THz Antennas 128

6.2.1. Basic Theory 129

6.2.2. Analytical Discussions on Different Modes in a THz Antenna 130

6.3. A Novel Simulation Method for THz Photoconductive Antenna Characterization 137

6.3.1. Modelling Technique 138

6.3.1.1. Optoelectronic Analysis 139

6.3.1.2. EM Analysis 139

6.3.2. Parametric Study and Analysis 141

6.4. Summary 145

Chapter 7. A Top Loaded Antenna for a THz Photomixer Antenna 147

7.1. Introduction 147

7.2. Equivalent Circuit of a THz Photomixer Antenna 147

7.3. Photomixer Analysis 150

7.4. Antenna Design Analysis 159

  7.4.1. Source Resistance of the New THz Photomixer Antenna 160

  7.4.2. Choke Filter Elements 162

  7.4.3. Proposed THz Photomixer Antenna 163

  7.4.4. Coupling of THz Wave to Air 170

7.5. Measurement Results 174

  7.5.1. Antenna as the Emitter 177

  7.5.2. Antenna as the Detector 179

7.6. Summary 181

Chapter 8. Conclusions and Future Work 183

8.1. Conclusions 183

8.2. Future work 188

References 190

Appendix A E-field of THz Small and Large Gap Antennas 216

A.1. Small Gap THz Antennas 216

A.2. Large-Aperture THz Antennas 219

List of Figures

Fig. 1.1 Schematic diagram showing the location of THz band in the electromagnetic spectrum .. 1

Fig. 1.2 Schematic diagram of a THz antenna as an emitter for both pulsed and CW THz systems, showing the optical laser illumination, photoconductive substrate, metallic antenna with a bias voltage, and the antenna gap 6

Fig.1.3 An outline of THz sources, average THz output power versus frequency. The same colours correspond to the same type of the device and more information on the devices in the same category is stated in the legend and relevant references. 7

Fig. 1.4 Block diagram of a THz heterodyne detector 8

Fig. 1.5 Schematic diagram of a THz antenna as a THz detector for both pulsed and CW THz systems, unlike the emitter, THz detector has no bias voltages and THz waves usually come from the substrate direction while the optical pulses hit the detector from the antenna side. 9

Fig. 1.6 Attenuation at sea level for different atmospheric situations, Rain = 4 mm/h, Fog = 100 m visibility, STD = 7.5 g/m^3 water vapour, and 2×STD = 15 g/m^3 water vapour [31] 10

Fig. 1.7 Schematic overview illustrating some of commercial and laboratory applications of THz pulsed imaging and spectroscopy across the various sciences 13

Fig. 1.8 Schematic diagram of THz communication links for (a) system of [60] with external modulator (b) system of [61] where voltage modulation of the THz antenna is used. 14

Fig. 2.1 Schematic diagram of (a) temporal electric field of optical laser pulses at the photoconductive substrate for a pulsed system (b) corresponding spectral distribution of electric field of an ultra-short pulse 22

Fig. 2.2 Schematic diagram of (a) temporal (b) spectral electric field of optical laser pulses at the photoconductive substrate for a CW system 22

Fig. 2.3 Diagram of the common arrangement for THz detection based upon an EO crystal, I_0 shows the optical (probe) pulse intensity and Δφ represents the differential phase retardation due to the Pockels effect while the waves propagate in EO crystal and it is proportional to the E_{THz}. 24

Fig. 2.4 Sketch of THz photoconductive antennas (a) small gap bowtie antenna (b) large-aperture coplanar strip line. For large-aperture antenna larger laser spot size is used; hence, the illumination area and the photoconductive gap size between two electrodes of the antenna are larger. 26

Fig. 2.5 (a) Schematic diagram of the THz pulsed setup including both the major optical and electronic components when the emitter is THz photoconductive antenna and the receiver is EO crystal (b) experimental THz setup 32

Fig. 2.6 Detected THz signal in the time domain using photoconductive antenna as the emitter and ZnTe crystal as the detector 33

Fig. 2.7 Corresponding Fourier transform amplitude spectrum of Fig. 2.6 with dynamic range of 25 dB 34

Fig. 2.8 Schematic diagram of the THz pulsed setup where the emitter and the receiver are both EO crystals. Here, the lock-in amplifier is referenced to the mechanically chopped pump beam. 34

Fig. 2.9 Temporal detected THz signal for the THz pulsed system when both the emitter and detector are EO crystals 35

Fig. 2.10 Corresponding Fourier transform amplitude spectrum of Fig. 2.9 with dynamic range of 18 dB 36

Fig. 2.11 Comparison of (a) forward and (b) backward THz wave detection from a photoconductive antenna 38

Fig. 2.12 Comparison of (a) forward and (b) backward THz wave generation from a photoconductive antenna 39

Fig. 2.13 Schematic diagram of a common THz CW system 43

Fig. 2.14 Size comparison of laser sources for THz systems (a) Ti: Sapphire laser with an external power supply and a separate chiller compound for pulsed systems, dimensions of pump laser is 152.4 × 60.9 × 23.6 cm [104] (b) the world most compact Ti: Sapphire laser with dimensions of

22.5 × 22.5 × 6.2 cm [105] (c) laser diode for CW systems with dimensions of 1.2 × 0.9 × 0.7 cm [106] 44

Fig. 3.1 Common (a) RF/MW antenna (b) THz antenna measurement setup (both the emitter and detector are antennas) 48

Fig. 3.2 Measured carrier lifetime of LT-GaAs as a function of growth temperature from references [86, 96, 123, 135-138] 52

Fig. 3.3 Measured THz output power from a THz photoconductive antenna as a function of average input optical power from references [69, 141, 160, 163, 164, 167, 168] 59

Fig. 3.4 Measured THz output power from a THz photomixer antenna as a function of average input optical power at various single working frequencies from references [100, 131, 162, 169-173] 59

Fig. 3.5 Contribution of each parameter on THz output power and optical-to-THz conversion efficiency 64

Fig. 3.6 Schematic view of THz large gap antenna with interdigitated fingers (a) without metallization layers (top view) (b) with metallization layers (top view) (c) with active layer lift-off between every other two electrodes (side view). The arrows demonstrate the direction of the E-field. 68

Fig. 3.7 (a) large gap interdigitated antenna without lens (top) and with micro-lens (bottom) [164] (b) large gap interdigitated antenna with binary phase mask to generate a single cycle THz pulse [190] 69

Fig. 3.8 (a) Mesa structured antenna, parts of substrate are removed and electrode contacts are in vertical position [165] (b) E-field distribution in planar electrode geometry (c) E-field distribution in mesa structured electrodes 70

Fig. 3.9 Schematic view of the material structure of a THz antenna with AR coating on top of the antenna electrodes and Bragg reflectors beneath the photoconductive layer, explanation for each layer and wave is numbered. 71

Fig. 3.10 SEM image of the THz photoconductive antenna with (a) nanorods [194] (b) nanoislands [195] in the photoconductive gap 72

Fig. 3.11 SEM image of plasmonic THz dipole arrays [141] , a middle ground electrode is added to collect the remaining electron-holes in the antenna gap quicker to prevent screening effect.... 73

Fig. 3.12 Schematic and SEM image of the (a) conventional bowtie antenna (b) nanoplasmonic bowtie antenna, under illumination of a transverse magnetic polarized optical pump, surface plasmon waves are excited along the periodic metallic grating interface [160] 74

Fig. 3.13 SEM image of the nanoplasmonic interdigitated antenna [199] 74

Fig. 3.14 SEM image of the tip-to-tip rectangular nano gap meander antenna [191] 75

Fig. 3.15 (a) dual dipole antenna [200] (b) dual slot antenna [200] (c) four-leaf-clover-shaped antenna [201] (d) Yagi antenna [202] 75

Fig. 3.16 (a) SEM image of THz horn antenna with interdigitated fingers for a CW system [173] (b) Schematic image of TEM horn antenna with CPW feeding for a pulsed system [205] 76

Fig. 3.17 Schematic view of a bullseye dipole antenna (left) and cross section of the grooved structure (right) [206] 77

Fig. 3.18 SEM image of (a) Sierpinski (b) complementary Sierpinski (c) Apollonian and complementary Apollonian THz photoconductive antennas [208] for various orders of a fractal structure 78

Fig. 3.19 (a) three-contact THz photoconductive antenna as a detector. Two lock-in amplifiers are connected to electrode 1 and electrode 2 [210] (b) four-contact THz photoconductive antenna as an emitter. The antenna is biased in a way to receive two electrical fields in + 45° and -45° directions [211]. 79

Fig. 4.1 Equivalent circuit for a (a) conventional RF/MW antennas, Z_c denotes the source resistance (b) THz photoconductive antenna, $G_s^{-1}(t)$ represent the source resistance. Here it is assumed that reactive loading to the antenna is negligible. 83

Fig. 4.2 Schematic geometry of a THz photoconductive antenna (a) side view (b) top view 84

Fig. 4.3 Comparison of the photocurrent from the exact and approximate source conductance equations 86

Fig. 4.4 The time-dependant source conductance of a THz photoconductive antenna for a common THz pulsed system where μ_e= 1000 cm^2.V^{-1}.s^{-1}, R = 0.318, α = 6000 cm^{-1}, f_l = 375 THz, f_{rep} =80 MHz, τ_l = 100 fs, P_{av} = 1 W, τ_c= 1 ps, L = 10 μm, W = 10 μm and $T_{LT\text{-}GaAs}$ = 1 μm. 87

Fig. 4.5 Variation of the time-dependant conductance of a photoconductive material by the average optical power 89

Fig. 4.6 Time-dependant source conductance of a THz photoconductive antenna for different laser pulse durations 90

Fig. 4.7 Dependency of temporal source conductance of a THz photoconductive antenna to various antenna gap areas for the fixed average input optical power 90

Fig. 4.8 Change of temporal source conductance of a THz photoconductive antenna as a result of various laser spot shape for a constant laser pulse intensity 91

Fig. 4.9 Behaviour of temporal source conductance of a THz photoconductive antenna for various carrier mobility 92

Fig. 4.10 Variation of temporal source conductance of a THz photoconductive antenna by changing the carrier lifetime 93

Fig. 4.11 Dependency of temporal source conductance of a THz photoconductive antenna on optical absorption coefficient 94

Fig. 4.12 Schematic geometry of a THz photomixer antenna (a) side view (b) top view 95

Fig. 4.13 The time-dependant source conductance of a THz photomixer antenna for a common THz CW system where μ_e= 1000 cm^2.V^{-1}.s^{-1}, R = 0.318, α = 6000 cm^{-1}, f_l = 374.5 THz, P_{av} = 15 mW (for one laer), τ_c= 1 ps, L = 10 μm, W = 10 μm , $T_{LT\text{-}GaAs}$ = 1 μm and f_{THz} = 1 THz. 97

Fig. 4.14 Average source resistance of a THz photomixer antenna versus total average optical power 98

Fig. 4.15 Variation of the average source resistance of a THz photomixer antenna as a function of antenna gap length (and width) at a constant optical power..98

Fig. 4.16 Dependency of average source resistance of a THz photomixer antenna on carrier lifetime of the photoconductive material...99

Fig. 4.17 Dependency of average source resistance of a THz photomixer antenna on carrier mobility of the photoconductive material 100

Fig. 4.18 Variation of average source resistance as a function of both the carrier mobility and lifetime 100

Fig. 4.19 Average source resistance of a THz photomixer antenna as a function of optical absorption coefficient..101

Fig. 4.20 Source conductance of an antenna in the time domain for (a) the pulsed system (b) the CW system with identical parameters. It is assumed that the average optical power on each antenna is 100 mW. 102

Fig. 4.21 Comparison of the average source resistance of the THz antenna in a CW setup and resistance of the same antenna corresponding to the peak conductance in a pulsed setup at different optical powers on the antenna 103

Fig. 4.22 Matching efficiency comparison for a 60° long bowtie antenna with $R_a = 90\ \Omega$ in the CW and pulsed systems 104

Fig. 5.1 Generation of THz waves using the THz photoconductive antenna under the illumination of laser pulses; antenna electrodes are shown in the inset..108

Fig. 5.2 The equivalent circuit of the THz photoconductive antenna as an emitter....................110

Fig. 5.3 Temporal behaviour of (a) $G_s(t)$ and (b) $C(t)$ for different average optical power 114

Fig. 5.4 Temporal behaviour of $C(t)$ as a function of various carrier recombination time..........115

Fig. 5.5 Time dependant characteristics of $C(t)$ for various carrier life time 115

Fig. 5.6 Dependency of temporal characteristics of $C(t)$ on the antenna gap length 116

Fig. 5.7 Temporal behaviour of the voltage across the antenna gap, V_c, the reverse voltage source responsible for the screening, $V_{e\text{-}h}$ ($=V_{bias} - V_c - V_{rad}$), and the voltage across the radiating element (the antenna), V_{rad}, for two different average optical powers. 117

Fig. 5.8 The average radiated THz power versus the average input optical power for different bias voltages for $Z_a = 65\ \Omega$. The measurement results are from [69] at $V_{\text{bias}} = 30$ V. 119

Fig. 5.9 (a) The average radiated THz power and (b) the peak optical-to-THz power conversion efficiency versus average optical powers for different antenna resistances when the bias voltage is 30 V.. 120

Fig. 5.10 The peak optical-to-THz power conversion efficiency as a function of the average optical powers for different bias voltages for $Z_a = 65\ \Omega$. The measurement results are from [69]. 121

Fig. 5.11 Comparison of the optical-to-THz power conversion efficiency and electrical-THz conversion efficiency for the bias voltage of 30 V and $Z_a = 65\ \Omega$... 122

Fig. 5.12 Dependency of (a) peak optical-THz power conversion efficiency (b) average radiated THz power on average optical powers for antennas with different gap lengths when V_{bias}= 30V, $Z_a = 65\ \Omega$, W=10 μm. 123

Fig. 5.13 Dependency of the peak optical-to-THz power conversion efficiency on the average optical power for different optical absorption when the bias voltage is 30 V, antenna resistance is 65 Ω and $R = 0.318$.. 124

Fig. 5.14 Variation of the peak optical-to-THz conversion efficiency versus optical powers for different reflection coefficients from the air-substrate interface, when the bias voltage is 30 V, $Z_a = 65\ \Omega$ and $\alpha = 6\text{x}10^5\ \text{m}^{-1}$ 124

Fig. 6.1 (a) Dipole antenna surrounded by air and its radiation pattern (b) Dipole antenna on a GaAs substrate and its radiation pattern.. 128

Fig. 6.2 Reflection and transmission of wave at an oblique angle on an interface of two media, θ_i is the incident angle, θ_r is the reflection angle, and θ_t is the transmission angle 130

Fig. 6.3 Radiated mode (solid line) and guided or surface mode (dash line) of a Hertzian dipole antenna on the semi-infinite substrate with permittivity of ε_r... 130

Fig. 6.4 Normalised radiated power of a Hertzian THz dipole antenna on an ungrounded semi-infinite GaAs substrate 132

Fig. 6.5 Schematic of the antenna on the substrate for guided (surface) mode analysis 133

Fig. 6.6 Guided wave power for each mode in relation to different electrical substrate thickness 134

Fig. 6.7 Total guided power for PC antenna versus ratio of substrate thickness to dielectric wavelength 135

Fig. 6.8 Radiation efficiency from the dipole antenna on a GaAs substrate 135

Fig. 6.9 TM and TE guided wave modes in the substrate with $\varepsilon_r = 12.9$ 136

Fig. 6.10 Schematic of the simulated antenna to derive the antenna gain for variable substrate thicknesses 136

Fig. 6.11 Simulated gain as a function of substrate electrical thickness 137

Fig. 6.12 Schematic geometry of a THz dipole antenna. The antenna gap is illuminated by laser and the field is probed along the antenna length at z = -1000 μm 138

Fig. 6.13 Numerically calculated photocurrent for the gap length × width of 5 × 10 μm, laser pulse duration of 120 fs, carrier lifetime of 1 ps, mobility of 200 cm^2 V^{-1} s^{-1}, optical absorption of 6000 cm^{-1}, and bias voltage of 30 V 139

Fig. 6.14 Spectral variation of the detected THz signal for the emitter antenna with H = 100 μm and carrier lifetime of 1 ps 141

Fig. 6.15 (a) amplitude of THz signal THz signal for spectral coverage comparison for H = 100 μm and laser pulse duration of 120 fs (b) normalised amplitude of the calculated, “em” stands for emitter and “rec” stands for the detector 142

Fig. 6.16 Detected THz signal amplitude for dipole antenna with a constant 10 μm gap width, laser pulse duration of 120 fs and carrier lifetime of 1 ps 143

Fig. 6.17 Amplitude of THz signal dipole antenna with a fixed gap length of 5 μm, H = 100, laser pulse duration of 120 fs and carrier lifetime of 1 ps 144

Fig. 6.18 (a) Simulation of the detected THz signal for various dipole antenna length (b) corresponding experimental results [237] 145

Fig. 7.1 Equivalent circuit of a THz photomixer antenna as an emitter 148

Fig. 7.2 (a) bare electrode (b) six-finger interdigitated electrode (c) six-finger tip-to-tip rectangular electrodes (d) six-finger tip-to-tip trapezoidal electrodes 152

Fig. 7.3 Comparison of the static electric field amplitude for the bare, interdigitated, rectangular and trapezoidal finger tips at different depth of substrate (substrate thickness is towards the –z direction) 155

Fig. 7.4 E-field profile (left) and amplitude of E-field in the near field (right) of (a) bare electrodes (b) interdigitated electrodes (c) tip-to-tip rectangular electrodes (d) tip-to-tip trapezoidal electrodes under illumination of a 1 THz plane with fixed amplitude of 1 V/m, polarisation of illuminated E-field is shown below of each figure. Please note that E-fields in near field of (a) and (b) are clamped to 15 V/m whilst those of (c) and (d) are clamped to 150 V/m. 157

Fig. 7.5 (a) Photomixer geometries, E-fields are monitored along the dashed lines (b) Monitored E-field on the electrode plane under illumination of a 1 THz plane wave with 1V/m amplitude. In the legend “Tra” stands for trapezoidal fingers and “Rec” stands for rectangular fingers 158

Fig. 7.6 (a) Bare electrodes with the equivalent circuit (R_{scw1} and C_{elec1} are respectively photoconductive resistance and electrode capacitance) (b) tip-to-tip trapezoidal finger electrodes with the equivalent circuit (n is the number of finger couples, R_{scw2} and C_{elec2} are respectively photoconductive resistance and capacitance between each electrodes and n shows the number of coupled electrodes) 161

Fig. 7.7 (a) Coplanar transmission line model (b) Choked transmission line model (c) Simulated S_{21} for the coplanar stripline without and with the choke filter ($L_{ch\text{-}h} = L_{ch\text{-}l} = 26$ μm) 163

Fig. 7.8 The proposed THz antenna structure consists of the top loaded antenna, and choke filter as a DC bias line and stop filter for 1 THz current 164

Fig. 7.9 Impedance of the full wavelength dipole antenna (108 × 2 μm) with and without photomixer capacitance and with choke filter (a) resistance (b) reactance (values of dipole with photomixer capacitance is magnified by a factor of 10) 166

Fig. 7.10 The resistance of the top hat load antenna with and without tuning stub.................... 167

Fig. 7.11 (a) Antenna resistance (b) matching efficiency curves for different L_{sep}..................... 168

Fig. 7.12 Matching efficiency in relation to different D_{t1} and the corresponding D_{t3}................. 169

Fig. 7.13 Comparison of matching efficiency variation by changing only D_{t2} and both D_{t2} and D_{t4} 170

Fig. 7.14 Radiation pattern of the photomixer THz antenna at 1 THz in (a) xoy plane (b) xoz plane... 170

Fig. 7.15 Integrated top loaded THz photomixer antenna in a conical horn. ITO layer is depicted partially transparent in order to see the THz photomixer antenna 171

Fig. 7.16 Geometry of the conical horn 172

Fig. 7.17 (a) 2D radiation pattern of conical antenna integrated with the photomixer THz antenna with and without ITO layer at xoz plane and (b) yoz plane at 1 THz 173

Fig. 7.18 3D radiation pattern of the completed antenna 174

Fig. 7.19 (a) Fabricated THz bowtie antennas with different photomixer geometries (b) A packaged antenna for the measurement. The black connection is for the biasing purposes when the antenna is employed as an emitter, and it is connected to the lock-in-amplifier when it is positioned in the detector side. 175

Fig. 7.20 Microscopic images of the THz bowtie antenna with trapezoidal tip-to-tip fingers (a) overall antenna view (b) zoom-in of the photomixer section (c) SEM zoom-in of the trapezoidal tip-to-tip finger (d) SEM zoom-in of a nanogap trapezoidal finger... 176

Fig. 7.21 THz CW measurement setup based upon fibre optics... 177

Fig. 7.22 Schematic image of the THz CW measurement setup when the antenna is used as an emitter. In this case, Golay cell was used as the detector.. 177

Fig. 7.23 Measured THz power for three various photomixer geometries used in the gap of identical bowtie antennas 179

Fig. 7.24 Measured THz power of different photomixer geometries in linear scale 179

Fig. 7.25 (a) Schematic image of the THz CW measurement setup when the antenna under test is employed as the detector (b) The employed log spiral antenna with a p-i-n gap as the emitter [253].......... 180

Fig. 7.26 Detected THz signal from three photomixer geometries used in the gap of identical bowtie antennas 181

List of Tables

Table 2.1 Comparison of two THz systems based on various emitters whilst the detector is fixed 36

Table 2.2 Dependency of THz signal to frequency based on the emitter and detector type 40

Table 2.3 Comparison of THz pulsed and CW systems 43

Table 3.1 Properties of various photoconductive materials in THz antennas 54

Table 3.2 Comparison of THz antennas with common RF/MW antennas 57

Table 5.1 Laser, photoconductive material and antenna parameters 113

Table 5.2 Parameter ranges for the maximum optical-to-THz efficiency for a desired average optical power range 125

Table 7.1 Laser, Photoconductive material and photomixer electrode parameters used in equation (4.18) 162

Table 7.2 Design parameters of the antenna 167

Table 7.3 Additional design parameters for the conical horn part 173

List of abbreviation

AlGaAs	Aluminium Gallium Arsenide
AR	Anti-Reflection
BW	Bandwidth
BWO	Backward Wave Oscillator
CAD	Computer Aided Design
CW	Continuous Wave
CPW	Coplanar Waveguide
DFG	Difference Frequency Generation
EM	ElectroMagnetic
EO	Electro-Optic
ErAs	Erbium Arsenide
FDTD	Finite Difference Time Domain
FWHM	Full Width at Half Maximum
GaAs	Gallium Arsenide
HEB	Hot Electron Bolometer
IMPATT	IMPact Avalanche and Transit Time
ITO	Indium Tin Oxides
LEC	Liquid Encapsulated Czochralski
LT-GaAs	Low Temperature-GaAs
MBE	Molecular Beam Epitaxy
MEMS	MicroElectroMechanical System
MMIC	Monolithic Microwave Integrated Circuits
MW	Microwave

QCL	Quantum-Cascade lasers
QTDS	Quasi Time Domain Spectroscopy
RF	Radio Frequency
RTD	Resonant Tunnelling Diodes
RX	Receiver
SEM	Scanning Electron Microscopy
Si	Silicon
SI-GaAs	Semi-Insulating GaAs
SI-InP	Semi-Insulating Indium phosphide
SIS	Superconductor–Insulator– Superconductor
SNR	Signal-to-Noise Ratio
TEM	Transverse ElectroMagnetic
THz	Terahertz
THz-TDI	THz Time Domain Imaging
THz-TDS	THz Time Domain Spectroscopy
Ti	Titanium
TWT	Travelling Wave Tube
TX	Transmitter
ZnTe	Zinc Telluride

Preface

tera:

Symbol T. A prefix used in the metric system to denote one million million times. For example, 10^{12} volts = 1 teravolt (TV).

Oxford Dictionary of Physics (6th ed.)

hertz:

Symbol Hz. The SI unit of frequency equal to one cycle per second. It is named after Heinrich Rudolf Hertz (1857-94), a German physicist, best known for his 1888 discovery of radio waves, as predicted by James Clerk Maxwell.

Oxford Dictionary of Physics (6th ed.)

antenna:

It is a means for radiating or receiving radio waves as defined by the IEEE Standard Definitions [1].

Chapter 1. Introduction

1.1. The Terahertz Spectrum

The THz radiation is typically used to describe the region of the electromagnetic spectrum in the range of 100 GHz (3 mm) to 10 THz (30 μm) [2, 3], which is between the millimetre and infrared frequencies. THz band has variously been named such as sub-millimetre, far infrared and near millimetre wave. At 1 THz, the radiated signal has a wavelength of 300 μm in free space, a period of 1 ps, a photon energy of 4.14 meV and hf/k_B = 48 K temperature; where h is Planck's constant, f is the frequency and k_B is Boltzmann's constant. The THz band in the electromagnetic spectrum is depicted in Fig. 1.1.

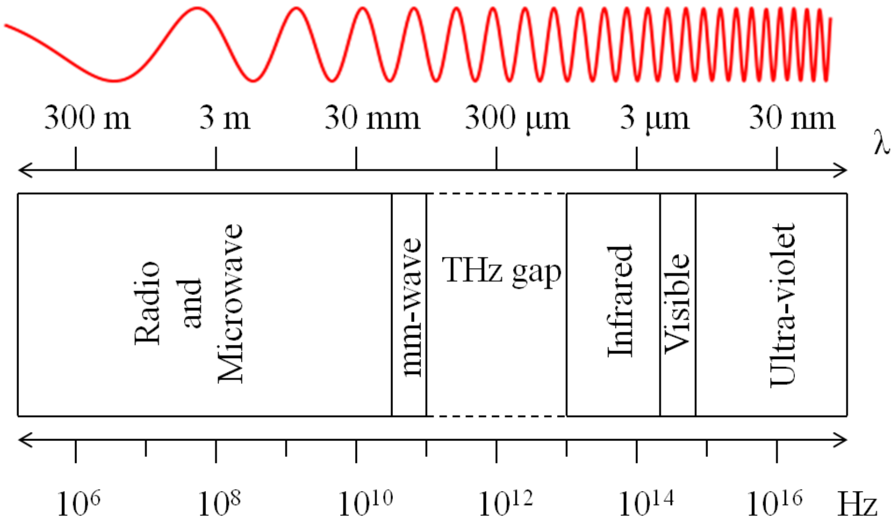

Fig. 1.1 Schematic diagram showing the location of THz band in the electromagnetic spectrum

This portion of the electromagnetic spectrum is the least investigated area because of the absence of efficient, coherent, and compact THz sources and detectors [3, 4]. These characteristics for the sources can be found in the common microwave-frequency sources such as transistors or RF/MW antennas, and in devices working in the visible and infrared range like semiconductor laser diodes [5]. However, it is not possible to adopt these technologies for operation in THz region without a significant reduction in power and efficiency. At the lower extreme of THz frequency range, the generated power by solid-state electronic devices, such as diodes, has roll-offs of $1/f^2$ [6] due to reactive-resistive effects and long transit times. On the other hand, optical devices, such as diode lasers, do not perform well at THz range limit because of the lack of materials with adequately small bandgap energies [5]. Hence the term "THz gap" is phrased to explain the infancy of this band as compared to well-developed neighbouring spectral regions. Recent advances have commenced to address this problem, and various types of new emitters and detectors based on semiconductor technology are emerging [4, 7-9].

In this chapter, first, different THz sources and detectors are reviewed and evaluated. Then, THz wave properties and potential applications are described. Based on the built foundation, the research motivations and objectives of this thesis are outlined.

1.2. THz Sources

The THz source has been considered the most difficult component to realise among all the elements in this technology [10]. A great deal of effort has been put to extend RF/MW and optical technologies to THz band, and even combine them in order to realise THz sources with better performance [11]. Thus, THz emitters are divided into three main groups: THz sources developed from RF/MW side, THz sources extended from optical side, and THz sources combining RF/MW and optical techniques. These are now summarised briefly in sequence.

1.2.1. THz Sources from RF/MW Side

In this category, diodes and THz vacuum tube sources are explained.

1.2.1.1. Diodes and Frequency Multipliers

On the lower end of THz spectrum, diodes can transfer the functionality of lower frequency electronics into the THz band. There are several types of diodes, such as Gunn diodes, IMPATT diodes and resonant tunnelling diodes (RTD). Although the operation bases of these diodes are different the principle of power generation from these diodes is alike, and it is based upon their negative differential resistance [12]. Each of these diodes has its own advantages and disadvantages [12-17]; nevertheless, in these components by increasing the frequency there is a dramatic reduction in powers [14].

Another method to reach THz band is the use of frequency multipliers, which outperform other solid-state electronic sources. This is because the diode multipliers are operationally and physically simple [13]. Since higher order multipliers are extremely inefficient, series arrangements of doublers and triplers have mostly been implemented [10]. In this method, chains of microwave sources, such as GaAs Schottky diodes, at lower GHz bands (20 – 40 GHz) can be used in a series in order to drive multiplication at THz ranges [13]. However, the output power from multipliers decreases at higher frequencies [18] and the bandwidth of these sources is limited.

1.2.1.2. THz Vacuum Tube Sources

Free electrons emission from microwave tubes is one of the traditional THz generation methods. THz tubes such as klystron, travelling wave tube (TWT), backward wave oscillator (BWO), and gyratron can produce strong power levels at lower end of THz band; for instance, a power level of 52 mW at about 0.6 THz from a BWO has been reported [19]. One of the main operational similarities in all of these tubes is the interaction of electron beam with an electromagnetic wave to produce THz energy. Although THz tubes can produce much stronger power levels at lower end of THz band as compared to previously explained solid-state components [12], they are very bulky and need large magnetic biases and high voltage power supplies. These restrict the use of these sources in wide operational settings.

1.2.2. THz Sources from Optical Side

THz sources from optical side are mainly divided in to lasers with different generation techniques and nonlinear crystals.

1.2.2.1. Molecular Lasers

Injection of grating tuned CO_2 lasers into low-pressure flowing gas cavities leads to generation of THz signals with a power level of few ten milliwatts [10]. The frequency of this THz power depends on the spectral line of gas; for example, a rotational transition of methanol occurs at 2.522 THz.

1.2.2.2. THz Semiconductor Lasers

Semiconductor diode lasers are very successful and prevalent in the near-infrared and visible frequency ranges, however; for THz bands materials with suitable band gaps are not available unless considering artificially engineered materials [5, 20]. Therefore, the concept of THz Quantum-Cascade lasers (QCL), which are intra-band lasers and require the creation of quantized sub-bands, was introduced [4]. For this purpose, several few-nm-thick GaAs layers separated by AlGaAs barriers need to be fabricated. Therefore, proper engineering of the thickness of the semiconductor layers (or quantum wells) and also choice of the appropriate bias voltage is required to achieve population inversion. The energy of the system is inversely proportional to the square of the layers thicknesses; therefore, by narrowing or widening the quantum wells, series of multi layers of energy can be created. The electron motion from one miniband to the next, results in an emission of a THz photon at each transition. QCL can operate in both pulsed and continuous-wave (CW) modes; its operating frequency is controlled by quantum well design (band gap engineering), and different wavelengths can be achieved in the same material. QCLs have been one of the most intensive research topics in THz area during the past decade. The survey on different THz QCLs show that the frequency range of these devices spans from 0.84 THz to 5 THz at various cryogenic working temperatures [21-24] with the peak optical power as high as about 200 mW at 4.5 THz [5] and the operation temperature as high as 200 K at about 3.2 THz [25]. It is good to add that a THz QCL with power of 8.5 μW at 4 THz has been demonstrated in room temperature situation [26]. To sum up, QCLs have larger output power at higher THz frequencies, and as frequency decreases the power reduces considerably. One of the main limitations of a THz QCL is that for THz operation, it needs cryogenic cooling, and this restricts operation of a QCL to the laboratory environments.

1.2.2.3. Optical Down Converters

One of the general methods for THz generation is the use of nonlinear crystals with large second order susceptibility, $\chi^{(2)}$, for down conversion of power from optical regime. Several nonlinear materials for this purpose can be employed [11]. THz parametric processes such as parametric oscillator or difference frequency generation (DFG) are techniques for generation of monochromatic highly tunable THz wave sources with high spectral resolution [27-29]. Another optical down conversion method is the optical rectification in which all possible difference frequencies of spectrally broad optical pulses are generated. The primary limitation of this technique is that phase matching between the optical fields and induced THz field is needed. This imposes careful design on thickness of the nonlinear material. The THz output power in this process is low; hence, high power optical sources are required for generating meaningful THz power. However, wide THz bandwidth from this method is achievable [3]. This scheme is explained further in detail in Chapter 2.

1.2.3. THz Sources Combining RF/MW and Optical Techniques

THz antennas that are based upon photoconduction can be allocated to this category of THz sources. As shown in Fig. 1.2, a THz antenna consists of a voltage-biased antenna mounted on a photoconductive substrate (commonly GaAs). Optical laser sources, as the excitation sources of THz antennas, are used to produce THz waves by inducing rapid changes in the carrier density of the photoconductive substrate. Depending on the type of optical excitation, there are basically two alternatives for THz antennas based upon the photoconduction technique:

1) THz photoconductive antennas in pulsed systems

2) THz photomixer antennas in CW systems

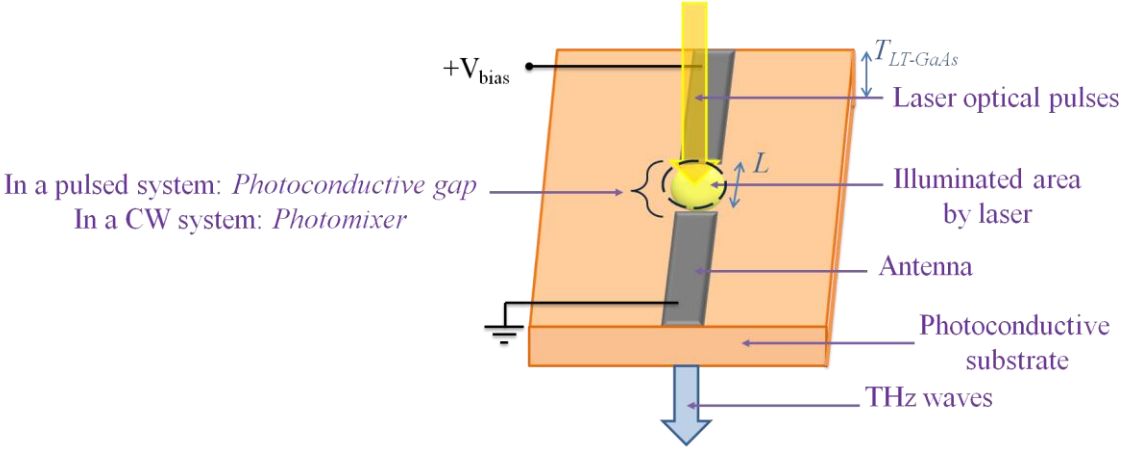

Fig. 1.2 Schematic diagram of a THz antenna as an emitter for both pulsed and CW THz systems, showing the optical laser illumination, photoconductive substrate, metallic antenna with a bias voltage, and the antenna gap

Although it is possible to use the same antenna in both systems, different excitation methods dictate different requirements for each antenna type and result in different THz waves and applications. In THz pulsed systems, because of the external bias field, the optically induced photo-carriers in the photoconductive gap give rise to rapid changes in the current density. These currents induce a THz electromagnetic field in the connected antenna and as a consequence ultrafast electrical pulses are produced and radiated into free space. In CW systems, the process is the same; however, usually two monochromatic lasers with slightly different optical frequencies (the difference is in THz) are used for THz emission from the antenna. This inherent excitation difference in THz pulsed and CW systems, leads to the generation of ultra wideband and narrow band THz waves respectively. In a CW system, the term of “photomixer” refers to the antenna gap (which can have various designs) in analogy of “photoconductive gap” in a THz pulsed system. The focus of this thesis will be on these types of sources. Detailed and comprehensive study and investigation on THz antennas will be presented in next chapters.

As a summary, THz emission power as a function of the frequency for different THz sources is illustrated in Fig.1.3. The results are gathered for various devices reported in the literature. The electronic sources reside in the lower frequency side of the graph and their power decreases with an increase of the frequency. The optical sources occupy the higher frequency side of the diagram and their power in general increases with the frequency.

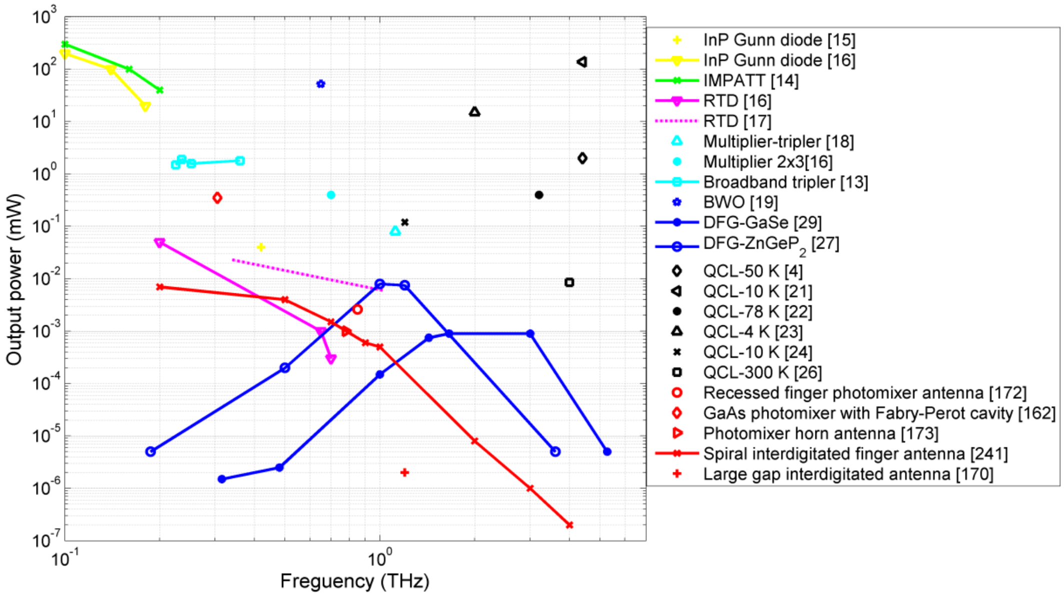

Fig.1.3 An outline of THz sources, average THz output power versus frequency. The same colours correspond to the same type of the device and more information on the devices in the same category is stated in the legend and relevant references.

1.3. THz Detectors

Progress in THz detectors have been faster than THz sources [10]. One of the main issues in detection of THz waves is that the photon energy in this frequency band is in the range of 0.41 to 41 meV, which is comparable to the background thermal noise energy. Therefore, to overcome this problem mainly two methods have been adopted: cryogenic cooling and signal integration for long enough periods [10].

It is possible to categorize THz detection into coherent and incoherent techniques. The main difference between them is that in coherent technique both the amplitude and phase of the received signal are determined; but, in incoherent technique only the intensity of the signal is measured.

Heterodyne detection is an important coherent technique in detecting weak and narrow band signals. In this method a mixer, a non linear device, as a local oscillator is used for frequency down conversion. The process of electronic heterodyne detection is demonstrated in Fig. 1.4. The amplitude of the detected signal is proportional to the amplitude of the THz signal [2]. There are various types of mixers in the THz range. A Schottky diode is a common and basic mixer type for room temperature detectors where a modest sensitivity is required. However, for high sensitivity applications, superconducting heterodyne detectors are employed which operate in cryogenic temperatures. Superconductor–Insulator–Superconductor (SIS) tunnel junction mixers and Hot Electron Bolometer (HEB) mixers are two examples of mixers in this category.

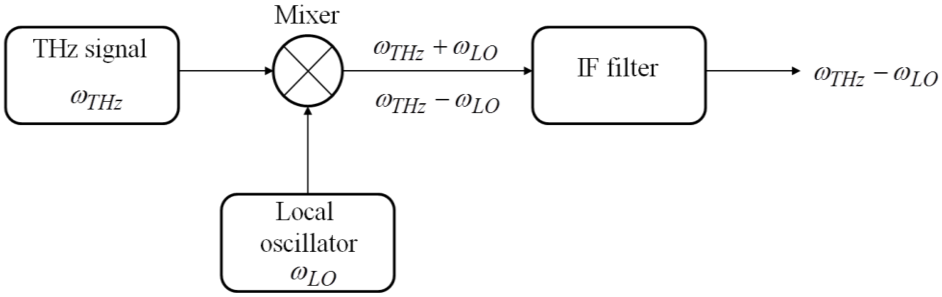

Fig. 1.4 Block diagram of a THz heterodyne detector

Electro-Optic (EO) and photoconduction samplings are also coherent methods. In the former, the amplitude and phase of the THz signal are measured by using a nonlinear crystal. In the latter type as shown in Fig. 1.5, the THz signal induces voltage across the antenna which leads to generation of THz current due to the existence of free electron-hole pairs in the antenna gap. The phase of the THz signal in these methods can be measured by varying the optical path length of the optical probe pulse. Working principle of these methods is elaborated in Chapter 2.

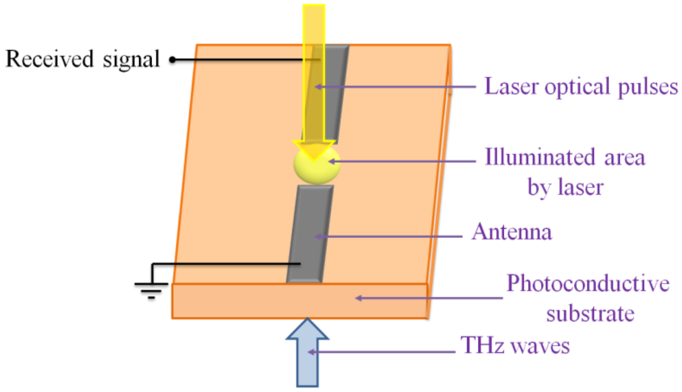

Fig. 1.5 Schematic diagram of a THz antenna as a THz detector for both pulsed and CW THz systems, unlike the emitter, THz detector has no bias voltages and THz waves usually come from the substrate direction while the optical pulses hit the detector from the antenna side.

Direct detectors such as Golay cells and bolometers are mainly incoherent detectors. These detectors in room temperature are appropriate for applications where high spectral resolution and rapid response time (it is in the order of seconds) are not required [10]. For a better sensitivity and dynamic range, cryogenic cooled direct detectors such as cryogenically cooled bolometers ,which have a response time in the order of microseconds, can be employed [10].

1.4. The THz Wave Properties and Applications

Although interest in the THz region dates back to the 1920s [30], extensive studies have been devoted to this region only within the past three decades. A key motivation for this is the exceptional wave properties and vast possible applications in the THz frequency range. Since the THz region lies between microwave-millimetre and infrared areas, it has mid-characteristics borrowed from the two bands. These properties can be summarised as follows:

1) *Penetration:* The wavelength of THz radiation is longer than the infrared wavelength; hence, THz waves have less scattering and better penetration depths (~ cm) compared to infrared ones (~ µm). Therefore, dry and non-metallic materials are transparent in this range but are opaque in the visible spectrum.
2) *Resolution:* THz waves have shorter wavelengths in comparison to the microwave ones; this gives a better spatial imaging resolution.

3) *Safety:* In contrast to X-rays, the photon energies in THz band are much lower. Therefore, THz radiation is non-ionising.
4) *Spectral fingerprint:* Inter- and intra-vibrational modes of many molecules lie in THz range.

1.4.1. Atmospheric Characteristics of THz Waves

THz radiation has distinct atmospheric characteristics compared to the microwave and infrared waves. THz waves have extremely high absorption in the atmospheric situation and the moist environment. The atmospheric attenuation across the electromagnetic spectrum is depicted in Fig. 1.6. It is obvious that signal degradation in this range- with the main peak attenuation between 1 to 10 THz- is considerably more than microwave and infrared bands. THz signal absorbs water significantly. Thus, for long range (> few hundred meters) applications the required power for signal transmission is high and impractical [6]. However, application of THz waves in the two following cases is different.

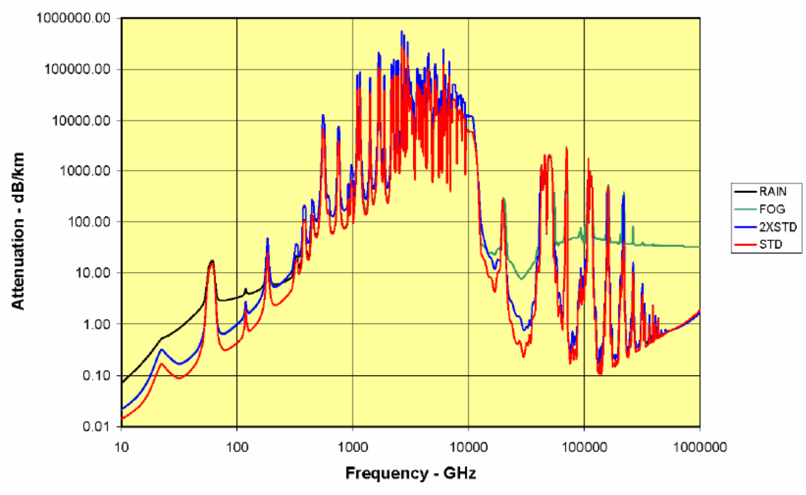

Fig. 1.6 Attenuation at sea level for different atmospheric situations, Rain = 4 mm/h, Fog = 100 m visibility, STD = 7.5 g/m^3 water vapour, and 2×STD = 15 g/m^3 water vapour [31][1]

1) In the space since the ambient is near-vacuum, signal absorption and attenuation due

---

[1] This graph has originally been presented in [33]; however, due to better presentation quality, for this thesis, it was taken from [31].

to water drops are not problems. Considering spectral signature of interstellar dust, which is located in THz region, and aforementioned advantage of THz signals in space, THz technology is a widely used technique in radio astronomy and space science [10]. For instance, Herschel Space Observatory, the largest infrared space telescope ever, was launched in 2009 in the THz region by the European Space Agency [32].

2) For short range applications (< 100 m [6]), atmospheric attenuation is not a significant issue. Hence, THz technology is a very versatile tool for fundamental investigations in various disciplines such as physics and chemistry.

It is good to add that despite adverse effect of water vapour lines on THz signals, these lines are narrow enough, and their positions have been known. Thus, this allows removal/recognition of their effect in THz applications such as spectroscopy [33].

1.4.2. Applications of THz Radiation

Based upon THz wave properties, THz radiation can be applied in many possible applications including imaging, spectroscopy and wireless communication [11, 34, 35]. Although THz applications have been widely investigated, only in the recent decade several commercial THz imaging and spectroscopy systems have entered the market by companies such as TeraView Ltd [36], Picometrix [37] and Toptica [38]. The first ever THz camera that can see and record in real-time at room temperature was introduced in early 2011 by Traycer [39]. Since the focus of this thesis is on THz antennas, THz applications related to optoelectronic (both pulsed and CW) systems are only briefly discussed in this section.

1.4.2.1. THz Pulsed System Applications

Since the work of pioneers in THz pulsed imaging [40] and THz CW imaging [41], applications based on THz imaging have been the focus of many research areas [34]. Indeed, medical imaging is one of the main subcategories in this field. THz waves can penetrate up to a few hundred micrometers (μm) in human tissues; therefore, it is a possible method for body surface diagnosis such as skin, breast and mouth cancer detection [36, 42, 43] and dental imaging [44]. Some of the benefits of this method can be named as, early detection of cancerous tissues and tooth decay or minimisation of the damage to the surrounding healthy skin in biopsy [36]. THz medical imaging has two major drawbacks; the equipment is expensive and data acquisition time is long. The latter disadvantage has been addressed by employing arrays of antennas and micro lenses [34].

THz pulsed spectroscopy has been another fascinating application for commercialising THz technology in diverse areas [10] since the first introduction of this method in [45]. Now THz spectroscopy is a very powerful technique to characterise material properties and understand their signature, which lies in the THz band (many molecules have rotational and vibrational transition lines in this range of frequency). One type of interesting THz spectroscopy applications is in biochemical science such as analysis of DNA signatures and protein structures [46].

Also, THz radiation is a suitable technique to investigate material integrity and inspect multi-layered materials such as wood, composites, and clothes which are transparent in THz frequencies. THz pulsed imaging and spectroscopy has been adopted for non-destructive testing; for example, on imaging antiquities [47, 48] to reveal the thickness of the different layers of the art work and to show types of their materials [49]. This technique can be used for in-line control of polymeric compounding processes as well [50].

Furthermore, THz pulsed imaging and spectroscopy are two strong quantitative and qualitative non-invasive methods for examining pharmaceutical solid dosage forms [51, 52].

THz systems have the potential market for security applications [34] because of the possibility of using these systems in personnel screening [36], solid explosive material detection [53, 54], and mail screening [55]. However, metals are not transparent to THz signals; therefore, they are not suitable for imaging inside the metallic suitcases. This method can be treated as a complementary scheme for the well-established monitoring techniques like X-ray [34].

Although high water absorption is one of the drawbacks of the THz technology, it can be manipulated positively to distinguish the hydrated substances from dried ones. For instance, in the paper industry, THz spectroscopy has been used for monitoring the thickness and moisture content of papers by manufacturers [56, 57].

Last but not least, THz pulsed imaging is a very convenient method to take 3D images from the inside of an integrated circuit device as compared to 2D images provided by the X-ray method [36].

As a summary, schematic overview of various THz applications based upon optoelectronic systems is depicted in Fig. 1.7.

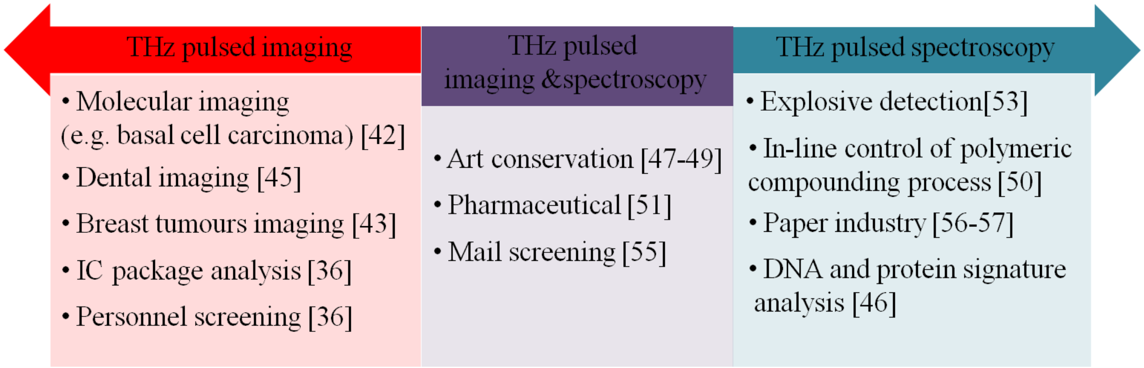

Fig. 1.7 Schematic overview illustrating some of commercial and laboratory applications of THz pulsed imaging and spectroscopy across the various sciences

It is good to mention that there is one interesting THz application which cannot be categorised in either THz pulsed imaging or spectroscopy; that is THz application in wireless communication. To provide sufficient transmission capacity for future high data rate demands, higher carrier frequencies need to be utilized and potentially THz frequencies can satisfy this need. However, THz communication links inherently have two main limitations: 1) THz signals can only propagate over a short path length without severe atmospheric attenuation 2) THz communication systems are only suitable for line of sight cases. Considering these restrictions, THz communication systems can be an appropriate option for indoor short distances (limited to several tens of meters) multipoint to point/multipoint basis at frequencies between about 0.2 to

0.3 THz [58]. From another point of view, these restrictions are beneficial for secure THz communication. Since the beam can be highly directional and it attenuates severely over the distance, unwanted signal detection is very difficult. Some THz data communications for short ranges (< 1m) based upon THz time domain systems have been tested at 0.3 THz in recent years [59]. In [60] external semiconductor THz modulator is used and in [61] audio signals through the voltage of the transmitter THz antenna modulates the THz frequency. Block diagrams of these two approaches are demonstrated in Fig. 1.8.

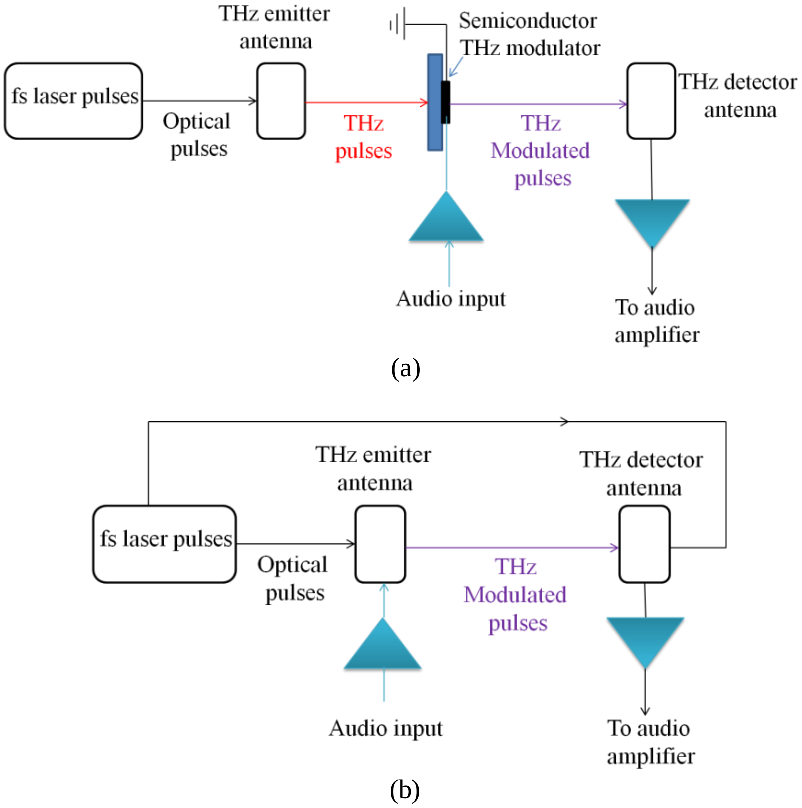

Fig. 1.8 Schematic diagram of THz communication links for (a) system of [60] with external modulator (b) system of [61] where voltage modulation of the THz antenna is used.

1.4.2.2. *THz CW applications*

Although THz pulsed imaging and spectroscopy can provide data on broadband frequency ranges, for some applications, such as gas-phase spectroscopy, high frequency dielectric measurements of electronic, metamaterials and nano-materials, and analyses of signatures in microliter DNA, narrowband high resolution systems are required [36, 62-64]. THz

CW imaging and spectroscopy systems can provide such an opportunity [65, 66]. It is good to add that for some applications like imaging of aircraft glass-fibre composites or determining the thickness of a sample, both pulsed and CW imaging methods can be used [59, 67].

1.5. Research Motivations and Objectives

A major limitation of the fast growing THz technology is the development of high output power and efficient sources – this is the primary motivation for this research.

In spite of explained fascinating and unique properties, THz technology has been largely avoided by the late of the twentieth century due to the lack of robust, coherent, efficient and cost effective THz sources and detectors. However, the advent of femtosecond lasers in the 1980s and later photoconductive antennas by Austin in 1984 [68] revolutionised accessibility to THz gap. Since then and over the last three decades, THz technology has witnessed unprecedented progresses due to interests in exciting THz applications in different fields as discussed previously. Some commercial THz imaging and spectroscopy systems have been introduced to the market; nevertheless, there are various issues, such as the low output power and working temperature of THz sources, which need to be addressed to ripen this technology like radio and optical technologies.

THz antennas based upon the photoconduction method are one of the key and common components in many THz systems. The popularity of these THz antennas is because of the several advantages that they offer as compared to the other THz sources discussed earlier. For instance, they work in the room-temperature environment, they are compact, and they can operate both in the emission and detection sides. Although these types of components have been widely employed in established THz systems, the radiated power from them is very low (about few microwatts) and they are inefficient [69]. For this purpose, it is crucial to distinguish the effect of various parameters of optical sources, photoconductive materials and antennas on the performance of the THz antennas. Thus, having a model which links these parameters can be very useful for both, designing a THz antenna and tuning a THz system to achieve the maximised power conversion efficiency and THz radiated power. Therefore, as a fundamental research work on the THz photoconductive antennas, an analytical model is developed in this study considering the interaction between laser beams, photoconductive materials and antennas in a typical THz scheme.

Using a package of commercial simulation tool is an essential part of RF antenna analysis. However, the major difference in analysing THz antennas as compared to RF antennas is the optoelectronic characteristics of THz antennas which are the result of the optical excitation and photoconductive material response. Some commercial semiconductor solvers such as TCAD Sentaurus [70] perform advanced simulations on characterising semiconductor devices considering their complex physical phenomena; and various information for instance on electric field distribution and charge concentration can be provided by them. However, for THz antenna analysis the THz current source is the main input that needs to be fed to full-wavelength simulation tools. Considering the required information, although the combination of semiconductor solvers with full-wave electromagnetic solvers can provide possibility of simulation of THz antennas, this method can be an expensive process. Thus, a new simulation and analysis procedure is developed that eliminates the requirement for two commercial tools. The THz current source can be analysed through the proposed analytical method and then antenna performance can be examined with a full-wave electromagnetic solver.

Furthermore, considering the difference in optical excitation sources of THz photoconductive antennas and THz photomixer antennas, different analysis method and antenna design considerations is required. Hence, the response of photoconductive material which acts as the source resistance for the antenna is examined and compared for both methods.

A THz photomixer antenna is usually integrated with electrodes, an antenna and a lens. Electrodes are main components which are responsible for generation of THz current. Geometrical modification and optimisation of electrodes can lead to generation of more THz current which couples to the antenna. Configuration of electrodes accompanied by photoconductive material characteristics also affects the source resistance of the antenna. Designing an antenna which has good impedance matching to the source resistance is very important because it results in an improved radiated THz power. In addition, coupling of the created THz field to air is crucial to have a directional pattern. Thus, in order to improve the radiated THz power, modifications in these components are required. By considering the role of each part, in this research an improved THz photomixer antenna is proposed and studied. Then, the performance of the new photomixer design (used with a common bowtie antenna) is characterised and evaluated.

As a summary, the main objectives of this research are as follows:

- To improve the radiated THz power and efficiency of photoconductive antennas
- To develop a new model which will encapsulate various THz antenna parameters and can be used for antenna performance analyses
- To develop a simulation method for THz photoconductive analysis
- To develop and characterise an antenna solution for THz CW systems

1.6. Thesis Overview

The thesis is organized as follows. Chapter 2 reviews THz time domain generation and detection systems based upon the antennas and EO crystals. It provides a comparison on performance of THz systems based upon THz photoconductive antennas and EO crystals with the aim of choosing the suitable pairs for THz applications. Also, the differences of THz pulsed systems and THz CW systems are addressed from the excitation source, system arrangement and system characteristics points of views. This is required to provide a big picture on the THz antenna position and its importance in a THz system.

To narrow down the scope of the research to THz antennas, Chapter 3 starts with providing comparisons of THz antennas with conventional RF/MW antennas from various aspects. This highlights necessity of the new look and approach on analysis of THz antennas as compared to RF/MW antennas, and it builds the foundation for the contributions of this thesis. In the second part of this chapter, the problems and reasons for THz antennas having low efficiency are elaborated, and some of the previous work on the performance improvement of THz antennas is reviewed.

Based upon the antenna feeding method in THz antennas, a new time-varying source conductance for THz photoconductive antennas is derived in Chapter 4. Effects of various parameters on the temporal behaviour of source conductance are discussed. Furthermore, source conductance (or 1/resistance) of THz photoconductive antennas and THz photomixer antennas are compared to show the difference of this antenna parameter based upon the excitation of the antenna. This is important for antenna matching efficiency evaluations.

Chapter 5 introduces a novel theoretical model of a photoconductive antenna in a THz pulsed system. This model uses physical concepts of THz wave generation and incorporates these principles to develop a new lumped-element network. Radiated power and optical-to-THz power conversion efficiency of a THz antenna based upon this model are studied, and the analytical results are obtained and compared with measured results from the literature.

Other two differences of THz antennas with RF/MW antennas are in the electrical thickness of the substrate and computer aided design procedures. These two are addressed in Chapter 6. First, effect of varying substrate thickness on performance of a THz antenna is reviewed and compared with the simulation result. In the second part, a new simulation method for characterising a THz photoconductive antenna is presented. Effect of several parameters of the system on the spectral THz emission is examined, and the procedure is validated by comparing the achieved results from this technique with the published measurement results in the literature.

A new photomixer antenna for THz CW systems is proposed in Chapter 7. A novel concept for enhancing the generated THz photocurrent in the photomixer is elaborated. Then, an antenna for enhancing the matching efficiency and improving radiation directivity is introduced. The antenna operation principle, design procedure, simulated and measurement results are systematically described in this chapter.

Finally, Chapter 8 draws the conclusion of the work. The main objectives are reviewed, and the achievements are highlighted. Furthermore, the challenges and suggestions worthwhile to investigate as future research topics are presented.

Chapter 2. THz Generation and Detection Systems Based upon the Antenna

2.1. Introduction

Various THz sources and detectors and also fascinating applications of THz technology were described in the previous chapter. Since the focus of this thesis is on THz antennas, in order to go one step forward on analysing the performance of this type of devices, it is important to consider the operation of the entire THz system of which the antenna is a crucial part of it. Therefore, the main objective of the current chapter is to study and investigate how THz generation and detection systems perform based upon the antennas employed.

In many established THz pulsed and CW systems, femtosecond laser pulses and CW laser sources are respectively used to excite optoelectronic sources as a start point of the system. Therefore, the characteristics of these laser sources are explained as a necessary background for the next chapters. The common optoelectronic emissive and detective components are THz antennas and EO crystals. In THz pulsed systems, different combinations of these components can be used as the emitter and detector. For the THz system analysis, in this chapter, the working principle and effective design parameters of EO crystals and THz photoconductive antennas are firstly discussed. After that, two different systems (one is the photoconductive antenna and the other is EO crystal as the emitter whilst in both cases EO crystal is the detector) are characterised in the THz pulsed system and examined from the signal-to-noise ratio (SNR) and bandwidth points of view. Furthermore, the merits of four ultra-wideband THz generation and detection systems using ultra-short laser pulses (< 20 fs) are reviewed. The goal of comparing these systems based upon EO crystals and/or photoconductive antennas is to aid the selection of the appropriate emitter-detector combination when setting up a THz coherent generation and detection system. Finally, in order to have a comprehensive summary on THz systems based upon THz antennas, other THz systems, namely THz CW systems and THz quasi time domain systems, are also briefly reviewed.

2.2. The Laser Pulses

The starting point of a THz system is a laser source. In a THz pulsed system, the time dependent electric field from a typical femtosecond laser source such as Ti: sapphire is depicted in Fig. 2.1a. The optical power, wavelength (1/frequency), pulse duration (defined by taking the full width at half maximum of the laser power), τ_l, and the pulse repetition time, t_{rep}, are the features that describe the characteristics of the radiated optical pulses.

The common photoconductive material, which is LT-GaAs, has the energy gap of 1.43 eV; therefore, the optical pulses should have larger photon energy to excite a single photon in LT-GaAs. This implies that the wavelength of laser pulses should be smaller than 867 nm. The pulse duration of femtosecond lasers is typically smaller than 200 fs and it even approaches 10 fs [71, 72]. The laser repetition rate ($1/t_{rep}$) is typically smaller than 100 MHz, and it indicates the amount of delivered energy per pulse according to the average optical power of laser (optical energy = average optical power /laser repetition rate). Fig. 2.1b shows the spectrum of a femtosecond laser pulse which it has a broad spectral distribution.

In a CW system, the electric fields of two above-bandgap monochromatic CW lasers (such as laser diodes) mix. Their angular frequencies, ω_1 and ω_2, are slightly different; as a result, the beating waveform at the photoconductive surface with angular frequencies of ω_2-ω_1 and ω_2+ω_1 are produced [73]. In Fig. 2.2a the temporal resulting optical electric field is schematically shown and Fig. 2.2b illustrates the corresponding frequency spectrum of two single mode laser waves and the eventual optical waves. The term of ω_2-ω_1 is located at THz frequencies and the photoconductive substrate only able to respond to this frequency, which is the envelope of the produced waveform shown in Fig. 2.2a.

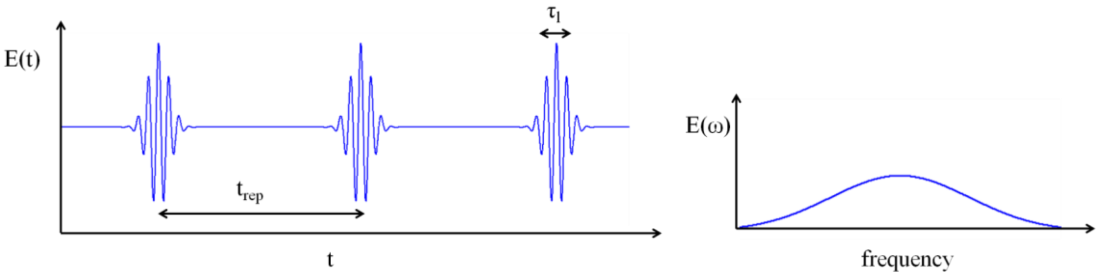

(a) (b)

Fig. 2.1 Schematic diagram of (a) temporal electric field of optical laser pulses at the photoconductive substrate for a pulsed system (b) corresponding spectral distribution of electric field of an ultra-short pulse

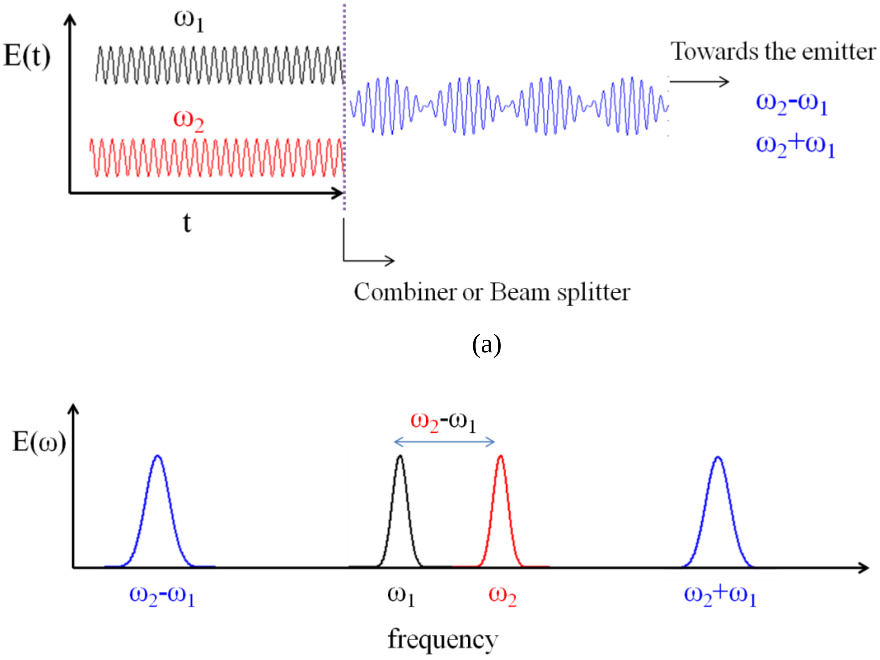

(a)

(b)

Fig. 2.2 Schematic diagram of (a) temporal (b) spectral electric field of optical laser pulses at the photoconductive substrate for a CW system

2.3. The EO Crystal

An EO crystal can be used as an emitter and a detector in a THz pulsed time domain system. ZnTe is the most commonly used EO crystal in THz pulsed systems with large second order nonlinear optical susceptibility of $\chi^{(2)}$. When EO crystals are employed as emitters, the radiation occurs due to response of electrons in the matter and their acceleration because of external electromagnetic waves. The energy of the THz radiation is extracted directly from the laser pulses and it is based on optical rectification process. Optical rectification is the generation of all possible difference-frequency components that exist in the broad frequency spectrum of ultra-short optical pulses.

There are some features in EO crystals that affect the generated THz waves. These factors can be summarised as follows:

- χ^2 affects the nonlinear polarisation and hence, it affects differently the radiated THz field in each tensor direction of nonlinear crystal. For instance, in ZnTe when optical polarisation lies in (110) plane the THz intensity can be maximised [2].
- In an ideal case in an EO crystal, it is desirable to have an equal optical refractive index and THz refractive index at all frequencies. This is required to satisfy the velocity matching condition between the optical and THz waves. Since the radiated THz electric field is proportional to the crystal thickness, THz wave is amplified while propagating through the crystal. However, in reality EO crystals have dispersive behaviour and this leads to destructive interference between THz waveforms. Thus, for broadband THz waves, the requirement of similarity in optical group velocity and the phase velocity of the central frequency of the THz spectrum can be met only at certain frequencies [2]. In order to alleviate this velocity mismatch the crystal should be kept thin. Therefore, there is a trade-off between the thick crystal for larger amplitude of THz field and thin crystal for velocity matching condition and avoiding destructive interference.

When an EO crystal is used as a detector, the incident THz field induces birefringence in the crystal. In other words, the crystal responds to the polarisation and the direction of the THz field. For further elaboration of this procedure, a typical experimental arrangement for THz detection based upon EO crystal is illustrated in Fig. 2.3. This illustrates that when THz field exists, polarisation ellipticity changes compared to the case without THz field. After that, through a Wollaston prism, the beam is split into two orthogonal components detectable by a pair of balanced photo detectors. The difference of the measured intensity by photodiodes is proportional to the amplitude of THz wave. The phase of the THz wave can be determined by plotting the ellipticity versus delay time due to the variation of the optical path length of the probe laser pulse.

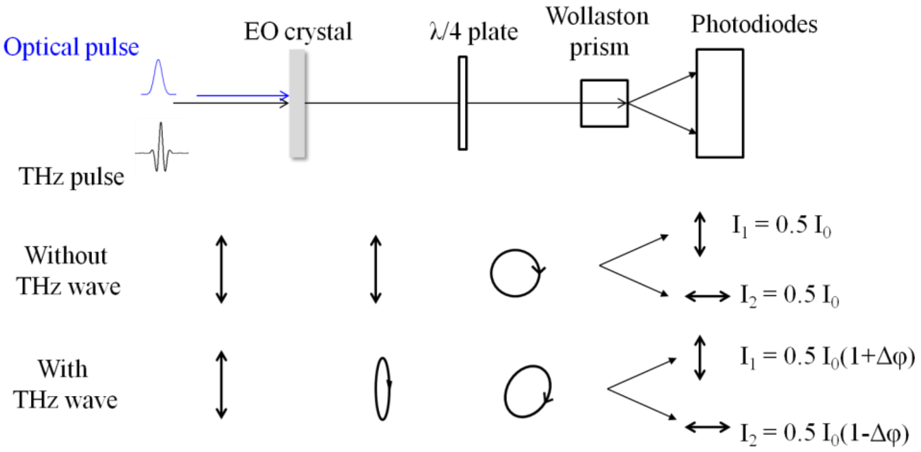

Fig. 2.3 Diagram of the common arrangement for THz detection based upon an EO crystal, I_0 shows the optical (probe) pulse intensity and Δφ represents the differential phase retardation due to the Pockels effect while the waves propagate in EO crystal and it is proportional to the E_{THz}.

2.4. The THz Photoconductive Antenna

In this section, the characteristics of a THz photoconductive antenna which is employed in a THz pulsed system are explained. This provides the necessary background for characterisation of THz pulsed systems based upon the antenna and theoretical analysis of the antenna. The working principle of a THz photomixer antenna in a CW system will be described in Chapter 7.

THz photoconductive antennas, which in the literature are sometimes referred as Auston switches [74][1], consist of two metal (usually gold) electrodes on a photoconductive substrate.

These electrodes act mainly as a means for biasing the device (when used as an emitter) and also as an antenna. The distance between the electrodes is referred as the photoconductive gap and it is the main part where the laser pulses illuminate and electron-hole pairs are produced. From photoconductive gap size point of view, THz photoconductive antennas can be categorised into three types; small gap antennas with gap size of about 5 to 50 μm, large-aperture antennas where the gap dimension is much greater than the centre wavelength of the emitted THz radiation (gap sizes are usually larger than few hundred micrometers) [75], and semi-large gap antennas which the gap size is between the two previous types [76]. Two main advantages of semi-large and large-aperture antennas are ease of fabrication, and better heating handling capability due to larger deposited electrode areas on the substrate [77]. On the other hand, with small gap antennas, larger spectral ranges can be achieved as compared to large-aperture antennas [76, 78]. Electrodes of a THz antenna are more influential on the THz power and bandwidth of a small gap antennas rather than large-aperture antennas [76]. More detailed performance comparison of small gap and large-aperture antennas are provided in next chapters.

An antenna electrode can have various shapes and some typical antenna geometries are illustrated in Fig. 2.4. Bowtie antennas are one of the favourable antenna types in THz pulsed systems due to their frequency independent characteristics. Moreover, the sharp ends of the antenna lead to high electric fields; hence, THz radiation from the device is enhanced [79]. A large gap coplanar strip line is favoured because it does not need necessarily micro-fabrication techniques like small gap antennas, and also it is not as sensitive as small gap antennas to laser focus alignment.

---

[1] The main difference of original Auston switch with a photoconductive antenna is that in an Auston switch two lasers with different wavelengths have been employed for turning the switch on and off; however, in a THz photoconductive antenna only one wavelength laser pulses are used.

2.4.1. Working Principle of a THz Photoconductive Antenna as an Emitter

When the THz photoconductive antenna as an emitter is excited by ultra-short laser pulses whose photon energy is higher than the bandgap energy of semiconductor material, electron-hole pairs are created. Because of the bias voltage across the electrodes of the antenna, transient photocurrents are produced owing to the acceleration and deceleration of the photo-generated carriers. When the density of generated electron-hole pairs is high they screen the applied bias field which leads to THz oscillation in the dipole moment [78]. Consequently THz wave is radiated into free space by the antenna[1].

Based upon the antenna gap size, analysis of THz photoconductive antennas may be very different [75]. Therefore, in the following sections the theory of generation of THz photocurrent from small gap and large-aperture antennas are explained.

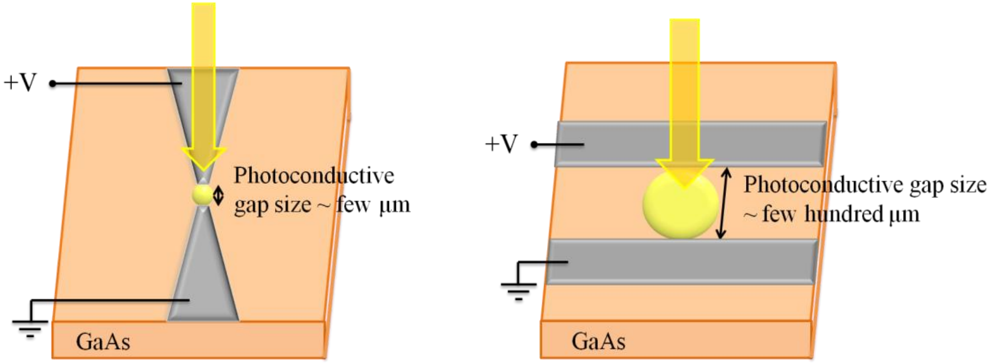

(a) (b)

Fig. 2.4 Sketch of THz photoconductive antennas (a) small gap bowtie antenna (b) large-aperture coplanar strip line. For large-aperture antenna larger laser spot size is used; hence, the illumination area and the photoconductive gap size between two electrodes of the antenna are larger.

2.4.1.1. *Small Gap Antennas*

A coherent single cycle of emission of THz radiation from a small gap antenna is in accordance to Hertzian dipole theory and, the radiated electric field is proportional to the time derivative of the current, I_{pc}, (or equivalently it is proportional to the current density, J_{pc}) as [34,

---

[1] This process is explained with further details in Chapter 5.

80][1]:

$$E_{THz}(t) \propto \frac{\partial I_{pc}(t)}{\partial t} \propto \frac{\partial J_{pc}(t)}{\partial t} \tag{2.1}$$

The photocurrent itself is generated due to the movement of electrons from the valence band to the conduction band under laser illumination. Assuming the electron (free carrier) density in the conduction band is $n(t)$ and the velocity of carriers is $v(t)$, the current density, $J_{pc}(t)$, is given by [81]:

$$J_{pc}(t) = -e \cdot n(t) \cdot v(t) \tag{2.2}$$

where e is the electron charge. The same current relation, but with a positive sign, holds for the hole. However, since the effective mass of a hole is much larger than that of the electron its contribution to THz current and radiation is much smaller [82]; hence it can be neglected.

For explaining main features of this photocurrent density and carrier dynamics, a simple one-dimensional Drude-Lorentz model has been developed by Jepsen *et al.* [78]. This model consists of three interlinked differential equations describing the relation of free carrier density, the velocity of carriers, and the polarisation caused by separated carriers under the bias field, P_{sc}. These equations are as follows:

$$\frac{dn(t)}{dt} = -\frac{n(t)}{\tau_c} + G(t) \tag{2.3}$$

$$\frac{dv(t)}{dt} = -\frac{v(t)}{\tau_s} + \frac{e}{m^*} E_{local} \tag{2.4}$$

$$E_{local} = E_{bias} - \frac{P_{sc}}{\zeta \varepsilon} \tag{2.5}$$

$$\frac{dP_{sc}}{dt} = -\frac{P_{sc}}{\tau_r} + J_{pc}(t) \tag{2.6}$$

where τ_c is the carrier trapping time (or carrier lifetime) and defined as the average time span that

---

[1] The detailed derivation of this equation through vector potential relations and the time-varying behaviour of the Hertzian dipole is presented in Appendix A.

excess free electrons survive before falling into an energy level caused by the presence of a defect ("trap"), τ_s is the momentum relaxation time (or carrier scattering time) defined as the average time between two collisions of each electron in the conduction band and it is in the order of the tenth of ps [81], τ_r is the carrier recombination lifetime which is very long and defined as the average time that electrons move from the "trap" into an empty valence band state [83], $G(t)$ is the generation rate of carriers by laser pulses, m^* is the effective mass, E_{local} is the electric field in the photoconductive gap, E_{bias} is the applied bias to antenna electrodes, and ζ is the geometrical factor [78]. Through numerical calculations of equations (2.3)-(2.6), it is possible to find $J_{pc}(t)$ and $E_{THz}(t)$. Therefore, considering equations (2.1) and (2.2), the radiated THz field can be related to carrier dynamics and calculated as:

$$E_{THz}(t) \propto \frac{\partial J_{pc}(t)}{\partial t} = e \cdot \frac{dn(t)}{dt} \cdot v(t) + e \cdot n(t) \cdot \frac{dv(t)}{dt} \tag{2.7}$$

This demonstrates two phenomena of 1) ultrafast variation in carrier density and 2) acceleration of photo-carriers, which together result in THz radiation. Applying large optical power and large bias field are two main methods that lead to enhancement of aforementioned factors respectively and as a result, increased THz radiation. However, there are some limitations on increasing these parameters. In Chapter 3, the methods that can improve THz power are comprehensively reviewed.

2.4.1.2. Large-Aperture Antennas

Emission of THz radiation from the large-aperture antenna is in accordance with the dipole antenna theory. Under laser illumination, the generated photocurrent can be assumed as surface current confined to a thin layer in the photoconductive gap [2, 75, 84]. Therefore, the on–axis radiated THz field in the temporal format can be written as [84]:

$$\vec{E}_{THz}(r,t) = -\frac{\mu}{4\pi}\int \frac{\partial \vec{J}_S(t)}{\partial t}\frac{dS}{r} = -\frac{\mu S}{4\pi z}\frac{d\vec{J}_S(t)}{dt} \tag{2.8}$$

where, μ is the permeability, S is the photo-excited area in the antenna gap, r is the observation distance, z is on-axis distance from the antenna gap, and $\vec{J}_s(t)$ is the surface current density.

According to the detailed explanations in Appendix A, the radiated THz field can be obtained as:

$$\vec{E}_{THz}(z,t) = -\frac{\mu S}{4\pi z}\frac{\frac{d\sigma_s(t)}{dt}}{\left(\frac{\sigma_s(t)\eta_0}{1+\sqrt{\varepsilon_r}}+1\right)^2}\vec{E}_{bias} = -\frac{\mu S}{4\pi z}\frac{e\mu_e\frac{dn(t)}{dt}}{\left(\frac{e\mu_e n(t)\eta_0}{1+\sqrt{\varepsilon_r}}+1\right)^2}\vec{E}_{bias} \tag{2.9}$$

where μ_e is the mobility.

By comparing equations (2.7) for small gap and (2.9) for large-aperture antennas, it can be interpreted that different antenna gap sizes impose different analysis criteria and different equations for the radiated THz field. The focus of this thesis is on small gap antennas.

2.4.2. Working Principle of a THz Photoconductive Antenna as a Detector

Essentially THz detection by photoconductive antennas is the reverse of the generation mechanism. In detection, no bias voltage is applied across the electrodes, and the incident THz radiation induces voltage across the antenna which accelerates photo-carriers generated by the gating laser pulse (which is the portion of the optical source). By a variable time delay, the arrival time of the gating pulse can be adjusted; thus, the temporal behaviour of the photocurrent due to THz radiation can be measured by a current meter (lock-in amplifier). The detected photocurrent at a time delay of *t* can be explained based upon Ohm's law as shown in equation (2.10).

$$J_{\det}(t) = E_{THz}(t) * \sigma_{\det}(t) = \int_{-\infty}^{\infty} E_{THz}(t')\cdot e\cdot \mu_e \cdot n_r(t'-t)dt' \tag{2.10}$$

where $\sigma_{det}(t)$ represents the time-varying conductivity of the detector, $E_{THz}(t)$ is the received THz signal on the detector, and $n_r(t)$ is the generated photo-carrier density by the gating pulse [80].

Based upon the behaviour of photo-carrier density two extreme situations can be assumed. If $n_r(t) = \delta(t)$ (for photoconductive materials with ultra-short carrier lifetime) then detected current from equation (2.10) will be proportion to the original income THz signal; *i.e.*

$J_{\det}(f) \propto E_{THz}(f)$. On the other end, if it is presumed that $n_r(t)$ has a behaviour like a step function (for materials with extremely long carrier lifetime like SI-GaAs); then $J_{\det}(f) \propto E_{THz}(f)/f$. This demonstrates that characteristics of the photo-carrier density in the detector antenna and its decay behaviour affect the bandwidth of the detected signal. The in-between case is the realistic situation where distortion effect of the detector on the incident THz field is considered by convolving the detector response with THz field (in the time domain) [82]. Thus, the detected photocurrent for the in-between situation can be explained considering the spectral behaviour of laser pulses, $I_l(f)$, and the frequency response of excited photo-carriers in the photoconductive antenna, $B(f)$, as equation (2.11) [34, 85].

$$J_{\det}(f) \propto I_l(f) B(f) E_{THz}(t) \tag{2.11}$$

The response time of the detector determines the amount of detected signal at high frequencies($B(f)$). This is governed by carrier lifetime of photoconductive material and RC time constant related to the device capacitance [86]. In other words, a THz photoconductive antenna on the detector side acts as a low pass filter [82].

2.5. The THz Pulsed Systems

Although various types of THz sources and detectors exist (as explained in Chapter 1), generally established THz pulsed systems are combinations of a photoconductive THz antenna and an EO crystal. Based upon the type of the application (spectroscopy and imaging), a THz systems is named as THz Time Domain Spectroscopy (THz-TDS) and THz Time Domain Imaging (THz-TDI). Although the names of these two systems are different, components and setup of them are same[1]. In order to understand how different emitter components affect the detected THz signal, in this section initially two THz time domain systems are characterised and compared from bandwidth and SNR (defined as peak amplitude of THz signal to the noise level)

---

[1] If THz-TDI system is used in reflection mode, which is mostly used in industrial imaging applications [52], usually additional apparatus such as more parabolic mirrors is required.

point of view. Then, four different combination setups based on ultra-short laser pulse duration (< 20 fs), presented in the literature, are evaluated. The aim is to provide a comparison between them, and this facilitates selection of the appropriate setup in practice for a desired application.

2.5.1. Characterisation of THz Pulsed Systems

In order to evaluate the effect of using different components as emitter, the detected signal from two THz pulsed systems are measured and compared. In these two setups, an EO crystal is kept fixed as the detector and the effect of using a THz photoconductive antenna and an EO crystal as the emitter is examined in terms of the SNR and bandwidth of the system.

First, the THz photoconductive antenna is employed as the emitter and ZnTe crystal is used as the detector. The schematic diagram and experimental setup of this combination are shown in Fig. 2.5.

The emitter is a large-aperture antenna with a 400 μm gap between the two electrodes on SI-GaAs substrate of a 530 μm thickness. The antenna is biased using 21 kHz chopped sinusoidal wave which is used as a reference for lock-in detection as well. The peak-peak amplitude of the bias voltage is 120 V. Since the antenna is the large-aperture antenna, this relatively high bias voltage can be applied across the antenna electrodes without causing damage to the THz photoconductive antenna (unlike small gap antennas). The excitation source is a Ti:Sapphire laser with an average power of 1.2 W, pulse repetition rate of 80 MHz, and a pulse width of < 200fs. A beam splitter is used to divide the amplitude of laser pulses into a pump (aimed at the emitter) and probe (aimed at the detector) beam as depicted in Fig. 2.5. Since the origin of the probe and pump beams is the same, the optical coherency of pump and probe pulses can be maintained [87]. The photoconductive gap of the antenna is excited by the pump laser pulses. Then, the generated THz waves are coupled out of the antenna from the substrate side. These waves are then collected and focused using a pair of parabolic mirrors onto a thin ZnTe crystal for detection. In the probe path, a time delay gate (which is a pair of corner reflector mirrors on a motorized stage) is used. That allows variation in the optical path length (and as a result phase shift) between the probe pulse and the pump pulse. Thus, probing THz waves at different time intervals is possible. When optical gating pulse passes through the crystal, its polarisation is modulated by the incident THz electric field (form the pump path) as explained in section 2.3 and this leads to the current change in photodiodes which can be measured by the lock-in amplifier.

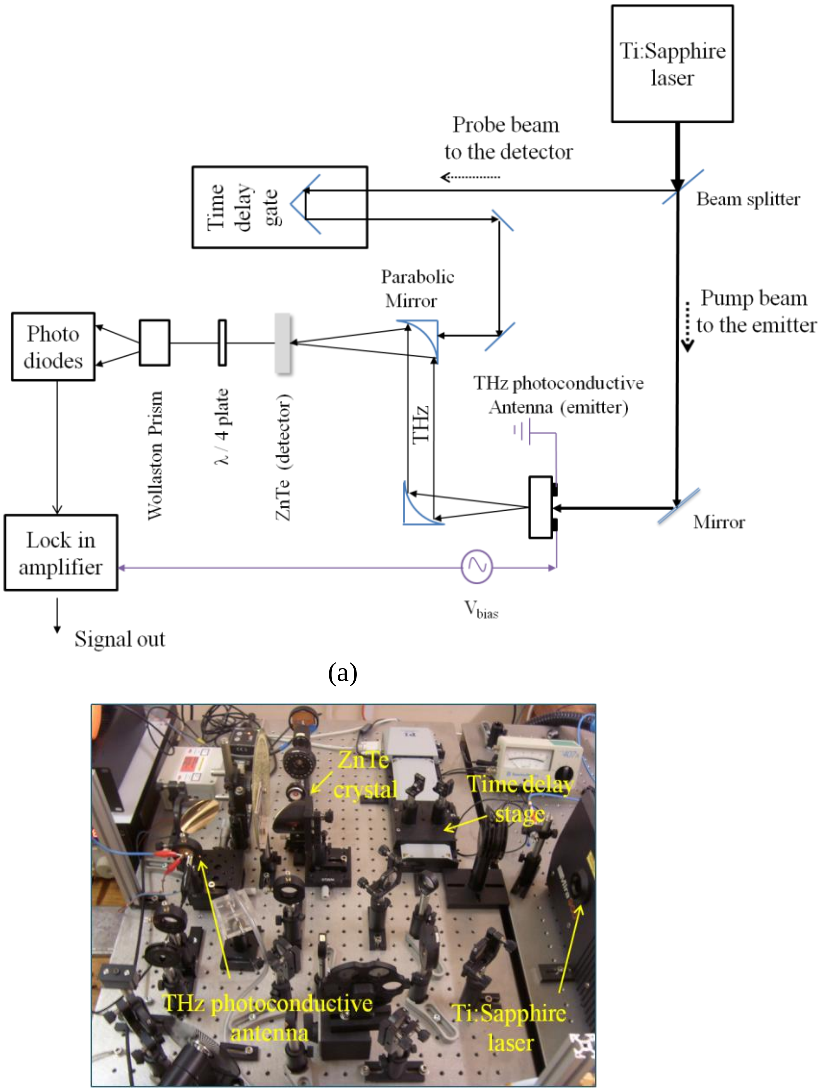

(a)

(b)

Fig. 2.5 (a) Schematic diagram of the THz pulsed setup including both the major optical and electronic components when the emitter is THz photoconductive antenna and the receiver is EO crystal (b) [1]experimental THz setup[2]

---

[1] The author would like to thank the EPSRC for the loan of the femtosecond laser system.

[2] In this photo between two parabolic mirrors a sample for the imaging purposes was located;

Fig. 2.6 shows the measured time-domain THz signal from the aforementioned system. The pulse shape is bipolar and it contains picosecond oscillations (corresponding to THz). The peak-peak value of the detected signal is ~12.7 mV and the noise level is ~ 0.03 mV which is very small compared to the peak value.

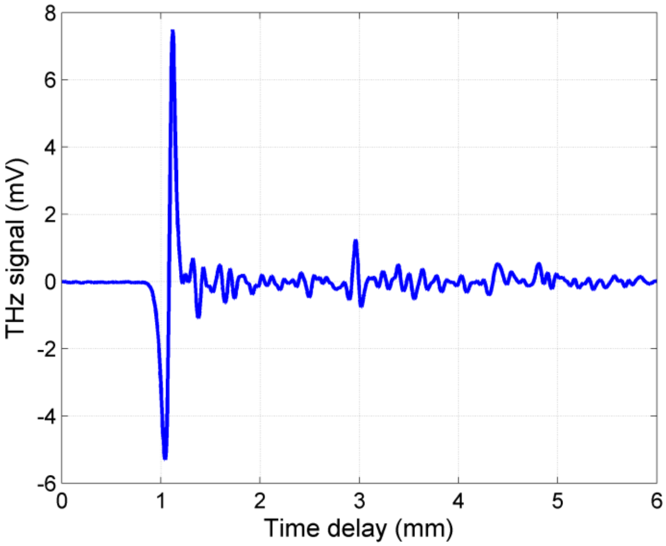

Fig. 2.6 Detected THz signal in the time domain using photoconductive antenna as the emitter and ZnTe crystal as the detector

Fig. 2.7 illustrates its corresponding Fourier transform spectrum. As frequency increases, this rolls off rapidly. The system full width at half maximum (FWHM) bandwidth is almost 1 THz. Due to the high power of the laser, a good SNR can be achieved; but, the resulted bandwidth is limited because the laser pulse width is broad (< 200 fs) and the substrate is SI-GaAs which has longer carrier lifetime compared to LT-GaAs. Moreover, it can be observed that there are some sharp features in the waveform. This experiment was performed in an ambient environment thus the THz signal is affected by water vapour absorption in the THz frequency range. Purging the test setup with a dry nitrogen gas is a solution to remove absorption lines from measured THz spectrum [72].

For the second experiment, the detector side is kept the same as the previous case whilst

---

however, in collecting the THz signal in this section there was no sample between mirrors.

the photoconductive antenna is replaced by a ZnTe crystal as the emitter. The other changes to the previous setup are that no bias voltage is required for the EO crystal; however, a mechanical chopper is used to modulate the laser pump beam at the rate of 3.1 kHz. The system setup for this case is depicted in Fig. 2.8.

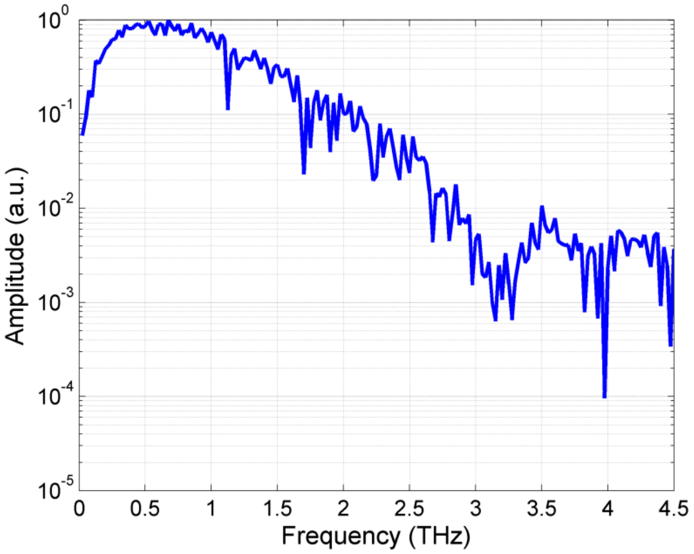

Fig. 2.7 Corresponding Fourier transform amplitude spectrum of Fig. 2.6 with dynamic range of 25 dB

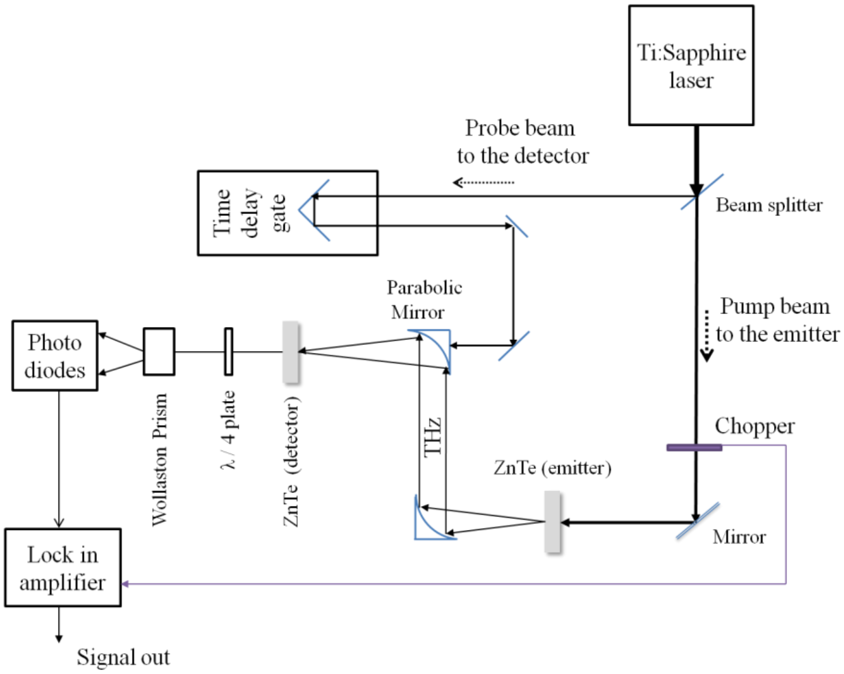

Fig. 2.8 Schematic diagram of the THz pulsed setup where the emitter and the receiver are both EO crystals. Here, the lock-in amplifier is referenced to the mechanically chopped pump beam.

The achieved signals from this setup in the time domain and frequency domain are shown in Fig. 2.9 and Fig. 2.10 respectively. As shown in Fig. 2.9, the peak-peak value of the signal is about 0.8 mV. The signal is subjected to noise because the main pulse level is low and the noise level is about 0.008 mV. Also, the waveform shows a strong ringing which is related to the main oscillation in the crystal. This may be removed by using a thinner crystal as the emitter [88]. According to Fig. 2.10 as the frequency increases, the detected signal declines and the FWHM of the system is 1.6 THz.

Comparison of the results from these two setups is summarised in Table 2.1. The results show that the combination of photoconductive antenna-EO crystal provides almost 4 times better SNR than EO crystal-EO crystal; although the latter system has a broader bandwidth as compared to the former. Therefore, the set of photoconductive antenna-EO crystal can provide a better performance for the cases where high power with moderate spectral range (in this situation) is required.

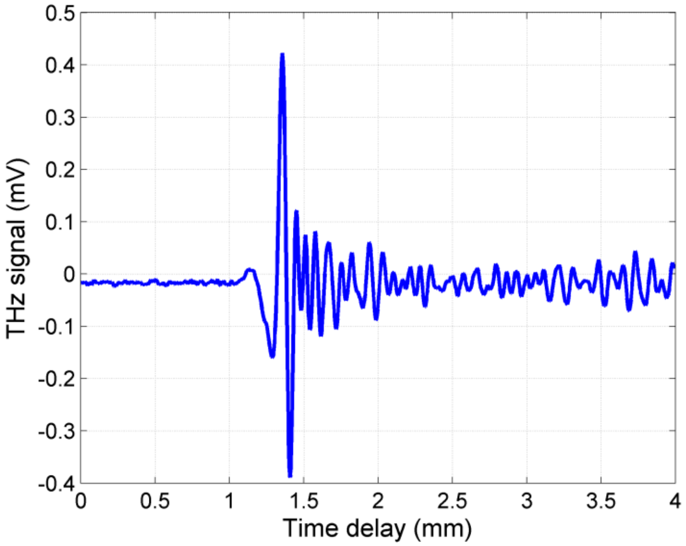

Fig. 2.9 Temporal detected THz signal for the THz pulsed system when both the emitter and detector are EO crystals

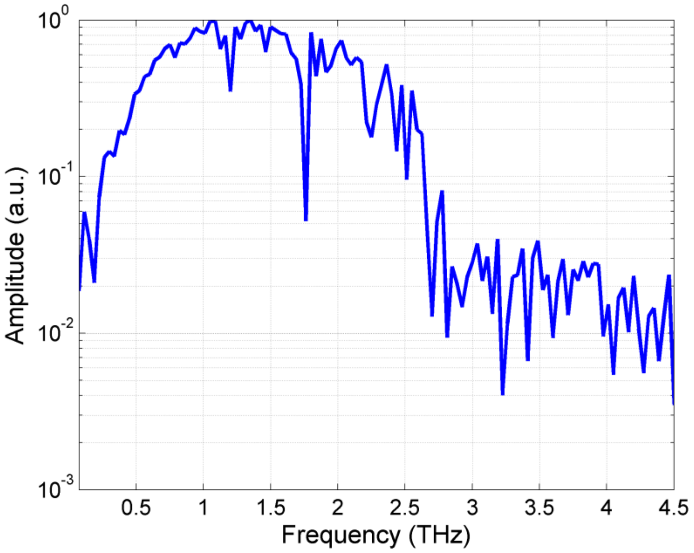

Fig. 2.10 Corresponding Fourier transform amplitude spectrum of Fig. 2.9 with dynamic range of 18 dB

Table 2.1 Comparison of two THz systems based on various emitters whilst the detector is fixed

Emitter - Detector	SNR (linear scale)	FWHM BW (THz)
Photoconductive antenna - EO crystal	~ 420	~ 1
EO crystal - EO crystal	~ 100	~ 1.6

2.5.2. Comparison of Ultra-Wideband THz Systems

There are more combinations that THz photoconductive antennas and EO crystals may be used in THz pulsed systems. For example; Cai *et al.* compared the two systems based on EO sampling and photoconductive sampling detection in the range of 0.1-3 THz when the emitter was the same. Their results showed that the achieved signal from EO detection extended beyond 3 THz with slow roll-off whilst the one from photoconductive antenna had a cut-off at 2 THz. From SNR point of view at low pump power modulation frequency, photoconductive sampling outperforms the EO sampling; however, by increasing the modulation frequency (above 1 MHz to overcome laser noise impact) both methods have almost the same SNR [89]. Similar reduction in the bandwidth of the system based upon photoconductive sampling compared to the one with EO sampling was reported by Park *et al.* [88]. More recently, both an EO crystal and a large-aperture THz photoconductive antenna have been used in emission side whilst the detector is an EO crystal. Due to constructive superposition of the pre-generated THz wave from the EO crystal with that of the antenna, detected THz signal enhanced almost twice of the only antenna case as the emitter. Nevertheless, there was a slight improvement in the detected bandwidth [90]. These efforts highlight the importance of the type of emitter and detector devices in a THz pulsed system. Therefore, selecting the appropriate THz emitter and detector for any desired THz application is an important issue, and the discussion based on performance of the each system is useful for choosing the suitable combination (of EO crystal and photoconductive antenna) when setting up a THz generation and detection system. Next, the merits of four different systems where the laser source has ultra-short laser pulses (smaller than 20 fs) are discussed. The use of published results will be cited as examples in order to supplement this comparison [91].

Case A: Emitter: EO crystal, Detector: EO crystal

Wu *et al.* [92] reported a spectral range as wide as 37 THz by using a 450-μm-thick GaAs crystal as the emitter, a 30-μm-thick ZnTe crystal as the receiver, and 12 fs laser pulses. In a further study, Huber *et al.* [71] demonstrated that, when both the emitter and receiver are thin EO crystals, a spectral range as broad as about 41 THz can be obtained, using a 10 fs laser system. These ultra-wideband spectral ranges are desirable for the experiments of condensed matter physics. However, these systems generally provide a lower emission power and smaller peak electric fields as compared to those of THz photoconductive antennas [77]. If phase matching in EO crystals is satisfied, the average detected power from this setup can be improved [93].

Case B: Emitter: EO crystal, Detector: THz photoconductive antenna

This case was investigated by Kono *et al.* [86]. The emitter was an SI-InP crystal, excited by 15 fs laser pulses. The receiving side employed a 30-μm-long dipole antenna with a 5-μm-long gap between the electrodes, fabricated a GaAs substrate, and embedded on a Si lens to enhance the THz collection efficiency. The detected spectral range was beyond 20 THz; however, there were some dips in the frequency response. The dips from 7 to 9 THz were attributed to the GaAs phonon resonance, and at 15.5 THz the absorption was related to the Si lens. It has been observed that the material property of the antenna influences the useful spectral range of the THz system. Moreover, it has been illustrated that spectral range can be broadened to almost 50 THz when the emitter changed to ZnTe crystal and the same photoconductive antenna detector positioned in the reverse direction [94]. Changes in emitter crystal resulted in phonon absorption in frequencies of 5.3 THz and 10.56 THz. Also, by using the antenna in the reverse direction, both the THz radiation and the probe beam hit the antenna on electrode side as shown in Fig. 2.11b. The advantage of this method over the forward setup (shown in Fig. 2.11a) is that dispersion and absorption from the photoconductive material may be avoided.

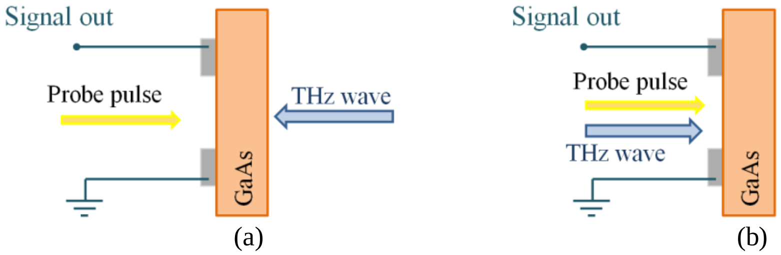

Fig. 2.11 Comparison of (a) forward and (b) backward THz wave detection from a photoconductive antenna

Case C: Emitter: THz photoconductive antenna, Detector: EO crystal

In this setup, a large-aperture antenna on GaAs substrate and a thin 20-µm-thick ZnTe crystal were employed as the emitter and detector respectively by Shen *et al.* [93]. Ultra-short laser pulses with a 15 fs pulse width were used to excite the antenna which was mounted in the backward position. This means that the THz wave was collected from the electrode side. Comparison of forward and backward setup for THz photoconductive antenna as an emitter is depicted in Fig. 2.12. The obtained spectral range from this combination was over 30 THz [93]. The reason for gaining such a wide bandwidth from this setup has been attributed to the method of antenna positioning which leads to reduction in absorption and dispersion from the photoconductive material. Another effective parameter in the wide bandwidth of the system is the use of EO crystal as the detector. Also from this setup a reasonable power is obtained due to the photoconductive emitter. Therefore, this is useful for practical applications such as ultra-wideband THz spectroscopy like detecting intra- and intermolecular vibrations, THz spectral imaging where spectrum of frequencies in each pixel is needed, and investigations on dynamical properties of materials in mid-infrared and THz ranges [93].

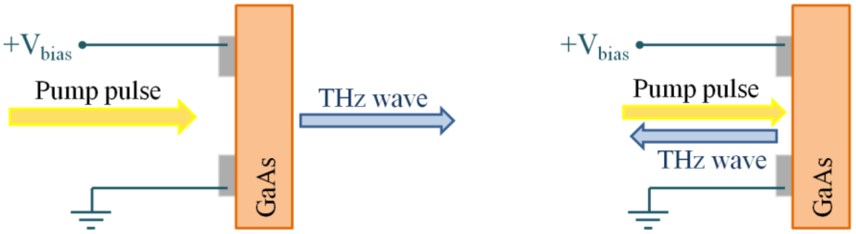

(a) (b)

Fig. 2.12 Comparison of (a) forward and (b) backward THz wave generation from a photoconductive antenna

Case D: Emitter: THz photoconductive antenna, Detector: THz photoconductive antenna

The wideband THz radiation from the system using photoconductive antennas, as both THz detector and emitter, was reported by Tani *et al.* [16] where 18 fs laser system was used. In that work, a coplanar stripline with 30 μm gap distance mounted on LT-GaAs grown on Si was used as the emitter and a small gap dipole antenna on SI-GaAs was employed as the detector. The obtained spectral range of that system extended beyond 10 THz [95]. In a more recent measurement system, the width of the gating pulse was 15 fs and two bowtie antennas with large gap and small gap configurations were employed as the emitter and the detector respectively (both in the backward methods as shown in Fig. 2.12 and Fig. 2.11) [72]. The frequency response of this system was over 15 THz, although the absorption at 8 THz related to GaAs phonon mode was observed. The good SNR and smooth spectral distribution in the 0.3- 7.5 THz range, with the short carrier lifetime in the detector, make this system an ideal choice for practical spectroscopy applications up to 8 THz.

In summary, EO crystals and THz photoconductive antennas can be compared from spectral range point of view as shown in Table 2.2. This table shows the dependency of the radiated THz field and detected THz signal on the frequency for each of these devices when employed as the emitter and detector.

The spectral range of THz pulsed systems based upon the combination of aforementioned devices as "Emitter-Detector" can be estimated by multiplication of their transfer functions which are as a function of the frequency.

Table 2.2 Dependency of THz signal to frequency based on the emitter and detector type

Component	Emitter	Detector
EO crystal	$E_{THz} \propto f$ [80]	Detected signal $\propto 1$
THz Photoconductive antenna	$E_{THz} \propto 1$	❖ Ultra short carrier lifetime: Detected signal $\propto 1$ ❖ Long carrier lifetime: Detected signal $\propto 1/f$

Therefore, the comparison of the spectral range of these systems as a combined "Emitter-Detector" can be presented as:

EO crystal- EO crystal > EO crystal- THz photoconductive antennas > THz photoconductive antennas- EO crystal > THz photoconductive antennas- THz photoconductive antennas

In other words, the system with EO crystals as both the emitter and detector has the largest spectral range, and the system with THz photoconductive antennas has the smallest spectral range.

In photoconductive antennas, the dominant noise is Johnson noise or thermal noise[1] and for a good SNR detection, photoconductive materials with a short carrier lifetime on the detector side are preferable. To elaborate further, thermal noise is proportional to the square root of conductivity of photoconductive material [85]. Considering the relation of conductivity with the carrier lifetime and mobility, the noise level on detector side, I_{noise}, is proportional to [96]:

---

[1] Another type of the noise in THz systems is the laser shot noise which is proportional to the square root of detected THz current (or the laser power) [77].

$I_{noise} \propto \sqrt{\sigma} \propto \sqrt{\mu_e \tau_c}$. This demonstrates that antennas with long-lived and high mobility photoconductive materials have poor SNR.

Comparison of THz pulsed systems from SNR point of view is not very straight forward because this factor is a very practical parameter and it depends mainly on laser and experimental situation such as system alignment. However, in general systems based upon THz photoconductive antennas as emitters have larger THz electric field amplitude than the EO crystals [3, 72]. From component combination point of view, at low frequencies combination of THz photoconductive antennas-THz photoconductive antennas have better SNR than THz photoconductive antenna-EO crystal and EO crystal-EO crystal [72, 88]. At high frequencies like 30 THz, set of EO crystal-EO crystal performs better than THz photoconductive antenna-THz photoconductive antenna from SNR point of view due to sensitivity reduction of the photoconductive antennas at high frequencies.

Therefore, considering application requirement; *i.e.* whether high power THz pulsed system is required or a system with a broad bandwidth and also considering losses due to absorption in special frequencies in antenna substrate material and EO crystal, a combination of these devices can be used. If we want good SNR with smooth spectral range and moderate spectral range, a combination of THz photoconductive antenna-THz photoconductive antenna can be the appropriate choice. If we want a system with high radiated power and broad spectral range, the set of THz photoconductive antenna-EO crystal can be a good option. Moreover, considering 1) different characteristic requirements for each of these components and 2) various factors that contribute in generation and detection of THz signals from them as an emitter and detector (*i.e.* for THz photoconductive antenna as an emitter, effective factors are the pump laser and the bias field whilst as a detector the probe pulse and radiated THz field are effective parameters), it *cannot* be concluded that a system combining EO crystal as an emitter-THz photoconductive antenna as a detector has the same performance as THz photoconductive antenna as an emitter-

EO crystal as a detector . Furthermore, if emitter and detector antennas have photoconductive materials with different characteristics such as carrier lifetime (due to for instance, usage of different photoconductive materials or variation in fabrication procedure for the same photoconductive material) and their place is exchanged within the experimental setup, the detected signal will be different [85]. Last but not least, these comparisons and analyses provide an overview of different setup combinations, and this is helpful in selecting a THz photoconductive antenna and EO crystal as an emitter and a detector in a THz pulsed system.

2.6. The THz CW Systems

THz pulsed systems are based on expensive femtosecond laser systems; however, for long term industrial operation they are not stable and reliable enough [97]. Also, they have issues in generation of narrow linewidth spectral data [66]. Therefore, a suitable alternative option is the THz CW systems; this is a coherent method same as the THz pulsed system and it can offer a better resolution on a pre-selected linewidth. A THz CW measurement system based on THz antennas using two CW Ti:sapphire lasers was first employed by Verghese *et al.* [98]. In THz CW systems, an antenna is always employed as the emitter (whether it is the reference antenna or the antenna under test). On the detection side, a THz photomixer antenna [65, 66] and a bolometer or Golay cell [99-101] are two commonly used methods (former is the coherent method and the latter is the incoherent one). The schematic of a THz CW system using a bolometer as a detector is shown in Fig. 2.13.

Two single mode laser pulses are made collinear and combined through a beam splitter and then the resulting beam is focused on the THz photomixer antenna. THz wave is coupled to the air through the antenna substrate and it is detected by a bolometer. The bias voltage of the antenna is used as the reference for the lock-in detection. The optical frequencies of laser beams may be varied by tuning of the laser cavity length [98], changing the operating temperature [99] or use of optical grating structures [102]. In this thesis, a THz CW system for characterisation of the new antenna design is employed. More details are described in Chapter 7.

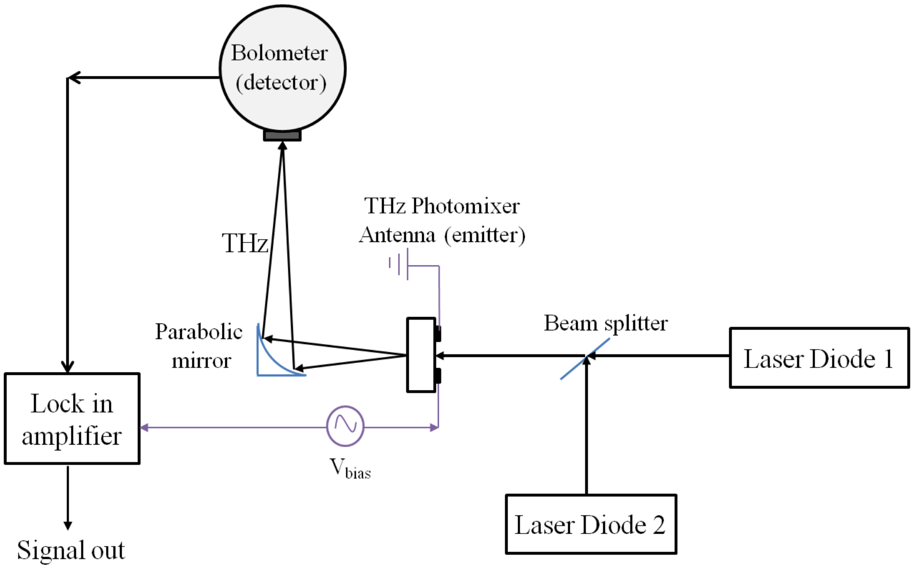

Fig. 2.13 Schematic diagram of a common THz CW system

Each of the THz pulsed systems and CW systems has advantages and disadvantages. Table 2.3 is a summarised comparison of them.

Table 2.3 Comparison of THz pulsed and CW systems

	THz pulsed system	THz CW system
Type of system	Broadband[1]	Narrowband
System complexity	High	Low
System weight	Heavy and bulky	Light and compact
Laser source	Femtosecond lasers	Laser diodes
System cost [103]	~ 6A*	A*
Spectroscopic information	Broadband and enormous amount of information	Limited information
Depth of imaging information [59]	Good	Poor

*A shows the amount of money.

---

[1] The upper limit of achievable bandwidth is determined by the femtosecond laser pulse duration.

In Fig. 2.14, the sources of these systems are depicted for size comparison. It shows that optical sources for CW systems are considerably smaller than those for pulsed systems.

Another recent type of THz systems is the THz quasi time domain spectroscopy (QTDS) which is based upon an inexpensive and commercially available multimode laser diode [97]. In this technique, equidistant frequency spacing of the laser modes results in pulses like the ones from a THz pulsed system. Thus, this method combines advantages of both pulsed and CW systems. In other words, it has a relatively broad bandwidth (the first reported system showed 600 GHz bandwidth [97]) and the optical source is cheap. This can be a suitable option for affordable commercial applications.

(a) (b) (c)

Fig. 2.14 Size comparison of laser sources for THz systems (a) Ti: Sapphire laser with an external power supply and a separate chiller compound for pulsed systems, dimensions of pump laser is 152.4 × 60.9 × 23.6 cm [104] (b) the world most compact Ti: Sapphire laser with dimensions of 22.5 × 22.5 × 6.2 cm [105] (c) laser diode for CW systems with dimensions of 1.2 × 0.9 × 0.7 cm [106]

2.7. Summary

A THz antenna is one of the main components of THz systems. It can be employed as an emitter and/or detector. The required background on major THz systems including THz pulsed systems and THz CW systems were reviewed. In THz pulsed systems, an EO crystal is another common component that may accompany the antenna. Hence, the working principles and features of both EO crystals and photoconductive antennas were explained. The performance of two THz pulsed systems based upon the combination of THz photoconductive antenna-EO crystal and EO crystal-EO crystal as the emitter-detector were measured and compared from bandwidth and SNR point of view. Since laser pulse duration has a crucial effect on the bandwidth of detected THz signal, merits of four different THz systems employing an EO crystal and a THz photoconductive antenna for ultra-short laser pulse duration (< 20fs) were reviewed. Finally, THz pulsed systems and CW systems were compared from various aspects. Working principle and requirements of THz antennas in THz systems depend on the entire system and the position that the antenna is used (emitter and/or detector). Thus, the presented measurement, comparison and analysis in this chapter have provided a useful summary on characteristics of each setup. This aids understanding differences of each combination and choosing the appropriate one for the practical application.

Chapter 3. THz Antennas

3.1. Introduction

After studying various THz systems, in this chapter the investigation is narrowed down to the specific part: the THz antenna. As emitters, it converts optical waves to THz waves. In the detector side, it transforms THz energy to electric energy detectable by a lock-in amplifier. As described in Chapter 2, in both THz pulsed and CW systems (for the case of THz antenna-THz antenna as the emitter-detector combination), the THz antenna is the final block on the emission side, and it is the first block on the detection side. Hence, it is a fundamental and essential component of a THz system. However, special excitation method of this antenna imposes new and different approaches for antenna analysis, simulation, fabrication and measurement as compared to a common RF/MW antenna. Thus, in this chapter after highlighting the necessity of having an antenna, THz antennas are compared with RF/MW antennas. This comparison is very important because it highlights research options in THz antennas and it builds the base for contributions of this thesis. The main challenges in development of THz systems and THz antennas are the low output power of the system and the small optical-to-THz efficiency. In order to analyse these problems and find out the reasons, a new approach is adopted; in which the optical-to-THz conversion efficiency from both THz photoconductive and photomixer antennas are shrunken to three distinct processes. Then based on the requirement for THz antennas, the main parameters affecting the radiated power and optical-to-THz conversion efficiency are summarised in a simplified block diagram. Along with each parameter, that is stated in this diagram, available techniques and mainly antenna solutions are introduced and studied from literature. Finally, some antenna geometries for various THz applications are reviewed.

3.2. Necessity of Having a THz Antenna in a THz System

THz waves can be generated in bulk, unbiased semiconductor materials like InP and GaAs as in the observation of surface field THz emission [107, 108]. Under illumination by femtosecond optical pulses, electron-hole pairs on the surface of the semiconductor substrate are separated and polarised perpendicularly to the surface of the semiconductor. Then, due to acceleration of the carriers in the electric field originating in the surface depletion layer of the semiconductor a THz wave is radiated [109]. Carrier mobility and the intensity of the static internal field affect the amplitude and phase of the radiated THz field [107]. Applying an external magnetic field enhances THz emission from semiconductor surfaces and this is because of the reorientation of the created dipole in semiconductor towards the surface [110]. Nevertheless, the emitted power based on this method is small. This can be improved by employing antenna electrodes on the semiconductors' surface and by applying an external bias field across the antenna which surpasses the surface depletion field [111]. Therefore, the THz antenna plays a very important role in stronger THz generation and detection. In recent years, THz antennas (both photoconductive and photomixer types) are commercially available from companies such as Menlosystem [112], Tetechs [113], Toptica [114] and Thorlabs [115].

3.3. Comparison of THz Antennas with RF/MW Antennas

Working principles of THz photoconductive antennas were described in Chapter 2. Measurement setups of common RF/MW and THz photoconductive antennas are respectively shown in Fig. 3.1a and Fig. 3.1b. It is apparent that THz antennas based upon laser excitation, which are excited by the laser optical source, are very different from the conventional RF/MW antennas from the feeding, measurement facility, and antenna structure points of views. In this section, these differences are elaborated and summarised [116, 117].

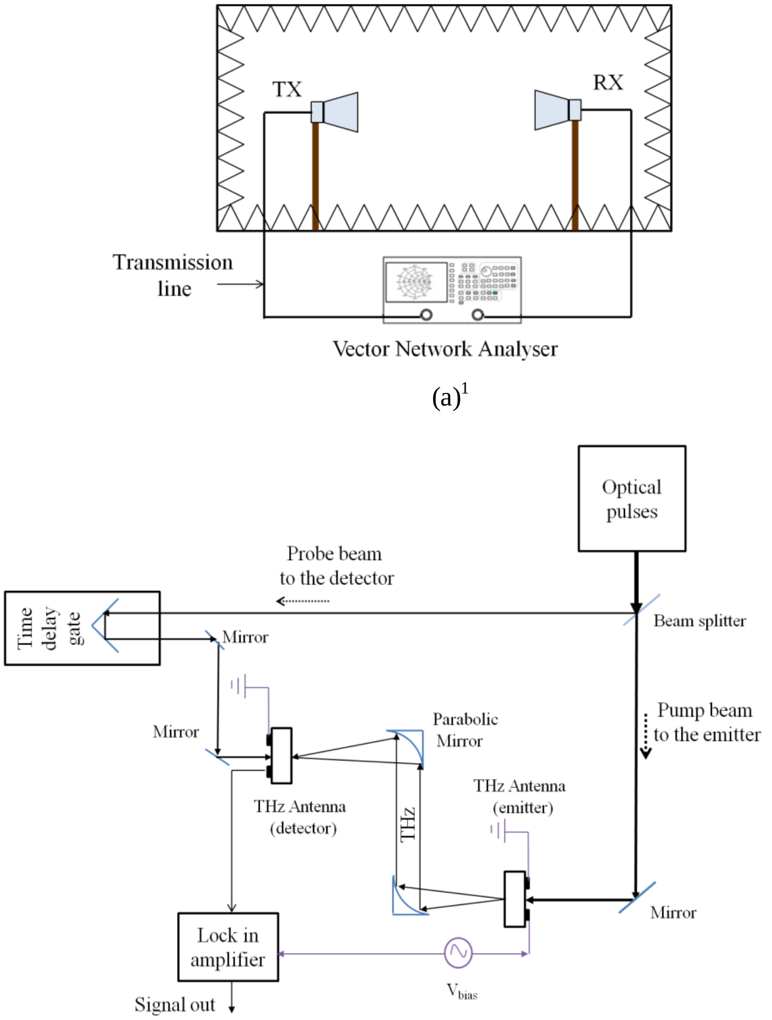

(a)[1]

(b)

Fig. 3.1 Common (a) RF/MW antenna (b) THz antenna measurement setup (both the emitter and detector are antennas)

3.3.1. Excitation Source, Feeding and Biasing

Various feed lines are available for conventional antennas such as coaxial cable, microstrip, and CPW; but, there is no analogous feed line for a THz antenna in reality. In fact,

---

[1] It is possible to test THz antennas (the ones that do not require optical excitation) by using vector network analyzers (for instance network analyzers by Agilent can measure up to 1.1 THz). However, the focus of this thesis is on the THz antennas with optical excitation and the provided discussion in this section covers comparison between this type of THz antennas and common RF/MW antennas.

there are two ways to couple the optical pulses to a THz antenna; one is through the air and the other one is through a fibre. In common THz time domain setups as explained in Chapter 2, optical waves are coupled to the antenna through the air. However, for some industrial applications flexible and movable emitters and detectors are an asset and this can be achieved by employing optical fibres. Recently some fibre-coupled THz systems have been presented for 800 nm laser pulses [118] and 1550 nm (telecom wavelength) pulses [119, 120]. Nevertheless, the feed line for THz antennas is actually a laser beam; therefore, the source impedance of the antenna is variable and this is very distinct to commonly 50 Ohms feed lines of RF/MW antennas. This imposes a requirement for new method of analysis for THz antennas which is one of the main scopes of this thesis, and it is investigated in Chapter 4.

Another difference between RF/MW and THz antennas is from bias voltage point of view. RF/MW antennas do not need any biasing[1]. However, as depicted in Fig. 3.1b THz antennas as emitters require biasing because it is the fundamental procedure of THz generation. THz antennas do not require bias voltage when they are employed on detection side.

3.3.2. Substrate Material

In planar RF/MW antennas, antenna substrate must be a low-loss dielectric material. One of the most common dielectric materials for this type of antennas is FR4, which consists of fibreglass reinforced epoxy laminate sheet. For a special MW antenna category, *i.e.* monolithic microwave integrated circuit (MMIC), GaAs is the main substrate material due to its high carrier mobility [12, 121]. In all THz antennas, the substrate is a photoconductive material which is basically a semiconductor, such as Si, GaAs, and InGaAs. LT-GaAs is the most popular material due to its desirable characteristics, namely ultra-short carrier lifetime (to get fast current pulses or CW current variation), relatively high electron mobility (to get strong THz signals), high intrinsic

---

[1] Some RF/MW antennas like the ones based upon RF-MEMS switches and p–i–n diodes require biasing.

resistivity and high breakdown voltage (to support applying high bias voltages) [122, 123]. Since photoconductive materials play an important role in THz wave generation and detection, characteristics and effective parameters of them with the main focus on LT-GaAs is described in the next sub-section.

Another substrate related difference between THz antennas and RF/MW antennas is the substrate thickness. In THz antennas, the substrate thickness becomes comparable to the radiated THz wavelength; hence, guided waves in the substrate need to be taken into account. This issue is explored in Chapter 6.

3.3.2.1. THz Photoconductive Materials

THz photoconductive material is one of the intensely studied topics in the THz field. The main reason is that, no naturally occurring material exists which allows an efficient and powerful THz emission [124]. The intrinsic carrier lifetime of materials is not fast enough to reach very high frequency ranges of THz spectrum. Thus, to reduce the carrier lifetime, material studies for THz are very crucial, and research and improvement of material characteristics for optoelectronic applications still continues [125, 126].

Silicon was employed as the photoconductive substrate material in the first THz antenna developed by Auston [68]. The bandgap of silicon is 1.12 eV at 300 K, with corresponding intrinsic resistivity of 2.3×10^5 Ω.cm. However, the bandgap of silicon is indirect which means that the minimum of conduction-band is misaligned compared to the maximum of valence-band [127]. Thus, optical recombination processes are relatively slow. In contrary, GaAs has a direct bandgap and photon emission is possible without phonon exchange with the lattice. The intrinsic resistivity of GaAs is 10^8 Ω.cm. Moreover, GaAs is an III-V compound; therefore, it is possible to modify the composition of alloys by adding defects to tune the electrical and optical behaviours. Indeed development in characteristics of GaAs is one of the main reasons that has made possible the steady progress of THz antennas [128].

GaAs crystal can be grown in semi-insulating (SI) form by the liquid encapsulated Czochralski (LEC) method. In this process, all dependencies of GaAs on quartz and carbon components are eliminated [129]. This forms a substrate where it is possible to grow another epitaxial layer. The carrier life time of SI-GaAs is in the range of hundreds of picoseconds. In order to have THz antennas with large bandwidth and good SNR, the carrier lifetime needs to be very small. This may be achieved by incorporating additional energy levels in the bandgap through various native point defect types (*i.e.* arsenic antisites As_{Ga} and gallium vacancy point defects V_{Ga}) [122]. Therefore, another recombination path can be provided by trapping electrons in intermediate states. For this purpose, point defects should be introduced into the crystal. Adding defects can reduce carrier lifetime of the material which is desirable. On the other hand, it reduces thermal conductivity and the carrier mobility because the mean free path is decreased as a result of new scattering centres introduced by trapping levels [81, 130]. These consequences are unfavourable. Thus, the main challenge in the development of ultrafast photoconductive materials is to have a material with sub-picoseconds carrier lifetime, a usefully high mobility, and a high dark resistivity simultaneously. Nevertheless, commonly the priority is given to the short carrier lifetime characteristic and adding defects is the dominant method for THz material fabrication.

There are various methods for introducing defects into the material, and a popular one is the low temperature molecular beam epitaxy (MBE). LT-GaAs is produced through this technique. In this method, GaAs is deposited at low growth temperature (typically between 200 to 250°C) in excess of As which leads to the formation of a relatively high density of point defects. After that, it is annealed under an As overpressure at high annealing temperature (typically between 500 and 600°C) [123, 131] to increase the resistivity. Usually a 1 to 2 μm-thick LT-GaAs layer as the active layer is grown on SI-GaAs [122]. LT-GaAs was first used by Smith *et al.* in 1988 as a substrate of a THz photoconductive antenna [87] and since then overwhelming research on the effect of various growth and annealing factors on properties of LT-GaAs has been performed [131-134]. However, still in the literature when a THz antenna on LT-GaAs is used the full parameters, related to the production of the LT-GaAs (growth and annealing temperatures) wafer and the derived carrier lifetime, are stated. The reason is that each MBE chamber is unique and even in a same chamber it is very difficult to reproduce the wafer with the same characteristics from one time to the next. This is because of the sensitivity of the fabrication process to the ambient condition and difficulty in controlling the exact growth temperature. A literature survey of the carrier lifetime versus the growth temperature is collected in Fig. 3.2. This shows the broad range of carrier lifetime values for LT-GaAs which is the result of the inconsistency between growth facilities. Yet it can be observed that the carrier lifetime of LT-GaAs is very short and this is because very fast carrier lifetime at localised defect sites created in the fabrication process. Another parameter of the photoconductive material influenced by the fabrication procedure is the material resistivity. By increasing the growth temperature the resistivity decreases [135]; however, the annealing process helps to increase the resistivity again.

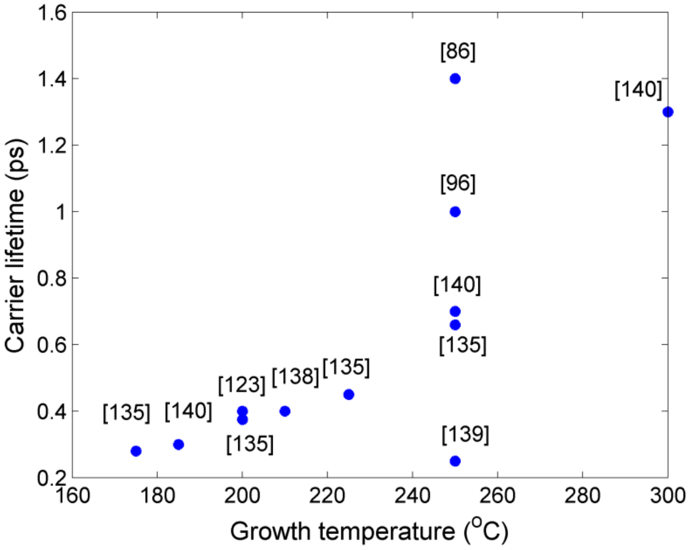

Fig. 3.2 Measured carrier lifetime of LT-GaAs as a function of growth temperature from references [86, 96, 123, 135-138]

It is good to add that other techniques to modify characteristics of GaAs have been practiced like ion-implantation [96] and self-assembled ErAs islands in GaAs [128, 139, 140]. These methods can lead to a substrate material with the similar carrier lifetime to that of LT-

GaAs. Ion-implanted GaAs has high mobility but with very low intrinsic resistivity and ErAs:GaAs has high resistivity but with low mobility. Therefore, LT-GaAs still provides the best material characteristics for THz antennas [124].

Another category of photoconductive materials for THz applications is the Indium based III-V compounds. These materials have narrower bandgap energy; for instance, bandgap of InGaAs is 0.75 eV compared to 1.43 eV of LT-GaAs. Thus, Indium based III-V compounds are suitable materials at high optical wavelengths (but their dark resistivity is low which is associated with their low bandgap energy). Same as LT-GaAs, a thin layer of InGaAs is grown on InP (the lattice-matched material for InGaAs). At optical wavelengths such as 1.06 μm, LT-InGaAs material with ultra-short carrier lifetime and high resistivity has been reported [126]; however, main interest on InGaAs is for the telecom wavelength of 1.55 μm. The advantage of this wavelength is that the lasers are cheaper and less bulky than lasers at 800 nm wavelength. In addition, in this wavelength well developed fibre technology can be employed. Fibre amplifiers with high power, narrow line-width and tunable wavelength in this frequency are also available [141]. Compatibility with 1.55 μm has been achieved with Fe-implanted InGaAs [142, 143], ErAs:InGaAs [144], heavy-ion irradiated InGaAs [145], embedded InGaAs layers between InAlAs trapping layers [119], and low-temperature-grown Be doped InGaAs [146].

As a summary, the properties of different main THz photoconductive materials for optical sources of 800 nm (SI-GaAs and LT-GaAs) and 1.55 μm (LT-InGaAs) are shown in Table 3.1. The advantage of SI-GaAs is its high mobility; however, since it has lower breakdown field compared to LT-GaAs the amount of applied dc bias field for THz antennas based on SI-GaAs is limited. In addition, its lower resistivity results in generation of larger dark current (when there is no laser illumination) in comparison to LT-GaAs which leads to heating of the device and quicker break down than LT-GaAs. Another issue of the SI-GaAs is its large carrier lifetime which limits the achievable spectral range and it leads to the more noise. For InGaAs, there are various fabrication techniques which subsequently lead to variation in the characteristic of the material.

For LT-InGaAs, the carrier lifetime, resistivity, and breakdown field at 1550 nm are very low. However, the greatest advantage of this material is that it can be used with well established communication optical sources; this can reduce the cost of THz system considerably. In general, LT-GaAs is the most popular photoconductive material for THz applications because of its excellent combined features.

Table 3.1 Properties of various photoconductive materials in THz antennas

Material	Carrier lifetime (ps)	Mobility ($cm^2.V^{-1}.s^{-1}$)	Resistivity (Ω.cm)	Breakdown field ($V.cm^{-1}$)
SI-GaAs	Several hundred [69]	8500 [76]	~ 10^7 [147]	4 ×10^5 [76]
LT-GaAs	< 1 [148]	200 [69]	>10^7 [87]	5 ×10^5 [69]
LT-InGaAs	Larger than LT-GaAs[149]	26 [146][1]	760 [146][1]	~ 6×10^4 [146][1]

3.3.3. Antenna Electrode Material

RF/MW antennas are usually made with highly conductive metals such as copper. In MMIC technique, gold metallization is used for transmission lines. In THz antennas, an AuGe alloy and a layer of Ti/Au (Titanium/Gold) are employed as the electrode material. These are suitable metallization types on LT-GaAs substrates and can provide ohmic contacts[2] [150]. AuGe alloys such as AuGe/Ni/Au have been used in THz antennas [69, 99]. However, Ti/Au (or Ti/Pd/Au) layer stack is more extensively employed [72, 90, 98, 111] where a thin layer of Ti is initially deposited to improve adhesion of the Au to the substrate [12]. The advantage of the Ti/Au contact over the AuGe alloy is that, after its deposition, no annealing is required and it is more thermally stable under laser illumination [150].

The electrical conductivity, σ, of Au is 45.2 × 10^6 S/m [2]. The skin depth or

---

[1] This is for LT- Be doped $In_{0.45}Ga_{0.55}As$ which improves resistivity of LT-InGaAs considerably.

[2] The I-V curve of the device is linear.

characteristic depth of penetration, $\delta = \sqrt{1/\pi f \mu \sigma}$, for Au at 1 THz is 74.9 nm. Thus, most of current flow occurs in a very thin region near the surface of the conductor. In this case, the surface resistance of a gold slab with an equal width and length size, by using $R = 1/(\sigma \times depth)$, is 0.29 Ω. In practice for THz antennas, usually 10-20 nm thick Ti followed by Au with thickness of more than few tens of nm is deposited on the photoconductive substrate.

Another type of material, which very recently has been theoretically studied as an antenna electrode material, is graphene [151, 152]. It is a one-atom-thick 2D carbon crystal which has extraordinary mechanical, electronic and optical properties [153]. It has a Young modulus of 1.5 TPa, carrier mobility of 200 000 $\text{cm}^2.\text{V}^{-1}.\text{s}^{-1}$ [154] and an absorption coefficient of 24×10^4 cm^{-1} [155]. The surface conductivity of graphene depends on various parameters such as temperature and chemical potential. Chemical potential is one of the parameters which can be tuned to achieve antennas with different radiation characteristics; *i.e.* reconfigurable antennas [156].

3.3.4. Type of Current

In RF/MW antennas, the current type is the conduction current which is due to the motion of conduction electrons. In THz antennas generation of current in the photoconductive material is attributed to two phenomena: 1) Generation of electron-hole pairs under electric bias field known as drift current 2) Displacement current which is due to second order nonlinear optical characteristics of the photoconductive substrate. However, the effect of displacement current is only considered at low bias fields. At high bias fields (more than 10^5 V.cm^{-1}), drift current is dominant [78, 157].

3.3.5. Fabrication and Measurement

Fabrication of a THz antenna is a complicated and expensive task due to small size of the device and requirement of special fabrication environment. Manufacturing of a THz antenna consists of 1) fabrication and preparation of the photoconductive substrate and 2) patterning the antenna on the substrate. The substrate preparation part was briefly explained in section 3.3.2. For the second part, depositing the metal part of THz antenna on the photoconductive substrate, two ways of photolithography and electron beam lithography are used. The latter method, which is more expensive than the former one, is employed for sub-micron dimensions that fall below the resolution of photolithography method.

From measurement setups and measurement techniques points of views, these two types of antennas are also very different. In RF/MW antennas as illustrated in Fig. 3.1a, both transmitter (TX) and receiver (RX) antennas are connected to a vector network analyzer and then various parameters of the antenna under test can be determined. Anechoic and reverberation chambers are commonly used measurement facilities[1]. In the THz measurement setup, which are based upon the laser excitation sources, as shown in Fig. 3.1b, there is no physical connection between the optical source and the emitter and/or detector antenna[2]. Various optical components, such as parabolic mirrors, are allocated between the emitter and detector antennas to direct the electromagnetic wave which may attenuate and broaden the THz signal. From the depicted setup in Fig. 3.1b, the amplitude and phase of the THz signal can be detected. In THz antennas based upon photoconduction technique, for THz wave generation and/or detection, the antenna should be illuminated by the laser source all the time, *i.e.* misalignment between the antenna and the optical source affects the THz wave generation and/or detection. Therefore, for antenna pattern measurement another measurement setup, such as using fibre coupled detectors, is needed [158, 159]. This assures that the antenna under test in the THz system does not lose laser illumination; therefore, the pattern of the antenna can be evaluated without any interruption. Last but not least, since THz signals are sensitive to water vapours, so a THz measurement bench is typically enclosed and purged in dry nitrogen.

---

[1] Required measurement methods and facilities are determined based upon the antenna type and size [1]

[2] If fibre coupled systems are used, the antenna is connected to the source through an optical fibre.

3.3.6. Computer Aided Design

Computer Aided Design (CAD) is now a common practice for conventional antenna designs; but, there is no one complete design tool available for THz antenna designs. In other words, generation of THz waves from the antennas consists of two processes 1) optoelectronic and 2) electromagnetic (EM) parts. The available commercial tools can only simulate the first or second part of the process. Hence, the development of a new method that can facilitate analysis of THz antennas by combining numerical and CAD methods is required. This is one of the contributions of this thesis that will be explained in Chapter 6.

To sum up, the major differences between these two types of antennas are reviewed in Table 3.2 (the exceptions were previously elaborated). The dissimilarities highlight necessity of having different analysis approach for THz antennas.

Table 3.2 Comparison of THz antennas with common RF/MW antennas

Parameter	THz antenna	RF/MW antenna
Excitation source/feeding	Laser pulses	Transmission line
Bias voltage	Emitter: biased Receiver: unbiased	Emitter: unbiased Receiver: unbiased
Substrate material	High resistive semiconductor	Low loss dielectric
Antenna electrode material	AuGe and Ti/Au	Highly conductive metals
Type of current	Drift current and displacement current	Conduction current
Fabrication	Complex and expensive	Larger availability of fabrication facilities
Computer aided design	Not available in one package	Available

3.4. Problems of THz Antennas

Advantages and disadvantages of different THz sources were reviewed and described in Section 1.2. Among all those various sources, THz antennas and EO crystals are the most common devices as discussed in Chapter 2. Although other THz sources may have better THz radiation performance in particular circumstances, THz antennas and EO crystals have gathered various useful characteristics in one place. These components can operate in room temperature (unlike QCLs), they are small (unlike BWOs), and they can operate over a wider range of THz frequencies (unlike diodes). However, the radiated THz power and the optical-to-THz conversion efficiency from them is very low [3].

In EO crystals, optical-to-THz conversion is inherently an inefficient process because of the mismatching between the optical group velocity and THz phase velocity. Moreover, thickness of the crystal is very important in wave absorption and amplitude of the radiated THz wave. In order to mitigate the drawback of the absorption, high optical power sources need to be used to generate meaningful THz powers [160]. Another restriction of this technique arises from the Manley–Rowe rule which is about the conservation of power in a nonlinear optical process [161]. Thus, the ratio between the energies of the generated THz photon and the optical source photon (*i.e.* the quotient of output THz and input optical frequencies) restricts the power efficiency of EO crystals. On the whole, EO crystals usually provide lower output power than photoconductive antennas in spite of their advantages on providing wider bandwidth [3].

THz wave generation through photoconduction process has shown promising performance [128, 162-165]. One of the major advantages of THz antennas is that under a laser illumination, for each absorbed photon by the photoconductive material one electron-hole pair is generated and when this pair reaches the antenna several THz photons can be emitted [166]. In practice, the radiated THz power is in the range of few μW and the optical-to-THz conversion efficiency of THz antennas is very low (< 2%). In Fig. 3.3 and Fig. 3.4 a literature survey of average THz output power versus the input optical power of several THz photoconductive and photomixer antennas are respectively presented.

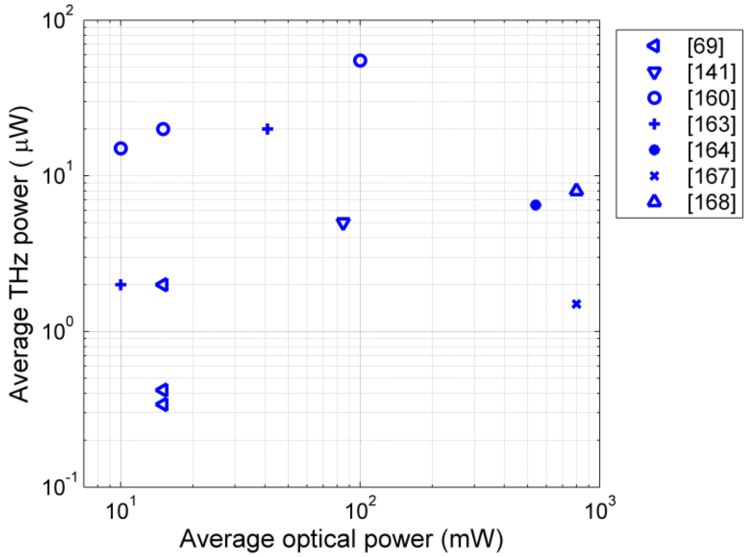

Fig. 3.3 Measured THz output power from a THz photoconductive antenna as a function of average input optical power from references [69, 141, 160, 163, 164, 167, 168]

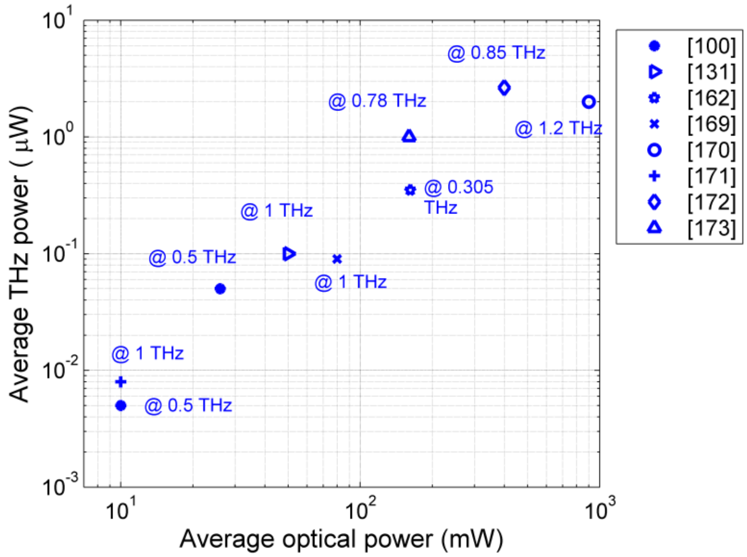

Fig. 3.4 Measured THz output power from a THz photomixer antenna as a function of average input optical power at various single working frequencies from references [100, 131, 162, 169-173]

In order to have a better view and understand the reason of having a low power level and efficiency, the entire wave generation process from a THz antenna needs to be considered. For this purpose, the new approach and the adopted method here is to divide the process into three parts:

1) Generation of THz photocurrent from optical power in the photoconductive material. The related efficiency; *i.e.* optical-to-electrical efficiency, η_1, can be defined as the ratio of the generated THz power in the photoconductive gap or photomixer to the optical power

2) The amount of coupled THz power from the photoconductive gap to the antenna electrodes; *i.e.* matching efficiency, η_2

3) The amount of coupled THz wave from the antenna to the free space; *i.e.* radiation efficiency, η_3.

The first two parts are different for THz antennas in a pulsed and a CW system due to the excitation type, and they are separately described in the next sections. However, the latter part; *i.e.* radiation efficiency, for both systems is the same and it depends on the antenna radiation characteristics- mainly the electrical thickness of substrate and the relative permittivity of photoconductive material. Since the photoconductive substrate has high permittivity ($\varepsilon_r = 12.9$ for GaAs), as substrate thickness increases, the radiation efficiency decreases sharply with a quasi periodic behaviour depending on substrate thickness. This is due to the generation of surface waves which is discussed in Chapter 6. In general, the efficiency of a dipole antenna on ungrounded substrate, η_3, is smaller than 0.25 which can be enhanced to about 0.5 by using a lens[1] [174].

3.4.1. Problems Related to THz Photoconductive Antennas

In order to find out how part one and two of the THz generation process contribute to the optical-to-THz efficiency, a simple and preliminary calculation with approximate assumptions is performed for a THz photoconductive antenna in a pulsed system [116].

1) The average photocurrent [7], I_{avp}, and approximate photoconductive resistance [175], R_{app}, are considered as equations (3.1) and (3.2) respectively:

---

[1] This is for the incident angle of 60°.

$$I_{avp} = \frac{e\mu_e \tau_c V_{bias} P_{av}}{hfL^2} \tag{3.1}$$

$$R_{app} = \frac{3hfL^2}{2e\mu_e P_{av} t_{rep}} \tag{3.2}$$

where , as shown in Fig. 1.2, V_{bias} is the bias voltage, L is the antenna gap length, and P_{av} is the average optical power. Then, the optical-to-electrical efficiency can be estimated as:

$$\eta_{1p} = \frac{R_{app} I_{avp}^2}{P_{av}} = \frac{3e\mu_e \tau_c^2 V_{bias}^2}{2t_{rep} hfL^2} \tag{3.3}$$

The index of "*p*" is added to represent THz photoconductive antenna in a pulsed system. Considering some typical values as μ_e = 1000 cm^2.V^{-1}.s^{-1}, τ_c = 0.5 ps, V_{bias} = 30 V, P_{av} = 50 mW, L = 5 μm, t_{rep} = 12.5 ns, and f = 375 THz and plugging in these values in equation (3.3), $\eta_{1p} = 7.2 \times 10^{-5}$.

2) The matching efficiency can be calculated according to equation (3.4) for a half-wavelength dipole antenna on the substrate with ε_r = 12.9. Assuming the antenna resistance in free space, Z_{free}, is 73 Ω and by using above values in equation (3.2) R_{app} is 0.89 Ω, then the matching efficiency will be η_{2p} = 0.16.

$$\eta_{2p} = 1 - \left| \frac{Z_{free}/\sqrt{\varepsilon_r} - R_{app}}{Z_{free}/\sqrt{\varepsilon_r} + R_{app}} \right|^2 \tag{3.4}$$

It is good to re-emphasise that more realistic photoconductive resistance of THz photoconductive antenna is derived and studied in Chapter 4.

The total antenna efficiency for this sample, which is multiplication of efficiencies from three described processes, is calculated as 5.7×10^{-6}. Although this value is comparable with what most people obtained in practice, it is smaller than some reported best efficiencies. This could be due to better parameters realised in the best cases.

3.4.2. Problems Related to THz Photomixer Antennas

As stated earlier, the same THz generation procedure also applies to a THz photomixer antenna in a CW system. The first two steps, optical-to-electrical efficiency and matching efficiency, are explained for this type of antenna.

1) The photocurrent generated by optical power , I_{avcw}, is [176]:

$$I_{avcw} = \eta_q \frac{eP_{av}}{hf(1+\omega^2\tau_c^2)^{1/2}} \tag{3.5}$$

where ω is the THz angular frequency and η_q is the quantum efficiency. Quantum efficiency is defined as the amount of the incident power effective in generation of the emitted electrons [177] and defined as shown in equation (3.6) [176].

$$\eta_q = \frac{4\sqrt{\varepsilon_r}}{(\sqrt{\varepsilon_r}+1)^2}\int_{-L/2}^{L/2}\int_0^{T_{LT-GaAs}} \frac{\mu_e E_{local}\tau_c}{L_e}\frac{\alpha e^{-\alpha y}}{L}dxdy \tag{3.6}$$

where $T_{LT\text{-}GaAs}$ is the thickness of substrate active layer (shown in Fig. 1.2), α is the optical absorption coefficient, and L_e is the carrier path length from one electrode to the another one. In equation (3.6), it is assumed that $\mu_e E_{local}$ is much smaller than the saturation velocity. The photoconductive resistance in a THz photomixer antenna, R_{cw}, is very high (> 10 kΩ) [98]. Using a very simplified assumption that $L_e=L$, E_{local} is uniform and considering some typical values as $T_{LT\text{-}GaAs}$ = 1 μm, τ_c = 0.5 ps, ω = 1 THz, L = 5 μm, μ_e = 1000 cm^2.V^{-1}.s^{-1}, α = 6000 cm^{-1}, E_{local} = 10^4 V.cm^{-1}, P_{av} = 50 mW, f = 375 THz, and R_{cw} = 10 kΩ, then optical-to-electrical efficiency, $\eta_{1cw} = \frac{R_{cw}I_{avcw}^2}{P_{av}}$ = 2.8 × 10^{-4}. The index of "*cw*" is added to represent THz photomixer antenna in a CW system.

2) Considering a half-wavelength dipole antenna on the substrate with ε_r = 12.9 and using equation (3.4) where R_{app} is replaced by R_{cw} = 10 kΩ, the matching efficiency is, η_{2cw} = 8.1 × 10^{-4}.

The total antenna efficiency for this example is determined as 1.13 × 10^{-7}. Same as the other antenna type, the total antenna efficiency of THz photomixer antenna obtained in this example is smaller than some presented best efficiencies in the literature. This could be because of better parameters chosen in the best cases.

To sum up sections 3.4.1 and 3.4.2, as rules of thumb, these analyses provide a good overall picture on different steps of THz wave generation for THz antennas. They have answered the question "why the efficiency for a THz antenna is so low?" It can be concluded that although impedance matching efficiency is low for a THz photoconductive antenna, optical-to-electrical efficiency is the smallest. Hence, the latter needs more attention. In a THz photomixer antenna, both optical-to-electrical and matching efficiencies are low and for enhancing the antenna performance, improvement in both is required. Also, comparison of matching efficiencies of these two antenna types demonstrates that the mismatch problem is more serious in a THz CW system than a pulsed system (*i.e.* $\eta_{2cw} << \eta_{2p}$).

It is good to note that, in THz photomixer antennas, some other parameters like finite capacitance limits the antenna performance at higher frequencies. A thorough analysis of this type of antenna is provided in Chapter 7.

3.5. Requirements for High Power and Efficient THz Antennas

Considering analyses of section 3.4, how to increase the radiated THz power and optical-to-THz efficiency are important tasks which involve consideration of several parameters from the optical source, antenna bias, and photoconductive material to the antenna design. After a comprehensive literature survey, the main parameters are summarised in a simplified block diagram as depicted in Fig. 3.5 [178]. This shows how each parameter results in high THz output power and high optical-to-THz efficiency from the antenna. In the literature, various techniques have been practiced and presented to provide solutions for improvement in antenna power and efficiency. Some of these techniques are purely dependent on optical sources or photoconductive materials such as excitation spot shape of the laser. On the other hand, some of them are antenna-related or can be modified based upon antenna geometrical parameters. These parameters are highlighted in Fig. 3.5.

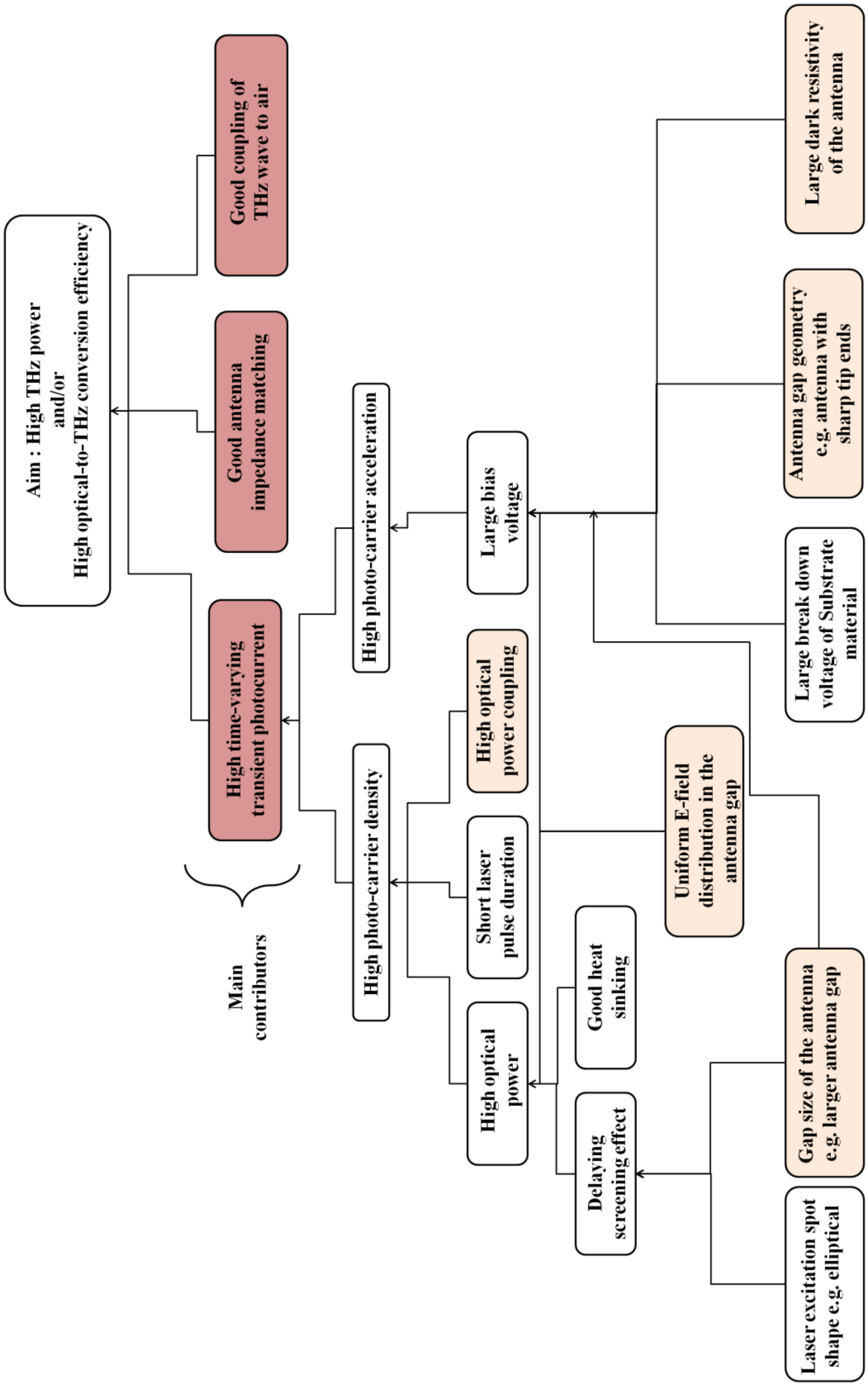

Fig. 3.5 Contribution of each parameter on THz output power and optical-to-THz conversion efficiency

In next sections, most of the effective parameters from the laser to the antenna, as shown in block diagram of Fig. 3.5, are sequentially explained and summarised and some of the main approaches involving antenna designs from the literature are reviewed, for each item.

3.5.1. Improvements in Time-Varying Transient Photocurrent

To improve the THz power, improvement in the time-varying transient THz photocurrent in an antenna is required. As shown in equation (2.7), time-varying transient THz photocurrent depends on both the photo-carrier density ($\partial n/\partial t$) and the local bias field in the antenna gap which provides the required acceleration for the mobile charges ($\partial v/\partial t$). As summarised in Fig. 3.5, high optical power, short laser pulses (in a pulsed system) and high optical power coupling lead to the high photo-carrier density. Also, large bias voltage results in high photo-carrier acceleration. The higher the optical power the more generated free carriers and the higher the bias voltage the more acceleration of free carriers. However, the laser power and the bias voltage cannot be increased steadily because of the device saturation and/or the device breakdown. Device saturation means that by increasing optical power, output power remains unchanged. In the case of THz antenna breakdown, THz wave cannot be radiated because generation of THz photocurrent in the antenna gap is disrupted. The reason is that grain boundaries are formed and electromigration of gold particles between the antenna electrodes is occurred [179]. Delaying screening effect and good heat sinking are two ways that enable application of higher optical power on the antenna. Therefore, in this section, parameters which lead to high time-varying transient photocurrent are explained.

3.5.1.1. Delaying Screening Effects

In order to push the saturation of the device towards a high optical power, the occurrence of space-charge screening needs to be delayed. Screening effect means a reduction of the effective electric field and as a result THz radiation due to separation of charges and creation of an electric field counteracting the bias field. In Chapter 5 this phenomena is considered and explained in our new theoretical modelling of THz photoconductive antenna; that is one of the main achievements of this thesis.

Delaying the screening can be achieved mainly by two methods. One is by using elliptical excitation spot shape with major axes along the direction of the bias field [180]. The excitation spot shape influences the initial spatial distribution of photo-excited carriers on the photoconductive gap of the antenna. Therefore, more photo-carriers are generated near the antenna electrodes rather than in the whole antenna gap and they can reach the antenna electrode faster. Thus, production of the electric field in reverse direction of bias field is lessened. Here, another issue concerns the length of this excitation spot. Although the antenna with line spot shape has a larger radiated THz power than that using common circular spot shape [181], this does not mean that longer line excitations result in higher efficiencies because a longer spot leads to reductions in collection efficiency.

The second method is enlarging the gap size of the antenna. Large-aperture antennas (described in section 2.4.1.2) are desirable configurations especially for the emitter because higher radiated powers can be achieved while the screening of bias field (saturation) occurs later as compared to small gap antennas. This is elaborated further in Chapter 5.

3.5.1.2. Heat Sinking

Although applying large laser power is very desirable for generation of larger density of photo-carriers, in practice, the device experiences degradation and failure. The damage threshold of an antenna is determined by power intensity; *i.e.* mW/μm^2. Thus, at a fixed optical power, large aperture antennas have better heat handling capability than small gap antennas [77]. Nevertheless for any antenna gap size, antenna overheat prevention is required. This may be achieved by using materials with high heat conductivity such as those employ AlAs heat spreader sheet beneath substrate active layer [128] or a diamond layer in contact with the photoconductive gap of the antenna [182]. Moreover, heat can be dissipated from the antenna gold electrodes due to higher thermal conductivity of Au as compared to GaAs substrate. In this situation antennas with wider electrodes can perform better than narrow electrodes. Also employing metal pads besides the antenna electrodes is another heat sinking technique [183].

3.5.1.3. Local Electric Field

Distribution and amount of the electric field in the photoconductive gap is another parameter that affects the photo-carrier density and its acceleration. One of the reasons for low THz power from THz antennas is that the local electric field is non-uniformly distributed across the photoconductive gap. Although non-uniform spatial distribution of the electric field is a drawback, this can be used in a positive way by exciting the antenna near the electrode contacts, where the electric field is stronger. Exciting the anode is more effective because the mobility of electrons is much higher than holes. Therefore, generated photo-carriers overlap better with the higher electric field region; thus, optical-to-THz conversion efficiency improves [184-186]. The benefit of this case is that less optical power is needed for illuminating the electrode gap area of the antenna rather than the whole gap; however, the device becomes more prone to break down. Several methods have been practiced to obtain uniform electric field in the antenna gap; for instance, antenna electrodes with Ohmic contacts can provide more uniform electric field across the photoconductive gap compared to Shottkey contacts [187]. Besides the electric field distribution, amount of bias voltage on the antenna electrodes is also important and larger bias voltage results in higher photo-carrier acceleration. This amount is mainly determined by the photoconductive material and the antenna gap size. The maximum applicable voltage on the device is limited by the material breakdown voltage; for this reason materials with higher breakdown voltages are desirable. Concerning the antenna gap size, the applicable bias voltage on small gap antennas is smaller than the large gap antennas.

In THz pulsed systems, although one of the potential advantages of using large gap antennas is the obtaining possibility of a large THz power; but, this requires application of large bias voltages, in the range of kV. This is undesirable due to the electronic interference with other laboratory equipment [188]. Therefore, a large gap antenna with interdigitated fingers can be a good substitution to reduce the amount of bias voltage on the antenna. Schematic view of this antenna is depicted in Fig. 3.6a. This antenna makes it possible to use most of the generated photo-carriers in the active layer of substrate because of the shorter travelling distance of the generated free charges between antenna fingers. Also, it needs considerably lower bias voltages; *i.e.* tens of volts (because the antenna electrode distance is reduced). However, the problem of this configuration is that the electric field across the active area is not at the same direction. In order to have constructive interference of E-fields in the far field and enhance the THz power, a second metallisation layer in every second period of the interdigitated finger as shown in Fig. 3.6b can be added [188]. This leads to a unidirectional E-field and carrier acceleration. The same concept has been employed by various techniques; such as etching away the LT-GaAs layers from between of every other two fingers (Fig. 3.6c) [189], applying a hexagonal micro-lens array to the antenna (Fig. 3.7a) [164], and using a binary phase mask (made of quartz, an optically transparent material) to give a time delay between the positive and negative polarity THz pulses and generate a boosted single-cycle THz pulse (Fig. 3.7b) [190]. Hence, a uniform electric field distribution in the antenna gap leads to a higher optical-to-THz conversion efficiency.

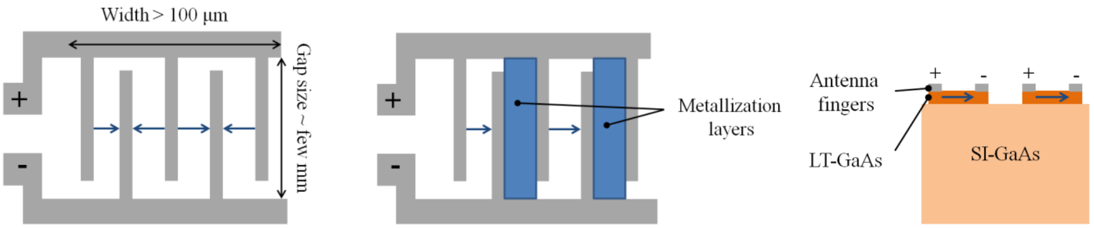

(a) (b) (c)

Fig. 3.6 Schematic view of THz large gap antenna with interdigitated fingers (a) without metallization layers (top view) (b) with metallization layers[1] (top view) (c) with active layer lift-off between every other two electrodes (side view). The arrows demonstrate the direction of the E-field.

---

[1] The upper metallization layer is isolated from the main electrodes by a thin polyimide layer or a sputtered SiO_x layer [188]

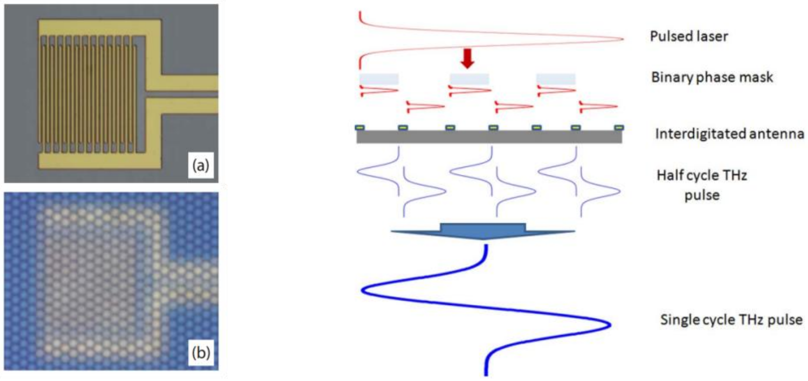

(a) (b)

Fig. 3.7 (a) large gap interdigitated antenna without lens (top) and with micro-lens (bottom) [164] (b) large gap interdigitated antenna with binary phase mask to generate a single cycle THz pulse [190]

The requirement of a uniform electric field distribution in the photoconductive gap applies to THz photomixer antennas as well. This is achieved by using interdigitated fingers in the small gap photomixer antennas [111] and nano gap tip-to-tip rectangular fingers [191].

3.5.1.4. Antenna Gap Geometry

Typical THz antennas are dipole, bowtie, and coplanar strip line. Although the length of dipole antenna affects the emission intensity [7, 192], antenna gap geometry is more important because it is the place that electron-hole pairs are generated and coupled to the antenna electrodes. It has been shown that antennas with sharp tip ends can produce larger THz power compared to the antennas with rectangular edges in the gap [69, 76, 79]. When the antenna tips are sharper, THz emission can be enhanced with less optical power because of the better overlap between the laser spot and the high electric field area in the gap. Therefore, the end shape of the electrodes is very important although, in practice, fabrication of such tiny sharp tips for small gap antennas is not easy.

3.5.1.5. Dark Resistivity of the Antenna

Dark resistivity of the antenna is one of the parameters related to the photoconductive material. A high dark resistivity permits applying higher bias voltages across the antenna without contributing to a considerable amount of heat, which can influence the performance of the device or even damage it [75]. Also, high dark resistivity, which means generation of lower dark current, reduces noise in the antenna and improves SNR.

To improve the dark resistivity of the antenna and decrease residual carrier concentration photoconductive material can be modified [125]. Improvement in dark resistivity also can be manipulated through antenna geometry; such as, mesa-etching of photoconductive material everywhere with the exception of the photoconductive gap and parts below the metal lines [163], and removing substrate from between of interdigitated fingers in the large gap antenna [189]. In [165] mesa-type structures with vertical side contacts have been proposed as shown in Fig. 3.8.

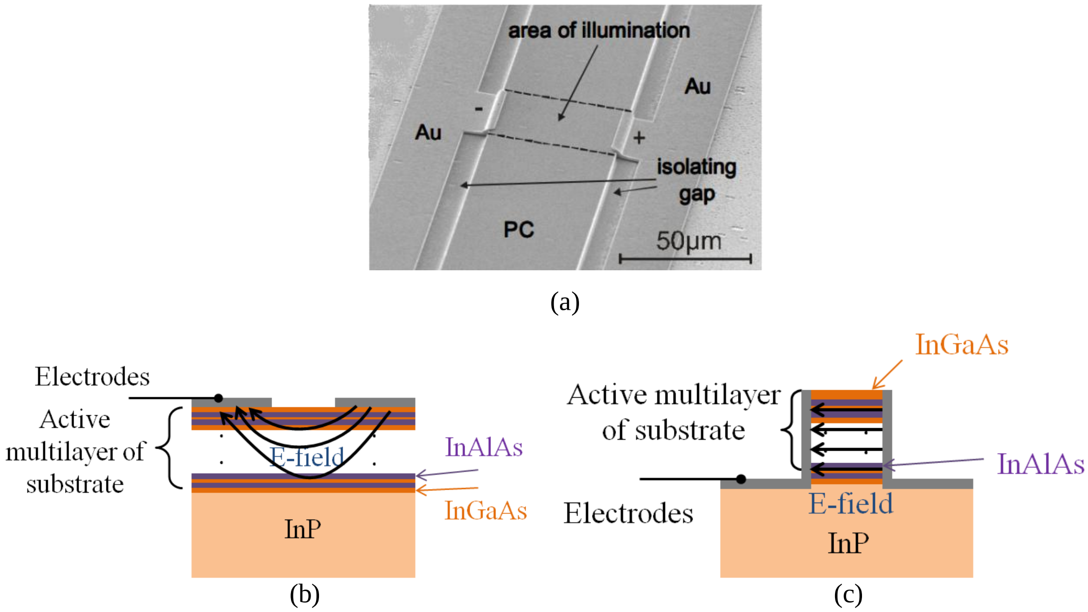

(a)

(b)

(c)

Fig. 3.8 (a) Mesa structured antenna, parts of substrate are removed and electrode contacts are in vertical position [165] (b) E-field distribution in planar electrode geometry (c) E-field distribution in mesa structured electrodes

This antenna has two advantages; first, it reduces dark current by eliminating parts of photoconductive material that have no contribution in generation of photocurrent. Second, the electrical field can be distributed more uniformly in the active layer of the substrate. Therefore, THz power can be increased compared to planar structures.

3.5.1.6. Laser Pulse Duration

Laser pulse duration is one of the parameters that affect the radiated THz field. It has been shown that for a fixed optical fluence, F_{opt}, in a large-aperture photoconductive antenna (defined as $F_{opt} = \sqrt{\pi} I_l \tau_l$ [84] where I_l is the peak laser intensity), the maximum of the radiated field increases with a decrease of optical pulse duration because the density of created photo-carriers increases [84].

3.5.1.7. Optical Power Coupling

Increase in absorption of infrared laser power by the antenna leads to a high photo-carrier density and transient photocurrent. One method is the use of an anti-reflection (AR) coating (such as Si_3N_4, which is an optically transparent layer) on the antenna electrode [128]. The main purpose of this layer is to suppress the reflection of optical waves from the surface of the device. A traditional method is to use a quarter wave length layer as an AR with refractive index of $\sqrt{n_{GaAs}}$, where n_{GaAs} is the refractive index of the photoconductive material. Another method is the use of AlAs:GaAs or AlAs:AlGaAs Bragg reflectors [128, 193]. This material is located beneath the active layer of substrate and it acts as a mirror for optical waves and it is transparent to THz waves. Thus, it increases the quantum efficiency. Schematic view of an antenna with both an AR coating and Bragg reflectors is depicted in Fig. 3.9.

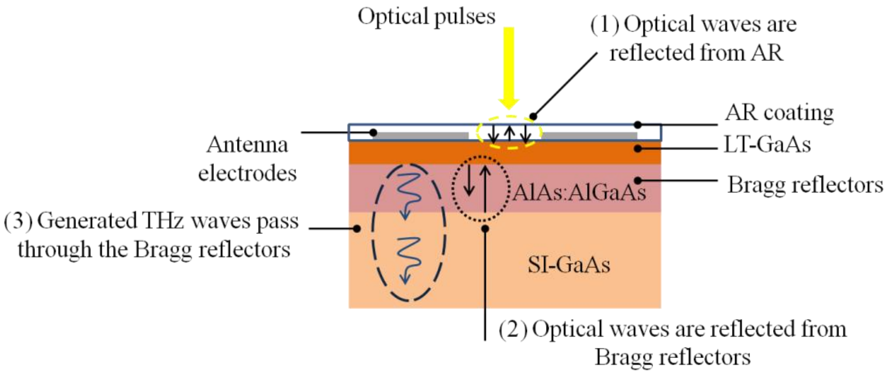

Fig. 3.9 Schematic view of the material structure of a THz antenna with AR coating on top of the antenna electrodes and Bragg reflectors beneath the photoconductive layer, explanation for each layer and wave is numbered.

Use of nanoantennas in the photoconductive gap of a THz photoconductive antenna is another very new approach to enhance generation of photo-carriers in the antenna gap [194, 195].

The optical nanoantennas can strongly concentrate the emitted laser waves and this leads to the locally enhanced electric field. Also, since nanoantennas are deposited on the substrate, more optical power can be confined to the substrate active layer (compared to a nanoantenna on air); as a result, THz power emission from the THz antenna increases[1]. Two types of nanoantennas in the form of nanorods and nanoislands in the photoconductive gap are shown in Fig. 3.10. The resonance frequencies of these antennas (e.g. for 800 nm) can be tuned by width of nanorods or thickness of nanoislands. Although these approaches are very promising, fabrication cost of these devices is high. Also, fabrication accuracy and distance of nanoantennas are very important to avoid electric short circuit.

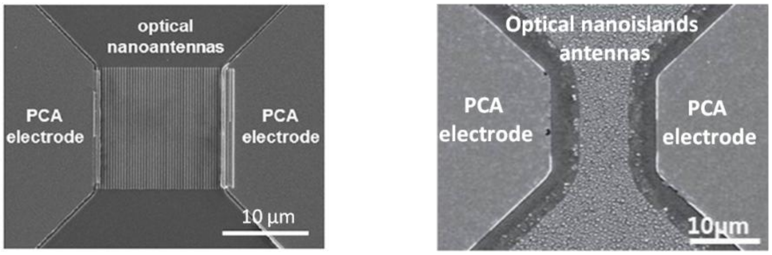

(a) (b)

Fig. 3.10 SEM image of the THz photoconductive antenna with (a) nanorods [194] (b) nanoislands [195] in the photoconductive gap

Although photoconductive materials with ultra-short carrier lifetime are desirable for broadband THz spectrum, with these materials the amount of generated photo-carriers that can be coupled to the antenna before being recombined is very limited (*i.e.* ~ 5% for a photoconductive gap length of 2 μm [141]). That is due to the ultra-short carrier transport time and the limited drift velocity of carriers [196]. This reduces quantum efficiency significantly. Incorporating nanoplasmonic electrodes (*i.e.* nano-structuring of metals) is another state-of-the-art method for improving the coupling of optical power to the antenna and the THz radiated power. In this approach, photo-carrier transport time is reduced by employing arrays of sub-micron electrodes. Indeed, here the optical power coupling is based upon the concept of extraordinary transmission

---

[1] Relation of polarisation of optical pump to the nanoantennas is also important in local power enhancement [194]

of light from sub-wavelength aperture arrays [197]. This happens due to coupling of light with the surface plasmon (defined as collective oscillation of free electrons at the boundary between a conductor and a dielectric material [2]) of the sub-wavelength arrays. Hence, the interaction and concentration of the emitted wave (here infrared laser waves) on noble metals (e.g. gold and silver) are increased [198].

Considering this concept, an array of dipole antennas with plasmonic contacts has been reported by Berry *et al*. [141] as shown in Fig. 3.11. In that structure, the antenna was mounted on a material with large electron mobility and large carrier lifetime. However, due to the short carrier transport time provided by electrodes and increased transmission of laser power to the sub-wavelength gaps of electrodes due to surface plasmon waves, ultra-short THz pulses with superior responsivity has been achieved from this device as an emitter.

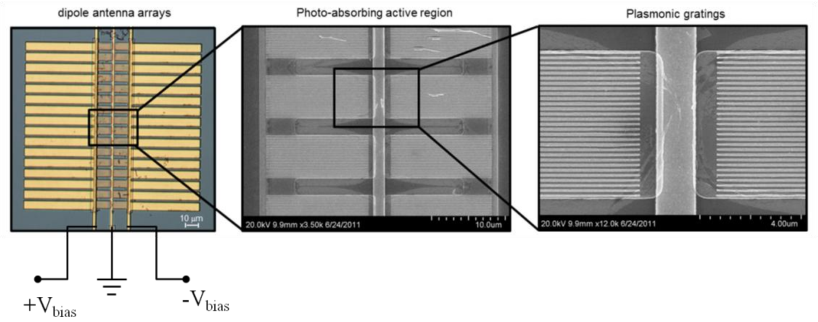

Fig. 3.11 SEM image of plasmonic THz dipole arrays [141] , a middle ground electrode is added to collect the remaining electron-holes in the antenna gap quicker to prevent screening effect.

Another geometry to overcome the problem of the low number of conversion of photon-to-electron is a bowtie antenna with plasmonic contact electrode gratings [160] as depicted in Fig. 3.12. This geometry increases generation of photo-carriers due to highly localised optical power near the metallic grating and increased transmission of optical pump power to the active layer of substrate via nano size metallic grating (because of exciting surface plasmon waves). Also, because of very short carrier transport path lengths as an effect of plasmonic contacts (~100 nm) high number of generated photo-carriers can be coupled to the antenna before recombination. A significant improvement in the emission of THz wave and sensitivity of the detected THz signal based upon this geometry in emitter and detector position has been reported [160].

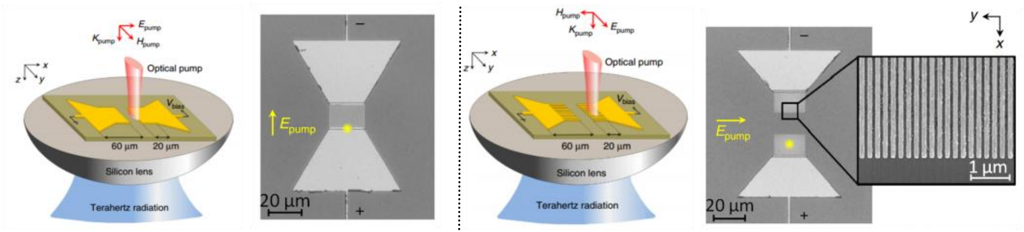

(a) (b)

Fig. 3.12 Schematic and SEM image of the (a) conventional bowtie antenna (b) nanoplasmonic bowtie antenna, under illumination of a transverse magnetic polarized optical pump, surface plasmon waves are excited along the periodic metallic grating interface [160]

Further proposed geometries for efficient THz detection is a small gap dipole antenna with nanoplasmonic interdigitated fingers on SI-GaAs as shown in Fig. 3.13 [199]. Here also, nano distance gaps (100 nm) permit coupling of generated photo-carriers to the antenna more efficiently due to reduced transport distance. Moreover, due to the occurrence of nanoplasmonic resonances in nano gaps more power can be absorbed in the active layer of substrate. However, drawback of this geometry is that due to very narrow distance between the fingers, it is prone to break down at high optical powers, so it is not suitable as an emitter device.

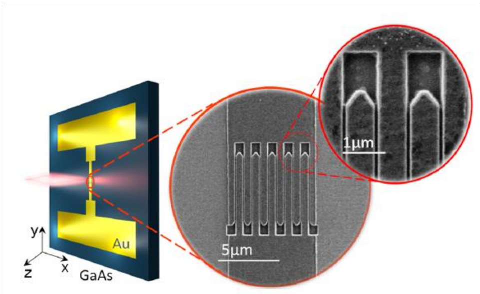

Fig. 3.13 SEM image of the nanoplasmonic interdigitated antenna [199]

The last geometry in this category is a tip-to-tip rectangular nano gap meander antenna as depicted in Fig. 3.14 [191]. It provides strongly enhanced electric field in the gap and reduces the photo-carrier transit time between the electrodes.

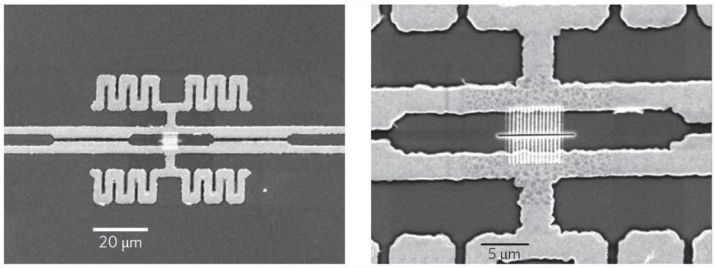

Fig. 3.14 SEM image of the tip-to-tip rectangular nano gap meander antenna [191]

3.5.2. Improvement in Antenna Impedance Matching

Good antenna impedance matching is another factor that enhances the performance of a THz antenna. One of the main challenges for THz antennas is the source impedance. As explained in section 3.3.1, RF/MW antennas connect to a constant 50 ohms independent of antenna input power and material. However, in THz antennas source impedance depends on many other parameters. This is extensively explained in Chapter 4. As described in section 3.4, antenna impedance matching in THz photomixer antennas is critical for improving optical-to-THz conversion efficiency. Various THz photomixer antenna geometries, as shown in Fig. 3.15, have been proposed to increase the antenna resistance and improve impedance matching like dual dipole and slot antennas [200], four-leaf-clover-shaped antenna [201], and Yagi antenna [202].

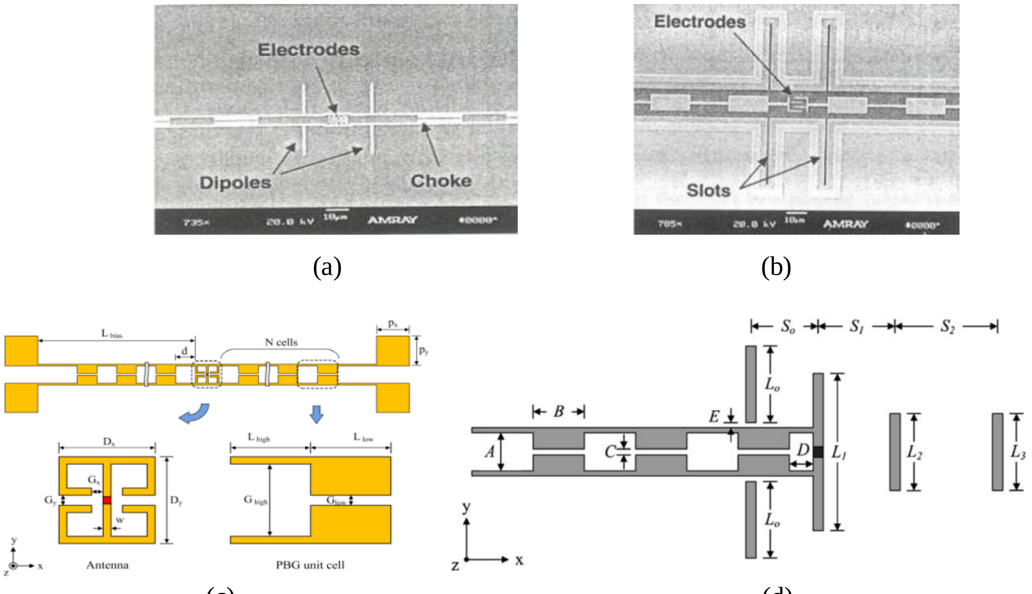

(a) (b)

(c) (d)

Fig. 3.15 (a) dual dipole antenna [200] (b) dual slot antenna [200] (c) four-leaf-clover-shaped antenna [201] (d) Yagi antenna [202]

The detailed analyses and comparison of antenna source resistances in THz pulsed and CW systems are studied in Chapter 4.

3.5.3. Improvement in Coupling of THz Wave to Air

Improving the coupling of the THz wave from the antenna to the air is another main requirement for high power and efficient THz antennas. Mounting a lens at the back of a THz antenna is the most common and established method to couple power from the antenna to air [203, 204]. However, the use of the lens has some drawbacks such as precise spatial alignment requirement and the inefficient illumination from the backside of the substrate [173]. There are alternative methods that can alleviate some of these drawbacks. One is a TEM horn antenna. This wideband THz antenna was proposed by Peytavit *et al.* in which THz wave radiates directly to the air without the substrate impact. This antenna has been employed both in CW and pulsed systems [173, 205] as depicted in Fig. 3.16.

Another method for THz power coupling is the use of a corrugated metal structure, known as a bullseye structure, surrounding of a dipole antenna [206] as shown in Fig. 3.17.

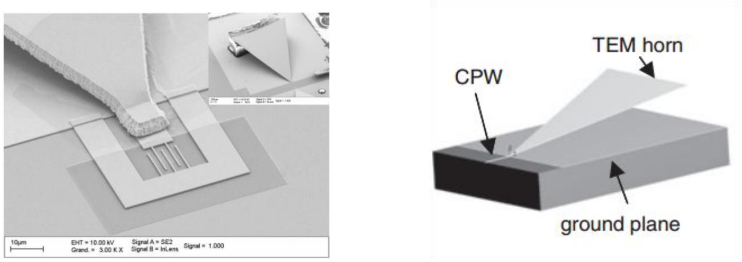

(a) (b)

Fig. 3.16 (a) SEM image of THz horn antenna with interdigitated fingers for a CW system [173] (b) Schematic image of TEM horn antenna with CPW feeding for a pulsed system [205]

Since the grooved structure surrounding the antenna is large, more THz power can be coupled to the dipole antenna located at its centre; hence, no substrate lens is required. Under the illumination of THz wave on this antenna as a detector (or analogously radiation of THz wave from the antenna as an emitter), surface plasmons are excited and the magnitude of the signal is enhanced based upon the number of grooves. According to the periodicity of grooves, detected

THz signal (or radiated THz signal) is also enhanced at a specific frequency. Therefore, this geometry is suitable for the narrowband or multiband THz wave coupling.

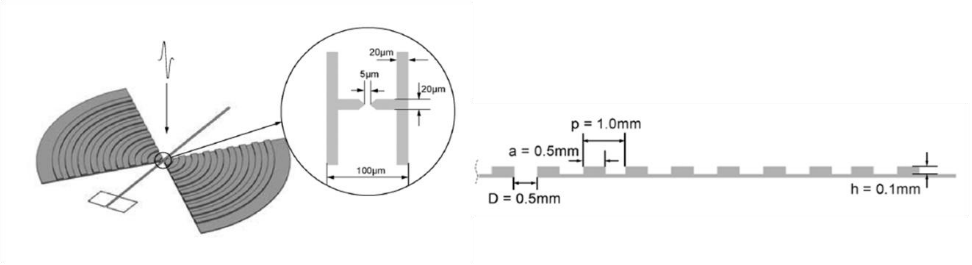

Fig. 3.17 Schematic view of a bullseye dipole antenna (left) and cross section of the grooved structure (right) [206]

3.5.4. Other Methods for Improving the THz Radiated Power

In conventional planar RF/MW antennas, tremendously various antenna geometries exist; however, this is very limited in THz antennas. The physical sizes of THz antennas are much smaller than MW antennas; hence, fabrication of detailed variations in antenna geometries is very difficult. Also, the effect of these delicate variations in geometries may not be captured in the real measurement setups due to various effective factors in real measurement environment. Also, the requirements for RF/MW antennas are very diverse due to various wireless technologies. But, in THz antennas the requirement is limited yet it is very challenging due to intrinsic characteristics of generated THz waves from these antennas. THz antennas require having high radiation power and efficiency, being broadband with smooth spectral behaviour for pulsed systems and being narrowband with high radiation resistance and low capacitance for CW systems.

For THz pulsed systems, bowtie and dipole are the most common antennas. One new type of THz antennas, which is borrowed from microwave antennas, is fractal antennas. Recently Sierpinski and Apollonian fractal emitters have been proposed as shown in Fig. 3.18 [207, 208]. In the microwave region, fractal antennas are multiband and the radiated power and directivity of the different orders of fractal antenna at the same resonance bands are similar; however, plasmonic feature of fractal antennas in the THz band lead to different radiated power emission profile.

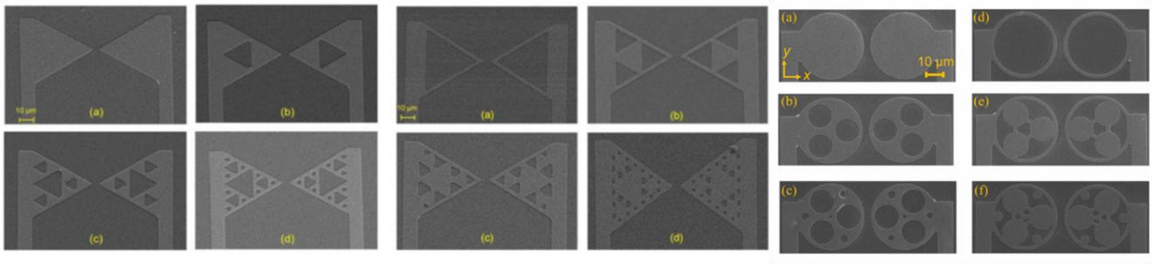

(a) (b) (c)

Fig. 3.18 SEM image of (a) Sierpinski (b) complementary Sierpinski (c) Apollonian and complementary Apollonian THz photoconductive antennas [208] for various orders of a fractal structure

Sub-wavelength confinement and surface plasmons can be obtained at frequencies near the plasma frequency of antenna electrode material [2]. However, the plasma frequency of gold is very high and it is not in THz range to support surface plasmons. Thus, structured surfaces[1] should be used for localisation and manipulation of THz current coupled from the photoconductive gap to the antenna [209]. This leads to enhanced THz power from the fractal antenna electrode surfaces compared to plane electrodes due to constructive interference of individual sub-wavelength radiators.

Another method to increase the radiated power of the antenna is the use of a longer dipole antenna. However, this leads to reduction of the detectable spectral range by the antenna [7, 192].

3.6. THz Antennas for Various Applications

Various THz antennas have been proposed for different applications. Explained antennas in the previous section are mainly employed in THz-TDS or THz-TDI systems. However, for some applications, specific adjustment in the antenna geometry is required. For instance, in THz time domain spectroscopic ellipsometry, the goal is to analyse polarisation behaviour of a sample. Hence, the THz emitter and detector should be able to emit and detect two orthogonal polarisations. For this purpose, three-contact [210] and four-contact [211] THz photoconductive antennas have been proposed as depicted in Fig. 3.19. These geometries facilitate simultaneous

---

[1] This can be achieved by drilling arrays of holes, grooving the structure or periodic corrugation on the metal’s surface [209].

detection of two orthogonal electric-field components of an arbitrarily polarized THz wave.

(a) (b)

Fig. 3.19 (a) three-contact THz photoconductive antenna as a detector. Two lock-in amplifiers are connected to electrode 1 and electrode 2 [210] (b) four-contact THz photoconductive antenna as an emitter. The antenna is biased in a way to receive two electrical fields in + 45° and -45° directions [211].

For some THz applications, greater sensitivity or larger emitted power at specific frequencies may be required. For this purpose, an H-fractal THz photoconductive antenna [212] and a multiple periodic grooved structure surrounding a dipole antenna [206] have been employed.

3.7. Summary

In this chapter, an overall view on THz antennas was provided. The necessity of having THz antenna and its differences from conventional RF/MW antennas in various aspects were elaborated. These differences highlight requirement of different methods in THz antenna analysis, simulation, fabrication, and measurement. The problem of low optical-to-THz conversion efficiency of THz antennas was addressed. To understand and elaborate the reason of low efficiency performance of THz antennas, a novel approach has been employed to analyse the total efficiency of THz antennas. In this approach, the wave generation process was divided into three parts. The analysis showed that, in the THz photoconductive antenna, optical-to-electrical conversion efficiency is the lowest; whereas in the THz photomixer antenna both optical-to-electrical and matching efficiencies are very low. Based upon the requirement of high power and efficiency for THz antennas, several parameters related to optical sources, photoconductive material and antennas were concisely summarised in a simplified diagram (Fig. 3.5). These parameters were discussed and various antenna-related approaches from the literature were reviewed. The required background for various topics including source resistance of antenna, screening effect, and challenges of THz antenna design were addressed in this chapter.

Chapter 4. Source Conductance in THz Antennas

4.1. Introduction

In Chapter 3 THz antennas were compared with conventional RF/MW antennas from various perspectives including excitation source and feeding. Also, the importance of impedance matching, as one of the main factors leading to low radiated power and efficiency of THz antennas (especially in CW systems) was elaborated. Although different methods in the literature have been investigated to improve the output power and efficiency (as described in the previous chapter), little research has been concentrated on source conductance of THz antennas which is very important for impedance matching. Therefore, the focus of this chapter is on the analysis of source conductance (or 1/resistance) of THz antennas for both THz pulsed and CW systems. Initially, a new source conductance equation for a THz pulsed system is derived and based upon that the impact of different parameters on the source conductance of the antenna is investigated. A similar theoretical approach is employed to examine the effect of operational parameters on the source conductance of a THz photomixer antenna. In accordance with the previous chapters where the differences of THz pulsed and CW systems were elaborated from system setup and application points of views, in this chapter, source conductance of THz photoconductive antennas and THz photomixer antennas are compared based upon their different excitation schemes. The purpose is to facilitate understanding the behaviour of the antenna source conductance based upon the used THz system type and its effect on the antenna impedance matching.

4.2. Source Conductance of THz Photoconductive Antennas

As shown in a conventional antenna setup in Fig. 3.1a, the input voltage is commonly transferred to the antenna through a transmission line. The resistance of the transmission line has a constant value, and it is considered as the source resistance for the antenna. The related equivalent circuit for this antenna type is depicted in Fig. 4.1a. In THz antennas, under illumination of laser pulses and its interaction with photoconductive material, input signal of the THz antennas is generated. Hence, the photoconductive material acts as the current source for the antenna and its resistance is considered as the source resistance of the antenna. Because of the time-varying behaviour of optical sources and photoconductive material response, the source resistance of a THz antenna is time-varying. The related equivalent circuit of a THz photoconductive antenna is shown in Fig. 4.1b. Thus, source resistance is one of the major differences between a conventional RF/MW antenna and a THz antenna.

To be able to calculate the radiated THz power from the antenna, THz photo-current flow needs to be obtained. The base of these calculations is the derivation of the exact conductance of the photoconductive gap. Hence, a precise attention on behaviour of source conductance of the antenna which supplies a time varying THz photo-current to the antenna electrodes is required.

In previous derivation of source resistance of a THz photoconductive antenna in the literature, some simplified assumptions have been made [175]. First, time variant behaviour of the generated photo-carriers in the photoconductive material was ignored and it was assumed as a simplified rectangular pulse shape. Also, the absorption of optical pulses in the active layer of the substrate was neglected. Therefore, for understanding the effect of various parameters on the antenna, exact analytical expression of the source conductance is required. That is the aim of this section and derivation of a new equation for source resistance of THz photoconductive antennas is elaborated.

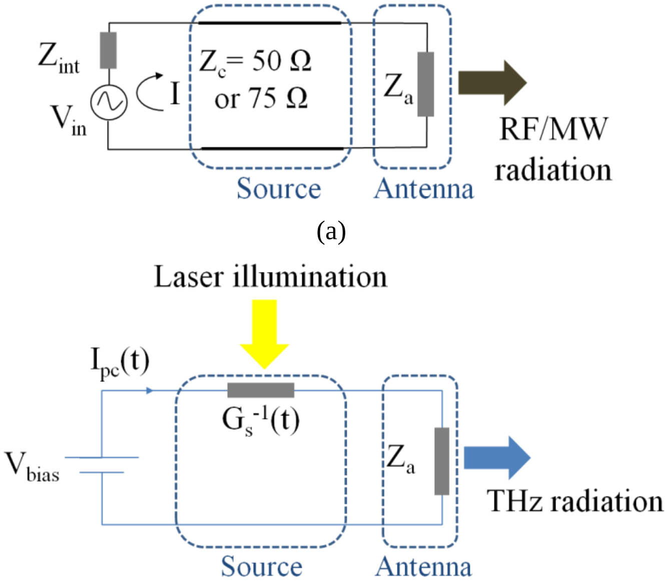

(a)

(b)

Fig. 4.1 Equivalent circuit for a (a) conventional RF/MW antennas, Z_c denotes the source resistance (b) THz photoconductive antenna, $G_s^{-1}(t)$ represent the source resistance. Here it is assumed that reactive loading to the antenna is negligible.

4.2.1. Derivation of the New Source Conductance Equation

For calculation of source conductance, a theoretical understanding of photoconduction process is required. As shown in Fig. 4.2, a THz photoconductive antenna, with the electrode gap of L, width of W and the substrate active layer thickness of $T_{LT\text{-}GaAs}$ (where electron-hole pairs are created), is assumed for analysis.

The electric field distribution of Gaussian laser pulses (and the related parameters) at any distance along the axis of propagation (here z) can be written as [213]:

$$E(r_1,z)=\left(\frac{w_0}{w}\right)\exp\left(-\frac{r_1^2}{w_0^2}-jkz-\frac{j\pi r_1^2}{D\lambda}+j\varphi_0\right) \tag{4.1}$$

where r_1 is the perpendicular distance from the z axis, w_0 is the beam waist radius at z = 0, w is the beam radius, k is the propagation vector. D and φ_0 are radius of curvature and the Gaussian beam phase shift respectively, defined by the following equations.

$$D=z+\frac{1}{z}\left(\frac{\pi w_0^2}{\lambda}\right)^2 \tag{4.2a}$$

$$\varphi_0 = \tan^{-1}\left(\frac{\lambda z}{\pi w_0^2}\right) \tag{4.2b}$$

Here, it is assumed that at z = 0, beam waist of laser pulses is on the gap of antenna. Also, to include the time dependency of the laser beam and the laser pulse duration, τ_l ,[214] equation (4.1) is modified as:

$$E(r,t) = \exp\left(-\frac{r_1^2}{w_0^2}\right)\exp\left(-\frac{t^2}{\tau_l^2}\right) \tag{4.3}$$

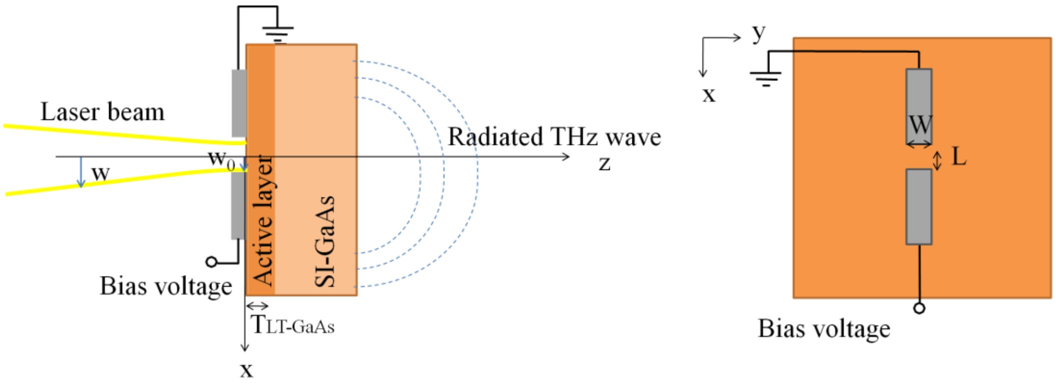

(a) (b)

Fig. 4.2 Schematic geometry of a THz photoconductive antenna (a) side view (b) top view

The transmitted optical pulse intensity to the semiconductor is directly proportional to the square of the incident electric field. By considering the optical power reflection coefficient in air-photoconductive material interface, $R= (n_{air}-n_{sub})^2/(n_{air}+n_{sub})^2$ (where n_{sub} and n_{air} are respectively the refractive index of substrate and air), the optical pulse intensity can be written as:

$$I(r,t) = I_l(1-R)\exp\left(-\frac{2r^2}{w_0^2}\right)\exp\left(-\frac{2t^2}{\tau_l^2}\right) \tag{4.4}$$

When the laser pulses illuminate the photoconductive material, free photo-carriers are generated. The time dependant behaviour of the generated carrier density is given by [78]:

$$\frac{dn(t)}{dt} = -\frac{n(t)}{\tau_c} + \frac{\alpha}{hf_l} I(r,t) \tag{4.5}$$

where f_l is the laser frequency.

By placing equation (4.4) in (4.5) and considering the appropriate initial value condition which matches with the photo-carrier generation; the solution of equation (4.5) becomes:

$$n(t) = I_l \exp(-\frac{2r_1^2}{w_0^2})(1-R)\frac{\alpha}{hf_l}\frac{\sqrt{2\pi}}{4}\tau_l \exp(-\frac{\tau_l^2}{8\tau_c^2})\exp(-\frac{t}{\tau_c})(erf(\frac{\sqrt{2}t}{\tau_l}-\frac{\sqrt{2}\tau_l}{4\tau_c})+1) \tag{4.6}$$

where $erf(x) = \int_0^x e^{-t^2}\,dt$.

Considering that the mobility of electrons is much higher than the mobility of holes (because the mass of holes is greater than that of electrons), the conductivity of a photoconductive material is given by [127]:

$$\sigma(t) = e.\mu_e.n(t) \tag{4.7}$$

According to basic principles, the conductance of a material based on its geometrical parameters and equivalent conductivity (considering the optical non-uniform absorption in the semiconductor along the z axis) is defined as:

$$G_s(t) = \int dG_s(t) = \int_0^{T_{LT-GaAs}} \sigma(t)e^{-\alpha z}\frac{W}{L}dz = \frac{W}{L\alpha}\sigma(t)\left(1-\exp(-\alpha T_{LT-GaAs})\right) \tag{4.8}$$

Here, it is assumed that beam radius of the Gaussian beam at the gap of antenna uniformly covers the whole gap of the shown antenna in Fig. 4.2 and $r_1^2 = w_0^2$. Also, it is assumed that most of the photo-carriers are generated within the thickness of the active layer, $T_{LT-GaAs}$, which is very thin. Thus, the time dependant conductance of the photoconductive material, $G_s(t)$, by using equations (4.6)-(4.8) is derived as [215]:

$$G_s(t) = \frac{W}{L}\left(1-\exp(-\alpha T_{LT-GaAs})\right).e.\mu_e.I_l \exp(-2)(1-R)\frac{\sqrt{2\pi}}{4hf_l}\tau_l \exp(-\frac{\tau_l^2}{8\tau_c^2}) \tag{4.9}$$

$$\exp(-\frac{t}{\tau_c})(erf(\frac{\sqrt{2}t}{\tau_l}-\frac{\sqrt{2}\tau_l}{4\tau_c})+1)$$

This equation shows clearly that the source conductance of a photoconductive antenna depends on different parameters of laser source (I_l and τ_l), antenna (W, L, $T_{LT-GaAs}$), and photoconductive material (τ_c, μ_e and α). Also, compared to the approximate old equation of

$G_{app} = \dfrac{We\mu_e(1-R)I_l\tau_l}{Lhf_l}$ in [175], equation (4.9) includes absorption of optical power in substrate active layer and it describes time dependent behaviour of source conductance in accordance with the real physical response of the photoconductive material. This describes source conductance of the antenna more realistically than [175] and it matches with the behaviour of the actual photocurrent pulse of the antenna [78] as shown in Fig. 4.3.

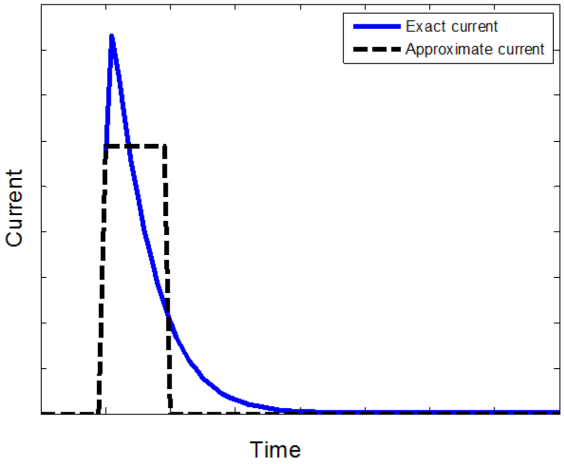

Fig. 4.3 Comparison of the photocurrent from the exact and approximate source conductance equations

In addition, the average conductance of the photoconductive material can be calculated based on the laser pulse period. The time average of the instantaneous conductance which includes both the on and off time in a period can be written as:

$$\overline{G_s} = f_{rep}\int_0^{1/f_{rep}} G_s(t)dt \tag{4.10}$$

where f_{rep} is the laser repetition rate. In order to solve equation (4.10) in a closed form, it is assumed that the duration of laser pulses is much shorter than the carrier lifetime of photoconductive material (which is a common situation in THz systems). By this simplified assumption, the *erf* term in equation (4.9) approaches one and then the average conductance of photoconductive source by using equation (4.10) will be:

$$\overline{G_s} \approx f_{rep}.e.\mu_e.I_l.\exp(-2)(1-R)\frac{2\sqrt{2\pi}}{4hf_l}\tau_l\tau_c\frac{W}{L}\left(1-\exp(-\alpha T_{LT-GaAs})\right)\left(1-\exp(-\frac{1}{f_{rep}\tau_c})\right) \tag{4.11}$$

To illustrate more clearly the time dependant source conductance of a THz photoconductive antenna, typical values of a THz pulsed system are chosen as an example as: μ_e = 1000 cm^2.V^{-1}.s^{-1}, R = 0.318 (for LT-GaAs), α = 6000 cm^{-1}, f_l = 375 THz (at λ = 800 nm), f_{rep} =80 MHz, τ_l = 100 fs, P_{av} = 1 W, τ_c= 1 ps, L = 10 μm, W = 10 μm and $T_{LT\text{-}GaAs}$ = 1 μm. It is good to add that since the energy contained in every pulse of laser is constant, the relationship between average and peak optical power can be written as: $P_{peak} = P_{av}/f_{rep}\tau_l$. With these values, the related time variant conductance of the photoconductive source in THz photoconductive antenna is depicted in Fig. 4.4.

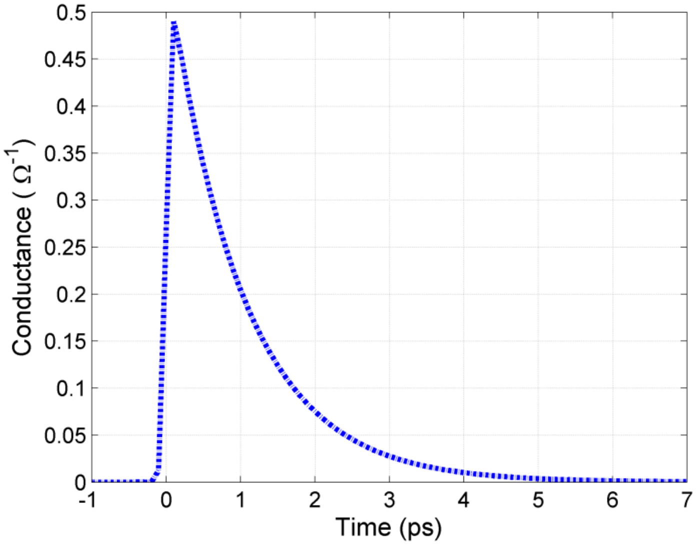

Fig. 4.4 The time-dependant source conductance of a THz photoconductive antenna for a common THz pulsed system where μ_e= 1000 cm^2.V^{-1}.s^{-1}, R = 0.318, α = 6000 cm^{-1}, f_l = 375 THz, f_{rep} =80 MHz, τ_l = 100 fs, P_{av} = 1 W, τ_c= 1 ps, L = 10 μm, W = 10 μm and $T_{LT\text{-}GaAs}$ = 1 μm.

Here, the resistance which corresponds to the maximum conductivity of the photoconductive material (under peak laser power illumination) is ~ 2.04 Ω. Achieving source resistance of few (ten) ohms in pulsed systems, during laser illumination has been reported in

[216]. By taking the inverse of equation (4.11), the average source resistance is found to be ~ 22.5 kΩ. This big difference between the resistance corresponding to the peak conductance value and average resistance is due to the long off time of laser and low conductance of source at those time intervals.

4.2.2. Parameter Analysis

As it is obvious from equation (4.9), the source conductance of the photoconductive antenna varies by changing optical source, photoconductive material and antenna gap properties. In order to gain a better understanding, in this section the effect of various parameters on the time variant source conductance is studied and analysed. Through this analysis, the contribution of one parameter at a time is investigated while other parameters are set to be the values used for Fig. 4.4.

4.2.2.1. Average Optical Power

In order to investigate the effect of optical power, the gap size of the antenna is kept fixed. As depicted in Fig. 4.5, by increasing the average pump power of laser the source conductance of the THz photoconductive antenna increases. The reason is that, a higher optical power results in a higher photo-carrier generation and hence greater conductance. This dependency behaviour of source conductance of THz photoconductive antennas to the input optical power is one of the main contrasts between these types of antennas and conventional RF/MW antennas; because in the latter types, the source impedance is constant and it does not differ by changing the input power. Therefore, the temporal characteristics of source conductance and its peak value which corresponds to the maximum generated photo-carrier should be determined for each THz pulsed system for further antenna analysis.

4.2.2.2. Laser Pulse Duration

Another parameter related to the optical excitation source is the laser pulse duration. As shown in Fig. 4.6 the rise time of the source conductance is determined by the laser pulse duration; but, the decay time of the source conductance is independent of the laser pulse duration and it is same for all. It can be observed that the shorter the laser pulse duration, the shorter the source conductance rise time. The peak values of source conductance are also affected by this parameter. By increasing the pulse duration, the peak source conductance decreases. This analysis highlights the necessity of using ultra-short laser pulses to have a larger source conductance and as a result larger transient photocurrent.

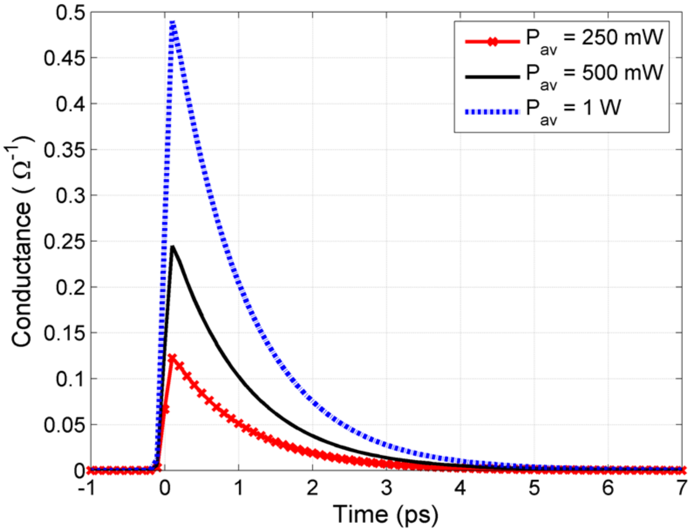

Fig. 4.5 Variation of the time-dependant conductance of a photoconductive material by the average optical power

4.2.2.3. Antenna Gap Area

Antenna gap size as discussed in section 2.4.1 is a very important factor and affects the amount of absorbed optical power and generated photo-carriers. Here while the average input optical power is fixed, the antenna gap area is enlarged and accordingly laser spot size is increased to cover the antenna gap. As depicted in Fig. 4.7 by increasing the antenna gap area, the peak value of the source conductance decreases. The reason is that when the optical power has a constant value, by increasing the gap area, the distance between the generated photo-carriers increases because of the decrease of carrier density in the antenna gap. Therefore, source conductance reduces. Although this shows that small gap antennas perform better than large gap ones, more optical power can be applied to large gap antennas before saturation and break down of the device unlike small gap antennas. This is discussed further in Chapter 5. In addition, if input optical power increases by enlarging the gap size, the carrier density is kept constant and according to equations (4.7) and (4.8), the source conductance will be the same.

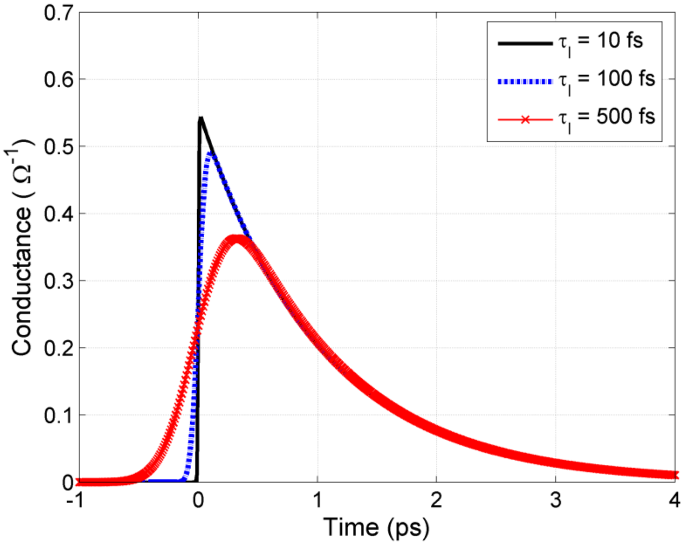

Fig. 4.6 Time-dependant source conductance of a THz photoconductive antenna for different laser pulse durations

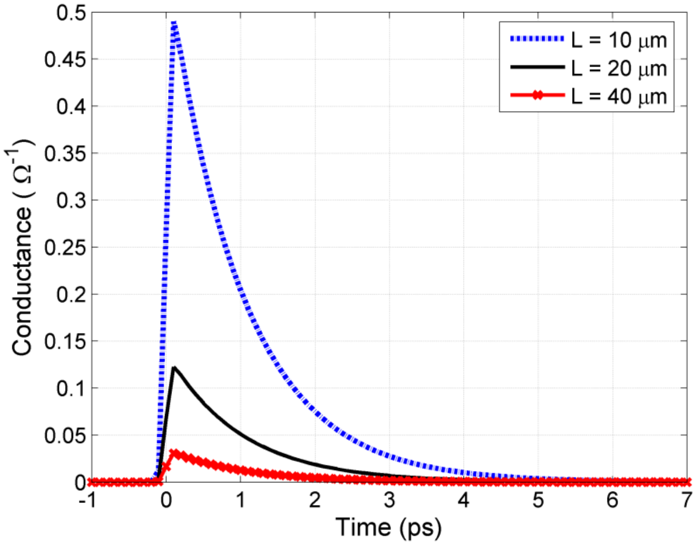

Fig. 4.7 Dependency of temporal source conductance of a THz photoconductive antenna to various antenna gap areas for the fixed average input optical power

4.2.2.4. Laser Spot Shape

In the derivation of temporal source conductance, it was assumed that laser pulse as shown in equation (4.4) is a symmetric fundamental Gaussian beam. For an elliptical Gaussian laser shape equation (4.4) needs to be updated as follows:

$$I_{ell}(r,t)=I_l(1-R)\exp(-\frac{2x^2}{w_x^2})\exp(-\frac{2y^2}{w_y^2})\exp(-\frac{2t^2}{\tau_l^2}) \qquad (4.12)$$

where w_x and w_y are beam waists in x and y directions at the antenna gap respectively. Since in elliptical spot laser case the semiconductor gap is partially illuminated, the total source conductance is the summation of source conductance of the illuminated area and conductance of the dark area ($G_{s\text{-}dark}$).Thus, the source conductance of illuminated area is:

$$G_{s-ell}(t)=\frac{2w_y}{L}\left(1-\exp(-\alpha T_{LT-GaAs})\right).e.\mu_e.I_l\exp(-2)(1-R)\frac{\sqrt{2\pi}}{4hf_l}\tau_l\exp(-\frac{\tau_l^2}{8\tau_c^2}) \qquad (4.13)$$
$$\exp(-\frac{t}{\tau_c})(erf(\frac{\sqrt{2}t}{\tau_l}-\frac{\sqrt{2}\tau_l}{4\tau_c})+1)$$

However, since in practice $G_{s\text{-}dark}$ is much smaller than the peak conductance at illuminated situation [96], $G_{s\text{-}dark}$ is neglected and the antenna source conductance will be $G_{s\text{-}ell}$. The effect of the laser spot shape on the temporal source conductance is shown in Fig. 4.8.

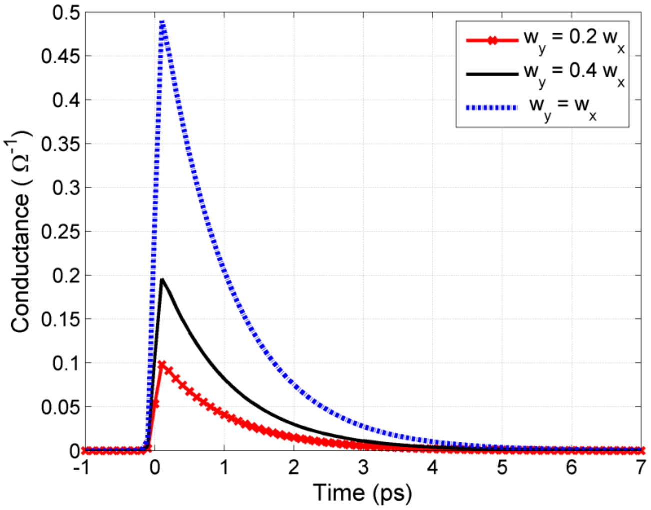

Fig. 4.8 Change of temporal source conductance of a THz photoconductive antenna as a result of various laser spot shape for a constant laser pulse intensity

By fixing the laser peak intensity (*i.e.* the photo-carrier density), in circular spot size more optical power is illuminated on the photoconductive gap than elliptical spot size; therefore, in that case source conductance is larger. Moreover, by considering various elliptical spot sizes, Fig. 4.8 shows that the narrower spot size leads to a lower conductance. Although the source conductance of the antenna in elliptical spot shape is smaller, the lower number of generated photo-carriers is an advantage. Because it avoids the generation of the excess amount of photo-carriers all over the antenna gap [180]. In other words, in elliptical case the photo-carriers are more tightly generated next to the antenna electrodes, hence residual effect of unpaired free photo-carriers decreases.

4.2.2.5. Carrier Mobility

Another parameter in source conductance of the antenna is the carrier mobility. Different photoconductive materials have different mobilities; for example as shown in Table 3.1 carrier mobility of SI-GaAs is larger than that of LT-GaAs. As shown in Fig. 4.9, source conductance values are larger for large carrier mobility which leads to a larger photocurrent. As stated in previous chapters, intrinsically high carrier mobility materials have long carrier lifetime which is undesirable. This effect is discussed next.

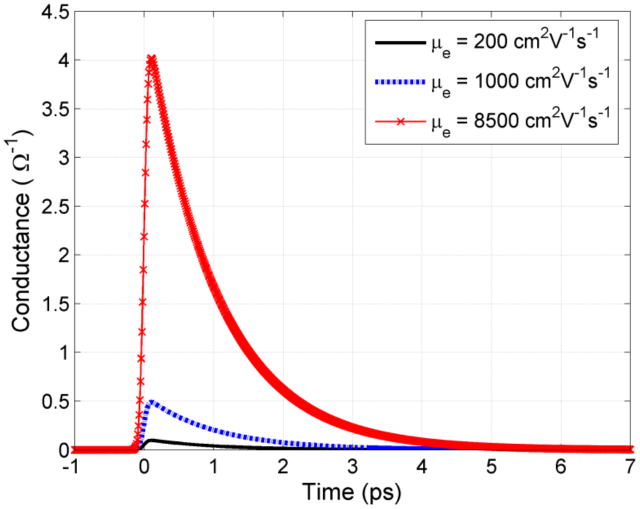

Fig. 4.9 Behaviour of temporal source conductance of a THz photoconductive antenna for various carrier mobility

4.2.2.6. Carrier Lifetime

In Fig. 4.10 the influence of carrier lifetime of photoconductive material on the time-variant source conductance is studied. It illustrates that the shorter the carrier lifetime, the sharper the conductance roll off. Higher carrier lifetime leads to high conductance values at longer time durations because of long-lived photo-carriers in the antenna gap. This is one of the main limitations of THz antennas because it prevents the creation of new electron-hole pairs and; therefore, it restricts generation of photocurrent. Here, the laser pulse duration is kept constant; thus, the rise time behaviour of the conductance in these three cases is identical. Although peak conductance of these antennas is very close, it is slightly larger for the longer carrier lifetime case compared to the other two. However, this is a very small positive effect compared to its terrible effect on limiting generation of photocurrent, heating the antenna and reducing the bandwidth.

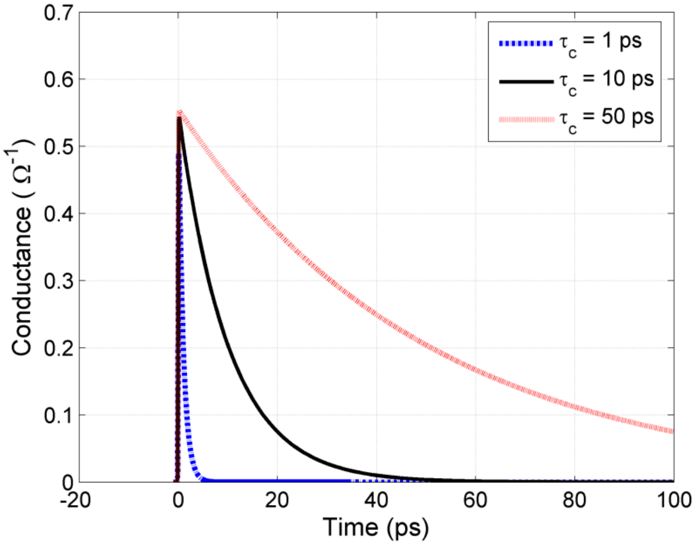

Fig. 4.10 Variation of temporal source conductance of a THz photoconductive antenna by changing the carrier lifetime

4.2.2.7. Optical Absorption Coefficient

Last investigated parameter is the impact of optical absorption coefficient, α. This coefficient in photoconductive materials is strongly dependent on optical wavelength of laser pulses. For common cases where the laser wavelength is around 800 nm and substrate material is

GaAs, α is between 1000 cm^{-1} to 10000 cm^{-1} [127]. Higher α means that most of laser power is absorbed in the active layer of the substrate; hence, more photo-carriers and ultimately photocurrent is generated. This agrees well with the source conductance behaviour shown in Fig. 4.11 where greater α results in higher conductance.

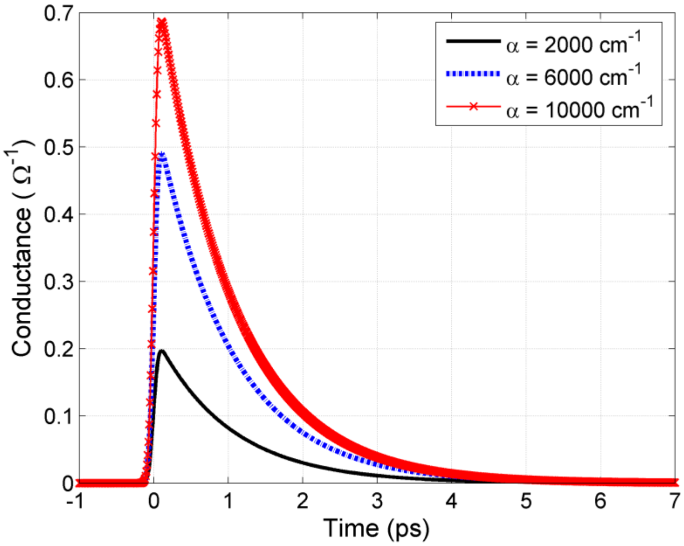

Fig. 4.11 Dependency of temporal source conductance of a THz photoconductive antenna on optical absorption coefficient

Parameter analyses in this section showed how different parameters affect temporal behaviour of the source conductance which could not be derived from previously provided approximate formula in [175]. Moreover, these analyses provide the required base for radiated power and efficiency studies of THz photoconductive antennas.

4.3. Source Conductance of THz Photomixer Antennas

As a first step of calculating source conductance of THz photomixer antenna, description of the time-varying optical electric field at the photoconductive surface is required. The schematic diagram of beam combination of optical lasers and generation of the resulting electric field profile travelling towards the antenna is shown in Fig. 2.2. Since this process is linear, according to Fig. 4.12 the produced electric field can be written as the summation of both optical electric fields, E_1 and E_2, as:

$$E(\vec{z},t)=|E_1|\sin(\omega_1 t-\vec{k}_1.\vec{z})+|E_2|\sin(\omega_2 t-\vec{k}_2.\vec{z}) \tag{4.14}$$

where k_1 and k_2 are phase constant vectors of optical fields and z is the position vector. The optical pulse intensity at the semiconductor is proportional to the square of the incident electric field. Assuming that the propagation vectors of optical pulses are at the same direction, the instantaneous intensity using trigonometric relations at the gap can be demonstrated as:

$$I(\vec{z},t)=\xi\left(E(\vec{z},t)\right)^2_{z=0}= \\ \xi\begin{pmatrix} E_1^2+E_2^2-E_1^2\cos^2(\omega_1 t)-E_2^2\cos^2(\omega_2 t)-E_1E_2\cos((\omega_1+\omega_2)t) \\ +E_1E_2\cos((\omega_1-\omega_2)t) \end{pmatrix} \tag{4.15}$$

where ξ is the proportionality constant. Photoconductive material is only able to respond to the slower frequency component of equation (4.15), hence; the pulse intensity at the antenna gap is:

$$I(\omega_{THz},t)=\xi(\frac{E_1^2+E_2^2}{2}+E_1E_2\cos(\omega_{THz}t))=I_0(1-R)(1+2\frac{\sqrt{mI_1I_2}}{I_0}\cos(\omega_{THz}t)) \tag{4.16}$$

where $\omega_{THz}=\omega_1-\omega_2$, $I_0=I_1+I_2$ (I_i= laser pulse intensity of each laser) and m is the mixing efficiency which shows the overlap between the two beam forms. That is affected by the polarisation of the laser beams and it is between 0 for no overlap case and 1 for perfectly overlapped case [8].

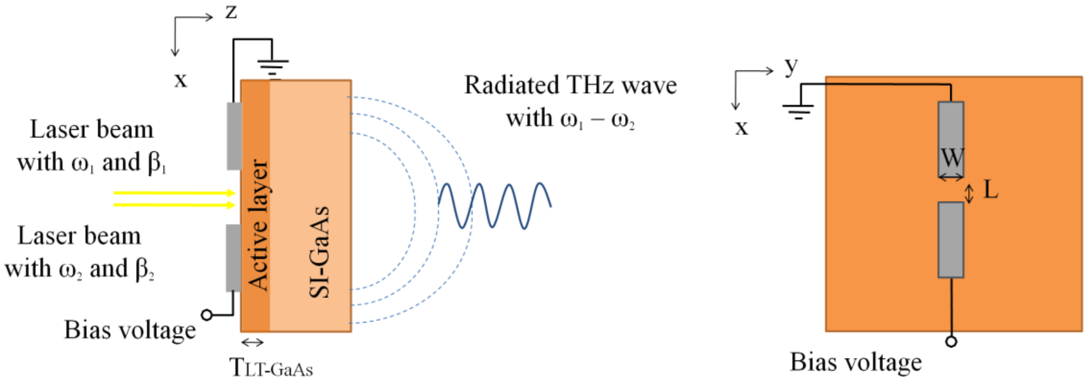

(a) (b)

Fig. 4.12 Schematic geometry of a THz photomixer antenna (a) side view (b) top view

Following the same procedure explained in section 4.2.1, using equations (4.5) and (4.16) and assuming that $I_1 = I_2$, the generated carrier density in the THz photomixer antenna is derived as:

$$n(\omega_{THz},t)=\frac{\alpha}{hf_l}I_0(1-R)\tau_c(1+\sqrt{m}\,\frac{\cos(\omega_{THz}t)+\omega_{THz}\tau_c\sin(\omega_{THz}t)}{1+(\omega_{THz}\tau_c)^2}) \tag{4.17}$$

Here, hf_l is the mean energy of both laser sources. In equation (4.17), the term of $C\exp(-t/\tau_c)$ is neglected because it decays very fast [111]. Using equations (4.7) and (4.8), the source conductance of a THz photomixer antenna is:

$$G_{scw}(\omega_{THz},t)=\frac{W\cdot e\cdot\mu_e}{Lhf_l}I_0(1-R)\tau_c\left(1-\exp(-\alpha T_{LT-GaAs})\right)$$
$$(1+\sqrt{m}\,\frac{\cos(\omega_{THz}t)+\omega_{THz}\tau_c\sin(\omega_{THz}t)}{1+(\omega_{THz}\tau_c)^2}) \tag{4.18}$$

To assess the source conductance in a CW system according to equation (4.18) and illustrate more clearly its time dependant characteristic, it is presumed that the wavelength of one laser is 800 nm, λ_1, and the wavelength of the second laser beam, λ_2, is tuneable to get the desired THz frequency according to $f_{THz}=c|\lambda_1-\lambda_2|/(\lambda_1\lambda_2)$ [73]. For instance for f_{THz} = 1 THz, when λ_1 is 800 nm then $\lambda_2 \approx$ 802 nm. Some typical values are chosen as an example as: R = 0.318 (for LT-GaAs), μ_e = 1000 cm^2.V^{-1}.s^{-1}, α = 6000 cm^{-1}, average power of each laser beam = 10 mW, m = 1, τ_c= 1 ps, L = 10 μm, W = 10 μm, and $T_{LT\text{-}GaAs}$ = 1 μm. With these values, the related time variant conductance of the photoconductive source in THz photomixing antenna is depicted in Fig. 4.13. The periodic behaviour of the source conductance follows the continuous wave behaviour of the envelope of the mixed laser beams. In this example, the source conductance varies between 6.64 μΩ^{-1} and 9.1 μΩ^{-1} and the corresponding mean resistance (1/mean conductance) of the photoconductive gap is ~128 kΩ. This matches with the achieved values of the photoconductive gap resistance in the literature which is >>10 kΩ [98].

The antenna resistance is commonly few hundred ohms. The proximity of the source resistance and the antenna resistance defines the impedance matching. The above analysis shows that there is a huge difference in values between the source resistance of the THz photomixer and that of the antenna. This highlights the importance of appropriate antenna design with higher impedance for a CW system.

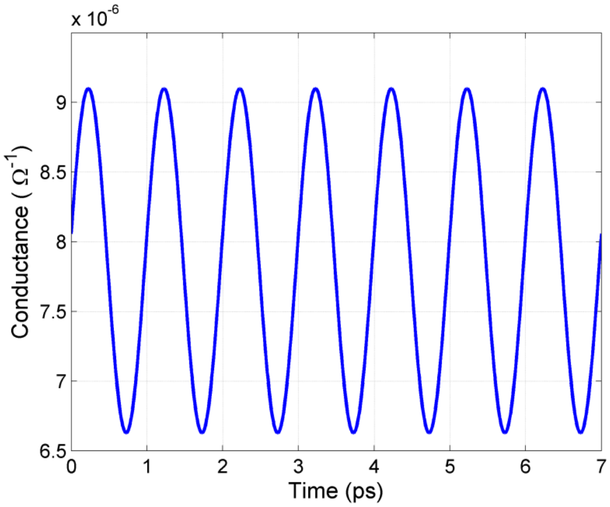

Fig. 4.13 The time-dependant source conductance of a THz photomixer antenna for a common THz CW system where μ_e= 1000 cm^2.V^{-1}.s^{-1}, R = 0.318, α = 6000 cm^{-1}, f_l = 374.5 THz, P_{av} = 15 mW (for one laer), τ_c= 1 ps, L = 10 μm, W = 10 μm , $T_{LT\text{-}GaAs}$ = 1 μm and f_{THz} = 1 THz.

4.3.1. Parameter Analysis

Understanding the behaviour of the source conductance (or 1/resistance) of the THz photomixer antenna is crucial for impedance matching between the photoconductive source and the antenna resistance. According to equation (4.18) time dependant source conductance has several variables. For antenna impedance matching the mean resistance of photoconductive antenna is required [111]; therefore, in this section the effect of various parameters related to optical source, photoconductive material and antenna gap on the average source resistance of a THz photomixer antenna is examined. In this study, the role of one parameter each time is investigated while other parameters are set to the values used in Fig. 4.13.

Initially the impact of the total average laser pump power is examined. In Fig. 4.14, it is illustrated that by increasing the average optical pump power the average source resistance declines. This is expected due to increase of generated photo-carrier density in the photoconductive gap at higher optical power. In addition, it shows that at higher average optical powers the problem of impedance mismatch between the source and antenna is less severe as compared to the lower average optical powers, where the average source resistance is much higher than that of the antenna.

The next investigation is on the dependency of average source resistance on the antenna gap area whilst the optical power of each laser is kept constant at 15 mW. In this case by increasing the antenna gap length and width (assuming that L = W) and laser spot size accordingly, the density of generated photo-carriers in the antenna gap decreases. As depicted in Fig. 4.15, this results in the rise of the source resistance and augmentation of impedance mismatching of the source and antenna.

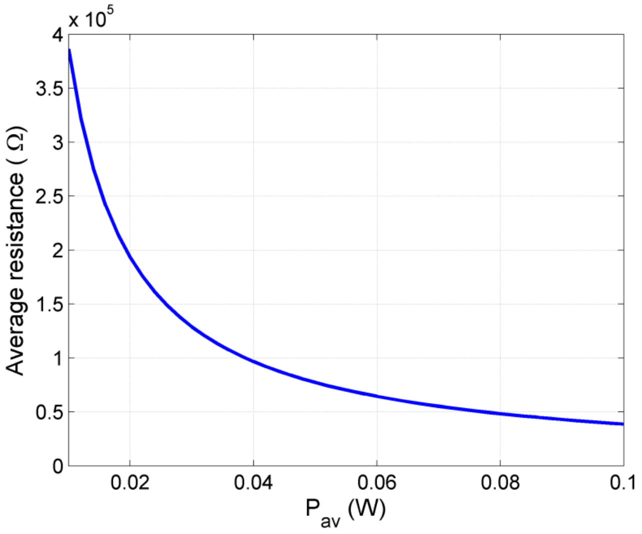

Fig. 4.14 Average source resistance of a THz photomixer antenna versus total average optical power

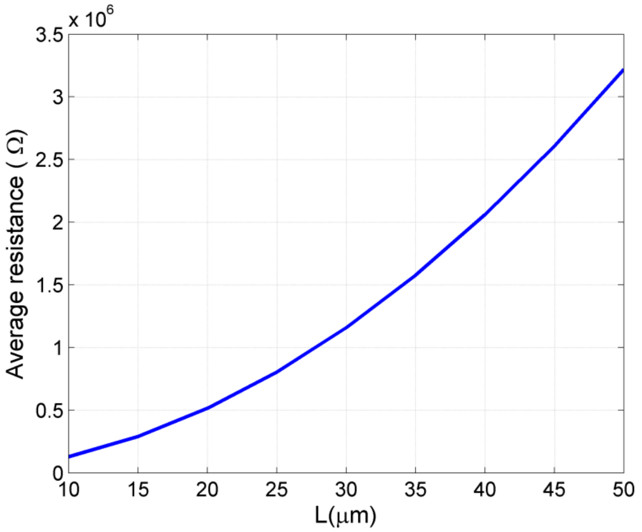

Fig. 4.15 Variation of the average source resistance of a THz photomixer antenna as a function of antenna gap length (and width) at a constant optical power

Furthermore, the influence of the carrier lifetime is assessed. As it is shown in Fig. 4.16, the average source resistance is smaller for longer carrier lifetime materials. The reason is that for photoconductive materials with longer carrier lifetime, free photo-carriers remain unpaired for a longer time; hence they can act as a conductor. Therefore, better impedance matching between the source and antenna can be obtained. However, the main drawback of this characteristic is the heat increment of the device which prevents application of more optical power in the antenna. On the other hand, too low carrier lifetime leads to generation of very few carrier densities which may not be enough for generation of photocurrent in the antenna gap. Therefore, an optimum carrier lifetime for the highest THz power has been defined as $\tau_{c-opt} = 1/2\pi f_{THz}$ [111]. Thus for this sample system at f_{THz} =1 THz, τ_{c_opt} is about 0.16 ps where the source resistance is ~ 112 kΩ; therefore, in optimum carrier lifetime very huge impedance mismatch between the source and the antenna exist.

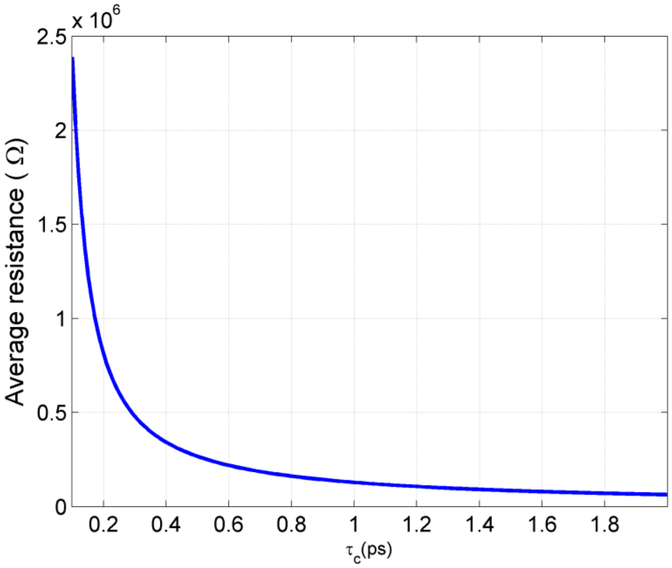

Fig. 4.16 Dependency of average source resistance of a THz photomixer antenna on carrier lifetime of the photoconductive material

Moreover, the effect of carrier mobility of photoconductive material on average source resistance is illustrated in Fig. 4.17. It is observed that by increasing the carrier mobility, average source resistance decreases, which is a desirable characteristic for a better impedance matching.

However, as stated previously, carrier mobility and carrier lifetime are contradicting parameters; Therefore, in Fig. 4.18 the effect of these two parameters on average source resistance is simultaneously illustrated. It shows that small average source resistances are possible when both the carrier mobility and carrier lifetime are large. However, as mentioned previously large carrier lifetimes cause thermal problem. This illustrates that there is a trade-off between good impedance matching and physical limitations/performance of the antenna.

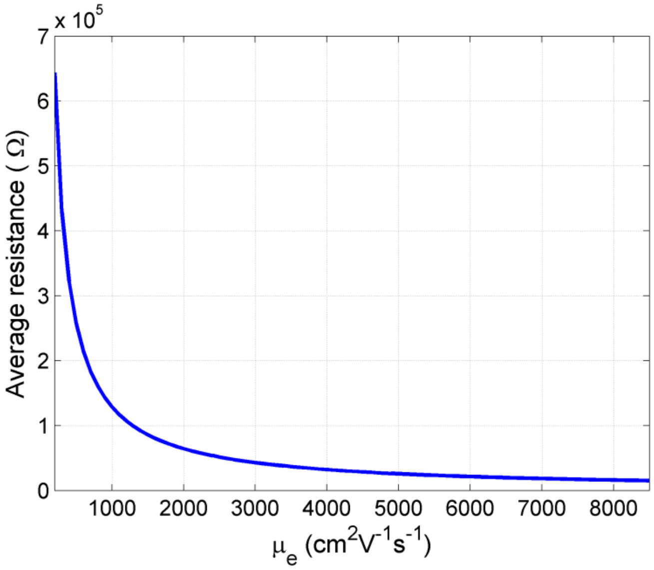

Fig. 4.17 Dependency of average source resistance of a THz photomixer antenna on carrier mobility of the photoconductive material

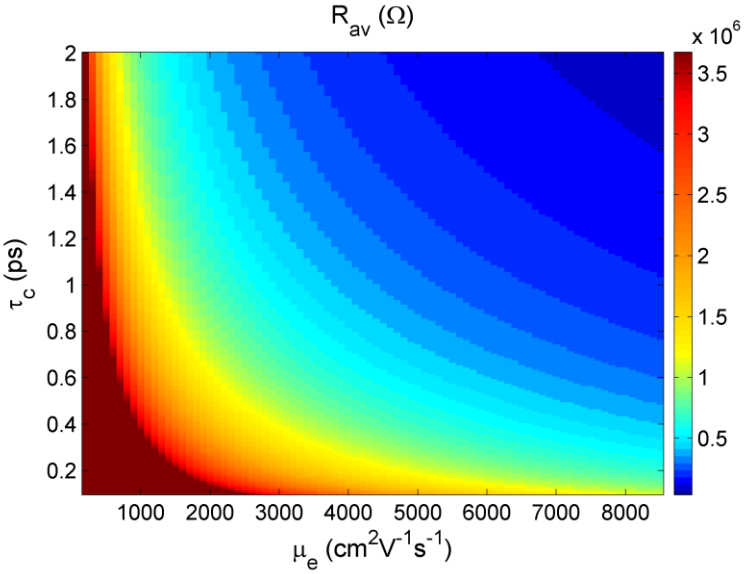

Fig. 4.18 Variation of average source resistance as a function of both the carrier mobility and lifetime

Finally, Fig. 4.19 depicts the impact of optical absorption coefficient on the average source resistance. It can be observed that by increasing the optical absorption coefficient source resistance reduces. Similar to the THz photoconductive antenna, in the THz photomixer antenna, when the optical absorption coefficient is large, more laser power is absorbed in the active layer of the substrate. This ultimately leads to generation of more photo-carriers. Therefore, the average source resistance reduces.

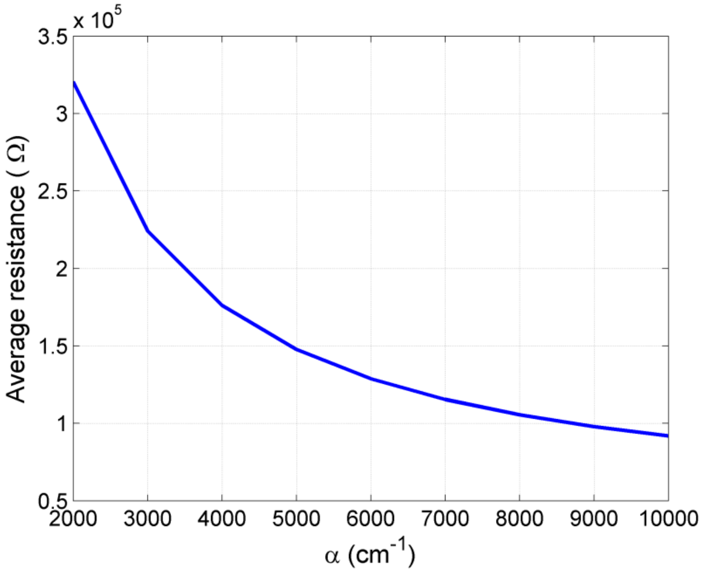

Fig. 4.19 Average source resistance of a THz photomixer antenna as a function of optical absorption coefficient

4.4. Comparison of Source Conductance of THz Antennas

In previous sections, source conductance (or equivalently source resistance) of two types of THz antennas has been analysed. How source conductance behaviour and its values differ for the same antenna when employed in a pulsed and CW system is important. Because it determines the importance of impedance matching for each types of the antenna. Therefore, in this section it is intended to compare the source conductance of an antenna in the identical situation and with the same parameters but with different excitation methods in a pulsed and CW system [217].

For this comparison it is assumed that in both systems the input average power of laser is 100 mW (In reality the power of laser diodes in CW systems are about a few ten mW), material properties (μ_e = 1000 cm^{2}V^{-1}s^{-1}, α = 6000 cm^{-1} at 800 nm, R = 0.318, τ_c = 1 ps) and antenna related dimensions (L = 10 μm, W = 10 μm, $T_{LT\text{-}GaAs}$ = 1 μm) are identical. The parameters related to the differences of these two systems are assumed as: f_{rep} = 80 MHz (laser repetition rate), τ_l = 100 fs for the pulsed system and the desired beating frequency of 1 THz for the CW system. Time variant behaviours of the source conductance of the antenna in the pulsed system and CW system are illustrated in Fig. 4.20a and Fig. 4.20b respectively.

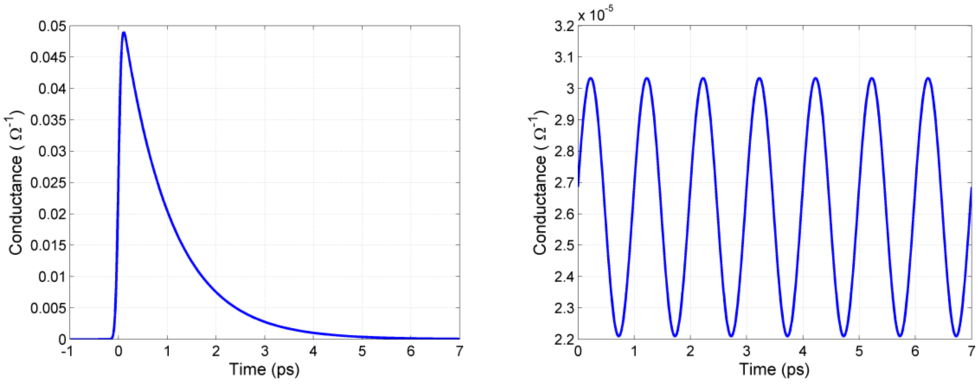

(a) (b)

Fig. 4.20 Source conductance of an antenna in the time domain for (a) the pulsed system (b) the CW system with identical parameters. It is assumed that the average optical power on each antenna is 100 mW.

Here, the source conductance for the pulsed system varies between 0 (equivalent to infinite resistance which corresponds to the off time of femtosecond laser) and 0.049 Ω^{-1} (or 20 Ω which corresponds to the peak conduction in the gap); while for the CW system it is between 22 and 30 μΩ^{-1} (33 – 45 kΩ). It is possible to compare the average source resistance of these two systems as well. In this case, the average resistance of the pulsed system is 225 kΩ while that of the CW system is 38 kΩ. This noticeable difference (about 6 times) between the average resistance values of these two systems can be explained by considering ultra-short laser pulse duration compared to the repetition time of laser. Because in a THz pulsed system $\tau_l << 1/f_{rep}$, and in the majority of the time when there is no illumination the source resistance is very high; whereas in a CW system, all the time, the laser is on and the source resistance fluctuates between relatively close values. Therefore, due to the difference in source excitations and as a result the photoconductive material response, for the impedance matching calculations, in a THz photoconductive antenna the peak conduction should be considered and in a THz photomixer antenna average conduction should be used.

As mentioned previously, one of the major differences of THz antennas (regardless of the type of excitation) with conventional antennas is variation of their source resistance according to the input optical power. Here to understand how source resistances of these two THz antennas change at the same situation, laser powers are varied. As shown in Fig. 4.21 the average source resistance of this antenna in the CW setup is very large and it is in the range of kΩs; however, the source resistance of the antenna in the pulsed setup (corresponding to the peak conduction) is less than few hundred ohms.

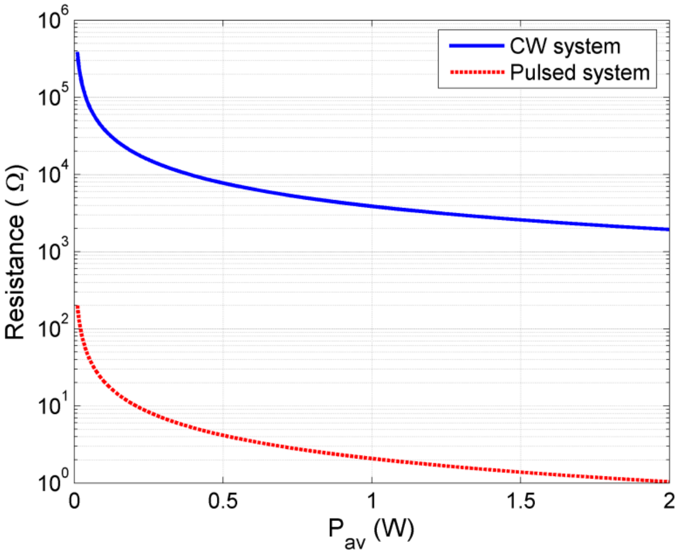

Fig. 4.21 Comparison of the average source resistance of the THz antenna in a CW setup and resistance of the same antenna corresponding to the peak conductance in a pulsed setup at different optical powers on the antenna

To compare the matching efficiency of the antenna in these two systems, as an example a frequency-independent long bowtie antenna with 60° bow angle on GaAs is selected. In this case the antenna resistance, R_a, is about 90 Ω [203]. Considering the impedance matching coefficient at the resonance frequency, $1-(\frac{R_a - R_s}{R_a + R_s})^2$ (where R_s is the source resistance);this parameter is calculated for THz photoconductive and photomixer antennas, at different total input optical powers.

As shown in Fig. 4.22, in the pulsed system at some optical powers (e.g. 24 mW here) matching efficiency is almost 1; however, this is dependent on the value of the input power. In other words, by changing the optical power the matching efficiency changes and it results in severe mismatching. In the CW system, although matching efficiency is improved at higher total input power, this parameter is extremely low for any input power; for instance at optical power of 24 mW it is 0.002. In reality, it is not possible to increase total optical powers of the CW excitation source steadily. This is because of the device heating problem. Thus, according to Fig. 4.22 it can be concluded that there exist much larger impedance mismatch for an antenna in a CW system compared to the case it is employed in a pulsed system. This analysis highlights that designing an antenna with larger resistance is very crucial in CW systems.

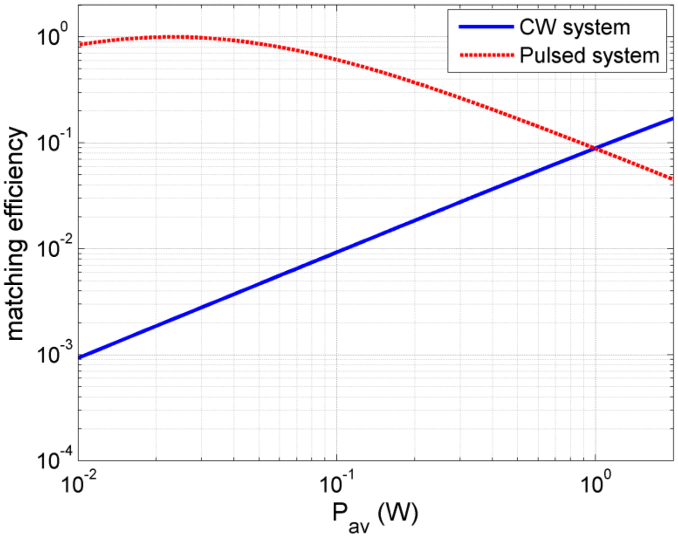

Fig. 4.22 Matching efficiency comparison for a 60° long bowtie antenna with R_a = 90 Ω in the CW and pulsed systems

4.5. Summary

The focus of this chapter was on the antenna source conductance analysis in THz systems. A new formula for the time variant source conductance of a THz photoconductive antenna has been derived. This newly derived equation describes more accurately the effect of various parameters on the source conductance of the photoconductive antenna than the previous approximate equation of [175]. This is because the time dependant behavior of the generated photo-carrier has been considered in the new derivation. This equation can be used as a part of circuit model for pulsed THz antennas and also for calculations of impedance mismatch between the photoconductive source material and the antenna. Analogously, source conductance of a THz photomixer antenna has been evaluated as a result of varying several parameters. The source conductance of a THz antenna in both pulsed and CW systems have been compared and it was showed that the impedance matching for a THz photomixer antenna is much smaller than that of a THz photoconductive antenna.

Chapter 5. Theoretical Modelling of a Photoconductive Antenna in a Terahertz Pulsed System

5.1. Introduction

A new equation for source conductance of a THz photoconductive antenna was presented and analysed in the previous chapter. This is necessary for a more accurate radiated power and efficiency assessment of a THz photoconductive antenna since the source conductance is an element of the equivalent circuit of the antenna.

An antenna as an emitter affects the entire THz system performance and as a result the detected power level of the system. Therefore, a detailed analysis of the emitter antenna is crucial. In order to analyse the performance of the THz antenna, there is a need for an equivalent circuit model. There are two types of equivalent circuit models readily available. One is obtained from an electrical perspective (large signal analysis) [218]. This model consists of a constant capacitance representing the gap capacitance of the antenna, the time-dependent resistance for the photoconductive material and the antenna resistance. It is simple due to employing lumped element components; however, because of its simplified nature it cannot predict the local fields (or voltages) of the device accurately. The other equivalent circuit is derived based on the real physical behaviour of the device considering the carrier dynamics in the generation of THz waves

[219]. This model includes the antenna resistance, the time-varying source resistance and a time-variant field due to the space-charge screening effect. In this model, the accuracy is enhanced from the simplified lumped element model because more physical aspects have been taken into account. However, the complexity in the derivation of equations is augmented. Moreover, when there is no laser illumination; *i.e.* in dark condition, the THz emitter can be regarded as a charged capacitance [78].

Therefore, mapping the microscopic behaviour of the antenna into a lumped element circuit which can predict the local fields of the antenna is required. Therefore, in this chapter a new equivalent circuit is developed with the aim to bridge the gap between the two previous models [117]. It uses a lumped element approach in modelling; retaining the simplicity, and at the same time it maintains accuracy since the lumped element components have been modeled and derived based on the complex physical mechanisms. Thus, this new equivalent circuit should serve as a useful tool to gain a better understanding of THz photoconductive antennas without the need for complex physical derivations. In addition, based upon the newly developed equivalent circuit, the low efficiency and radiated power issue of the photoconductive antenna is studied from various facets and the simulated results are compared with published measured results. Finally, through an example, it is demonstrated that how this theoretical analysis can be applied to maximize the optical-to-THz conversion efficiency for a desired laser optical power range based on the available photoconductive material and the antenna. These results are useful in designing THz antennas and tuning the system with improved efficiency.

5.2. Generation of THz Wave from a THz Photoconductive Antenna

The working principle of a THz photoconductive antenna as an emitter was described in section 2.4.1. Here, a more in-depth explanation on THz wave generation is provided. The purpose is to highlight the necessity of different elements for antenna performance analysis through an equivalent circuit.

Schematic picture of the generation of a THz pulse from a photoconductive antenna is shown in Fig. 5.1. With the illumination of femtosecond laser pulses, electron-hole pairs are created in the photoconductive material when the laser pulses have higher photon energy than the band gap energy of the photoconductive material. The applied bias voltage across the antenna, more precisely electric field (E_{bias}), then accelerates these photo-excited carriers. Because of the physical separation of the charges (electrons and holes), an electron-hole field ($E_{e\text{-}h}$) in the reverse direction of the bias field is created. By generating more electron-hole pairs, $E_{e\text{-}h}$ increases and after a while, the total electric field at the position of carriers is screened. The quick change in the electric field at the gap results in a transient current and finally an electromagnetic pulse in the THz frequency range is radiated.

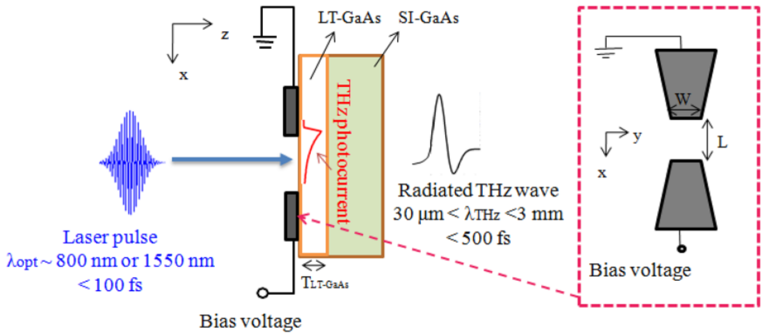

Fig. 5.1 Generation of THz waves using the THz photoconductive antenna under the illumination of laser pulses; antenna electrodes are shown in the inset.

According to the operational principle of the antenna, the separation of electron-hole pairs and their accumulation near the antenna electrodes result in the THz radiation. However, this at the same time counteracts on the performance of the antenna due to the screening effect. To further elaborate the concept of screening, the bandgap structure of photoconductive material and response of material under laser illumination needs to be considered. As described in section 3.3.2, in the low temperature growth fabrication process, defects are introduced into GaAs. This results in the creation of new energy states. Under the illumination of laser and generation of free electrons, the electrons which do not reach the antenna electrode are trapped by free defects; *i.e.*

one electron neutralises one free defect. In this situation, the occupied defect does not contribute to the trapping process until the trapped electron recombines with a hole [220]. Since the recombination time is much longer than the trapping time (or carrier lifetime) [83], the recovery of free defect density takes very long time. This leads to long-lived unpaired charge carriers in the photoconductive gap. This is more severe at higher optical powers. Therefore, field screening effect, which is a restriction phenomenon in the generation of the THz photocurrent, is built up [219, 221].

Since the residual space-charge pairs cannot find the opposite sign pair for recombination [166], they remain in the proximity of the antenna electrodes. This phenomenon can be interpreted as the formation of a time-dependant capacitance influenced by the generated carrier density in the antenna gap and the recombination time of the photoconductive material. Moreover, these remaining pairs produce a voltage in the reverse direction of the externally applied bias voltage which can be inferred as the time-dependant voltage controlled source.

Developing a circuit model considering all aforementioned parameters is required for the THz photoconductive antenna analysis. Therefore, in the next section a new equivalent circuit for the THz photoconductive antenna is proposed.

5.3. Antenna Equivalent Circuit Analysis

The gap size of THz small gap photoconductive antennas is commonly smaller than the generated wavelengths of the THz radiation. Therefore, it is possible to model these devices by an equivalent time varying lumped-element circuit operating in the THz frequency range [222, 223]. Similar equivalent circuit techniques can be found within literature employed in scenarios for microstrip photoconductive switches in [223], THz antennas in CW systems[1] in [8], and photoconductive switches based on single-walled carbon nanotube in [224].

---

[1] The equivalent circuit of a THz photomixer antenna in a CW system is explained in Chapter 7.

Fig. 5.2 illustrates the proposed time-dependant equivalent circuit of the THz antenna in which the capacitance characteristics and the screening effect are considered by introducing a time-varying capacitance and controlled voltage- dependant source.

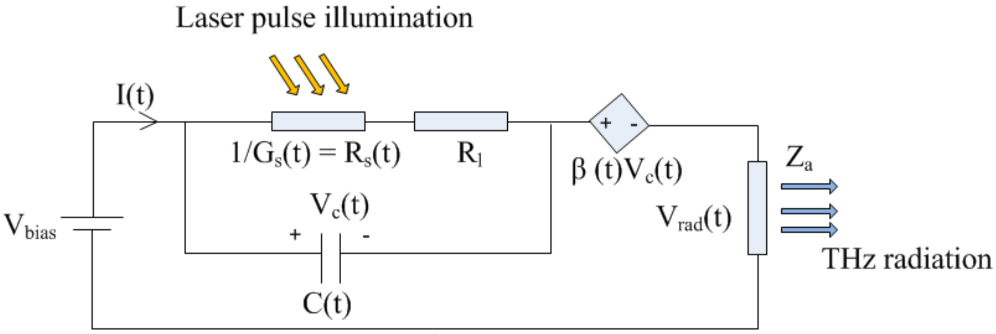

Fig. 5.2 The equivalent circuit of the THz photoconductive antenna as an emitter

This model includes the following components:

1) A time-varying conductance according to equation (4.9), $G_S(t) = 1/R_S(t)$, describing the conduction current across the gap by taking into account time-varying behaviours of the laser pulses and the photoconductive material. This element was elaborated in section 4.2.

2) A time-varying capacitance, *C(t)*, based on the aforementioned phenomenon of accumulation of the unpaired electron-hole pairs near the antenna electrodes;

3) A time-dependant voltage-controlled source controlled by the voltage across the capacitance, $\beta(t)\ V_c(t)$;

4) A loss resistance, R_l, corresponding to the electrode loss resistance;

5) The antenna impedance, Z_a, which has frequency independent resistance [203] and

6) A bias voltage, V_{bias}, corresponding to the external applied bias voltage.

From the basics of THz photoconductive antenna, the current density in the antenna gap as stated in equation (2.2) is $J(t) = e \cdot n(t) \cdot v(t)$. The average carrier velocity is defined by $v(t) = \mu_e \cdot E_C(t)$ where $E_c(t)$ is the electric field at the position of carriers in the antenna gap [219]. Moreover, here it is assumed that $V_i(t) = E_i(t)L$, (where *i* = *bias* or, *c*) and *L* is the antenna gap as depicted in Fig. 5.1. Therefore, the voltage across the radiating element is:

$$V_{rad}(t) = Z_a \cdot e \cdot n(t) \cdot \mu_e \cdot V_c(t) \cdot \frac{S}{L} \tag{5.1}$$

where $V_c(t)$ is the voltage at the antenna gap and S is the antenna active area. Also, it is assumed that the antenna electrodes are good conductors [187], hence R_l is neglected.

The time-dependent characteristic of the capacitance is considered for calculation of the voltage across the antenna gap. And by using circuit analysis:

$$I(t) = V_c(t) \cdot G_s(t) + C(t)\frac{dV_c(t)}{dt} + \frac{dC(t)}{dt}V_c(t) \tag{5.2}$$

Therefore, the time-dependant gap voltage will be:

$$\frac{dV_c(t)}{dt} = \frac{1}{Z_a C(t)}V_{bias} - \frac{1}{Z_a C(t)}V_c(t) - \frac{\beta(t)}{Z_a C(t)}V_c(t) - \frac{G_s(t)}{C(t)}V_c(t) - \frac{1}{C(t)}\frac{dC(t)}{dt}V_c(t) \tag{5.3}$$

In order to solve equation (5.3) numerically, it is important to match the characteristics of the lumped elements in the equivalent circuit method to the carrier transport behaviour of the antenna under laser illumination. The electric field in the antenna gap considering the screening effect can be formulated as [225]:

$$\frac{dE_c(t)}{dt} = \frac{1}{K}\begin{bmatrix} \frac{1}{\tau_r}E_{bias} - \frac{1}{\tau_r}E_c(t) - \frac{e \cdot \mu_e \cdot n(t)}{\zeta\varepsilon}E_c(t) - \frac{e \cdot \mu_e \cdot Z_a \cdot S \cdot n(t)}{L\tau_r}E_c(t) \\ -\frac{e \cdot \mu_e \cdot Z_a \cdot S}{L}\frac{dn(t)}{dt}E_c(t) \end{bmatrix} \tag{5.4}$$

where $K = \left(1 + \frac{e \cdot \mu_e \cdot Z_a \cdot S \cdot n(t)}{L}\right)$. τ_r, the recombination lifetime, is in the range of ps to few ns [166] and ζ, the geometrical factor of the substrate denotes the screening factor, is of the order of 10^3 determined experimentally [78].

Knowing the source conductance of the antenna, $G_s(t)$, from equation (4.9), it is needed to characterize $C(t)$ and $\beta(t)V_c(t)$; *i.e.* the contributing elements to the screening of the antenna. A comparison of equations (5.3) and (5.4) results in time-dependent capacitance; *i.e.* $C(t)$ in equation (5.5),

$$C(t) = \frac{\tau_r}{Z_a}\left(1 + \frac{e \cdot \mu_e \cdot Z_a \cdot S \cdot n(t)}{L}\right) \tag{5.5}$$

and the coefficient of the time-dependant voltage-controlled source; *i.e. β(t)* in equation (5.6).

$$\beta(t) = \frac{e \cdot \mu_e \cdot \tau_r \cdot n(t)}{\zeta\varepsilon} \tag{5.6}$$

From equation (5.5), it can be interpreted that the capacitance between the antenna electrodes has the time-dependent behaviour which demonstrates the accumulation of the electron-holes in the proximity of the electrodes. This depends on the density of generated carriers and the recombination lifetime of the carriers. A similar dependency of the reverse voltage coefficient, *i.e. β(t)*, in respect to the external bias voltage on the carrier density and the recombination lifetime can be observed through equation (5.6).

It is good to mention that some simplified assumptions are used in this model. For example, it is assumed that the excitation laser spot and the electric field in the gap are uniform. Furthermore, based on [225], it is presumed that the carrier momentum relaxation time and as a result, the carrier mobility is small. Thus, this circuit is applicable for photoconductive materials with small carrier mobilities. In addition, the dark resistivity here is supposed to be infinite which is typical for sub-picosecond photoconductors [222]; hence the dark current is negligible. Also, in this model it is assumed that the antenna electrodes are electrically long compared to the THz working frequency as in almost all existing systems, thus only the antenna gap size and bow angle have an impact on the system performance. Finally, it is assumed that antenna radiation efficiency is one and all generated THz power is radiated into the air. In Chapter 6, the effect of substrate on radiation efficiency of the antenna is discussed in detail.

In order to investigate the behaviour of the device based on the new equivalent circuit, parameters of a common THz photoconductive antenna (emitter) driven by ultra-short laser pulses are chosen as shown in Table 5.1.

Table 5.1 Laser, photoconductive material and antenna parameters

Parameter	Notation	Value
Electron mobility for LT-GaAs [69]	μ_e	200 $cm^2.V^{-1}.s^{-1}$
Reflection coefficient in air-photoconductive material interface	R	(for GaAs) 0.318
Optical absorption coefficient	α	6000 cm^{-1}
Laser frequency /(laser wavelength)	$f_{opt}/(\lambda_{opt})$	375 THz /(800 nm)
Laser repetition rate	f_{rep}	80 MHz
Laser pulse duration	τ_l	100 fs
Carrier lifetime [148]	τ_c	1 ps
Carrier recombination time [78]	τ_r	100 ps
Screening factor [78]	ζ	900
Antenna gap length	L	10 μm
Antenna gap width	W	10 μm
Depth of excitation region	$T_{LT\text{-}GaAs}$	1 μm
Bias voltage	V_{bias}	30 V
Antenna resistance (for 90° bowtie antenna [203])	Z_a	65 Ω

Gap source components of the circuit have time-dependant characteristics and they are variable based on the laser pumping power. Therefore, the dynamics of $G_s(t)$ and $C(t)$ based on values of Table 5.1 are depicted in Fig. 5.3. This demonstrates that by increasing the input optical power and generation of photo-carriers, the time-dependent source conductance and capacitance increase. Variation of temporal source conductance of the antenna according to the variation of various factors was discussed in detail in Chapter 4. Here, the effect of some of the parameters on $C(t)$ is investigated.

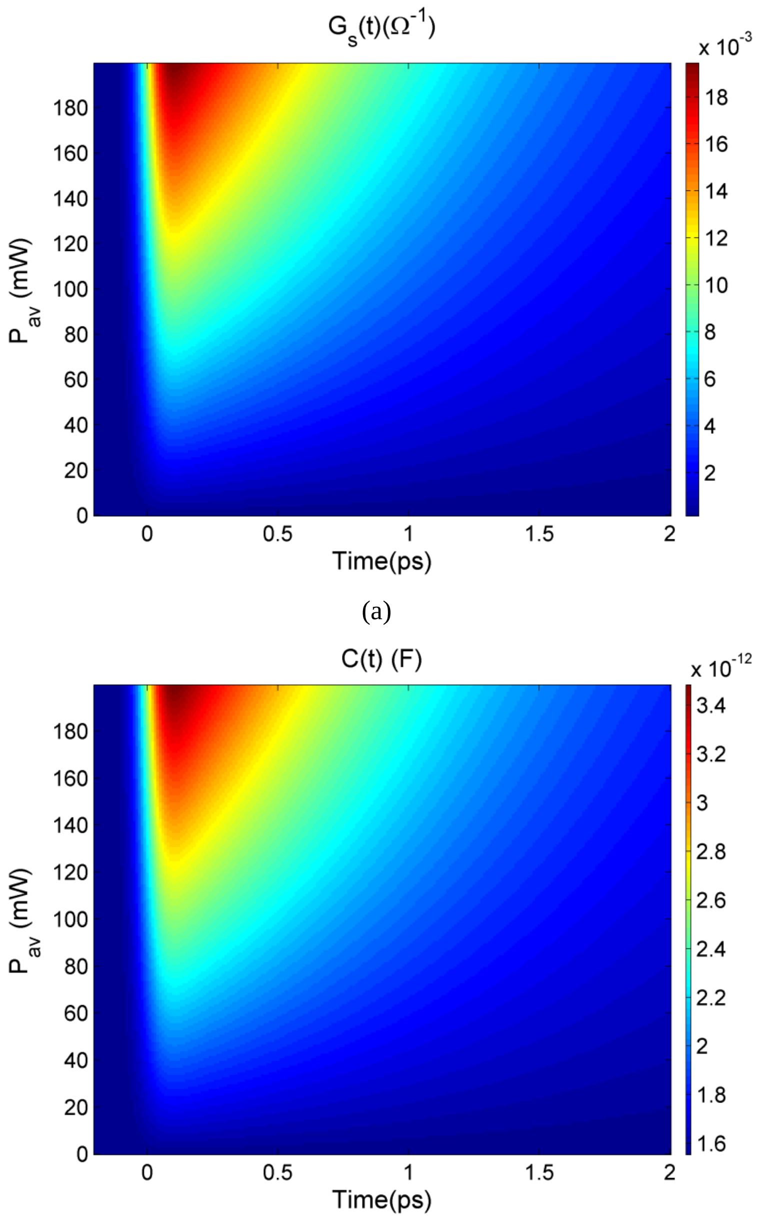

(a)

(b)

Fig. 5.3 Temporal behaviour of (a) $G_s(t)$ and (b) $C(t)$ for different average optical power

As stated in the previous section, carrier recombination lifetime is a parameter that determines how long the unpaired free carriers remain in the antenna gap. As shown in Fig. 5.4 by increasing the carrier recombination time the capacitance increases. This is an undesirable characteristic because it leads to a stronger field screening.

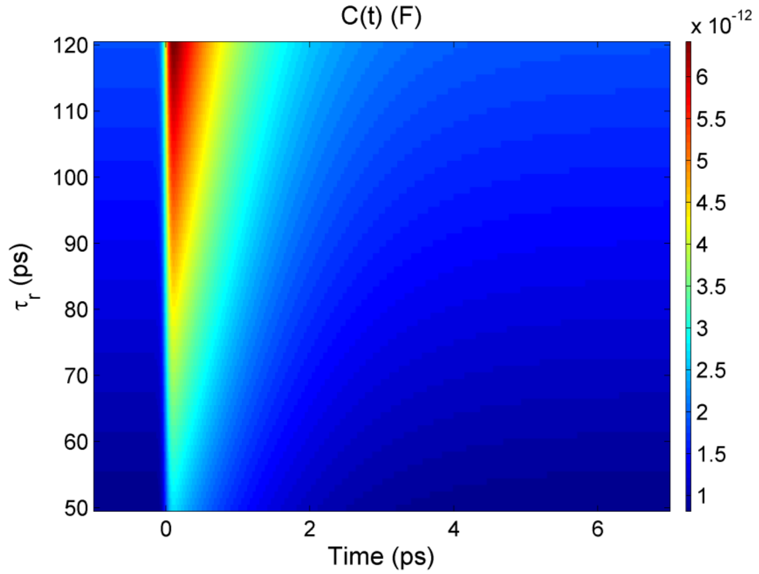

Fig. 5.4 Temporal behaviour of *C(t)* as a function of various carrier recombination time

Next investigation as depicted in Fig. 5.5 is about the impact of carrier lifetime on *C(t)*.

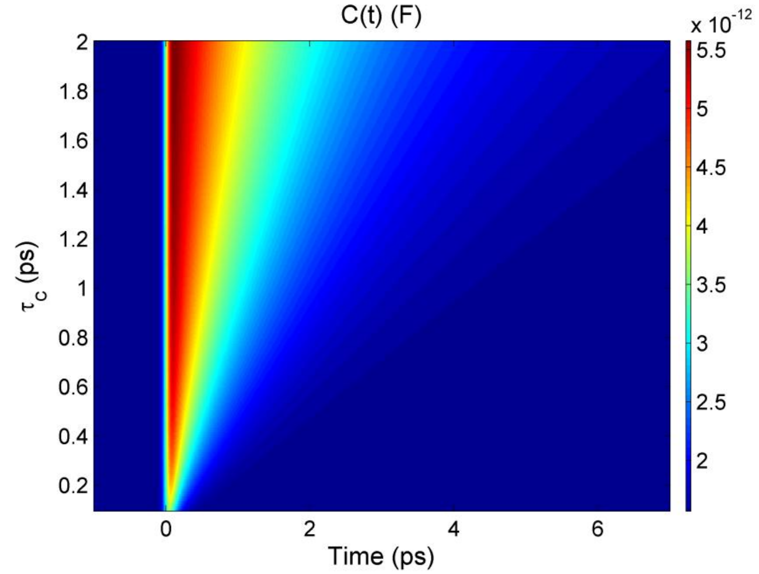

Fig. 5.5 Time dependant characteristics of *C(t)* for various carrier life time

It shows that by increasing the carrier lifetime the capacitance enlarges. Also, since the carrier lifetime determines the decay trend of generated photo-carriers it can be observed that capacitance follows the same trend; *i.e.* for long carrier lifetimes capacitance of the antenna remains larger for a longer time duration compared to the ultra-short carrier lifetime. This again highlights the necessity of short carrier lifetime photoconductive materials to alleviate adverse effect of long carrier lifetime on the device capacitance and field screening.

Furthermore, the influence of antenna gap distance on capacitance is investigated where the optical power is kept fixed. Fig. 5.6 shows that for small gap lengths the capacitance is much larger. This matches with the basic relation of capacitance to the gap length of antenna (capacitance is inversely proportional to the gap length) and also, it confirms that opposing effect of field screening in larger gap antennas is smaller.

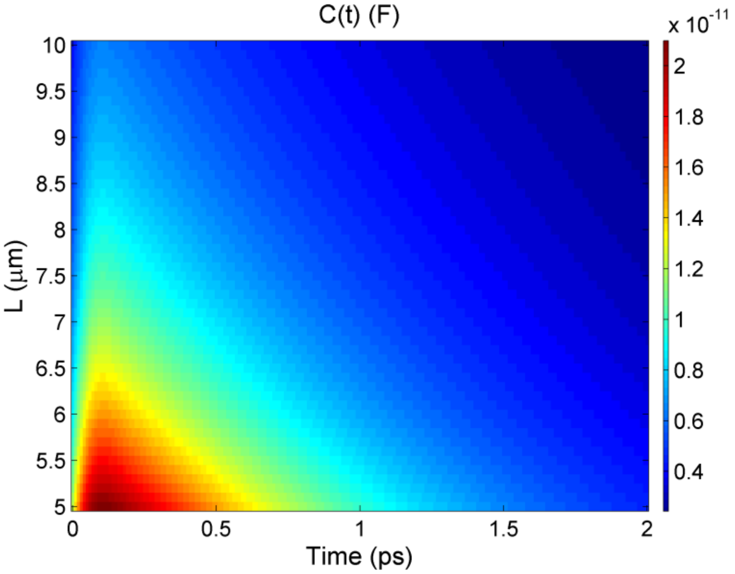

Fig. 5.6 Dependency of temporal characteristics of *C(t)* on the antenna gap length

After investigating the effect of different parameters on time-dependent capacitance of the antenna, temporal variation of antenna voltages is studied. Temporal behaviour of different voltage components in respect to different average optical powers, P_{av} are shown in Fig. 5.7. The higher P_{av} leads to a larger voltage across the antenna. However, due to the generation of a larger carrier density, more unpaired carriers remain near the antenna electrodes and the capacitance does not charge to the initial bias voltage level. Therefore, the reverse bias voltage corresponding to the screening effect, $V_{e-h} = V_{bias} - V_c - V_{rad}$, increases. The results presented here for local voltages are based on mapping the macroscopic process of the THz wave generation to the lumped elements, which matches the temporal evaluation of the local electric field in [219].

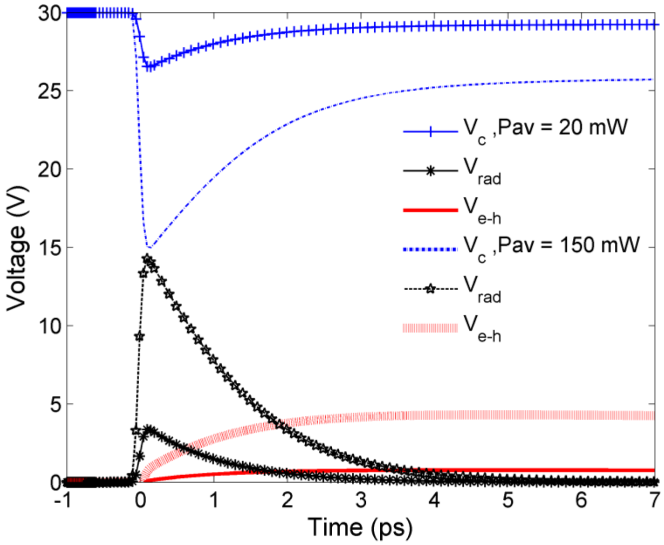

Fig. 5.7 Temporal behaviour of the voltage across the antenna gap, V_c, the reverse voltage source responsible for the screening, $V_{e\text{-}h}$ (=$V_{bias} - V_c - V_{rad}$), and the voltage across the radiating element (the antenna), V_{rad}, for two different average optical powers.

5.4. Antenna Radiated Power and Efficiency Analysis

Large photo-carrier density and high photo-carrier acceleration are two main phenomena that lead to obtaining a high THz power and/or high optical-to-THz conversion efficiency. There exist various methods to improve these factors as elaborated in section 3.5.1. In this section, it is focused on explaining the reason for some of these improvements based on the new equivalent circuit model.

The analyses are focused for the time domain behaviour of the device and the main interest is maximising the THz current and power. Therefore, the values of the elements in the equivalent circuit are considered corresponding to that point for the subsequent analysis.

Using equation (5.1), the temporal radiated THz power is

$$P_{THz}(t) = \frac{V_{rad}^2(t)}{Z_a} \tag{5.7}$$

Average THz power is a common measureable parameter and it can be calculated by deriving the peak radiated THz power and THz pulse duration from equation (5.7).

Also, here optical-to-THz conversion efficiency is defined as:

$$\eta_t = \frac{P_{THz}(peak)}{P_{opt-peak}} \tag{5.8}$$

where $P_{THz}(peak)$ is the peak radiated THz power and $P_{opt\text{-}peak}$ is the peak optical power which can be obtained from $P_{opt-peak} = P_{av} / (\tau_l f_{rep})$. For completeness, it is worth noting that from the system point of view, another type of efficiency, namely electrical-THz power conversion efficiency (η_e), can be defined. This efficiency can be described as the ratio of the THz power to the delivered power from the bias voltage at peak optical power.

In THz systems, usually the average optical power from the laser and the external bias voltage are the most appropriate adjustable parameters after the experimental setup. In our research method to follow, one parameter at a time will be varied whilst keeping all others fixed (as in Table 5.1).

For the first analysis, variations of the average radiated THz power for the system of Table 5.1 at different bias voltages are depicted in Fig. 5.8. It illustrates that the larger the applied bias voltage, the larger the radiated THz field. However, the amount of the applied bias voltage depends on breakdown voltage of the photoconductive material and antenna gap size (the larger the antenna gap size, the higher applicable bias voltage) so it cannot be increased steadily. In addition, it can be interpreted that by increasing the optical power, the radiated power from the device increases until it reaches saturation. To assess the accuracy of the new theoretical model the average radiated power is compared with the experimental results for a 90° bowtie antenna on LT-GaAs with a bias voltage of 30 V [69]. Through depicted results in Fig. 5.8, it can be seen that a good agreement is observed between theoretical and measured trends. This validates the theoretical model with the differences being potentially explained by the simplified assumption regarding the complete coupling of THz power to the air and the collection losses from the emitter to the receiver, a loss which could be evident from the real experimental situation.

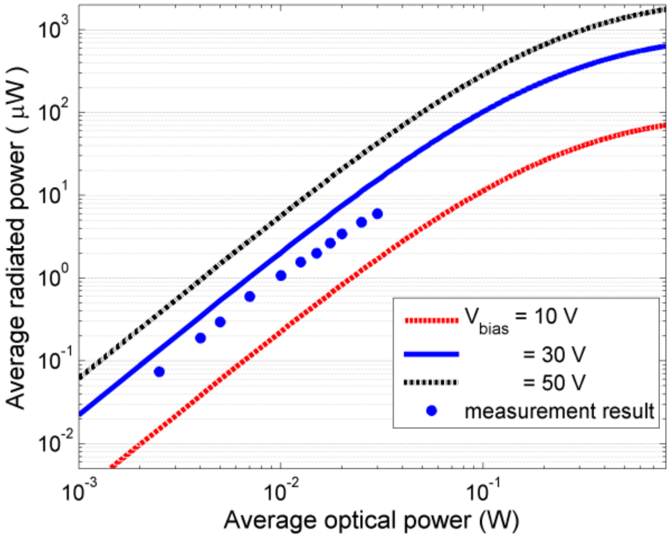

Fig. 5.8 The average radiated THz power versus the average input optical power for different bias voltages for $Z_a = 65\ \Omega$. The measurement results are from [69] at V_{bias} = 30 V.

Another effective parameter on the performance of the device is the antenna resistance. Fig. 5.9a depicts the influence of different antenna resistances, which varies based on the bow angle of the bowtie antenna [203], on the average THz power. It can be interpreted that at lower optical power, the antenna with larger resistance has better radiated power than the one with smaller resistance. However, antennas with smaller resistance remain in the linear region and radiate more THz power at larger input optical power.

Also, it is possible to compare these antennas from optical-to-THz conversion efficiency point of view. From Fig. 5.9b it can be seen that the peak efficiency occurs at different optical powers for the antenna with different resistance. For example for the antenna with $Z_a = 65\ \Omega$, peak efficiency of 0.0167% can be reached when the optical power is 146 mW while the antenna with $Z_a = 120\ \Omega$ has the same efficiency at optical power of 60 mW. This shows that the value of Z_a does not change maximum value of the efficiency considerably and it only defines the range of optical power that this maximum occurs. Moreover based on this analysis, for a given system and a fixed pumping power, it is possible to derive the antenna with the optimised impedance for the best possible efficiency. For instance, for the defined system at a fixed pumping power of 146 mW, the optimum efficiency of 0.0167% can be obtained when $Z_a = 65\ \Omega$ whereas for antennas with other resistance values the efficiency is slightly lower.

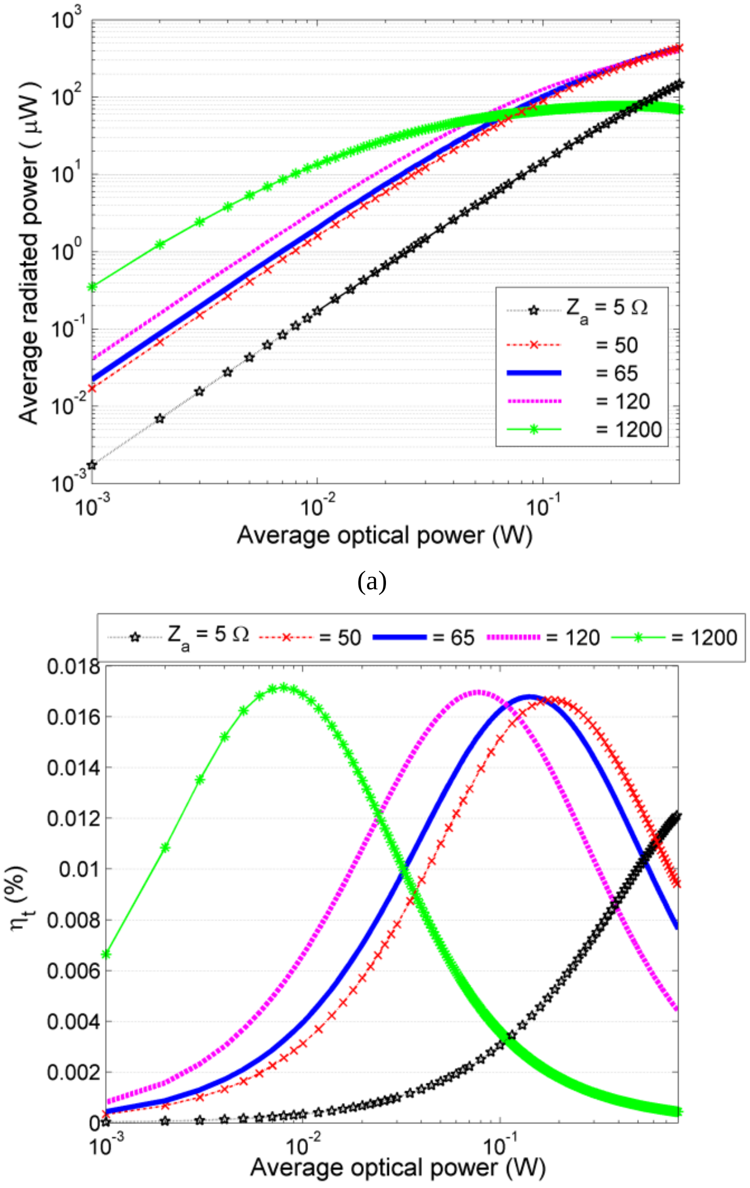

(a)

(b)

Fig. 5.9 (a) The average radiated THz power and (b) the peak optical-to-THz power conversion efficiency versus average optical powers for different antenna resistances when the bias voltage is 30 V.

Fig. 5.10 illustrates that at the same optical power, the higher the bias voltage the larger the efficiency. For example, at an optical power of 146 mW (Z_a = 65 Ω), by increasing the bias voltage from 10 V to 30 V, the efficiency changes from 0.002% to 0.016% (8 times improvement). Thus, it can be interpreted that the variation in bias voltage has a more significant effect on the antenna efficiency as compared to antenna resistance change. Furthermore, comparison of the optical-to-THz power conversion efficiency from both the proposed model and the measurement results in [69] is depicted in Fig. 5.10. Again, a good agreement is observed. The experimental results are slightly lower. Losses in the emitter and the detector and also neglecting the effect of substrate modes may contribute to this efficiency difference.

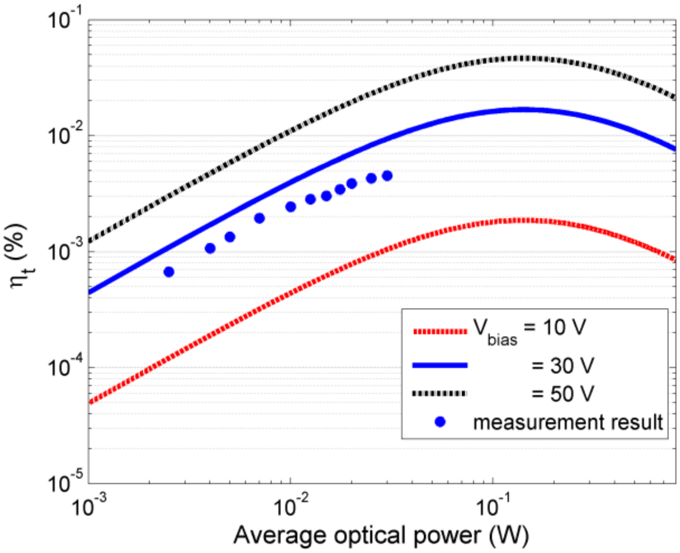

Fig. 5.10 The peak optical-to-THz power conversion efficiency as a function of the average optical powers for different bias voltages for Z_a=65 Ω. The measurement results are from [69].

Fig. 5.11 compares the optical-to-THz power conversion efficiency and the electrical-THz conversion efficiency for different input optical powers. It is obvious that there is a huge difference in the magnitudes of these two efficiencies. This means that, although the optical-to-THz efficiency is very low, the electrical power from the bias voltage can be delivered to the radiation resistance more efficiently. Also, such electrical power reaches a saturation level according to the saturation of the photocurrent.

Another important parameter affecting the antenna output power and efficiency is the antenna gap length. In Fig. 5.12a, it can be interpreted that the radiated power from the antenna with a smaller gap saturates earlier while the one with a greater gap size still operates in a linear region and still reacts to more optical power. The reason is that in the latter, the generated electron-holes are located tighter due to a smaller illuminated area. Therefore, in large gap antennas more optical power and bias voltage can be applied with less concern about the saturation and device breakdown.

Also as it is evident in Fig. 5.12b, the maximum efficiency for the antenna with a smaller gap occurs at lower optical power levels. This also demonstrates that the choice of the THz photoconductive emitter in a real experimental situation depends on the available optical source type. In other words, when laser sources with low optical powers are only available, then the use of a small gap antenna results in a greater radiated power and optical-to-THz power conversion efficiency as compared to a large gap antenna.

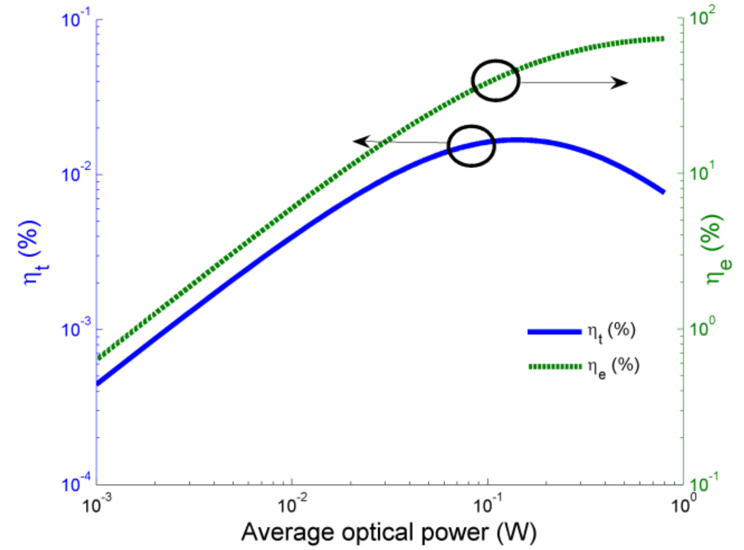

Fig. 5.11 Comparison of the optical-to-THz power conversion efficiency and electrical-THz conversion efficiency for the bias voltage of 30 V and $Z_a = 65\ \Omega$.

One of the main methods which can enhance the efficiency of the THz antenna is to improve the optical coupling efficiency (*i.e.* coupling of laser power to the antenna). For this purpose, the influence of two important parameters, α and R, on the total optical-to-THz power conversion efficiency of the antennas is depicted in Fig. 5.13 and Fig. 5.14. It is observed that the larger the optical absorption, the higher the efficiency. Also, it can be seen tha the smaller the reflection from the air-substrate interface, the greater the efficiency. Both α and R are mainly dependant on the substrate material. Also, α depends on optical wavelength of the laser. Various methods exist for the reduction of the reflection from the photoconductive gap as stated previously in Chapter 3.

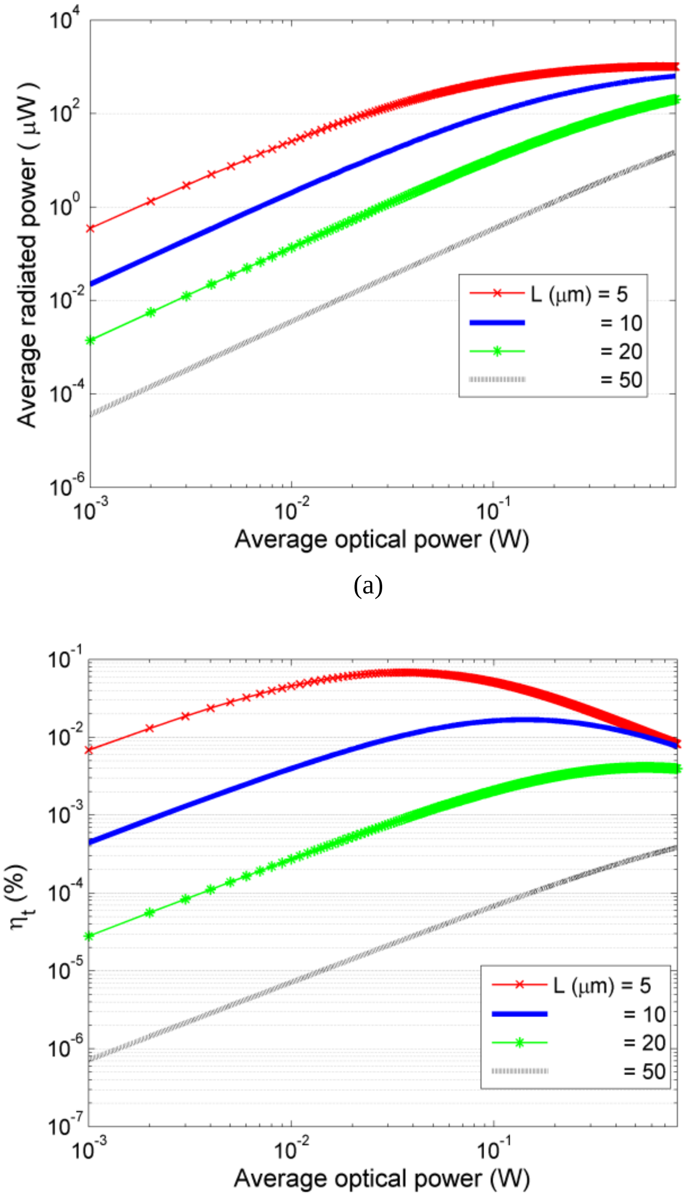

(a)

(b)

Fig. 5.12 Dependency of (a) peak optical-THz power conversion efficiency (b) average radiated THz power on average optical powers for antennas with different gap lengths when V_{bias}= 30V, Z_a = 65 Ω, W=10 μm.

It is shown throughout that many interlinked or independent parameters affect the overall performance of THz antennas. The theoretical analysis can now be applied to maximize the optical-to-THz conversion efficiency for a desired laser optical power range based on the available photoconductive material and the antenna. From Fig. 5.9b, for Z_a = 65 Ω, the optical-to-

THz conversion efficiency does not deviate a lot from the maximum efficiency for an optical power of 80 to 250 mW. Therefore, it can be said that is the optimum range of optical power for this antenna. In order to enhance the efficiency in this range, optimum values for all other parameters need to be chosen. Table 5.2 depicts the variation in efficiency for different values of the parameters.

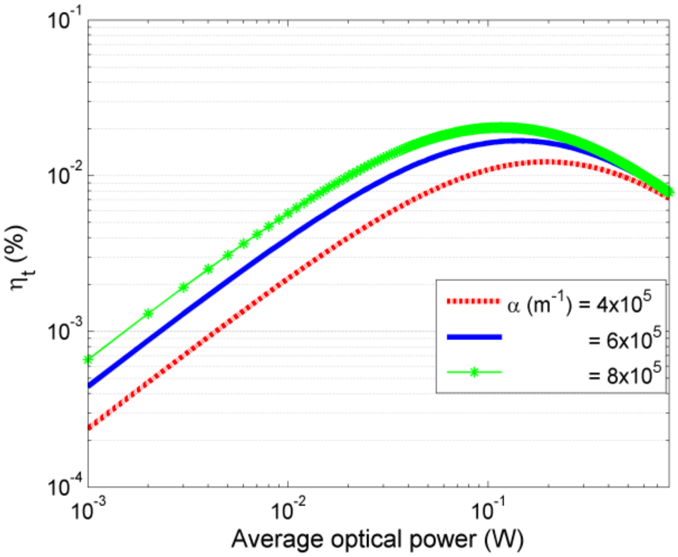

Fig. 5.13 Dependency of the peak optical-to-THz power conversion efficiency on the average optical power for different optical absorption when the bias voltage is 30 V, antenna resistance is 65 Ω and R = 0.318

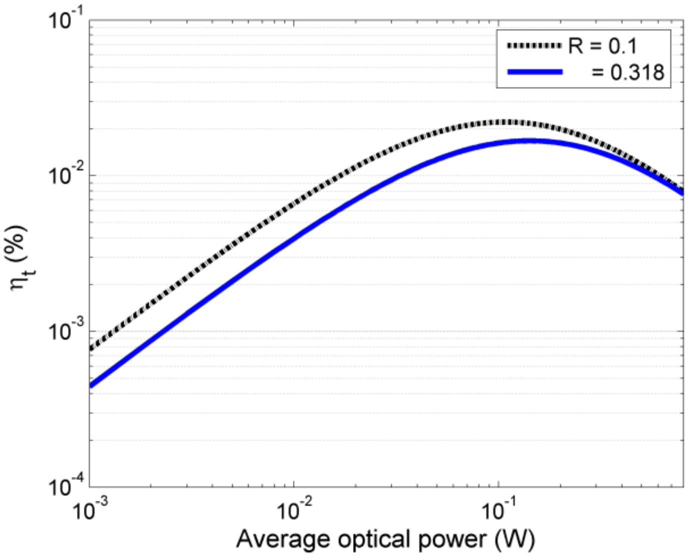

Fig. 5.14 Variation of the peak optical-to-THz conversion efficiency versus optical powers for different reflection coefficients from the air-substrate interface, when the bias voltage is 30 V, Z_a = 65 Ω and α = $6x10^5$ m^{-1}

Table 5.2 Parameter ranges for the maximum optical-to-THz efficiency for a desired average optical power range

Parameter	Range	Fixed values	η_t(%): min – max
Bias voltage (V)	10 - 30	L = 10 μm, R = 0.318, α = 6000 cm^{-1}	0.0017 - 0.0167
Antenna gap length (μm)	20 - 10	V_{bias} = 30 V, R = 0.318, α = 6000 cm^{-1}	0.0017 - 0.0166
Reflection coefficient	0.318 - 0.1	V_{bias} = 30 V, L = 10 μm, α = 6000 cm^{-1}	0.0154 - 0.0221
Optical absorption coefficient (cm^{-1})	4000 - 8000	V_{bias} = 30 V, L = 10 μm, R = 0.318	0.01 - 0.0204

For example, for this setup the values that give the maximum efficiency are V_b = 30 V, L= 10 μm, R = 0.1 and α = 8000 cm^{-1}. By calculating efficiency based upon them, the maximum achievable efficiency is 0.0269%. This shows that by proper selection of parameters (considering practical constraints), the efficiency is improved more than 1.5 times as compared to 0.016% (which is the peak efficiency value from Fig. 5.9b for the antenna resistance of 65 Ω). Therefore, by using the proposed theoretical process and analysis, it is possible to appropriately select the parameters corresponding to the maximum achievable efficiency before entering into a practical set-up; hence it can serve as a very useful guide for practice. This represents one of the major novelties of this study.

5.5. Summary

In this chapter, a unified THz photoconductive antenna model bringing together both the physical and the equivalent circuit models has been developed. This not only enables a more realistic description of the THz antenna but also provides a direct link between the parameters of the equivalent circuit model and the material properties and structures of THz antenna. One of the unique features of this new circuit is the incorporation of a time-dependent capacitance and a voltage-controlled source. This new model can characterize the behaviour of the antenna in a more transparent manner, since this configuration is more representative of the reality based on the existing physics theories of THz photoconductive antennas. The performance of the antenna, through the use of this model, has been examined from several aspects (bias voltage, antenna gap size and reflection from air- substrate) and the calculated values agree well with published measurement results. Moreover, it is shown that based on this analysis and considering practical constraints on choosing parameters, it is possible to tune the average input optical power to achieve the maximum optical-to-THz conversion efficiency. Thus, this analysis should be very useful in designing and tuning the optical source and the emitter antenna to maximize the radiated THz power and optical-to-THz conversion efficiency.

Chapter 6. Further Investigation of THz Antennas from Substrate Effect and CAD Analysis Perspectives

6.1. Introduction

As discussed in Chapter 3, THz antennas and RF/MW antennas are dissimilar from different perspectives. In Chapter 4 and Chapter 5 the source conductance of THz photoconductive antenna and modelling of this type of antenna in the time-domain, according to the temporal response of the photoconductive material under laser illumination, were analysed and discussed. Those novel investigations were required as a result of different feeding methods of THz antennas as compared to RF/MW antennas.

Other dissimilarities between THz and RF/MW antennas, as stated in Chapter 3, are from substrate thickness and CAD analysis points of views which are elaborated more in detail in this chapter.

Therefore, first this chapter reviews the effect of substrate thickness on the performance of a THz antenna and then, the numerical results are compared with the simulation results. After that, a novel method for simulating THz photoconductive antennas in a pulsed system is developed.

6.2. Effect of Substrate Thickness on Performance of THz Antennas

When a dipole antenna is located in free space, as shown in Fig. 6.1a, antenna has an omni-directional pattern in azimuth and it radiates in all directions along the plane perpendicular to the electric field of dipole. By using the photoconductive substrate, radiation pattern of the antenna is affected as depicted in Fig. 6.1b, the radiation pattern becomes asymmetric and it is enhanced towards the substrate [226].

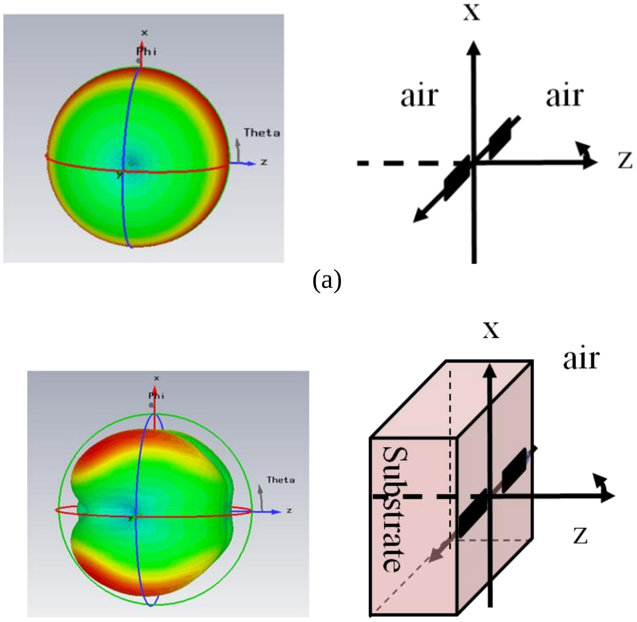

(a)

(b)

Fig. 6.1 (a) Dipole antenna surrounded by air and its radiation pattern (b) Dipole antenna on a GaAs substrate and its radiation pattern

Although photoconductive substrate is the crucial component in the creation of THz waves, substrate thickness and the generation of guided modes degrade output power and the bandwidth of THz antennas. The absorption of optical photons in the photoconductive material substrate which is more severe for high frequency components (above 3 THz) limits the bandwidth of the antenna [211]. The substrate effect is a well studied subject [203, 227, 228]. In contrast to RF/MW antennas, the thickness of the substrate for a fabricated THz antenna is comparable with the wavelength; *i.e.* electrical thickness of THz antennas is larger than RF/MW antennas. In addition, the high dielectric constants of photoconductive materials like Si (ε_r ~ 11.7) or GaAs (ε_r ~ 12.9) results in the absorption of most of the power in substrate rather than radiation into free space. Therefore, the radiated power and radiation efficiency of the antenna are substantially affected by the substrate thickness in THz.

The origin of THz current is commonly stated to be from a Hertzian dipole [78]. Thus, here the performance of a Hertzian dipole on GaAs substrate with $\varepsilon_r = 12.9$ is investigated. In this investigation, the presented method and formulas for the radiated power and surface wave power in [203] and [227] are employed. After that, the numerical results are compared with simulation results.

6.2.1. Basic Theory

To demonstrate the analytical results for performance of the THz antenna and propagation of the wave inside the substrate, a brief review on some basic reflection and transmission concepts is needed. The incident EM wave on the interface of two media (here from substrate to air) can be divided to TE and TM waves when respectively the electric and magnetic fields are parallel to the plane of the interface. The related reflection coefficients for each wave type based upon the parameters in Fig. 6.2 are defined as [229]:

$$R_{TE} = \frac{\eta_2 \cos\theta_i - \eta_1 \cos\theta_t}{\eta_2 \cos\theta_i + \eta_1 \cos\theta_t} \tag{6.1}$$

$$R_{TM} = \frac{-\eta_1 \cos\theta_i + \eta_2 \cos\theta_t}{\eta_1 \cos\theta_i + \eta_2 \cos\theta_t} \tag{6.2}$$

When θ_i is greater than the critical angle (defined as $\theta_c = \sin^{-1}(\sqrt{\varepsilon_2 / \varepsilon_1})$, the magnitude of reflection coefficients is equal to 1 for both TE and TM modes and the phase of R_{TE} and R_{TM} ,φ_{TE} and φ_{TM}, would be (considering $\mu_1 = \mu_2$):

$$\varphi_{TE} = 2\tan^{-1}(\frac{\sqrt{\sin^2\theta_i - \varepsilon_2/\varepsilon_1}}{\cos\theta_i}) \tag{6.3}$$

$$\varphi_{TM} = 2\tan^{-1}\left(\sqrt{\frac{\varepsilon_1}{\varepsilon_2}}\frac{\sqrt{\varepsilon_1/\varepsilon_2 \sin^2\theta_i - 1}}{\cos\theta_i}\right) \tag{6.4}$$

These phases of reflection coefficients are important for calculating propagation modes inside the substrate.

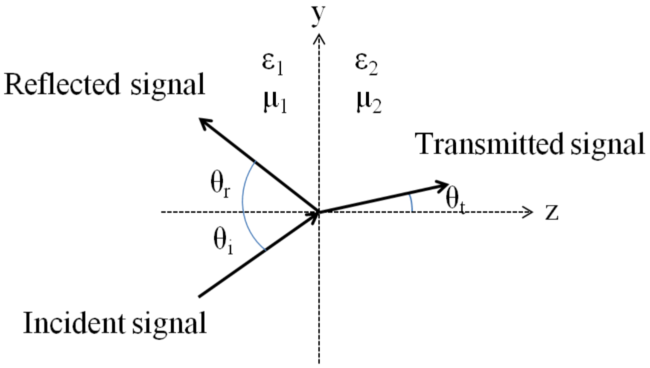

Fig. 6.2 Reflection and transmission of wave at an oblique angle on an interface of two media, θ_i is the incident angle, θ_r is the reflection angle, and θ_t is the transmission angle

6.2.2. Analytical Discussions on Different Modes in a THz Antenna

According to Fig. 6.3, for the incident angles smaller than the critical angle, radiated modes created (solid line). If the incident angles are larger than the critical angle, the wave is trapped inside the substrate and guided or surface modes are generated (dashed line).

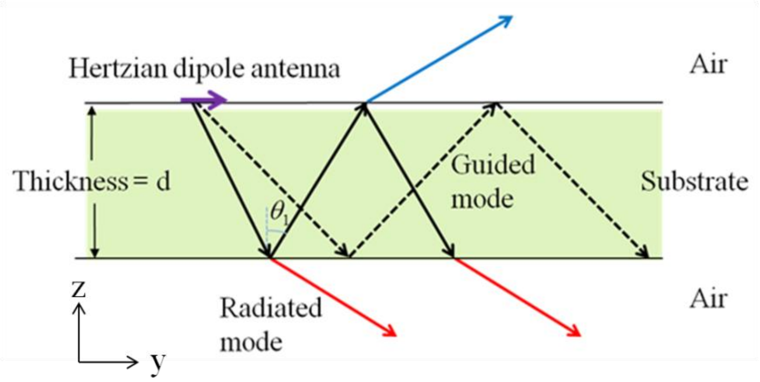

Fig. 6.3 Radiated mode (solid line) and guided or surface mode (dash line) of a Hertzian dipole antenna on the semi-infinite substrate with permittivity of ε_r

For calculation of the radiated wave power, the electrical thickness of the substrate, which is along the direction of wave propagation vector, is defined as [227]:

$$\psi = \frac{2\pi}{\lambda_0}\sqrt{\varepsilon_r}\, d\cos\theta_1 \tag{6.5}$$

where θ_1 is the refracted angle inside the substrate.

The radiated power down below the substrate (red lines in Fig. 6.3), $P_{r\_sub\_side}$, and the radiated power to air in antenna direction (blue lines in Fig. 6.3) , $P_{r\_ant\_side}$, are calculated from [227]:

$$P_{r\_sub\_side} = \frac{3}{8}\int_0^1 \left(\frac{1}{B_1} + \frac{u^2}{B_2}\right) du \tag{6.6}$$

$$P_{r\_ant\_side} = \frac{3}{8}\int_0^1 \left(\frac{A_1}{B_1} + u^2\frac{A_2}{B_2}\right) du \tag{6.7}$$

where $u = \cos\theta_0$ and θ_0 is the angle of wave in the air. Considering the normalised wave impedance for TE and TM modes as equations (6.8) and (6.9), the quantities of A_1, A_2, B_1, and B_2 are defined as equations (6.10)-(6.13) [227].

$$\eta_{TE} = \frac{\cos\theta_0}{\sqrt{\varepsilon_r}\cos\theta_1} \tag{6.8}$$

$$\eta_{TM} = \frac{\cos\theta_1}{\sqrt{\varepsilon_r}\cos\theta_0} \tag{6.9}$$

$$A_1 = \cos^2\psi + \eta_{TE}^2 \sin^2\psi \tag{6.10}$$

$$A_2 = \cos^2\psi + \eta_{TM}^2 \sin^2\psi \tag{6.11}$$

$$B_1 = \cos^2\psi + \left(\frac{\eta_{TE} + \eta_{TE}^{-1}}{2}\right)^2 \sin^2\psi \tag{6.12}$$

$$B_2 = \cos^2\psi + \left(\frac{\eta_{TM} + \eta_{TM}^{-1}}{2}\right)^2 \sin^2\psi \tag{6.13}$$

Using equations (6.6) to (6.13), the radiated powers to air through the substrate and to air in antenna side are plotted in Fig. 6.4 which are normalised to the total radiated power of the dipole in free space given by [203]:

$$P_0 = \frac{\omega^2 \mu_0^{3/2} \varepsilon_0^{1/2} I^2 h^2}{12\pi} \tag{6.14}$$

where ω is the angular frequency, I is the current and h is the effective length of the dipole. As shown in Fig. 6.4, the power radiated into the substrate is almost always greater than radiated power into the air in antenna direction. In THz antennas, commonly the radiated power is collected from the substrate side which uses this advantage. Also, it can be interpreted that the peak radiated power occurs when the substrate thickness is the multiple of a half wavelength in dielectric substrate.

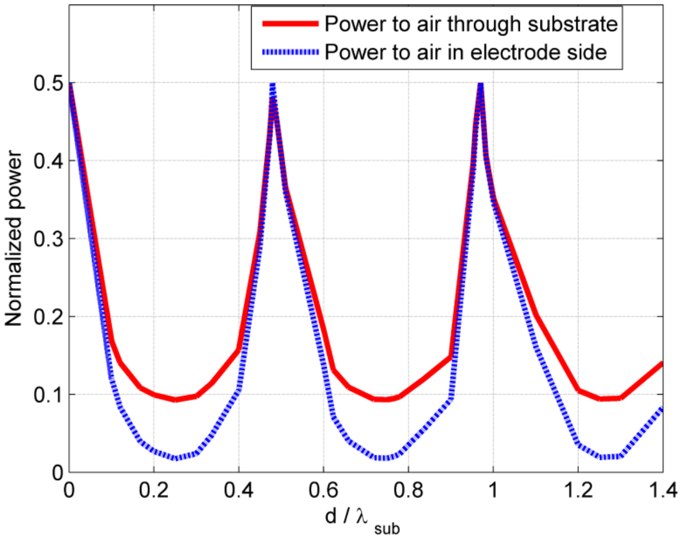

Fig. 6.4 Normalised radiated power of a Hertzian THz dipole antenna on an ungrounded semi-infinite GaAs substrate

For calculation of the guided (surface) wave power, definition of substrate effective thickness, d_e, based on Goos-Hanchen shift (lateral shift of the wave) is needed [230]. As depicted in Fig. 6.5 the effective thickness and its values for TE and TM waves are [203]:

$$d_e = d + 2s \tag{6.15}$$

$$s = \frac{1}{\sqrt{\beta_{yd}^2 - k_0^2}} \qquad \text{For TE mode} \tag{6.16}$$

$$s = \frac{1}{\sqrt{\beta_{yd}^2 - k_0^2}} \frac{1}{\beta_{yd}^2 / k_d^2 + \beta_{yd}^2 / k_0^2 - 1} \qquad \text{For TM mode} \tag{6.17}$$

where k_0 is the propagation constant in air, k_d is the propagation constant along the wave vector inside the substrate and β_{yd} is the propagation constant along y which is equal to $k_d \sin\theta_1$.

In this case, to have an axial independent wave pattern along y axis, phase shifts inside the substrate for Fig. 6.5 should be [229]:

$$2k_d d\cos\theta_1 - 2\varphi = 2m\pi \qquad m = 0, 1, \ldots \quad (6.18)$$

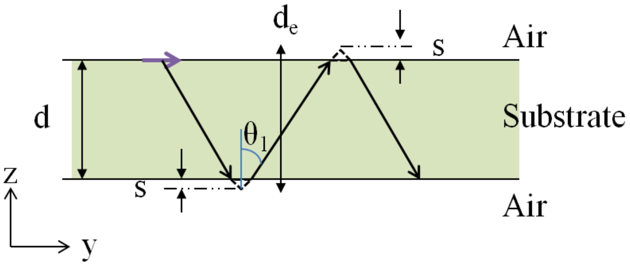

Fig. 6.5 Schematic of the antenna on the substrate for guided (surface) mode analysis

In equation (6.18), φ represents phase of reflection coefficients at the substrate-air interface and for TE mode and TM mode, this can be calculated from equations (6.3) and (6.4) respectively (θ_i is same as θ_1). Therefore, substrate thickness and incident angle are variable parameters that affect the number and the type of the modes propagating along the substrate.

The power of guided (surface) wave for each mode is [227]:

$$P_{sub-TE} = \frac{3\lambda_0 \cos^2 \varphi_{TE}}{4d_e} \tag{6.19}$$

$$P_{sub-TM} = \frac{3\lambda_0 \sin^2 \varphi_{TM} \cos^2 \theta_1}{4d_e} \tag{6.20}$$

In Fig. 6.6 the normalised guided (surface) mode power for each mode of TE and TM is presented as a function of substrate thickness. One can interpret from this figure that two modes of TE_0 and TM_0 are dominant modes with zero cut off frequency. In other words, these two modes are independent of the substrate thickness and they exist in the device. The total guided (surface) mode power is the summation of the powers of all modes in each thickness and in Fig. 6.7 the total power for only the first 4 modes as a function of the ratio of substrate thickness to substrate wavelength is depicted. It can be found that by increasing the thickness, the peaks and dips appear due to generation of higher modes in the photoconductive substrate. It can be understood from Fig. 6.4 and Fig. 6.7 that when the substrate thickness is much smaller than $\lambda_{sub}/10$, the radiated power to air in both sides is strong and also the guided mode power is small. This is a desirable situation for an antenna. In RF/MW antennas, the substrate thickness is few millimetres which falls in the range of thickness smaller than $\lambda_{sub}/10$. Therefore, substrate thickness and generation of guided modes is not a severe issue over there. In THz antennas also a thin substrate is ideal for efficient power radiation; but, in reality this type of substrate has several issues. For instance, it is fragile; it is not very easy to fabricate mechanically membrane layers, and also it is costly.

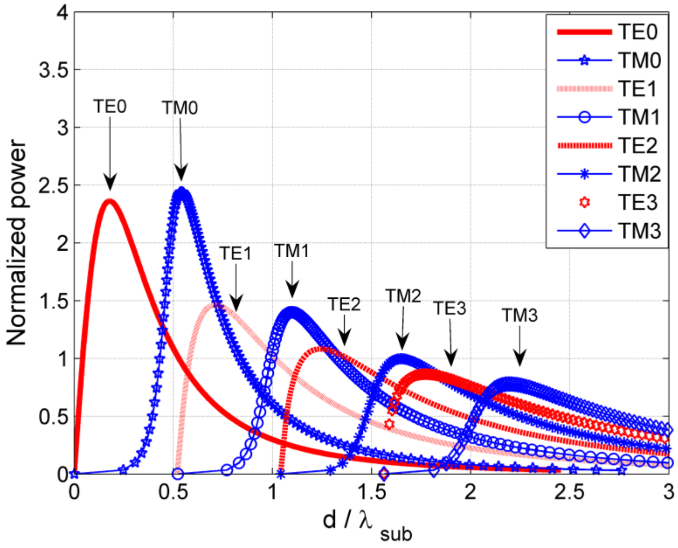

Fig. 6.6 Guided wave power for each mode in relation to different electrical substrate thickness

In THz applications usually the substrate thickness is in the range of 300 μm – 500 μm. Considering the THz band frequencies, the THz wavelength range in the substrate is between 11.3 μm and 1130 μm. Hence the ratio of the substrate thickness to the wavelength of dielectric, for instance for a 300-μm-thick substrate, varies between 0.26 to 26. Thus, in practice THz photoconductive substrates are electrically thick and according to [227] the total guided (surface) wave power in them approaches a limited value (*i.e.* $\sqrt{\varepsilon_r}$).

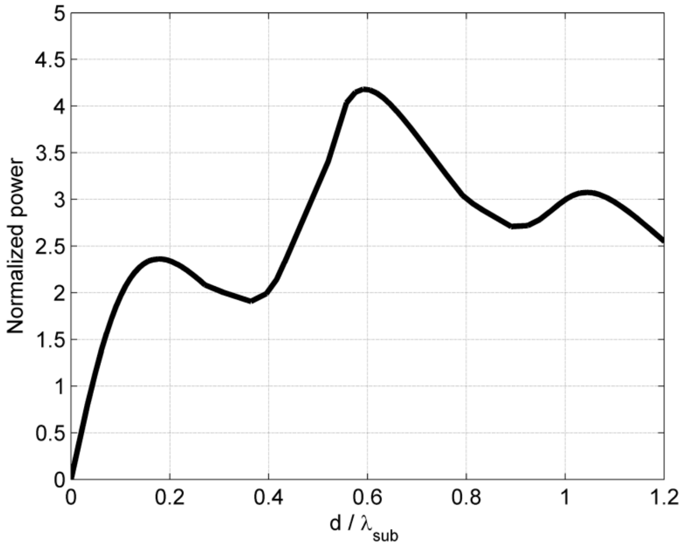

Fig. 6.7 Total guided power for PC antenna versus ratio of substrate thickness to dielectric wavelength

Based on the definition of the radiation efficiency, $P_r/(P_r+P_g)$ where P_r is the radiated power and P_g is the guided mode power, radiation efficiency is plotted in Fig. 6.8. This result matches with [231]. It can be observed that the efficiency has a kind of oscillatory behaviour as a function of electrical thickness of the substrate and it is very low.

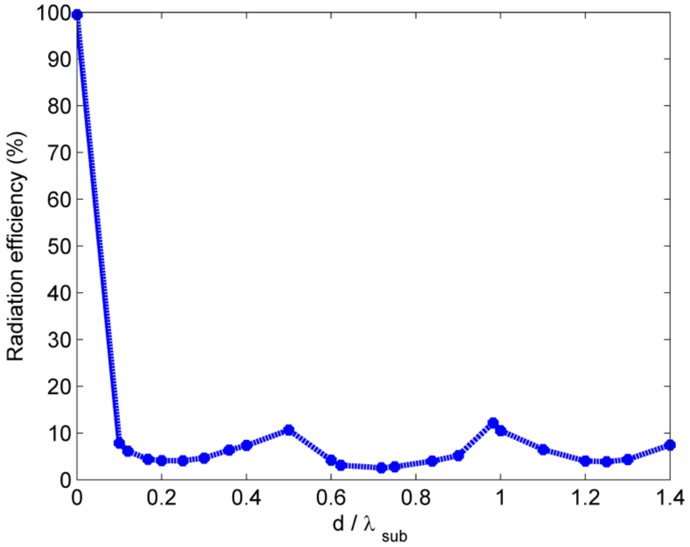

Fig. 6.8 Radiation efficiency from the dipole antenna on a GaAs substrate

It is possible to plot the propagation constant for the guided modes in the substrate considering the even modes and odd modes for TE and TM [229]. The guided wave modes as a function of electric thickness of the substrate are depicted in Fig. 6.9. Considering both Fig. 6.8 and Fig. 6.9, it can be understood that the peaks of the efficiency correspond to onset of new TE and TM modes.

In order to compare the analytical results with simulation, a 50-µm-long dipole antenna is situated on a loss-free GaAs substrate. The simulation is run by using CST [232] where the input power is constant. The field probes (along the dipole antenna) are located in the far-field of the antenna as shown in Fig. 6.10 and they are monitored whilst substrate thickness varies.

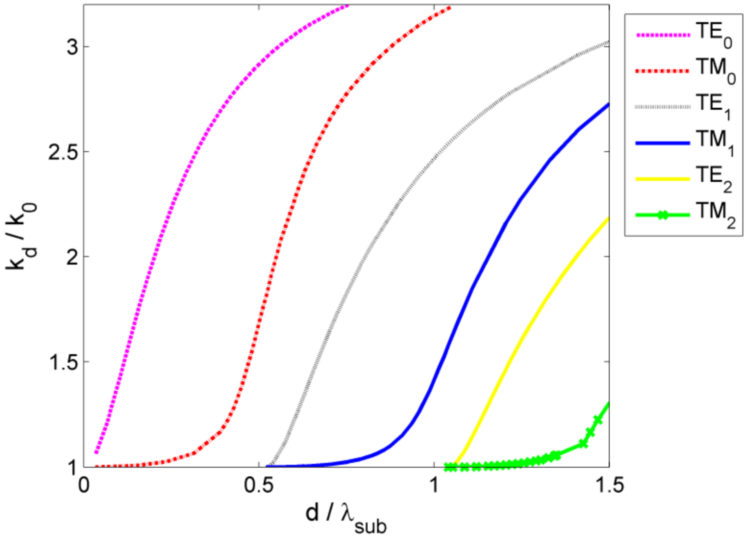

Fig. 6.9 TM and TE guided wave modes in the substrate with ε_r = 12.9

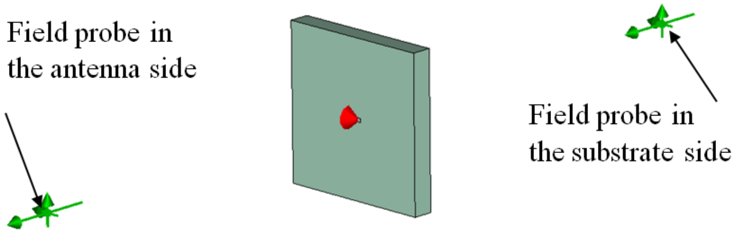

Fig. 6.10 Schematic of the simulated antenna to derive the antenna gain for variable substrate thicknesses

The obtained gain of the antenna is shown in Fig. 6.11. Qualitative comparison of the gain derived from the simulation tool for the practical dipole antenna has a good agreement with the analytical results provided in [227] for an infinitesimal antenna. It is obvious that the antenna gain is larger in the substrate side compared to the antenna side. This is similar to the obtained conclusion from the normalised power behaviour in Fig. 6.4. Again, this result shows that the antenna gain is large when the substrate thickness is small and as the substrate thickness increases, the gain drops considerably and it has successive peaks and troughs. Same as the observed behaviour for the radiation efficiency in Fig. 6.8, the gain has the local maxima when the substrate thickness is a multiple of half dielectric wavelength. This is due to de-generation of TE and TM guided wave modes as depicted in Fig. 6.9. These analyses are useful for the THz antenna design specifically for THz photomixer antennas where the antenna is narrowband and substrate thickness can be chosen at the local maxima according to the working frequency.

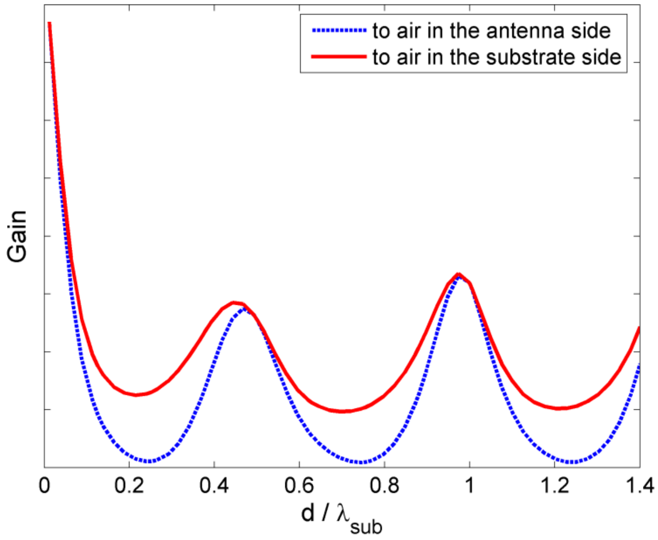

Fig. 6.11 Simulated gain as a function of substrate electrical thickness

6.3. A Novel Simulation Method for THz Photoconductive Antenna Characterization

Planar antennas such as dipole and bowtie are commonly used for making photoconductive antennas. In the past three decades, different antenna geometries from these families have been fabricated, measured and used for THz applications [7, 69, 72, 192]. In most investigations, although the antenna region is approximated as a simple Hertzian dipole, the calculated radiated THz field gives an accurate estimation [233, 234]. Only in the past few years have the geometrical characteristics of THz antennas become to be considered. For example in [192, 233] vector Maxwell's equations and the carrier rate equations are solved simultaneously using a finite difference time domain (FDTD) method for dipole antennas; in [235] detected THz signals from dipole antennas are studied by incorporating a modified Smith model. In these pure numerical models evaluating the effect of different antenna designs on the radiated THz field is not a straight forward task. Commercially available full-wave electromagnetic solvers are good options to deviate from such complicated numerical calculations. However, the major difference in analysing THz antennas as compared to microwave antennas is the optoelectronic characteristics of THz antennas which are the result of the optical excitation and photoconductive material response. This necessitates the development of a new simulation and analysis procedure incorporating both the optical excitation and the antenna geometrical effects. Thus, the main goal of this section is to address this issue. This work can alleviate any ambiguity in designing THz antennas and it can provide a more realistic insight into the emission characteristics of the antenna beforehand [236].

6.3.1. Modelling Technique

The schematic example of a photoconductive antenna is shown in Fig. 6.12. The first step is to analyse the effect of the laser pulse illumination in the photoconductive gap and derive the transient generated current. A full-wave EM solver is then used for the calculation of the probed E-field and spectral characteristics.

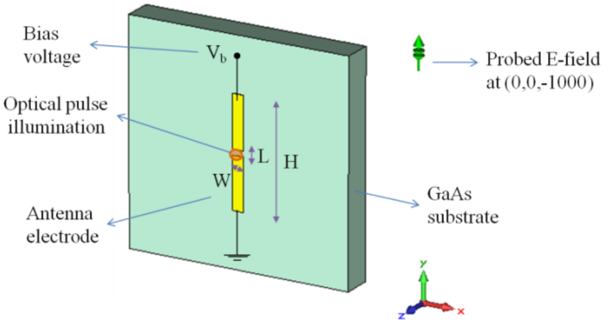

Fig. 6.12 Schematic geometry of a THz dipole antenna. The antenna gap is illuminated by laser and the field is probed along the antenna length at z = -1000 μm

6.3.1.1. Optoelectronic Analysis

Under laser illumination, the free carrier density in the substrate and as a result, the photocurrent in the antenna gap change. Using the numerical modelling described in Chapter 5, it is possible to derive the local voltage of the antenna ($V_c(t)$) in the photoconductive gap through equation (5.3). Then the THz photocurrent is calculated via $i_{pc}(t) = e \cdot n(t) \cdot \mu_e \cdot \frac{V_c(t)S}{L}$. Considering measurement parameters in the THz experimental setup of [192], the numerically calculated photocurrent is illustrated in Fig. 6.13. As explained previously, the rise time of the photocurrent is determined by the laser pulse duration and its decay time is influenced by the carrier lifetime of the photoconductive material. This photocurrent is the input signal for the EM tool.

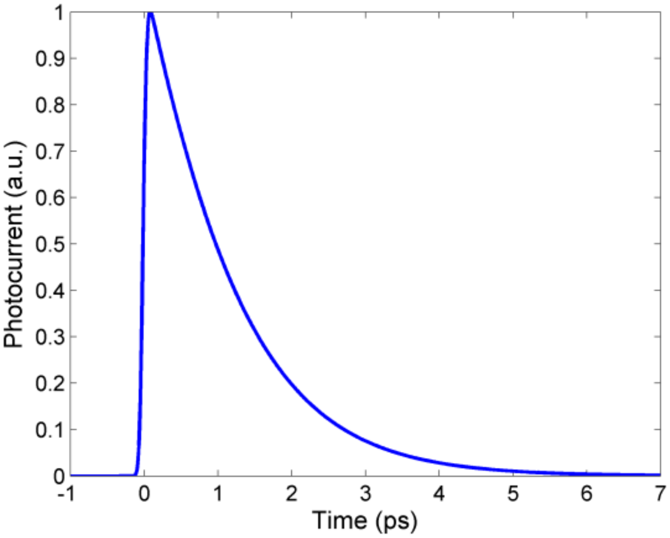

Fig. 6.13 Numerically calculated photocurrent for the gap length × width of 5 × 10 μm, laser pulse duration of 120 fs, carrier lifetime of 1 ps, mobility of 200 cm^2 V^{-1} s^{-1}, optical absorption of 6000 cm^{-1}, and bias voltage of 30 V

6.3.1.2. EM Analysis

For the full-wave simulation of the antenna, CST Microwave studio has been used. The antenna is assumed to be located at the interface of half free space and the GaAs substrate as shown in Fig. 6.12. Hence, absorbing boundaries are employed at the edges of the substrate. In a

THz setup, due to the nature of the measurement and equipment arrangement, the THz signal is detected in the broadside. Therefore, as a second step of this procedure, the antenna is excited by the default signal (i_1), which is a Gaussian-shaped excitation function in the desired frequency range, and the E-field is probed at (0, 0,-1000) μm as depicted in Fig. 6.12. Then, the transfer function of the antenna can be calculated as:

$$H_{ant}(f) = \frac{FFT(E(t))}{FFT(i_1(t))} \tag{6.21}$$

The main reason here for choosing the default signal is to make sure that the stability in the simulation is achieved regardless of the photocurrent signal duration.

As a third step, in order to determine the real response of the THz photoconductive antenna, $E_{pc}(f)$, the calculated photocurrent from the optoelectronic analysis needs to be inserted. Therefore by the use of equation (6.21), the radiated THz E-field can be derived as in equation (6.22).

$$E_{pc}(f) = FFT(i_{pc}(t))H_{ant}(f) \tag{6.22}$$

This radiated THz field impinges the THz photoconductive antenna in the detection side. To consider the effect of detector, the detected signal from photoconductive antenna in the receiver side is calculated from [94]:

$$J_{\det}(t) = e\mu_e \int_{-\infty}^{\infty} E_{pc}(t) n(\tau - t) dt \tag{6.23}$$

By using the convolution theorem, as a final step of this procedure, the detected THz signal in the frequency domain can be derived from:

$$J_{\det}(f) \propto E_{pc}(f) N(f) \tag{6.24}$$

where $N(f)$ is the carrier density of the detector in the frequency domain.

Therefore, based upon the explained simulation steps, spectral response of detected THz signal for various antenna factors can be analysed.

6.3.2. Parametric Study and Analysis

In this section, the effect of several parameters on the detected THz signal is investigated. Variations in these parameters affect the photocurrent, the radiated THz field and consequently the detected THz signal. In this study, it is assumed that parameters in the detector side are the same as the emitter side unless it is stated.

First, the laser pulse duration of the optical excitation signal is varied. This parameter affects the rise time of the photocurrent shown in Fig. 6.13. As illustrated in Fig. 6.14, changes in the laser pulse duration do not influence the peak detected frequency but at larger laser pulse durations, the signal spectrum is smaller. This implies that for a larger bandwidth, optical sources with shorter laser pulses are required. The trend of real measurement setups is the use of optical sources with shorter laser pulse durations for broader detected signals [72] and this simulation results match well with that.

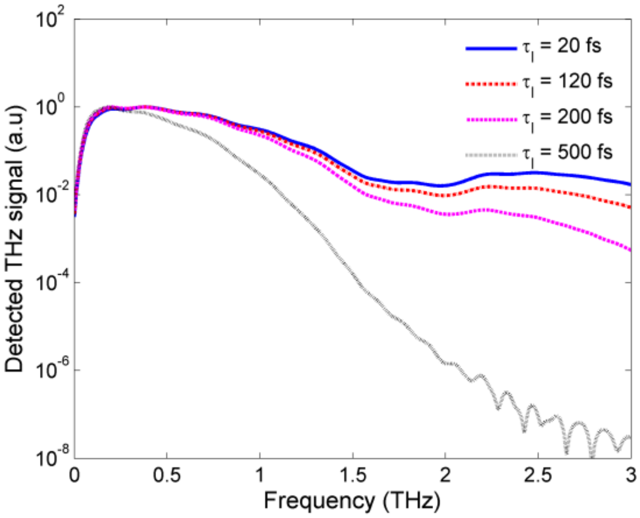

Fig. 6.14 Spectral variation of the detected THz signal for the emitter antenna with H = 100 μm and carrier lifetime of 1 ps

Next, the impact of carrier lifetime of photoconductive material is investigated. According to Fig. 6.15a, by increasing the carrier lifetime, the amplitude of the detected signal is increased. However, spectral range of the signal with a shorter carrier lifetime is larger as shown in Fig. 6.15b. In other words, devices with a short carrier lifetime have larger amplitudes at higher frequencies. Therefore, there is a compromise between having a large signal amplitude and wide bandwidth in THz antennas.

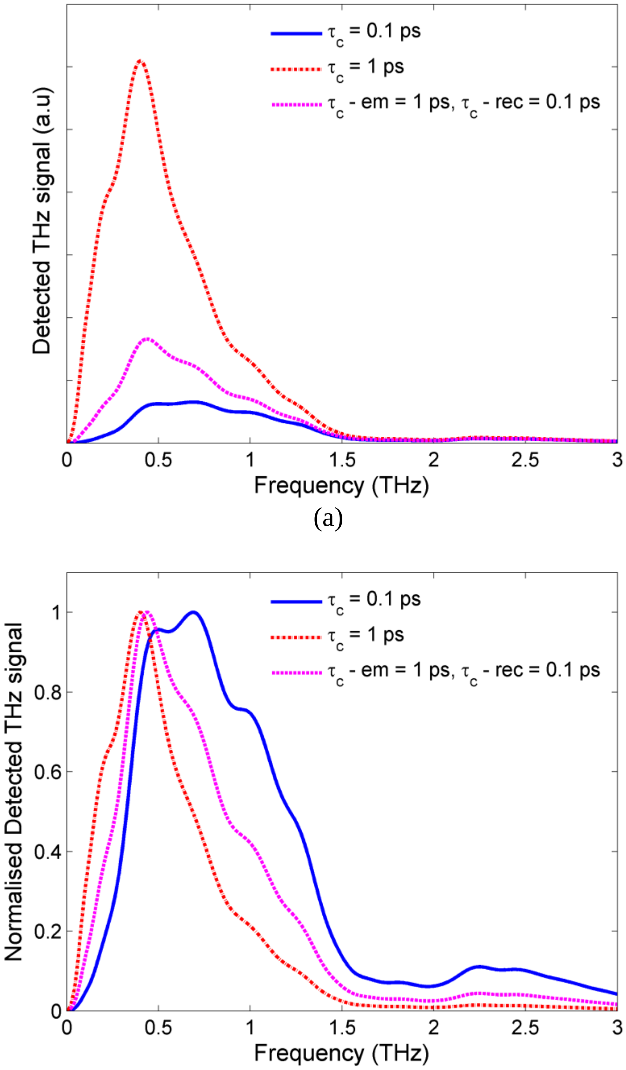

(a)

(b)

Fig. 6.15 (a) amplitude of THz signal THz signal for spectral coverage comparison for H = 100 μm and laser pulse duration of 120 fs (b) normalised amplitude of the calculated, “em” stands for emitter and “rec” stands for the detector

In practical cases, usually photoconductive materials with large carrier lifetimes are used in the emitter side and materials with short lifetimes are employed in receiver. To study this case when the carrier lifetime in the emitter is long and in the receiver is short, the amplitude of the signal and its spectral range is moderate as shown in Fig. 6.15. In other words, these characteristics are in between the two cases where both the emitter and receiver have large or short carrier lifetime. Moreover, by varying the carrier lifetime, the peak frequency of the detected signal shifts. This shows that the peak frequency of the THz signal from the antenna is not only dependent on the antenna geometry, but also it is influenced by the carrier lifetime. This resonance shift in detected signal was reported in measurement results in [7, 69].

The effect of antenna gap length change is considered as shown in Fig. 6.16 where the optical laser power is assumed to be the same, by increasing the antenna gap length, the amplitude of the detected signal decreases considerably. The reason is attributed to the reduction in the optical power density in the antenna gap, which leads to smaller creation of free carriers in the antenna gap and photocurrent.

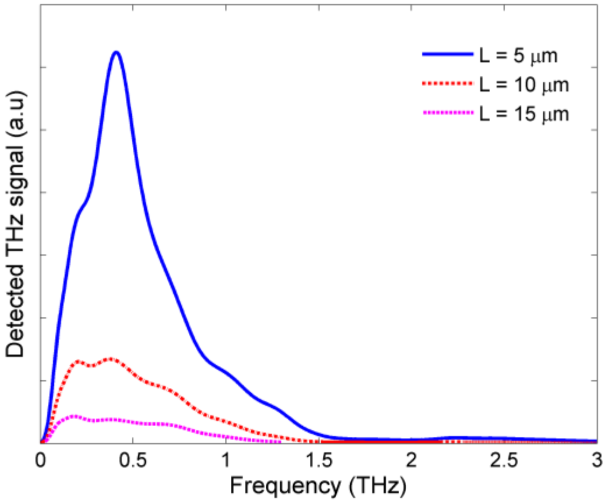

Fig. 6.16 Detected THz signal amplitude for dipole antenna with a constant 10 μm gap width, laser pulse duration of 120 fs and carrier lifetime of 1 ps

The impact of the antenna gap width is studied next ensuring the optical power is kept fixed for all situations. When the antenna gap length is constant, as illustrated in Fig. 6.17, enlarging the antenna width has a consequence of reducing the amplitude of the detected signal.

The investigations on the gap geometry of the antenna demonstrate that to have a larger detected THz signal the antenna gap length and width should be kept small. It is good to mention that there are some practical limitations; such as device breakdown threshold; which limit the antenna gap area in relation to the input optical power.

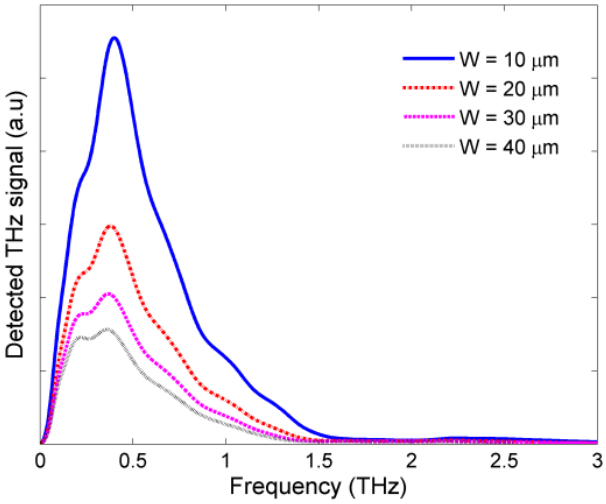

Fig. 6.17 Amplitude of THz signal dipole antenna with a fixed gap length of 5 μm, H = 100, laser pulse duration of 120 fs and carrier lifetime of 1 ps

In order to validate this procedure, the simulated result is compared with measurement results from literature for different dipole lengths [192, 237]. Fig. 6.18 shows a very good agreement with the measurement result, with an increased length of dipole resulting in an enlarged peak detected signal and the peak frequency shifted downwards. Moreover, numerical results presented in [192, 237] deviate considerably from their measurement (Fig. 6.18b); however, the simulation results through this method matches better with the real measured results as shown in Fig. 6.18.

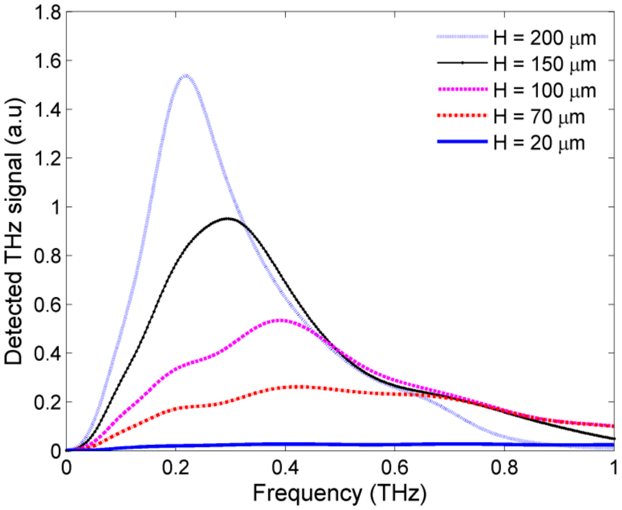

(a)

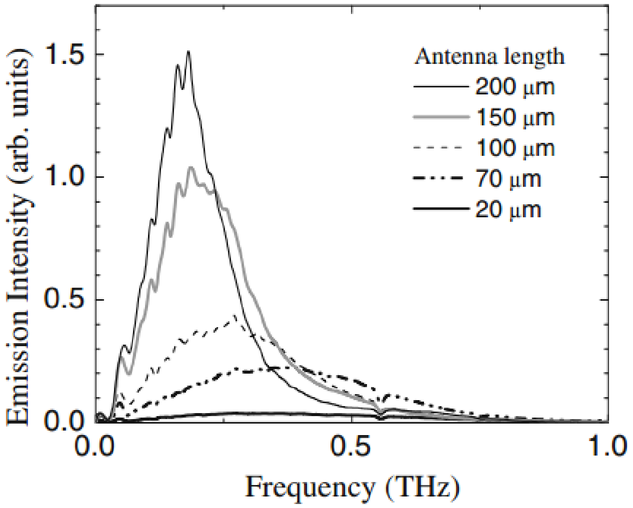

(b)

Fig. 6.18 (a) Simulation of the detected THz signal for various dipole antenna length (b) corresponding experimental results [237]

6.4. Summary

Two other dissimilarities of THz antennas with RF/MW antennas, *i.e.* substrate thickness and numerical simulation of the antenna, were discussed in this chapter. Investigation on the effect of the substrate thickness on the THz antenna performance showed that when the substrate thickness is set larger than one tenth of wavelength, (*i.e.* $> \lambda_{sub}/10$) the efficiency drops severely and starts to oscillate notably. Such an oscillation provides an opportunity to tune the antenna for the local maxima efficiency in peaks. The analytical study was compared with simulation result and it showed a good agreement. Also, a new computational simulation method for characterizing the detected signal from THz photoconductive antennas was developed. The approach was based on employing both optoelectronic and full-wave EM properties of the antenna. Effects of several parameters, related to the excitation and geometry of the device, were studied. The detected THz signal for different dipole antenna lengths from this method matched very well with measurement results reported in the literature. This simulation method is an easier procedure as compared to the full numerical method and it enables prediction of the antenna performance more accurately compared to the other full numerical methods used in [192, 237]. Thus, it is now possible to more accurately examine the THz antenna performance and understand the influence of different parameters before the antenna is fabricated.

Chapter 7. A Top Loaded Antenna for a THz Photomixer Antenna

7.1. Introduction

In Chapter 1, it was described that narrowband or CW systems were in great demand for high resolution applications. Compared with broadband systems, CW systems offer advantages such as the compactness, low cost and low weight. Although for room temperature applications, photomixing (named sometimes as optical heterodyne conversion [58]) to generate continuous THz wave is an attractive approach, as depicted in Fig. 3.4, the output power from a THz photomixer antenna is very low. In section 3.4.2, low optical-to-electrical conversion, matching and coupling efficiencies were addressed as reasons of low output power and efficiency of these types of antennas. In order to gain a better view on performance of a THz photomixer antenna and further possible limiting factors, initially in this chapter the equivalent circuit of a THz photomixer antenna is reviewed. Then, considering the restriction factors in the performance of the antenna, a new THz photomixer antenna solution is proposed and the antenna is systematically studied and characterised.

7.2. Equivalent Circuit of a THz Photomixer Antenna

Unlike THz photoconductive antennas, the working principle of a THz photomixer antenna had been well explained through the equivalent circuit [8, 111]. The THz photomixer antenna can be modelled as the circuit shown in Fig. 7.1. The photomixer part of the antenna can be modelled by C_{elec}, which represents the capacitance between the antenna electrodes, in parallel with $G_{scw}(\omega_{THz},t)$ (the time-varying source conductance formulated in (4.18)) and the antenna is modelled as a resistance of R_a[1].According to the equivalent circuit, the total impedance is:

$$Z_t(\omega_{THz},t)=\frac{1}{j\omega_{THz}C_{elec}+G_{scw}(\omega_{THz},t)}+R_a \tag{7.1}$$

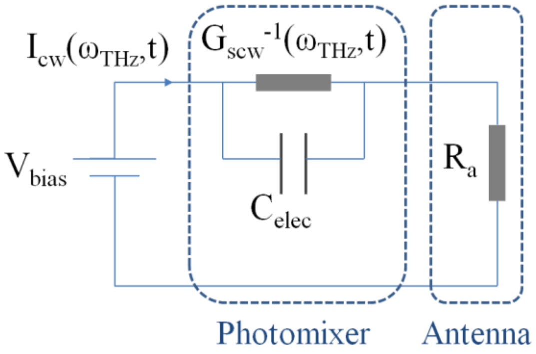

Fig. 7.1 Equivalent circuit of a THz photomixer antenna as an emitter

The radiated power from the antenna can be calculated from:

$$P_{THz}(\omega_{THz},t)=R_a\left(\frac{V_{bias}}{Z_t(\omega_{THz},t)}\right)^2 \tag{7.2}$$

Substituting equations (4.18) and (7.1) in (7.2), taking the real part and considering that $R_aG_{scw}<<1$, the instantaneous radiated THz power is [111]:

$$P_{THz}(\omega_{THz},t)\approx R_a\frac{V_{bias}^2G_{scw}^2(\omega_{THz},t)}{1+(\omega_{THz}R_aC_{elec})^2} \tag{7.3}$$

By averaging equation (7.3) and neglecting the constant part [111] the mean radiated power can be derived as below:

---

[1] Choke filter is another element in THz photomixer antennas which minimises leakage of the created THz current to the bias lines. The impedance of this line can be included in that of the antenna in analysis.

$$P_{THz}(\omega_{THz}) \approx R_a \frac{m V_{bias}^2}{(1+(\omega_{THz} R_a C_{elec})^2)(1+(\omega_{THz}\tau_c)^2)} \left(\frac{W \cdot e \cdot \mu_e}{Lhf_l} I_0 (1-R) \tau_c \left(1 - \exp(-\alpha T_{LT-GaAs})\right) \right)^2 \tag{7.4}$$

In equation (7.4), it is assumed that the two optical sources have the same laser pulse intensities. It demonstrates that at low frequencies the radiated THz power is independent of $\omega_{THz} R_a C_{elec}$ and $\omega_{THz}\tau_c$. At high frequencies, these two terms become significant which result in about 12 dB/octave roll off of the output power ($P_{THz}(\omega_{THz}) \approx \omega_{THz}^{-4}$). Therefore, equation (7.4) shows that radiated THz power in a THz photomixer antenna at high frequencies is limited by carrier lifetime of substrate and finite capacitance of the device.

By considering previously stated analyses on reasons of low output power of THz photomixer antenna and the above equivalent circuit, the required conditions for enhancing THz power from this antenna type can be summarised as follows.

First, the carrier lifetime of the photoconductive material should be small. In THz devices, the effective lifetime, τ_{eff}, is also used and defined as [238]:

$$\frac{1}{\tau_{eff}} = \frac{1}{\tau_c} + \frac{1}{\tau_{drift}} \tag{7.5}$$

where τ_{drift} is the carrier drift time and it is defined as the ratio of the electrode distance to the electron drift velocity. One method to reduce the effective carrier lifetime may be sought through fabrication techniques [131, 239] which leads to the reduction in carrier lifetime. Another method to improve the effective carrier lifetime is the reduction of carrier drift time. This can be achieved by appropriate electrode designs in the photomixer part. Electrode designs in the photomixer also affect the electric field distribution and as a result, generated photocurrent in the photomixer and optical-to-electrical efficiency. Various geometries, such as recessed interdigitated fingers [240] and tip-to-tip rectangular fingers [191], have been proposed to improve the radiated THz power through the structures of the photomixer part of the antenna.

Second, finite electrode capacitance restricts radiated THz power at high frequencies. Same as the previous case, the capacitance value can be modified through modifications in the electrode designs of the photomixer as proposed in [171, 191].

Third, impedance matching between the photomixer (*i.e.* source) and the antenna needs to be improved for better coupling of power from the photomixer to the antenna. Different antenna geometries, which have high antenna radiation resistance and as a result better impedance matching, were reviewed in section 3.5.2.

Fourth, enhanced coupling of the THz wave from the antenna to the air can improve the radiated THz power from the device. To enhance this coupling, a lens whose refractive index matches that of the photoconductive material is the most commonly used solution. It reduces reflection in air-substrate interface and collimates the radiated waves.

All previous research work has been concentrated on only one or two of the aforementioned conditions in order to improve the radiated THz power. In this chapter, a new THz photomixer antenna is designed which takes all four conditions into account. Thus, the aim of the design for the photomixer section is to reduce the carrier drift time, capacitance and at the same time maintain a large electric field in the gap. For the antenna section, the goal is to improve the impedance matching between the photomixer and the antenna. In addition, an enhancement in the antennas directivity is sought. To achieve these goals, a new top hat loaded antenna with trapezoidal fingers in the photomixer embedded to a conical horn is proposed and a modular study on each part of the new design is thoroughly carried out to optimise each section. Finally, the antenna with the new photomixer design is characterised and its performance is compared to the previous conventional designs.

7.3. Photomixer Analysis

The photomixer is an essential part of THz antennas based upon CW technique, and its geometrical arrangements affect the generated THz current and the performance of the whole antenna. To generate more photocurrent in the photomixer, a uniform E-field across the gap is desired (as summarised in block diagram of Fig. 3.5). The amount of induced photo-carriers to the antenna per absorbed photon (*i.e.* photoconductive gain) can be written as equation (7.6) [176]:

$$g = \frac{\tau_c \mu_e E}{W_g (1 + \mu_e E / v_{sat})} \tag{7.6}$$

where E is the electric field, W_g is the gap length between the electrodes (here it is simply assumed that the carrier path is the straight line between the electrodes) and v_{sat} is the saturation velocity. It can be interpreted that for a large g the E-field needs to be large and since the photocurrent is proportional to g [176], this leads to the generation of larger photocurrent. In addition, the gap between the electrodes, W_g, should be small. This provides a uniform E-field and also maintains a small drift time. Therefore, more generated free carriers may reach the electrodes. It should be pointed out that, in a pulsed system since the peak optical excitation power is very large (in the order of kW); the gap size cannot be highly reduced because of the destructive effect on the antenna. However, in a CW system the optical power on the antenna is small and reduction of the gap size is viable. Another factor for a large THz power, according to equation (7.4), is to have a small C_{elec} (especially at higher frequencies), which is a geometrical parameter. Therefore, the geometry of the photomixer is a crucial factor in determining the E-field distribution and electrode capacitance.

Extension of the active area in the photomixer is a way that can satisfy uniform E-field distribution in the gap, enhance the power coupling from the laser beams, and increase generation of photocurrent. For instance, addition of the interdigitated fingers to a bare photoconductive gap has been demonstrated to be an efficient way of achieving evenly distributed E-field in the active area [8, 111] although this geometry has larger capacitance as compared to bare electrodes. One alternative solution to mitigate the drawback of large capacitance, while maintaining the extended active area (by using fingers), can be nanogap rectangular tip-to-tip electrodes [191]. The main reasons for expecting a better performance of this geometry are: (1) it has enhanced THz E-field in the active region due to nanogap electrodes [241]; (2) it has a shorter drift time between electrodes as compared to the bare gap and interdigitated finger antennas. It is good to note that the idea of tip-to-tip electrodes has also been proved as an efficient geometry for high THz radiation powers in pulsed systems [160] as mentioned in section 3.5.1.6.

In order to improve the performance of photomixer part of the antenna further, a new trapezoidal tip-to-tip finger is proposed. For a comprehensive study and comparison, in this section the effect of the photomixer geometry and the shape of the fingers (for. the bare electrodes, interdigitated fingers, rectangular tip-to-tip fingers and new trapezoidal tip-to-tip fingers), on the capacitance and the E-field in the active region of the antenna is investigated. These geometries are depicted in Fig. 7.2.

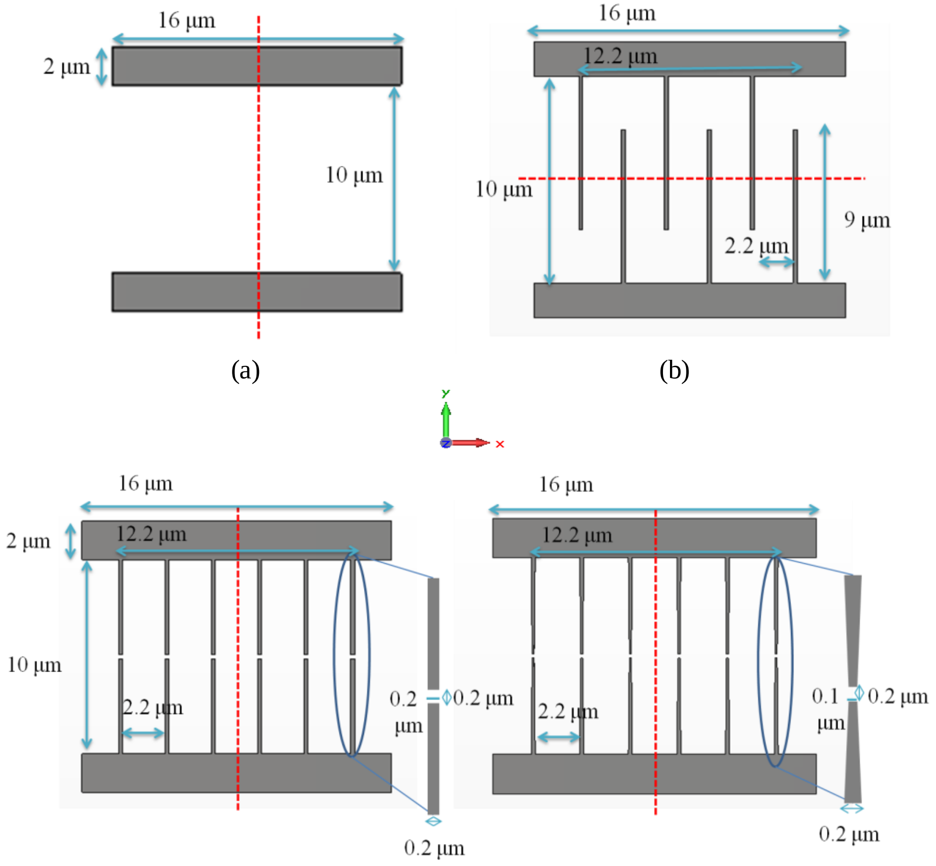

(a) (b)

(c) (d)

Fig. 7.2 (a) bare electrode (b) six-finger interdigitated electrode (c) six-finger tip-to-tip rectangular electrodes (d) six-finger tip-to-tip trapezoidal electrodes

In these analyses, the active area is kept fixed at 160 μm^2 where electrodes occupy fixed width of 12.2 μm. Thus, for the six-finger electrodes (interdigitated and tip-to-tip geometries) the electrode lateral spacing is 2.2 μm. In both tip-to-tip configurations, the vertical gap distance between the electrode tips are kept constant at 0.2 μm. This gap width is chosen to satisfy the requirement of small drift time. This increases absorbance of the generated photo-carriers by the electrodes before recombination [199] (considering the limited electron drift velocity [196]). In Fig. 7.2b and Fig. 7.2c the width of rectangular electrodes are 0.2 μm (common electrode width in a photomixer [242]). In Fig. 7.2d the upper base of the trapezoidal electrodes is 0.2 μm and the lower base, at the gap area, is narrowed to 0.1 μm.

The capacitance of these photomixers is derived numerically using a commercial software package, CST. For this calculation, the metal fingers were defined as perfect electrical conductors with a thickness of 0.15 μm. The photomixer is isolated on a truncated half-space substrate, and the mesh points were set at 40 per wavelength. In order to neutralise the effect of simulation parameters and mesh numbers on the derived results, all geometries are simulated in the completely identical situation with the same number of meshes. Numerical analysis has shown that the capacitance of bare electrodes is 1.26 fF and by adding interdigitated fingers, it is increased to 2.63 fF. However, by changing the geometry to the one with tip-to-tip rectangular electrodes the capacitance is reduced to 2.4 fF, and by using a trapezoidal shape, the capacitance can be further reduced to a value of 2.28 fF. Considering the equation (7.4), that $P_{THz}(\omega_{THz}) \propto \frac{1}{1+(\omega_{THz} R_a C_{elec})^2}$, this reduction in the capacitance value is desirable because it leads to a larger radiated THz power at higher frequencies. Hence, among photomixer designs with an extended active area, the trapezoidal configuration has larger THz power especially at high frequencies; thus, it is the preferred structure from the capacitance value perspective.

The next step in this analysis concerns the evaluation of the E-fields of these structures. First, the field magnitudes in the lateral direction of these structures are evaluated. Previous studies of photomixers showed that the field strength for planar structures is the greatest at the photoconductive gap surface and its magnitude reduces as it penetrates into the substrate [242]. Penetration of strong electric fields in the substrate decreases optical power coupling to high electric field area (which is at the electrode surface). Therefore, the photomixer geometry with the large electric field at the substrate surface is a desirable structure.

For this purpose, the static fields of these photomixer geometries distributed laterally in the substrate are compared. It is assumed that thickness of the electrode increases from z = 0 to z = 0.15 μm (commonly this thickness is between few ten nm to hundreds of nm [111, 150, 207]) and the substrate thickness starts from z = 0 and increases towards the negative z direction. A comparison of the static E-field distribution on the substrate beneath electrodes, for these geometries under the same DC bias voltage, is depicted in Fig. 7.3. It shows that in tip-to-tip geometries the static electric field confines more strongly to the upper part of the photoconductive substrate (where the optical excitation is intense) as compared to bare and interdigitated fingers. Also, it illustrates that an improvement at the surface of the substrate (z = 0) for trapezoidal tip-to-tip fingers is the largest. To elaborate further, it can be observed that the static E-field intensity for the trapezoidal fingers on the substrate is 5.7×10^{6} V/m whereas for the bare electrodes, interdigitated fingers and rectangular fingers it is 9.26×10^{5} V/m, 2.1×10^{6} V/m , and 4.47×10^{6} V/m respectively. In the same order, trapezoidal electrode geometry shows 84%, 63%, and 22% larger static E-field at the surface of the substrate than the bare electrode, interdigitated, and rectangular geometries. This shows another advantage of the new trapezoidal photomixer design.

Second, the E-field distribution on these structures are evaluated and compared. This is important because it is linked to the THz photocurrent, and a large photocurrent in the photomixer leads to a large radiated THz power. The E-field distributions on the electrode plane of these geometries are compared using CST under the illumination of the plane wave at 1 THz. For bare electrodes and tip-to-tip finger geometries the polarisation of the plane wave is along the y axis, which is in the direction of electrode lengths. However, since in interdigitated geometry the bias electric field is along the x axis, the polarisation of the plane wave is chosen in parallel to the x axis.

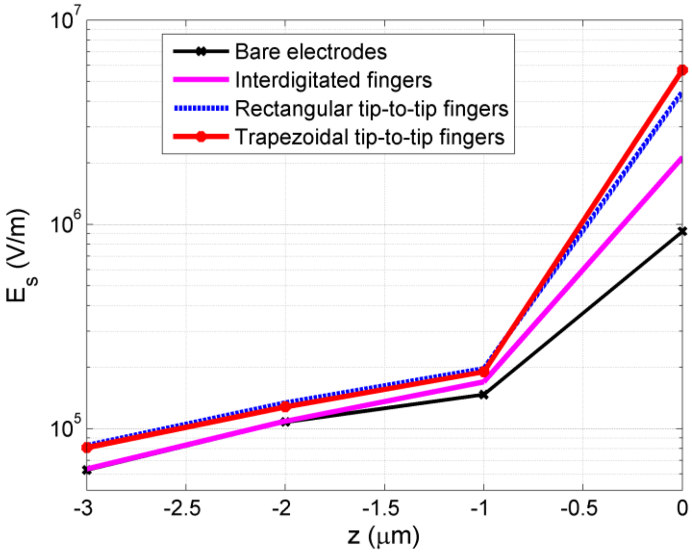

Fig. 7.3 Comparison of the static electric field amplitude for the bare, interdigitated, rectangular and trapezoidal finger tips at different depth of substrate (substrate thickness is towards the –z direction)

The effect of adding electrodes to bare electrodes on profile of E-field along the depicted dash lines in Fig. 7.2 is presented on the left hand sides of Fig. 7.4a-Fig. 7.4d. For the sake of comparison the scale of graphs on the y axis in Fig. 7.4a-Fig. 7.4d is kept similar. According to Fig. 7.4a, it can be observed that in bare electrode case, the E-field is strong near the positive electrode; but, it declines rapidly towards the other electrode. This matches with the measurement observation in [111] where the electric field is strong near the electrodes and it severely drops only a few micrometer away from the electrode. The difference between this theoretical analysis and the measurement is that in practice, the applied bias alters for lock-in amplifier detection and the anode and cathode are interchangeable; therefore, enhancement was seen in proximity of either electrodes [111]. The E-field of the interdigitated configuration has a more uniform profile compared to the bare electrode as shown in Fig. 7.4b (zeros in E-field in Fig. 7.4b show the location of metal electrodes). Here since the distance between the adjacent electrodes is slightly large, the strong E-field areas do not fully overlap and the E-field reduces a little between the interdigitated fingers. In tip-to-tip geometries, to compare E-fields with that of the bare electrode at the same place, dash lines are selected along the centre of photomixer as shown in Fig. 7.2c and Fig. 7.2d (although in tip-to-tip fingers, the strongest E-field profile exists at tip ends). By adding tip-to-tip electrodes, the E-field is enhanced in the central part of the photomixer where horizontally it is along the finger gaps as depicted in Fig. 7.4c and Fig. 7.4d. The E-field of trapezoidal tip-to-tip fingers is more than two folds stronger than the rectangular one in the centre. The magnitudes of E-fields adjacent to the transmission lines at two sides of electrodes are almost same unlike the values in the bare electrodes. This can be attributed to the increment in the E-field interaction between the electrodes and transmission lines at the end of electrodes.

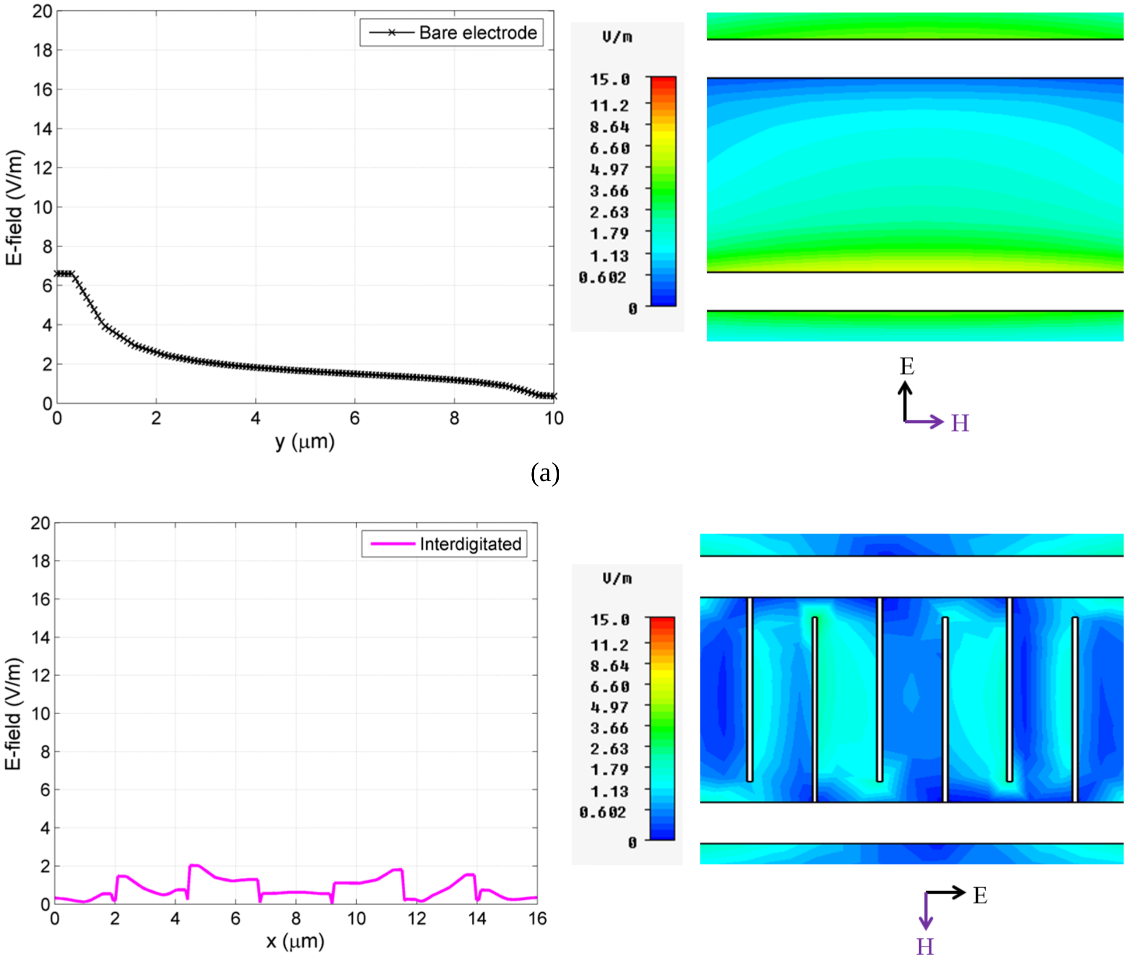

(a)

(b)

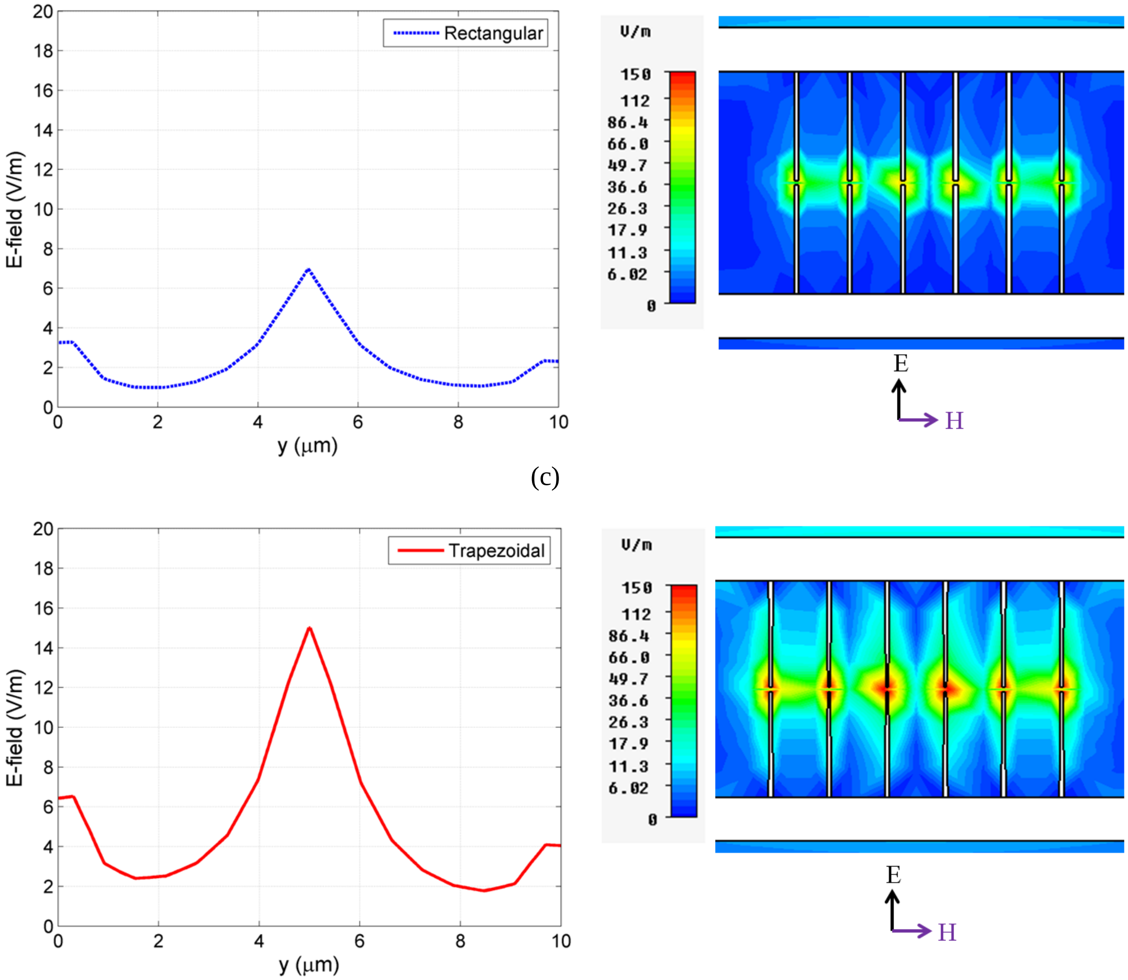

(c)

(d)

Fig. 7.4 E-field profile (left) and amplitude of E-field in the near field (right) of (a) bare electrodes (b) interdigitated electrodes (c) tip-to-tip rectangular electrodes (d) tip-to-tip trapezoidal electrodes under illumination of a 1 THz plane with fixed amplitude of 1 V/m, polarisation of illuminated E-field is shown below of each figure. Please note that E-fields in near field of (a) and (b) are clamped to 15 V/m whilst those of (c) and (d) are clamped to 150 V/m.

Fig. 7.4 also shows the E-field distribution on these geometries. As depicted on the right side of this figure, it can be observed that the E-field distribution of the new tip-to-tip trapezoidal geometry has the largest magnitude with a high concentration in the gap area. To have a better quantitative comparison on the E-field values in the nanogaps of tip-to-tip geometries, E-fields are plotted along a line passes all nanogaps of the electrode, as shown in Fig. 7.5a. According to Fig. 7.5b, the E-field amplitude in the gap area of the trapezoidal geometry is more than doubled as compared to the rectangular design geometry. This enhancement is attributed to the electrode geometries. Since the new trapezoidal electrode designs are sharper and any charges accumulate on the tip ends, the surface charge density can increase and enhance the E-field. Hence, more THz current in the photomixer can be generated and propagated to the antenna. This simulation results agree well with the measured one in [79], where a dipole with sharper tip ends outperformed a dipole antenna with rectangular tip end under laser illumination. Furthermore, since singular electric fields near the sharp structures are larger, less optical power is required for the excitation [79]- this is a common situation in CW systems.

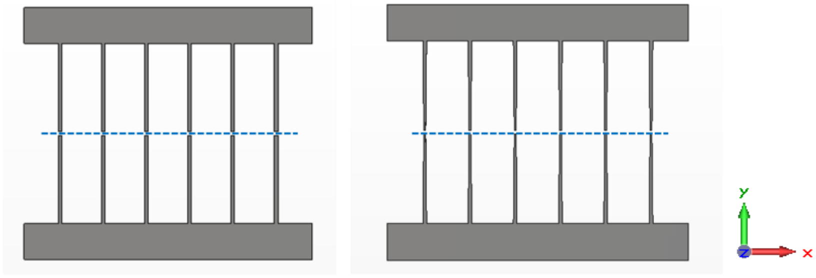

(a)

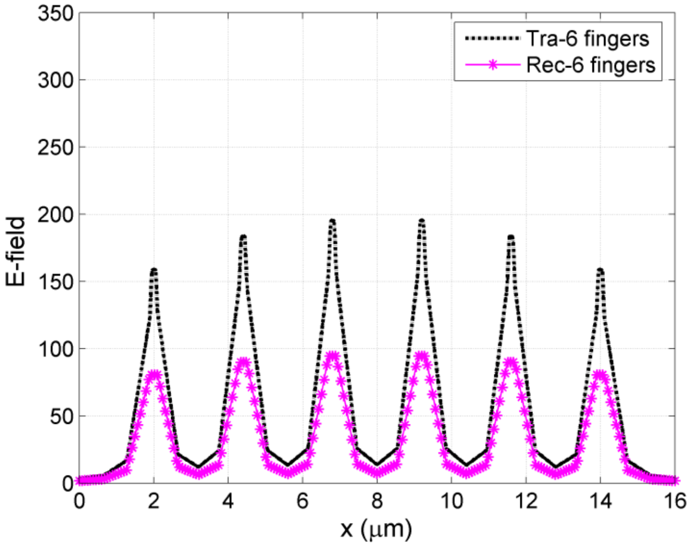

(b)

Fig. 7.5 (a) Photomixer geometries, E-fields are monitored along the dashed lines (b) Monitored E-field on the electrode plane under illumination of a 1 THz plane wave with 1V/m amplitude. In the legend “Tra” stands for trapezoidal fingers and “Rec” stands for rectangular fingers

As a summary, tip-to-tip trapezoidal photomixer has better characteristics than other conventional photomixer designs. This is because it has smaller capacitance than the others and it has a stronger local E-field, which is due to confinement of the electric field to the upper epilayer of substrate. Also, more charges at the sharp tip end of trapezoidal electrodes are accumulated, which result in a larger photoconductive gain, enhanced photocurrent and the radiated THz power.

7.4. Antenna Design Analysis

The antenna is a very important part of a THz photomixer device because by coupling of the produced THz current in the antenna gap into the antenna; THz waves propagate in the air. In THz pulsed systems since a broad range of frequencies are generated, broadband antennas are required. In CW systems broadband antennas are also desirable because it enables tunability of the device. One of the most popular broadband antennas is the bowtie antenna which its input impedance is variable with the bow angle [203]. An alternative type of broadband antennas is a log periodic antenna, which is in principle an array of discrete dipole antennas, and it resonates at different frequencies according to the length of these dipole elements [100]. The self-complementary log-spiral is another very common THz photomixer antenna [243]. The radiation impedance of this antenna has a nominal value of 72 Ω on GaAs (considering input impedance of self-complementary geometries as $60\pi/\sqrt{\varepsilon_{eff}}$ [1])

Impedance mismatching problem as discussed previously implies that increasing the input impedance of the THz antenna improves the radiated THz power and optical-to-THz efficiency. However, there exist two main challenges; one is that, obtaining impedance matching for the entire frequency range is difficult; second, in practice, impedance matching is not easy because the source resistance is very huge. Thus, resonant antennas (like dipole and slot antennas) are of interest because they can be designed to have much larger impedance at a particular desired frequency [111, 200, 244, 245].

For the maximum power transfer in the antenna, conjugate impedance matching criteria needs to be fulfilled (*i.e.* $R_a = R_{scw}$ and $X_a = -X_s$ where X_a is the imaginary part of antenna impedance and X_s is the source reactance due to the photomixer electrode geometry). By designing inductive reactance in the antenna, it is possible to cancel the capacitive reactance of the photomixer [200]. It is difficult to estimate the inductance analytically; thus, the electromagnetic simulation software is employed for the design.

Considering the new electrode design in section 7.3, in this section, the focus is on the design of a new resonant antenna at 1 THz with increased radiation resistance as compared to the conventional full wavelength dipole antenna. In this kind of antenna, the resonant frequency is affected not only by the antenna, but also by the choke filter and the photomixer. Hence, the whole structure of the antenna (consists of antenna, choke filter and photomixer) should be taken into account for increasing the radiation resistance.

7.4.1. Source Resistance of the New THz Photomixer Antenna

In the source conductance analysis of a THz photomixer antenna presented in section 4.3, the photomixer was treated as a bare photoconductive gap. However, addition of electrodes modify the photomixer and as a result the source conductance. Therefore, the effect of new photomixer design on the source resistance and impedance matching is to be considered.

As previously discussed, by adding electrodes, the total capacitance of tip-to-tip finger photomixer becomes larger than that of the bare one. In this case, due to very small electrode gaps, the thermal performance of the photomixer could be a problem. However, a more uniform and stronger E-field in the gap can be achieved than the bare electrode. Another effect of the photomixer geometry is on the photoconductive resistance, which acts as the source resistance for the antenna. The equivalent circuits of the photomixer for a bare electrode and tip-to-tip electrodes are depicted in Fig. 7.6. The source conductance of a THz antenna in a CW system can be calculated from equation (4.18). In a bare electrode, as shown in Fig. 7.6a, the source resistance may be modelled as R_{tot1}. In a tip-to-tip electrode the total resistance, as illustrated in Fig. 7.6b, can be modelled as a series of parallel resistances.

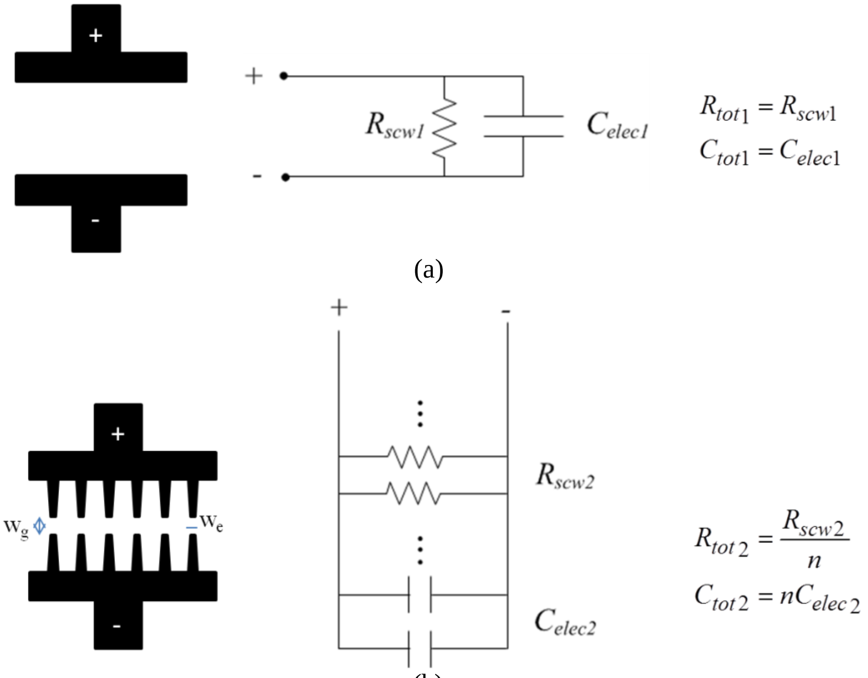

(a)

(b)

Fig. 7.6 (a) Bare electrodes with the equivalent circuit (R_{scw1} and C_{elec1} are respectively photoconductive resistance and electrode capacitance) (b) tip-to-tip trapezoidal finger electrodes with the equivalent circuit (*n* is the number of finger couples, R_{scw2} and C_{elec2} are respectively photoconductive resistance and capacitance between each electrodes and *n* shows the number of coupled electrodes)

In order to calculate the photoconductive resistance, the values for different parameters of the optical sources and photoconductive material for a sample CW system used in equation (4.18) are summarised in Table 7.1. Here, it is assumed that the optical power density of laser diode is 20.8 kW/cm^2 (where the average power of the laser is 20 mW and the laser spot area is 0.958 μm^2). In the bare electrode case, it is assumed that W_e = 12.2 μm and W_g = 10 μm. Using equation (4.18) and Table 7.1 and considering that $R_{scw} = 1/G_{scw}$, the average photoconductive resistance is about 483 kΩ. By keeping all parameters constant and adding the tip-to-tip electrodes where W_e = 0.1 μm and W_g = 0.2 μm, the photoconductive resistance for one pair of electrodes will be 1.17 MΩ. This increment is due to the smaller area of the trapezoidal electrode. Considering Fig. 7.6b, for the 6-finger electrode geometry, the total photoconductive resistance will be 196 kΩ. This illustrates that mismatching between the antenna and photoconductive resistance will decrease because the source resistance is reduced 2.5 times in the new photomixer design. However, since the antenna radiation resistance is about few hundred ohms, still a new antenna design with a large radiation resistance is required for a good matching efficiency and large radiated THz power at the desired working frequency.

Table 7.1 Laser, Photoconductive material and photomixer electrode parameters used in equation (4.18)

Parameter	Notation	Value
Laser angular frequency difference (THz)	ω_1-ω_2	$2\pi\times 1$
Electron mobility for LT-GaAs [69]	μ_e	200 $cm^2.V^{-1}.s^{-1}$
Power reflection coefficient in air-photoconductive material interface	R	(for GaAs) 0.318
Optical absorption coefficient [127]	α	6000 cm^{-1}
Carrier life time	τ_c	1 ps
Depth of excitation region	$T_{LT\text{-}GaAs}$	1 μm

7.4.2. Choke Filter Elements

The next design step before presenting the complete antenna geometry is the choke filter design. Ideally, the resonant antenna should be decoupled from the electrical bias pads in a selected operation frequency. Choke filter is a bandstop filter with quarter-wavelength and open-circuited stubs. Choke filter stops THz transmission while maintaining a perfect transmission of bias current [246]. To illustrate the effect of choke filter, the transmission of THz travelling wave along coplanar striplines with and without the choke filter is modeled and S_{21} parameter which measures the amount of the transmitted THz energy from port 2 to port 1 is obtained. Coplanar transmission line geometries and S_{21} of them are shown in Fig. 7.7.

Variation of the length of choke defines the blocked frequency. Here, the length of alternate high and low impedance elements of the choke filter is 26 μm, which are ~ $\lambda_{eff}/4$ (for 1 THz), and are tuned through the simulation. The simulation result shows a strong minimum in S_{21} around 1 THz, implying that this energy is reflected back and it cannot flow through the transmission line.

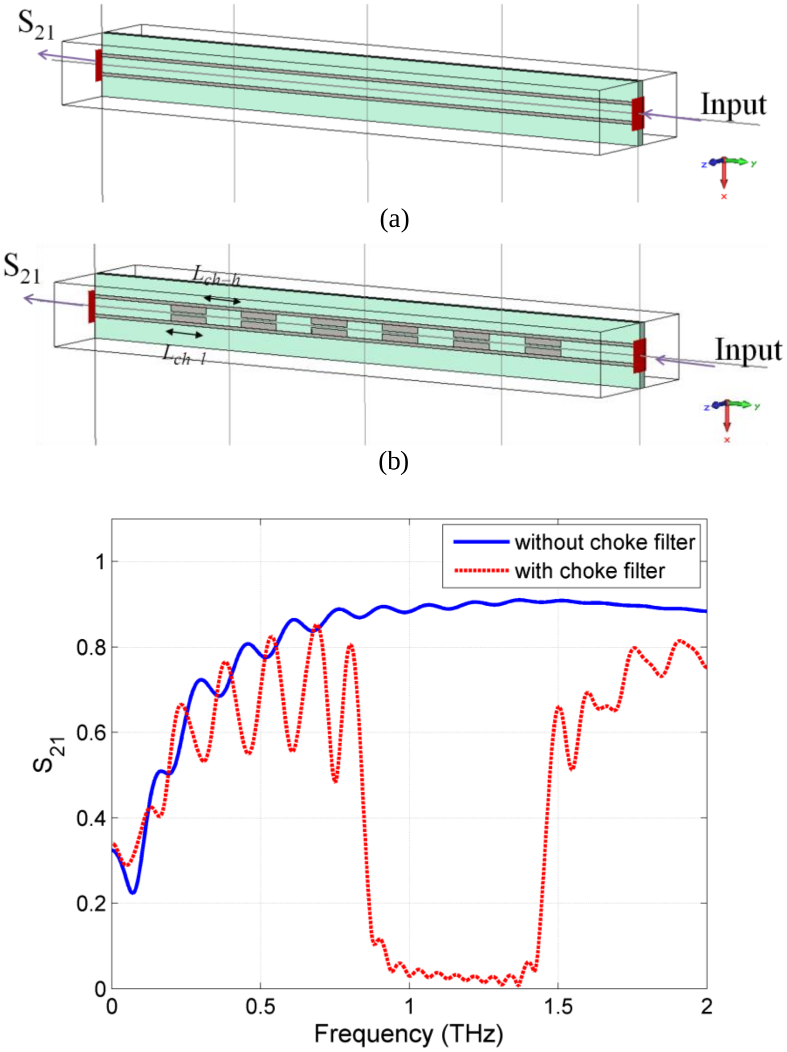

(a)

(b)

(c)

Fig. 7.7 (a) Coplanar transmission line model (b) Choked transmission line model (c) Simulated S_{21} for the coplanar stripline without and with the choke filter ($L_{ch-h} = L_{ch-l} = 26$ μm)

7.4.3. Proposed THz Photomixer Antenna

For the design of the new antenna, separately described parts need to be merged. According to the photomixer analysis in the previous section, the related capacitance was calculated. In the simulation of the new antenna, the capacitive effect of the photomixer (the 6-finger electrode geometry) is added to the simulation by the introduction of a lumped element. The lumped capacitance model for electrodes is applicable since the dimension of the photomixer is smaller than λ/10 [12]. Also, the choke filter dimension, which results in a very small transmission at 1 THz, was derived. Now, the center-fed antenna is to be designed. In practice, the resonances of the dipole antenna and choke are dependant; so, the device as a whole (antenna, feeds and photomixer) should be simulated and optimised.

The proposed new THz photomixer antenna design is depicted in Fig. 7.8. The antenna structure is modelled as a perfect electric conductor with metal thickness of 0.15 µm. To attempt to overcome the problem of substrate modes, the antenna is integrated on a thin membrane as discussed in Chapter 6. The advantage of this method is the elimination of the dielectric loss and substrate modes compared to the use of a thick substrate (at the expense of more difficult substrate fabrication). Hence, the antenna is situated on a GaAs substrate with a thickness of 5 µm and ε_r = 12.9.

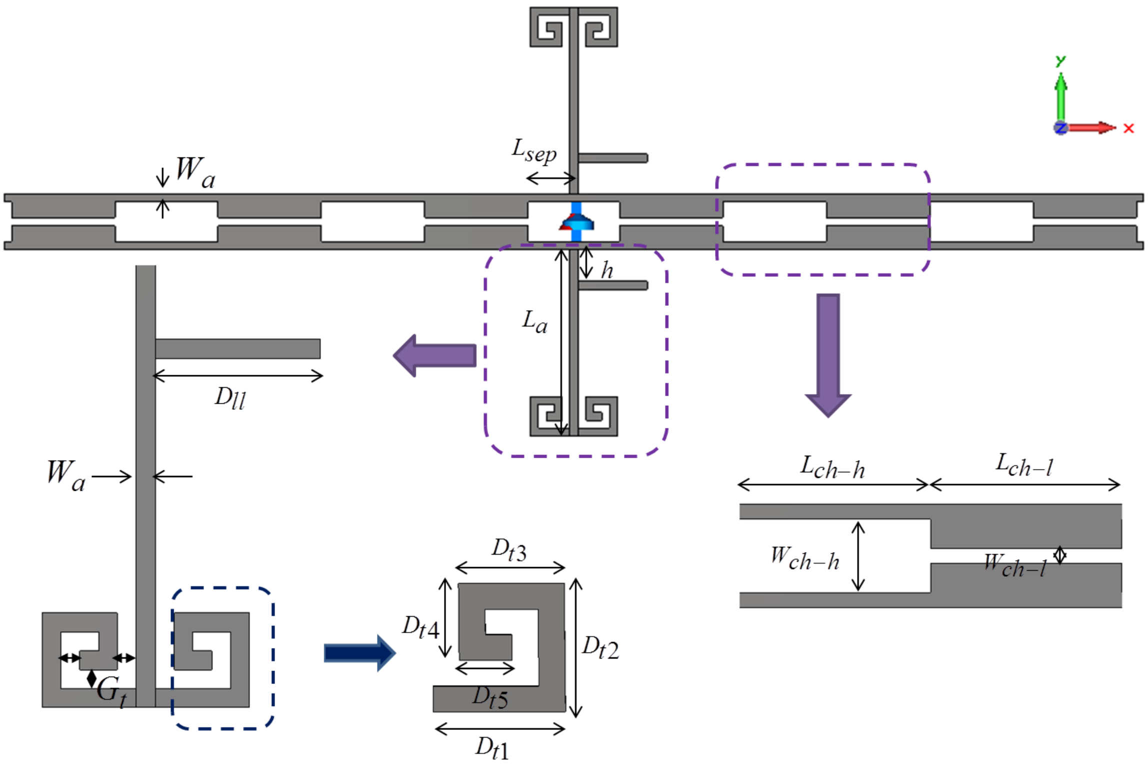

Fig. 7.8 The proposed THz antenna structure consists of the top loaded antenna, and choke filter as a DC bias line and stop filter for 1 THz current

The initial dimensions of the dipole antenna (alone) to resonate at 1 THz are L_a = 47 µm and W_a = 2 µm. As shown in Fig. 7.9a, the resistance value of the antenna at 1 THz is 420 Ω. By adding the photomixer capacitance in the gap, a larger capacitance will be in parallel to the antenna that shifts the resonance frequency lower (according to Fig. 7.9b the resonance frequency is ~ 0.73 THz). It also reduces the value of the antenna resistance resonance considerably. By adding the choke filter, not only is the resonance frequency affected (moved to ~ 0.99 THz shown in Fig. 7.9b), but also the antenna will have a sharper anti-resonance behaviour with greater resistance value of 1.8 kΩ as depicted in Fig. 7.9a. The reason is that, by the addition of a choke filter, a high value inductance becomes parallel to the antenna hence the resonance frequency is shifted higher.

To have a better matching to the photoconductive resistance for a larger radiated power, the antenna resistance is to be increased further. For this purpose, we need to enlarge the area under the current distribution curve of the antenna [247]. Folded structures and top hat loaded geometries are suitable candidates to increase the current distribution on the antenna whilst the original length of the antenna is kept unchanged [1]. Therefore, two square spiral loads as planar top hats are added at the end of the antenna. Newly added square spiral loads have inductive characteristics [246] which modify the resonance frequency of the antenna. As presented in Fig. 7.10, the peak resistance value of the antenna with top loads increases to 2.74 kΩ, which is doubled as compared to the case without top loads in Fig. 7.9a; this yields an enhanced radiated power.

In this geometry due to the increase in inductance of the whole antenna, the resonance frequency is slightly shifted to lower frequencies. Therefore, in order to have a highly resonant antenna at 1 THz, two tuning stubs with length of D_{ll} and width of W_a are added to the geometry. By adding the tuning stubs, the resistance value is slightly decreased and the frequency is shifted to 1 THz. The reason is that according to transmission line theory, tuning stubs are open stubs; thus, they demonstrate capacitive behaviour in series to capacitance of the antenna.

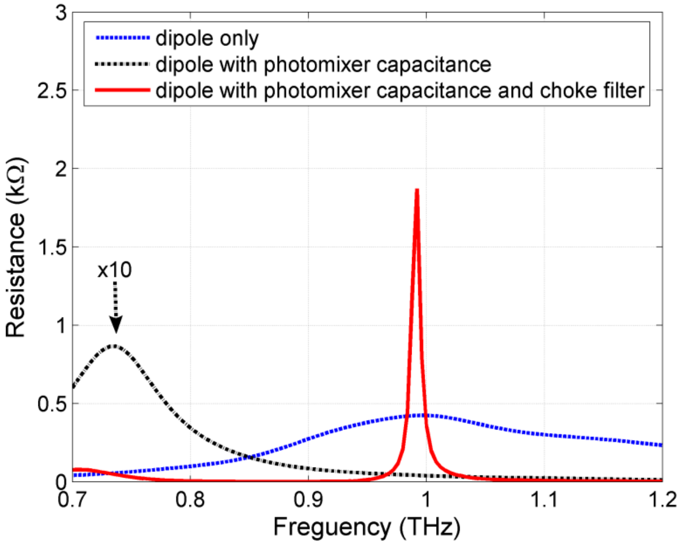

(a)

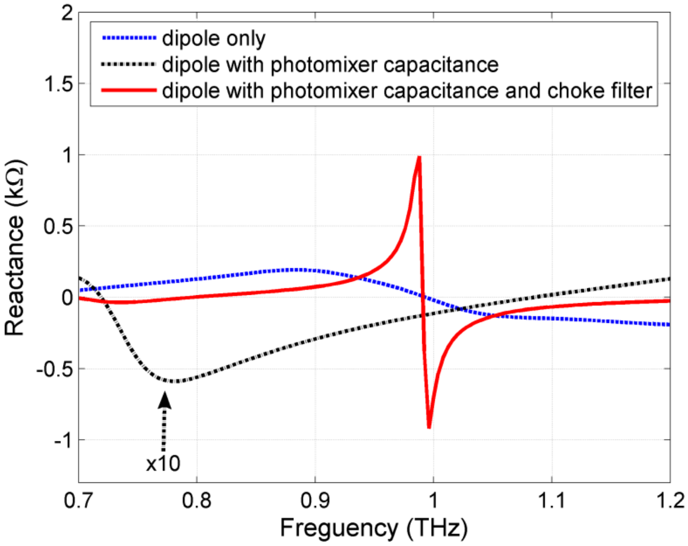

(b)

Fig. 7.9 Impedance of the full wavelength dipole antenna (108 × 2 μm) with and without photomixer capacitance and with choke filter (a) resistance (b) reactance (values of dipole with photomixer capacitance is magnified by a factor of 10)

The matching efficiency of the newly designed antenna (to photoconductive resistance of 196 kΩ) is 5% which has been improved considerably (more than 160 times) as compared to about 0.03% matching efficiency of full wavelength dipole antennas (108 × 2 μm) at 1 THz.

The optimized design parameters of the proposed antenna for the maximum matching efficiency at 1 THz are demonstrated in Table 7.2.

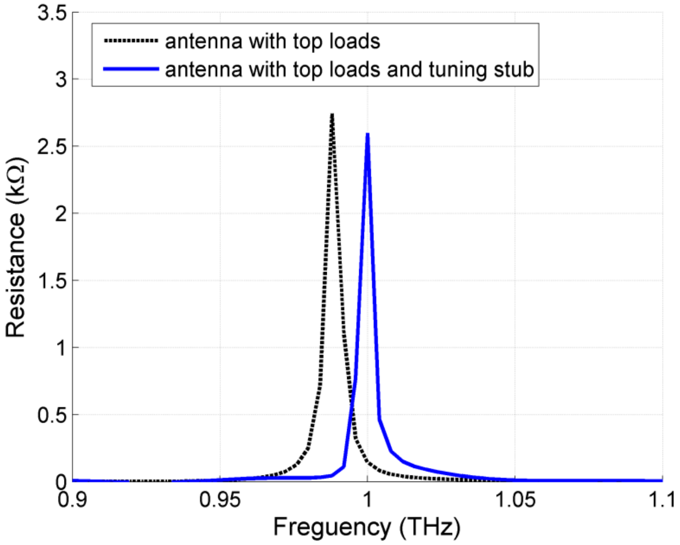

Fig. 7.10 The resistance of the top hat load antenna with and without tuning stub

Table 7.2 Design parameters of the antenna

Parameter	Value (μm)	Parameter	Value (μm)
L_a	47	D_{t3}	8
W	2	D_{t4}	6
L_{sep}	11.5	D_{t5}	4
h	8	L_{ch-l}	26
D_{11}	30	W_{ch-l}	2
D_{t1}	10	L_{ch-h}	26
D_{t2}	10	W_{ch-h}	10
G_t	2		

7.4.3.1. Antenna Parametric Study

In order to gain a better view of the operating principle of this design, a parametric study has been carried out for some fundamental parameters. Through this analysis, the contribution of one parameter at a time (unless stated) on antenna resistance is studied and discussed while other parameters are set to values shown in Table 7.2.

- *Distance of first element of choke filter from the antenna (L_{sep})*

L_{sep} is the connection part of the choke filter with the main body of the antenna. Since the choke filter acts as a bandstop filter at 1 THz, it can be assumed as an open load. Therefore, the impedance of the transmission line with length of L_{sep} may have purely imaginary characteristic and the impedance of it can be written as $Z_{sep} = -jZ_0 \cot(\beta_{THz} L_{sep})$ based on transmission model. Change in L_{sep} varies the impedance which is in parallel to the antenna. The effect of this variation on the antenna resistance is shown in Fig. 7.11a.

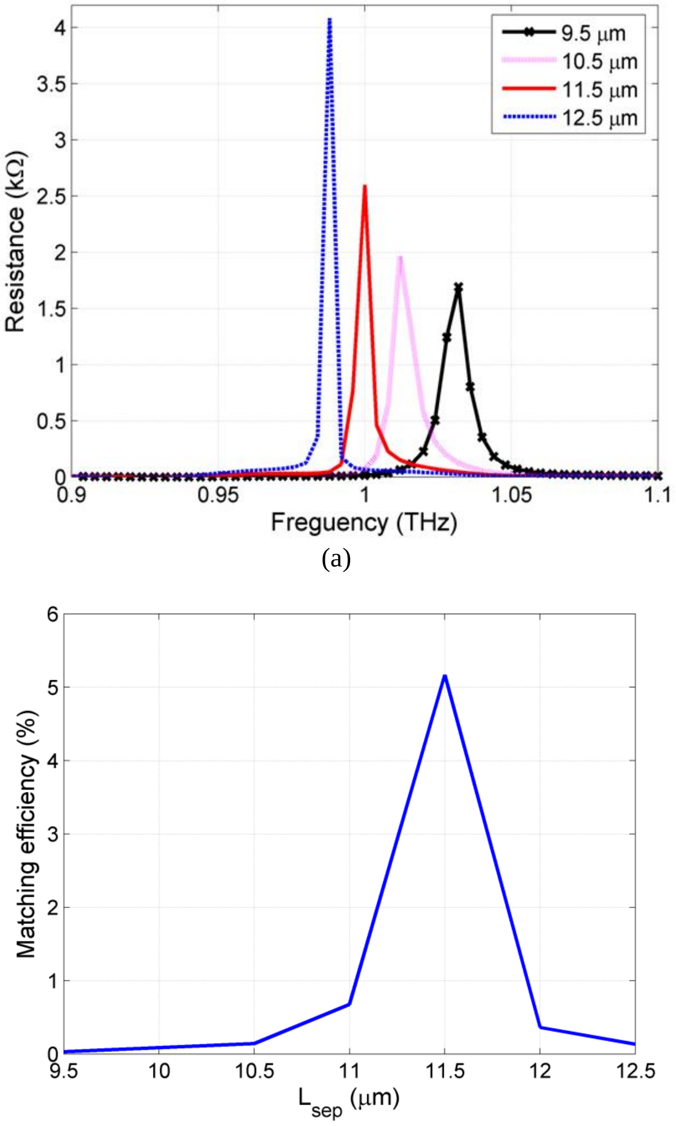

(a)

(b)

Fig. 7.11 (a) Antenna resistance (b) matching efficiency curves for different L_{sep}

It can be observed that by increasing this length, Z_{sep} becomes more capacitive; hence the anti-resonance frequency shifts to lower frequencies. Also, calculation of the matching efficiencies at 1 THz as presented in Fig. 7.11b implies that the best value of the L_{sep} for the maximum matching efficiency is 11.5 μm.

- *Antenna top loads parameters*

Antenna top loads have five parameters and the effects of some of these parameters are stated. By varying only D_{t1} from 10 to 14 μm, no change in the peak frequency is observed and only the peak resistance values are slightly decreased. However, when both D_{t1} and D_{t3} are increased the peak resistance values reaches the maximum value of 2.6 kΩ at 1 THz when D_{t1} and D_{t3} are respectively 10 and 8 μm; but further increment in these parameters leads to resistance reduction and detuning. Matching efficiency in relation to variation of these parameters is illustrated in Fig. 7.12 which shows the optimum values of D_{t1} and D_{t3} for the maximum efficiency respectively.

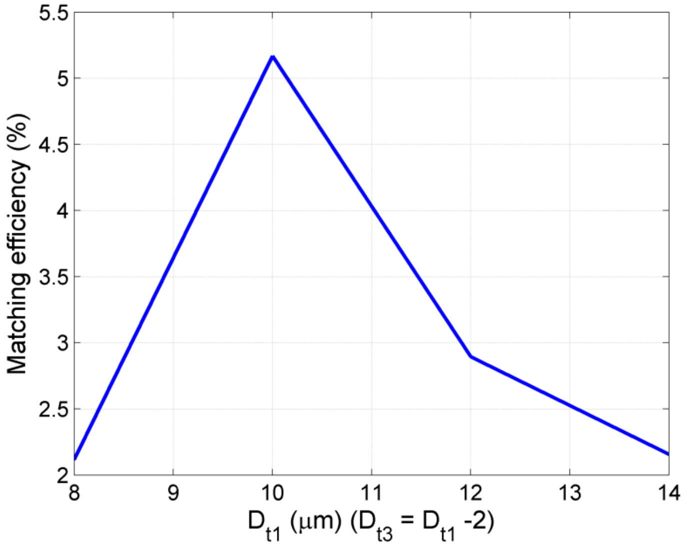

Fig. 7.12 Matching efficiency in relation to different D_{t1} and the corresponding D_{t3}

By varying only D_{t2} from 10 to 16 μm, reduction in peak values of the antenna resistance is viewed. Also by changing both D_{t2} and D_{t4} simultaneously, resistance values reduce. Matching efficiencies for these two cases are compared in Fig. 7.13. It demonstrates that by changing only

D_{t2} or both D_{t2} and D_{t4}, the matching efficiency decreases; however, the trend of this degradation is sharper for the latter case. It is not possible to decrease D_{t2} further, due to physical limitation of the antenna. Thus, D_{t2} = 10 μm and D_{t4} = 6 μm result in the largest matching efficiency.

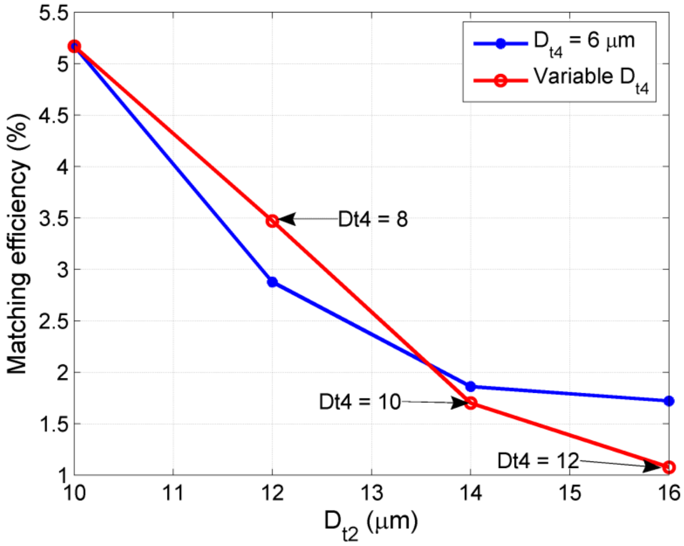

Fig. 7.13 Comparison of matching efficiency variation by changing only D_{t2} and both D_{t2} and D_{t4}

7.4.4. Coupling of THz Wave to Air

The radiation patterns of the proposed antenna on a thin membrane are illustrated in Fig. 7.14. It can be observed that the main pattern direction of the antenna is towards “-x” with the maximum directivity of 3.65 dBi.

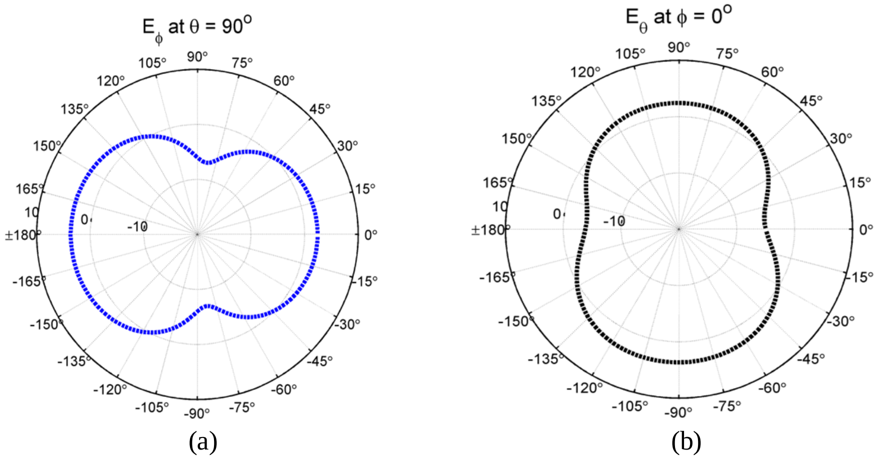

(a) (b)

Fig. 7.14 Radiation pattern of the photomixer THz antenna at 1 THz in (a) xoy plane (b) xoz plane

In order to increase the antenna directivity and have the radiation pattern in broadside towards the desired direction of “-z”, a horn antenna can be used as an appropriate choice. The concept of integrated planar antennas on horn has been used mainly in millimeter-wave and lower end of THz frequencies [248]. In the THz range and for a THz pulsed system, the use of a conical horn with Indium Tin Oxides (ITO) layer at the back of horn for a bowtie antenna was proposed in [249]. Here, this concept is employed for a CW system and the new photomixer antenna. The full geometry of the integrated conical horn antenna on the THz photomixer antenna is shown in Fig. 7.15.

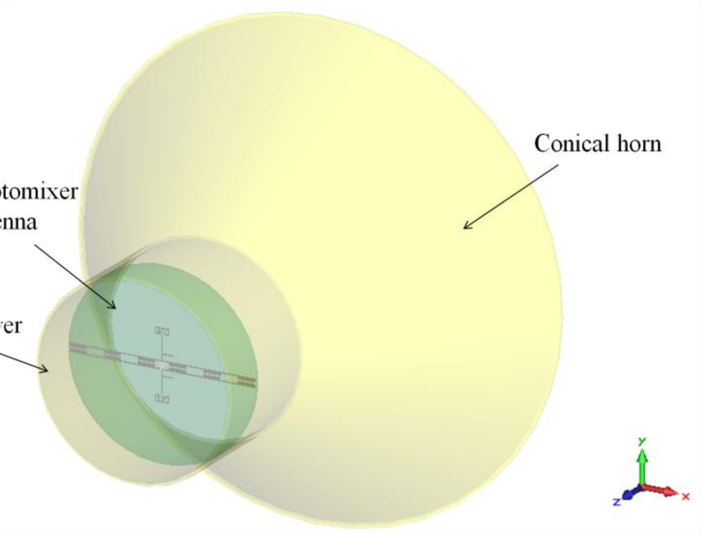

Fig. 7.15 Integrated top loaded THz photomixer antenna in a conical horn. ITO layer is depicted partially transparent in order to see the THz photomixer antenna

The design parameters of a conical horn, as shown schematically in Fig. 7.16, for a desired gain at a specific frequency (λ is the corresponding wavelength in the air) can be derived from [250]:

$$a_i = \frac{3\lambda}{2\pi} \tag{7.7}$$

$$a_0 = \frac{\lambda}{2\pi}\sqrt{10^{(G_{dBi}+2.91)/10}} \tag{7.8}$$

$$R_h = \frac{4a_0^2}{3\lambda} \tag{7.9}$$

$$\theta_h = \arcsin(\frac{a_0}{R_h}) \tag{7.10}$$

$$L_{h1} = \frac{a_0 - a_i}{\tan\theta} \tag{7.11}$$

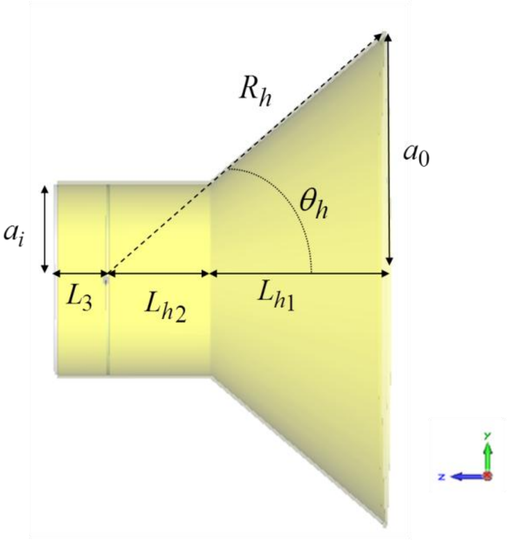

Fig. 7.16 Geometry of the conical horn

By incorporating the horn to the THz photomixer antenna the radiation pattern will be in broadside as shown in Fig. 7.17 (dash line) and the directivity of the antenna enhances to 9.2 dBi with the main lobe in “-z” direction. The radiation pattern at the plane of φ= 90° has symmetrical behaviour; however, in φ= 0° the pattern is asymmetrical in the +z direction. That is because the added tuning stubs are only on one side of the antenna.

As illustrated in Fig. 7.17, radiation towards the unwanted direction (which is “+z”) exists. Therefore, in order to get use of that power the waveguide part of the horn antenna is extended by length of L_3 and a back wall made of ITO is added according to Fig. 7.16. ITO is a material which has interesting optical and electrical characteristics. At frequencies higher than its plasma frequency, ITO exhibits high transmittance [251]. Since the plasma frequency of ITO ($In_{30}Sn_2O_{48}$) is in near infrared (plasma wavelength varies between 769 nm to 1.09 μm depending on Brillouin zone directions [252]) and it is smaller than optical frequencies of laser diodes (wavelength of laser diodes at 800 nm), this layer is transparent to the laser excitation. However, the frequency of the created THz waves is much smaller than plasma frequency; hence, at THz frequencies the ITO layer acts as a reflector.

Another important parameter here is the distance of this ITO wall to the planar antenna. The aim is to have an in-phase reflected continuous THz wave from ITO to sum with the signal generated at the antenna. In order to satisfy this phase requirement the extension length, L_3, should be λ/4. In this simulation, a simplified assumption of modelling the ITO as a perfect electric conductor has been applied. The added design parameters and their values due to implementation of the horn are summarised in Table 7.3.

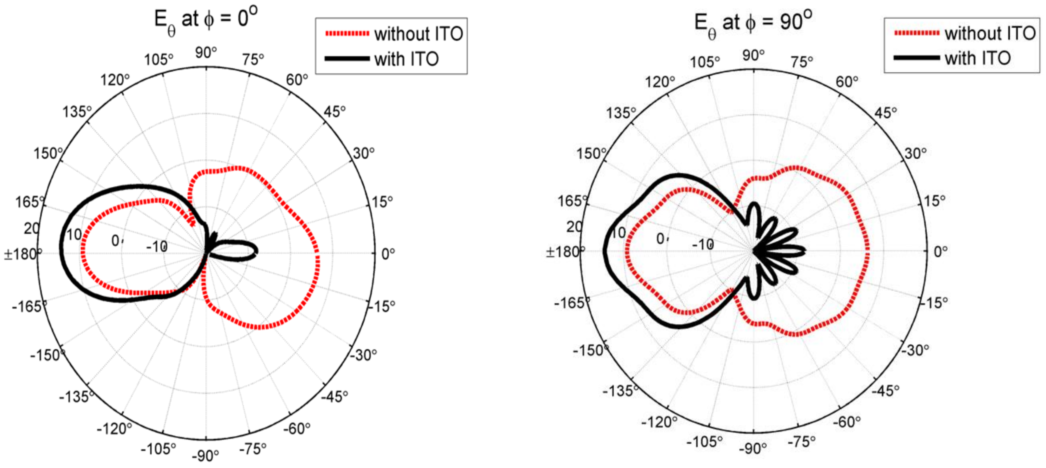

(a)

(b)

Fig. 7.17 (a) 2D radiation pattern of conical antenna integrated with the photomixer THz antenna with and without ITO layer at xoz plane and (b) yoz plane at 1 THz

Table 7.3 Additional design parameters for the conical horn part

Parameter	Value (μm)	Parameter	Value (μm)
a_0	375.5	L_{h2}	116
a_i	150	L_3	75
L_{h1}	315		

The directivity of the new integrated horn antenna with an ITO layer and the THz photomixer antenna increases to 14.3 dBi as shown in Fig. 7.17. This demonstrates a 4 times and 1.5 times improvement respectively compared to the THz photomixer antenna without the conical horn and the antenna with horn but without the ITO layer. The 3D radiation patterns of the completed antenna are depicted in Fig. 7.18. It shows that with this new design the unidirectional antenna pattern in the desirable direction (-z) is achieved. Again, the slight asymmetrical pattern in the electrode side is attributed to the used tuning stubs on one side of the antenna.

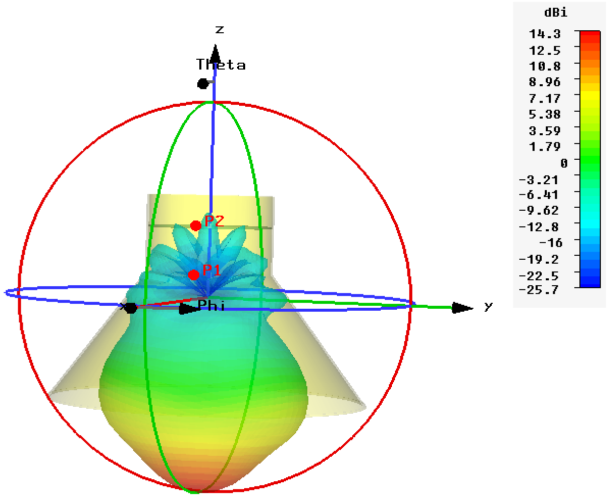

Fig. 7.18 3D radiation pattern of the completed antenna

Another point that needs consideration is the effect of the horn antenna on the matching efficiency of the whole device. By adding the horn and ITO layer to the designed THz photomixer antenna, the anti-resonance frequency is slightly shifted from 1 THz; hence D_{ll} is set to 17.5 μm to tune the antenna peak resistance value to 1 THz. The peak resistance value at 1 THz rises to 5.57 kΩ that is more than twice increment as compared to the peak resistance of the antenna without horn and ITO. Thus, the matching efficiency to the photoconductive resistance of 196 kΩ enhances to 10.7% which is doubled as compared to the case without the horn and ITO layer. Therefore, both directivity and matching efficiency of the new antenna have improved.

7.5. Measurement Results

The next step is the assessment of the performance of the new THz photomixer antenna. The fabrication and measurement of THz antennas are expensive and challenging. Therefore, as categorised in the simulation process of the antenna, it is important to evaluate the contribution of each new part carefully. For this purpose, the adopted procedure is to test the effect of the new photomixer design when it used a common bowtie antenna and a lens. The reason is to ensure that the enhancement is due to the photomixer design because the performance of a bowtie antenna with the lens is well known in the THz area.

The integrated bowtie antenna has the bow angle of 60°, antenna length of 582 µm, and antenna gap length of 10 µm. The three fabricated geometries are a bowtie antenna with the bare gap (no fingers), a bowtie antenna with rectangular tip-to-tip fingers, and a bowtie antenna with trapezoidal tip-to-tip fingers. The photoconductive substrate is the GaAs with thickness of 350 µm and a 0.5-1 µm SiO_2 layer as an antireflection on top of the wafer. The deposited antenna gold layer has 4nm/25nm Ti/Au thickness. The antennas were fabricated by using photolithography and electron-beam lithography for patterning the nano-scale photomixer part. The fabricated and packaged THz antennas are depicted in Fig. 7.19. The microscopic images of the THz bowtie antenna with 6-finger trapezoidal tip-to-tip photomixer are shown in Fig. 7.20.

The measurement is performed in a THz CW system based on fibre (Menlo system) as shown in Fig. 7.21. The excitation laser source is at 800 nm with the total optical power of 30 mW[1]. The devices are evaluated in two cases; once as an emitter and once as a detector. The results are presented and discussed next.

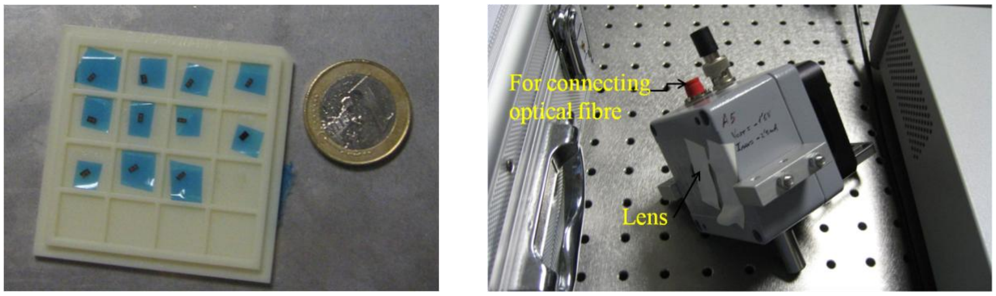

(a) (b)

Fig. 7.19 (a) Fabricated THz bowtie antennas with different photomixer geometries (b) A packaged antenna for the measurement. The black connection is for the biasing purposes when the antenna is employed as an emitter, and it is connected to the lock-in-amplifier when it is positioned in the detector side.

---

[1] The antenna fabrication and measurement have been performed by A. Rivera-Lavado and L. E. Garcia-Muñoz as a collaborative work between the University of Liverpool and the Universidad Carlos III de Madrid.

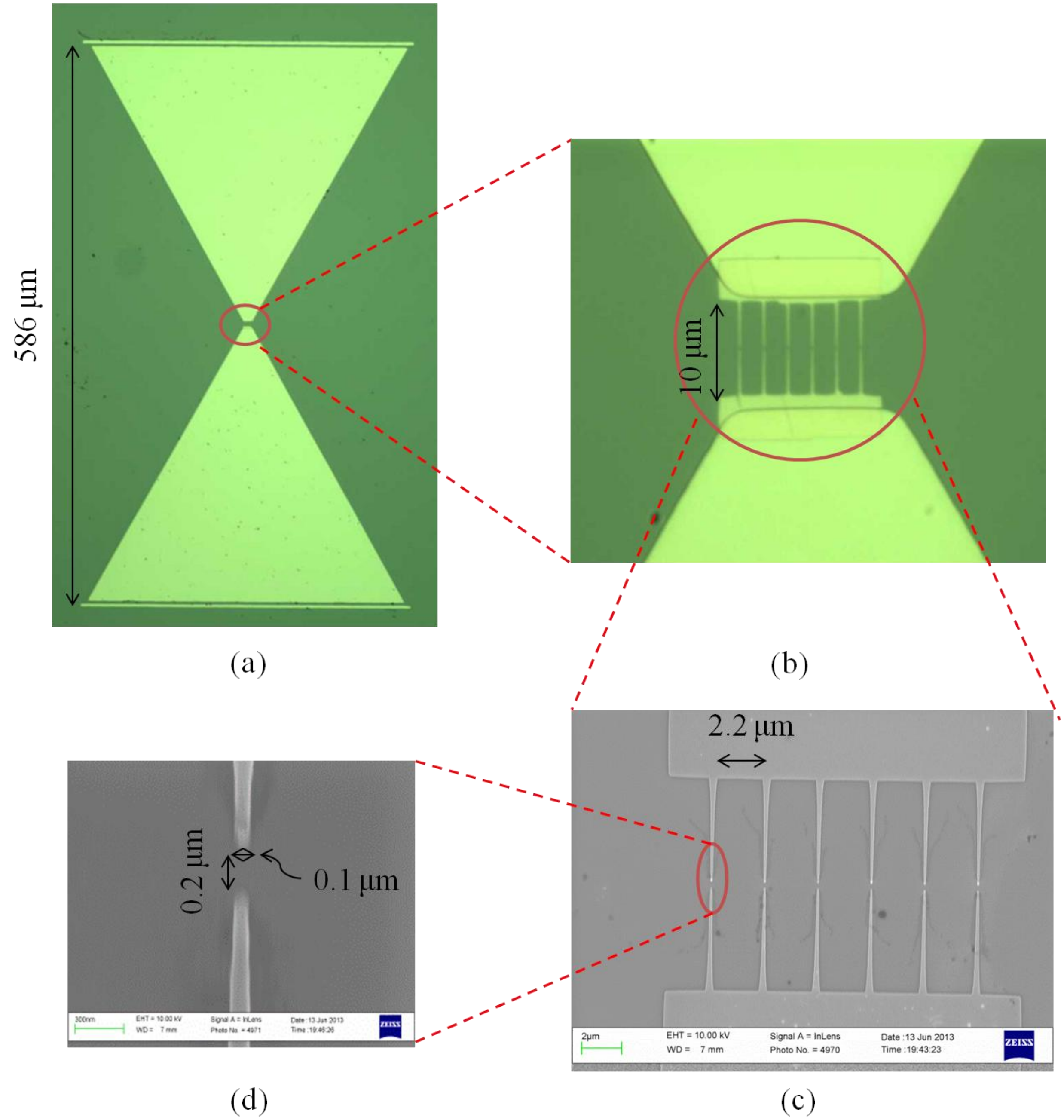

Fig. 7.20 Microscopic images of the THz bowtie antenna with trapezoidal tip-to-tip fingers (a) overall antenna view (b) zoom-in of the photomixer section (c) SEM zoom-in of the trapezoidal tip-to-tip finger (d) SEM zoom-in of a nanogap trapezoidal finger

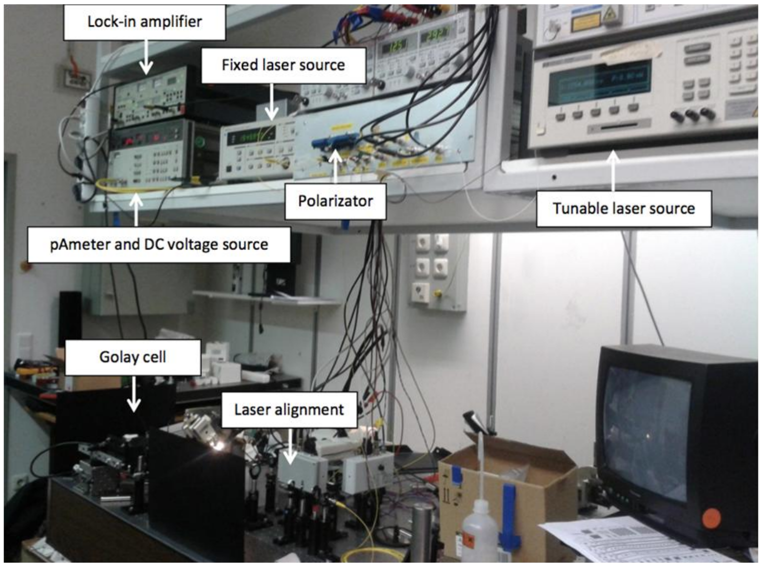

Fig. 7.21 THz CW measurement setup based upon fibre optics

7.5.1. Antenna as the Emitter

First, the antennas are employed as emitters. In this case, the detector is the Golay cell with a diamond window (TYDEX). The schematic image of the measurement setup is depicted in Fig. 7.22. The measurements of devices were performed in identical situations. The finger gap length for the tip-to-tip geometries is 0.2 μm. Therefore, to prevent the voltage breakdown in this nanogap and considering that 30 kV/cm is a commonly accepted breakdown field for devices on LT-GaAs, the applied bias voltage on the antenna is set to 0.6 V.

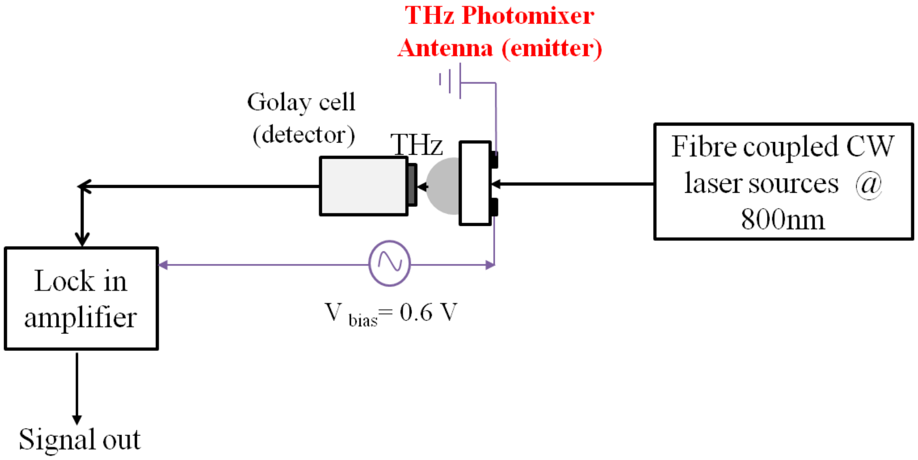

Fig. 7.22 Schematic image of the THz CW measurement setup when the antenna is used as an emitter. In this case, Golay cell was used as the detector.

The measured photocurrent across the antenna for the bare gap is 1.7 μA, for the rectangular fingers is 1.9 μA, and for the trapezoidal fingers is 2.2 μA. The measured dark current is around 30 dB (32 times) smaller than the photocurrent under laser illumination. This illustrates that the device is fabricated well; it has a good heat handling capability, and also it ensures us that the measurement results are due to the devices.

The measured THz power for these three devices is depicted in Fig. 7.23. In this measurement the frequency sweep is achieved by varying the operating temperature of laser sources. It can be observed that the bowtie antenna with trapezoidal tip-to-tip photomixer outperforms the other two devices, and the detected power from it is more than seven times and two times better than the antennas with bare and rectangular tip-to-tip geometries respectively. For instance, the detected THz power at 0.17 THz for trapezoidal is 1.37 μW whilst for the bare gap and rectangular tip-to-tip it is 0.19 and 0.68 μW respectively. In all three geometries as frequency increases the detected THz power decreases. For the trapezoidal structure, the power at 1 THz reduces to 0.081 μW; however, this power is still larger than that of the bare gap and rectangular geometry which are respectively 0.013 μW and 0.042 μW.

In Fig. 7.23, there exist some dips for all three devices as shown by arrows. From the literature, the water absorption frequencies are known (which are at 0.558, 0.753, 0.989, 1.099, 1.115, 1.165 THz [45]). However, in this case, Golay cell has been almost touched the emitter; so, there is not that much of free space and no water absorption is detected at known water vapor absorption frequencies. The dips occurred at different frequencies, especially at lower frequencies are attributed to the resonances in the bias line. The measured spectral THz power in linear scale is shown in Fig. 7.24. In fact, this graph is same as Fig. 7.23 and it illustrates clearer that the peak power occurs at almost 0.17 THz and the bandwidth extends up to about 1.2 THz.

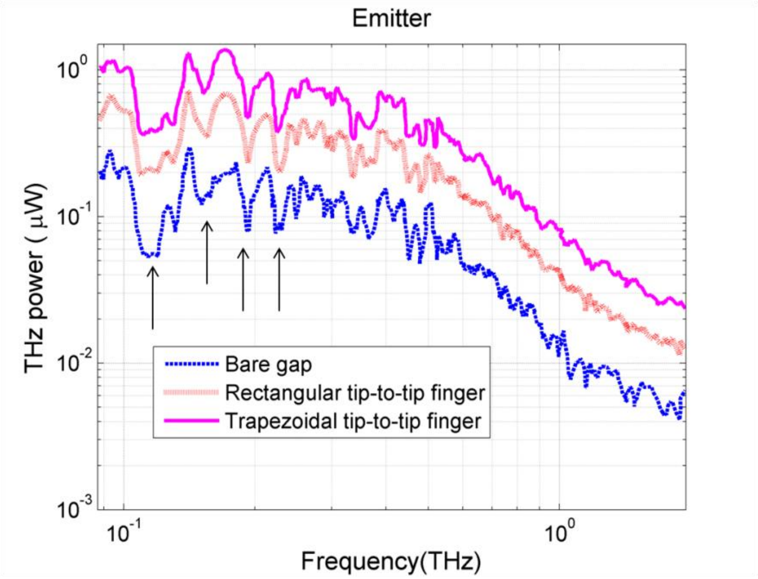

Fig. 7.23 Measured THz power for three various photomixer geometries used in the gap of identical bowtie antennas

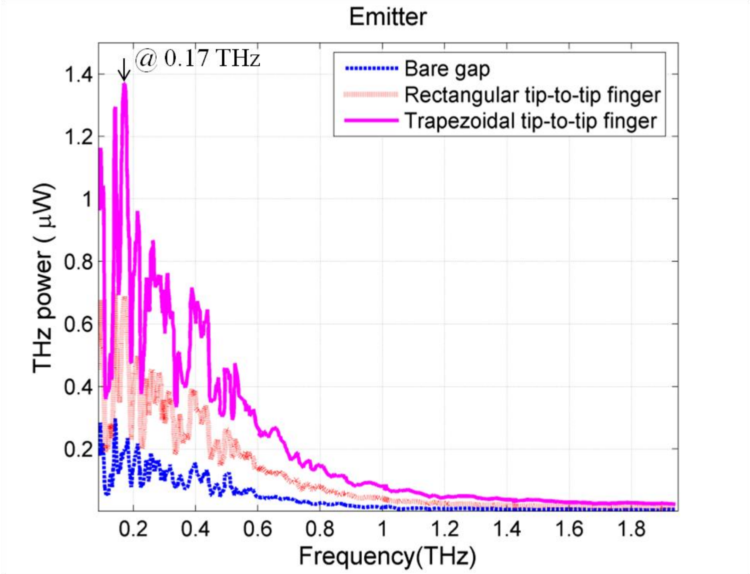

Fig. 7.24 Measured THz power of different photomixer geometries in linear scale

7.5.2. Antenna as the Detector

Second, the antenna is located as a detector and in this case there is no biasing. The schematic image of the detection setup is illustrated in Fig. 7.25a. In this case, the THz emitter is a 3×3 array of broadband log spiral antennas [253] as shown in Fig. 7.25b (other elements of the array antenna are used as dummies) which provides a very directive beam [253].

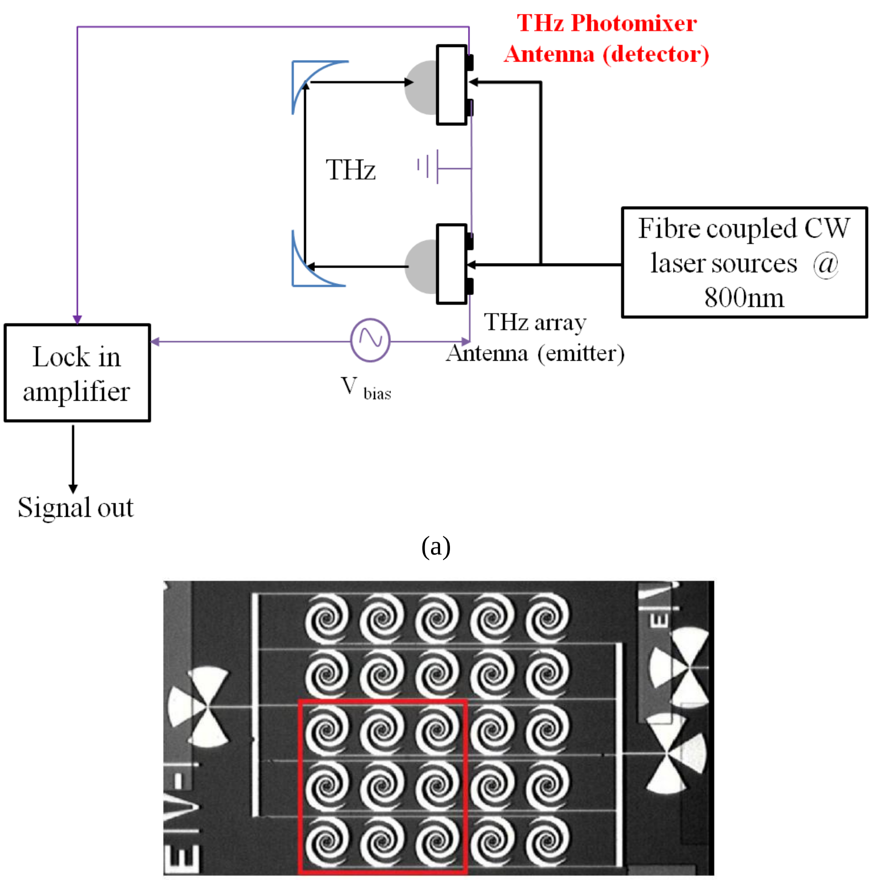

(a)

(b)

Fig. 7.25 (a) Schematic image of the THz CW measurement setup when the antenna under test is employed as the detector (b) The employed log spiral antenna with a p-i-n gap as the emitter [253]

In this case, the measured noise level (when there is no laser illumination) is 0.8×10^{-10} W/ $\sqrt{\text{Hz}}$ .The measurement SNR results as the detectors are illustrated in Fig. 7.26. It can be observed that the antenna with trapezoidal fingers also has a better SNR as compared to the antenna with bare gap and rectangular finger tips. To be more precise, the SNR from the trapezoidal device is more than 15 dB and 10 dB better than that of the bare gap and device with rectangular fingers. This means that the new photomixer antenna can detect lower power signals as compared to the other two conventional designs. Also, the dynamic range of devices is about 30 dB.

In the detector side, effect of water absorption is more evident and as shown by arrows, the reduction at 0.54 and 0.74 are attributed to that as expected from [45]. Also, the observed dips at the lower end of the THz frequency range are attributed to the resonances in the bias lines of the emitter antenna.

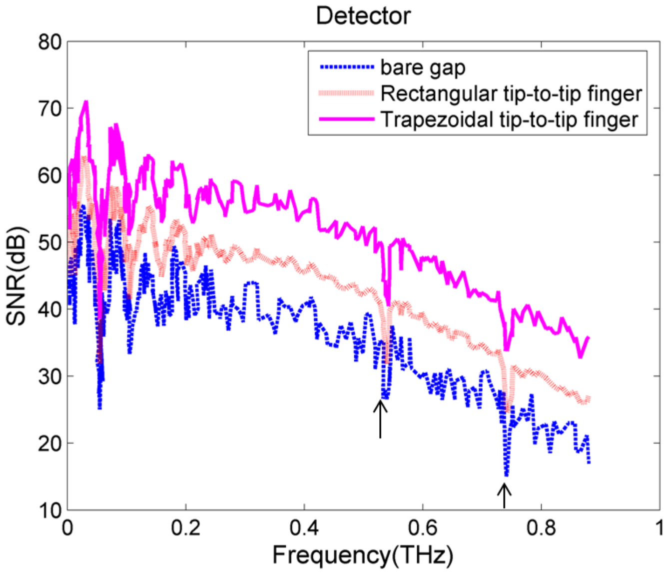

Fig. 7.26 Detected THz signal from three photomixer geometries used in the gap of identical bowtie antennas

7.6. Summary

A top hat loaded antenna with trapezoidal tip-to-tip fingers in the photomixer part integrated with a conical horn was proposed in this chapter. The modular analyses on the generation of the THz field in the photomixer section, the matching issue of the planar antenna and coupling the THz waves to air have been performed. The complete package of the new antenna showed an improved impedance matching with a unidirectional radiation pattern and a good directivity which makes it suitable for line of sight THz systems. In the photomixer part, simulation results demonstrated a reduction in capacitance value and improvement in E-field intensity for the trapezoidal tip-to-tip configuration. This should lead to a larger THz current generated in the antenna gap. Moreover, by introducing a top hat loaded antenna, input resistance of the antenna was increased by a factor of six compared to a full wavelength dipole antenna of the same length. This showed an enhanced impedance matching between the antenna and the photoconductor resistance. This improvement in the matching efficiency leads to a significant augmentation in coupling power from the photomixer to the antenna and THz power radiation. By adding the horn antenna and ITO layer, the directivity of the antenna was enhanced more than a factor of four and the matching efficiency was improved further. Moreover, experimental results confirm the simulation outcomes. Considerable enhancement in the detected THz power and SNR of the signal was achieved when respectively the new photomixer design was employed in the emission and detection side. Therefore, the proposed THz photomixer antenna with trapezoidal tip-to-tip fingers has enhanced performance as compared to the previous designs (*i.e.* THz photomixer with no fingers and THz photomixer with rectangular tip-to-tip fingers).

Chapter 8. Conclusions and Future Work

8.1. Conclusions

The THz technology has been witnessing an unprecedented growth mainly due to attractive and unique characteristics of THz waves as compared to microwave and optical waves. These distinctive characteristics provide opportunities to explore new scientific features, for instance in material spectroscopy, which were not possible previously. In recent years, traditional and bulky THz laboratory measurement setups have evolved into commercial THz imaging and spectroscopy systems which are compact and moveable. THz short-range wireless communication can provide very high data rates which seems to be one of the potential solutions for intensively high bandwidth demand of future. However, several key challenges should be tackled.

One of the main issues is the development of high power and high sensitive THz emitters and detectors. Several existing THz emitters and detectors have been evaluated in Chapter 1, and their output power, performance and working environmental requirement have been discussed. THz antennas are one of the most common types of THz emitters and detectors which are categorized into two groups, *i.e.* the THz photoconductive antenna and the THz photomixer antennas, based upon the kind of optical excitation sources as described in Chapter 2. As compared to the THz solid state components, THz antennas can work at higher THz frequency ranges; in contrast to vacuum tube sources they are smaller in size, and in comparison to QCLs they do not need cryogenic cooling environment. These advantages are added values for THz antennas as compared to other THz sources but similar to others the output power of THz antennas is still very low, and this is the bottleneck for wide uptake of THz technology. How to enhance the performance of such an antenna is therefore a subject of great interest. Thus, the focus of this research has been on how to analyze and design a THz antenna with improved output power and efficiency.

THz antennas based upon the photoconduction, which are considered as optoelectronic devices, have combined both RF/MW and optical techniques for THz wave generation and detection. Hence, they are very different from conventional RF/MW antennas as explained in Chapter 3. These differences are the main reasons that dictate new approaches for the antenna analysis and design. Focusing on these differences, exploring them, and presenting new proposals based upon these differences have been the major targets of this thesis.

One of the main ambiguities in THz antenna analysis (especially in THz photoconductive antennas) has been the reason of the low output power and low efficiency of the antenna. In order to address the problem and answer this key question, a new approach was adopted in Chapter 3. The total efficiency of these devices was divided into three parts; optical-to-electrical efficiency, matching efficiency and radiation efficiency. It was shown that, for both THz antenna types, optical-to-electrical efficiency is the lowest. This means that for a greater THz power, the amount of generated THz photocurrent needs to be enhanced.

Although those approximate analyses provided an insight into the problem of THz antennas, for antenna performance analysis more in-depth investigation was required. Analytical analyses of THz photomixer antennas have been well explained in the literature. However, for THz photoconductive antennas, to distinguish the effect of each parameter on its performance, more detailed analysis and modelling were required. The prerequisite for that modelling was the derivation of accurate source conductance of the antenna.

Source conductance (or 1/resistance) is one of the main differences of THz antennas with conventional RF/MW antennas and that is the result of different antenna excitation and feeding methods. A new equation for the source conductance of a THz photoconductive antenna was obtained in Chapter 4, by considering time-varying photoconductive material response to the laser pulses and antenna gap geometry. A parametric study was conducted to understand the performance of source conductance. Also, the source conductance of the THz photomixer antenna and the THz photoconductive antenna were compared. The difference in excitation schemes of these two types of antennas affects the time variant and time averaged source conductance. Hence, this influences the matching between the antenna and source resistance. Comparison of matching efficiencies showed that matching efficiency in THz photomixer antennas is much lower than that of the THz photoconductive antennas. This highlights necessity of designing THz photomixer antennas with high input resistance.

After calculating the exact source conductance (which is more demonstrative of the reality, based on existing physics theories of THz photoconductive antennas, as compared to the previous approximate equation), a new equivalent circuit model using lumped elements was developed in Chapter 5. In this novel circuit, a time-dependent capacitance and a voltage-controlled source have been incorporated. The time variant capacitance corresponds to accumulation of unpaired free electron holes in the antenna gap and time variant voltage controlled source is related to the reverse bias in relation to the externally employed bias voltage. In this circuit whilst the simplicity of the lumped element approach has been kept, the underlying physical behaviour of the device has been taken into account when calculating the circuit elements. Based upon the model, the influences of various parameters on the optical-to-THz power conversion efficiency and radiated power have been investigated. The simulated results agreed well with published measured results. The model predicted that an increase in the laser power and/or bias voltage, and a reduction in reflections from the air-substrate can improve the optical-to-THz power conversion efficiency of the device. It was observed that by changing the antenna resistance the occurrence of peak efficiency in relation to the input optical power shifts;

however, there was no difference in the peak efficiency values. This novel model is very helpful for both designing a THz photoconductive antenna and adjusting a THz system to obtain the maximized optical-to-THz power conversion efficiency and THz radiated power.

Another difference of THz antennas with RF/MW antennas is on CAD analysis. In Chapter 6, a new simulation procedure was developed for THz photoconductive antennas, which incorporates both optoelectronic and EM behaviours of the antenna. By deriving the excitation signal through the proposed equivalent circuit, entering it to the full-wave EM tool and considering the effect of the detector, the THz emission response of the antenna for various parameters was investigated. The achieved results from this method were validated by measurement results published in the literature, and a good agreement was observed. This approach showed better agreement with the measurement results as compared to the previously presented numerical method. This method also facilitates a more realistic prediction of THz photoconductive antenna performance in a pulsed system before costly fabrication. In addition, in Chapter 6, the effect of substrate thickness was reviewed, and it was shown that the antenna radiated power, guided mode power, and gain have semi-oscillatory behaviour as a function of the substrate electrical thickness increment- that behaviour is due to the creation of more modes.

In THz photomixer antennas as stated earlier, besides increasing the photocurrent in the antenna gap, increasing the antenna resistance for a better impedance matching and reducing the capacitance for high THz power are also required. Therefore, in Chapter 7, a detailed and sequential approach has been explained for improvement in performance of THz photomixer antenna including both the photomixer and the antenna. For this purpose, a novel THz top loaded photomixer antenna was proposed to enhance the THz output power. This antenna consisted of tip-to-tip trapezoidal electrodes in the photomixer part and a full wavelength dipole loaded with planar hat loads embedded on a modified conical horn. The six-finger trapezoidal electrode showed more than twice enhancement in the E-field distribution in the photomixer gap as compared to the rectangular electrode geometry. Considering the effect of the new photomixer configuration on antenna source resistance, a new top loaded antenna with high input resistance and as a result, an enhanced impedance matching was designed. The input resistance of the device was increased more than six times as compared to a full wavelength dipole antenna; which yields an enhanced matching efficiency from 0.03% to 5%. Furthermore, by using a modified conical horn with ITO layer, the directivity of the antenna was augmented by a factor of four and the matching efficiency was augmented to more than 10%. In addition, the THz antenna with the new photomixer design was characterised both as an emitter and detector. According to the measurement results, the emitter antenna with the trapezoidal tip-to-tip fingers demonstrated more than seven and two times improvement in the detected THz power as compared to the antenna with the bare gap and rectangular tip-to-tip finger antenna respectively. When the antennas were employed in the detection side, the measured SNR of the antenna with the trapezoidal fingers was respectively 15 and 10 dB better than the photomixers with the bare gap and rectangular fingers. Therefore, experimental results proved that the new photomixer design has higher THz power and better SNR in comparison to previous designs. In summary, the proposed THz photomixer antenna improves THz output power and SNR in detection due to its improved characteristics which is desired for THz applications.

To sum up, the main contributions of this research are as follows:

- Theoretical establishment of why the THz photoconductive antenna and the THz photomixer antenna are inefficient. The findings of this investigation have been published in [116].
- Derivation of a new equation for the source conductance of a THz photoconductive antenna which is published in [215] and investigation on differences of source conductance of THz photoconductive and photomixer antennas [217].
- Development of a novel equivalent circuit model for performance analysis and optimisation of a THz photoconductive antenna in a THz time domain system as published in [117].

- Development of a new simulation method and procedure for performance analysis of a THz photoconductive antenna by considering both optoelectronic and electromagnetic effects as reported in [236]
- Development of a novel top loaded THz photomixer antenna with trapezoidal fingers in the antenna gap embedded on a modified conical horn. The improvements in the radiated THz power and SNR of the new photomixer have been validated experimentally and the results are under peer review for the publication.

8.2. Future work

Since the first demonstration of the THz antenna by Auston three decades ago, THz technology had been explored by different researchers from various disciplines, and it is still ongoing. Through the many THz related published papers, it is evident that in the recent decade we have already seen a significant advance of this infant technology. To this time, most researchers have focused on physics of THz antennas, *i.e.* properties of suitable photoconductive materials, and applications of THz systems; and considerably less interest has been pointed towards the antennas working based upon photoconduction principle and their role on shaping the detected THz signal. Therefore, it is supposed that there may be more antenna related concepts and designs.

In the modelling of the THz photoconductive antenna through a lumped-element equivalent circuit, it has been assumed that the antenna is frequency independent. Indeed, the presented modelling technique can be employed to a wide range of frequency independent antennas. Investigation and combining the performance of frequency-dependent antennas and including the substrate effects, which are also frequency-dependent, can be a future work. For this purpose from the beginning, the analyses should be started in the frequency domain by considering the frequency spectrum and the phase noise of the exciting lasers. The effect of the substrate may be included through a transmission line model between the source resistance and the antenna resistance. This principle can also be applied for antennas with Graphene substrates as the use of Graphene enables tunable conductivity and reconfigurable radiated power.

In all antenna related simulations, it has been assumed that the laser pulses shine on the antenna perpendicularly. Having a tilted laser can be a further approach for the antenna source conductance and the equivalent circuit analysis.

In the calculation of source resistances, the gap areas were assumed to have rectangular shapes. The effect of various shapes of antenna tips, like tapering, on the source conductance can be another future work path.

For THz antenna analysis, combining optoelectronic and EM simulations is the approach which should be adopted. Comparison of the results from the proposed simulation method by using an optoelectronic tool (e.g. TCAD) instead of analytical calculation can be a further validation of the proposed simulation method.

The subject of THz antennas is still relatively new. There are many design variables even for a “simple” THz dipole antenna. In the real measurement situation, there are many factors that all of them cannot be easily incorporated into the simulation. This may obscure the improvements which come from the partial modified antenna designs. Instead, novel design techniques, such as plasmonics concept, that can enhance the antenna performance at least an order of magnitude as compared to what exists, may suffer less from this issue. Thus, those approaches may be one possible future path in THz antenna design.

References

[1] C. A. Balanis, *Antenna theory : analysis and design*, 3rd ed. Hoboken, NJ: John Wiley, 2005.

[2] Y. Lee, *Principles of terahertz science and technology*, 1st ed. New York, NY: Springer, 2008.

[3] B. Ferguson and X. Zhang, "Materials for terahertz science and technology," *Nat Mater,* vol. 1, pp. 26-33, 2002.

[4] R. Kohler, A. Tredicucci, F. Beltram, H. E. Beere, E. H. Linfield, A. G. Davies, D. A. Ritchie, R. C. Iotti, and F. Rossi, "Terahertz semiconductor-heterostructure laser," *Nature,* vol. 417, pp. 156-159, 2002.

[5] B. S. Williams, "Terahertz quantum-cascade lasers," *Nat Photon,* vol. 1, pp. 517-525, 2007.

[6] C. M. Armstrong, "The truth about terahertz," *IEEE Spectrum,,* vol. 49, pp. 36-41, 2012.

[7] P. R. Smith, D. H. Auston, and M. C. Nuss, "Subpicosecond photoconducting dipole antennas," *IEEE Journal of Quantum Electronics,,* vol. 24, pp. 255-260, 1988.

[8] E. R. Brown, F. W. Smith, and K. A. McIntosh, "Coherent millimeter-wave generation by heterodyne conversion in low-temperature-grown GaAs photoconductors," *Journal of Applied Physics,* vol. 73, pp. 1480-1484, 1993.

[9] J. Faist, F. Capasso, D. L. Sivco, C. Sirtori, A. L. Hutchinson, and A. Y. Cho, "Quantum Cascade Laser," *Science,* vol. 264, pp. 553-556, 1994.

[10] P. H. Siegel, "Terahertz technology," *IEEE Transactions on Microwave Theory and Techniques,* , vol. 50, pp. 910-928, 2002.

[11] M. Tonouchi, "Cutting-edge terahertz technology," *Nat Photon,* vol. 1, pp. 97-105, 2007.

[12] D. M. Pozar, *Microwave engineering*, 4th ed. Hoboken, NJ: Wiley, 2012.

[13] T. W. Crowe, W. L. Bishop, D. W. Porterfield, J. L. Hesler, and R. M. Weikle, II, "Opening the terahertz window with integrated diode circuits," *IEEE Journal of Solid-State Circuits,*, vol. 40, pp. 2104-2110, 2005.

[14] R. J. Trew, "High-frequency solid-state electronic devices," *IEEE Transactions on Electron Devices,* , vol. 52, pp. 638-649, 2005.

[15] H. Eisele, "InP Gunn devices for 400-425 GHz," *Electronics Letters,* vol. 42, pp. 358-359, 2006.

[16] H. Eisele and R. Kamoua, "Submillimeter-wave InP Gunn devices," *IEEE Transactions on Microwave Theory and Techniques,*, vol. 52, pp. 2371-2378, 2004.

[17] N. Orihashi, S. Suzuki, and M. Asada, "One THz harmonic oscillation of resonant tunneling diodes," *Applied Physics Letters,* vol. 87, p. 233501, 2005.

[18] A. Maestrini, J. Bruston, D. Pukala, S. Martin, and I. Mehdi, "Performance of a 1.2 THz frequency tripler using a GaAs frameless membrane monolithic circuit," in *2001 IEEE MTT-S International Microwave Symposium Digest,* , 2001, pp. 1657-1660 vol.3.

[19] J. Tucek, D. Gallagher, K. Kreischer, and R. Mihailovich, "A compact, high power, 0.65 THz source," in *IEEE International Vacuum Electronics Conference, 2008. IVEC 2008.* , pp. 16-17.

[20] A. G. Davies, E. H. Linfield, and M. B. Johnston, "The development of terahertz sources and their applications," *Physics in Medicine and Biology,* vol. 47, p. 3679, 2002.

[21] B. S. Williams, S. Kumar, H. Qing, and J. L. Reno, "High-power terahertz quantum cascade lasers," in *Conference on Lasers and Electro-Optics and Quantum Electronics and Laser Science Conference. CLEO/QELS 2006.* , 2006, pp. 1-2.

[22] S. Kumar, B. S. Williams, S. Kohen, Q. Hu, and J. L. Reno, "Continuous-wave operation of terahertz quantum-cascade lasers above liquid-nitrogen temperature," *Applied Physics Letters,* vol. 84, pp. 2494-2496, 2004.

[23] C. Worrall, J. Alton, M. Houghton, S. Barbieri, H. E. Beere, D. Ritchie, and C. Sirtori,

"Continuous wave operation of a superlattice quantum cascade laser emitting at 2 THz," *Opt. Express*, vol. 14, pp. 171-181, 2006.

[24] C. Walther, M. Fischer, G. Scalari, R. Terazzi, N. Hoyler, and J. Faist, "Quantum cascade lasers operating from 1.2 to 1.6 THz," *Applied Physics Letters*, vol. 91, p. 131122, 2007.

[25] S. Fathololoumi, E. Dupont, C. W. I. Chan, Z. R. Wasilewski, S. R. Laframboise, D. Ban, A. Mátyás, C. Jirauschek, Q. Hu, and H. C. Liu, "Terahertz quantum cascade lasers operating up to about 200 K with optimized oscillator strength and improved injection tunneling," *Opt. Express*, vol. 20, pp. 3866-3876, 2012.

[26] Q. Y. Lu, N. Bandyopadhyay, S. Slivken, Y. Bai, and M. Razeghi, "Room temperature single-mode terahertz sources based on intracavity difference-frequency generation in quantum cascade lasers," *Applied Physics Letters*, vol. 99, p. 131106, 2011.

[27] W. Shi, Y. J. Ding, and P. G. Schunemann, "Coherent terahertz waves based on difference-frequency generation in an annealed zinc–germanium phosphide crystal: improvements on tuning ranges and peak powers," *Optics Communications*, vol. 233, pp. 183-189, 2004.

[28] K. Suizu and K. Kawase, "Monochromatic-Tunable Terahertz-Wave Sources Based on Nonlinear Frequency Conversion Using Lithium Niobate Crystal," *IEEE Journal of Selected Topics in Quantum Electronics*, vol. 14, pp. 295-306, 2008.

[29] W. Shi, Y. J. Ding, N. Fernelius, and K. Vodopyanov, "Efficient, tunable, and coherent 0.18-5.27-THz source based on GaSe crystal," *Opt. Lett.*, vol. 27, pp. 1454-1456, 2002.

[30] E. Nichols and J. Tear, " Joining the infra-red and electric wave spectra," *Astrophysical Journal*, vol. 61, pp. 17-37, 1925.

[31] M. C. Kemp, "Millimetre wave and terahertz technology for the detection of concealed threats: a review," pp. 64020D1-19, 2006.

[32] T. de Graauw, et al, "The Herschel-Heterodyne Instrument for the Far-Infrared (HIFI)," *A&A*, vol. 518, p. L6, 2010.

[33] R. Appleby and H. B. Wallace, "Standoff Detection of Weapons and Contraband in the 100 GHz to 1 THz Region," *IEEE Transactions on Antennas and Propagation,* , vol. 55, pp. 2944-2956, 2007.

[34] P. U. Jepsen, D. G. Cooke, and M. Koch, "Terahertz spectroscopy and imaging – Modern techniques and applications," *Laser & Photonics Reviews,* vol. 5, pp. 124-166, 2011.

[35] D. L. Woolard, R. Brown, M. Pepper, and M. Kemp, "Terahertz Frequency Sensing and Imaging: A Time of Reckoning Future Applications?," *Proceedings of the IEEE,* vol. 93, pp. 1722-1743, 2005.

[36] http://www.teraview.com/.

[37] http://www.picometrix.com/.

[38] http://www.toptica.com/.

[39] http://www.traycer.com/.

[40] B. B. Hu and M. C. Nuss, "Imaging with terahertz waves," *Opt. Lett.,* vol. 20, pp. 1716-1718, 1995.

[41] T. Kleine-Ostmann, P. Knobloch, M. Koch, S. Hoffmann, M. Breede, M. Hofmann, G. Hein, K. Pierz, M. Sperling, and K. Donhuijsen, "Continuous-wave THz imaging," *Electronics Letters,* vol. 37, pp. 1461-1463, 2001.

[42] V. P. Wallace, A. J. Fitzgerald, S. Shankar, N. Flanagan, R. Pye, J. Cluff, and D. D. Arnone, "Terahertz pulsed imaging of basal cell carcinoma ex vivo and in vivo," *British Journal of Dermatology,* vol. 151, pp. 424-432, 2004.

[43] A. J. Fitzgerald, V. P. Wallace, M. Jimenez-Linan, L. Bobrow, R. J. Pye, A. D. Purushotham, and D. D. Arnone, "Terahertz Pulsed Imaging of Human Breast Tumors," *Radiology,* vol. 239, pp. 533-540, 2006.

[44] D. Crawley, C. Longbottom, V. P. Wallace, B. Cole, D. Arnone, and M. Pepper, "Three-dimensional terahertz pulse imaging of dental tissue," *Journal of Biomedical Optics,* vol. 8, pp. 303-307, 2003.

[45] M. v. Exter, C. Fattinger, and D. Grischkowsky, "Terahertz time-domain spectroscopy of water vapor," *Opt. Lett.,* vol. 14, pp. 1128-1130, 1989.

[46] D. F. Plusquellic, K. Siegrist, E. J. Heilweil, and O. Esenturk, "Applications of terahertz spectroscopy in biosystems," *Chemphyschem,* vol. 8, pp. 2412-31, 2007.

[47] K. Fukunaga, Y. Ogawa, S. i. Hayashi, and I. Hosako, "Terahertz spectroscopy for art conservation," *IEICE Electronics Express,* vol. 4, pp. 258-263, 2007.

[48] J. B. Jackson, M. Mourou, J. F. Whitaker, I. N. Duling Iii, S. L. Williamson, M. Menu, and G. A. Mourou, "Terahertz imaging for non-destructive evaluation of mural paintings," *Optics Communications,* vol. 281, pp. 527-532, 2008.

[49] A. J. L. Adam, P. C. M. Planken, S. Meloni, and J. Dik, "TeraHertz imaging of hidden paintlayers on canvas," *Opt. Express,* vol. 17, pp. 3407-3416, 2009.

[50] N. Krumbholz, T. Hochrein, N. Vieweg, T. Hasek, K. Kretschmer, M. Bastian, M. Mikulics, and M. Koch, "Monitoring polymeric compounding processes inline with THz time-domain spectroscopy," *Polymer Testing,* vol. 28, pp. 30-35, 2009.

[51] Y. C. Shen, "Terahertz pulsed spectroscopy and imaging for pharmaceutical applications: a review," *Int J Pharm,* vol. 417, pp. 48-60, 2011.

[52] J. A. Zeitler and Y. Shen, *Terahertz Spectroscopy and Imaging*. Berlin Heidelberg: Springer 2013.

[53] Y. C. Shen, T. Lo, P. F. Taday, B. E. Cole, W. R. Tribe, and M. C. Kemp, "Detection and identification of explosives using terahertz pulsed spectroscopic imaging," *Applied Physics Letters,* vol. 86, p. 241116, 2005.

[54] Y. Shen, P. F. Taday, and M. C. Kemp, "Terahertz spectroscopy of explosive materials," *Proceedings of SPIE,* vol. 5619, pp. 82-89, 2004.

[55] K. Kawase, Y. Ogawa, Y. Watanabe, and H. Inoue, "Non-destructive terahertz imaging of illicit drugs using spectral fingerprints," *Opt. Express,* vol. 11, pp. 2549-2554, 2003.

[56] P. Mousavi, F. Haran, D. Jez, F. Santosa, and J. S. Dodge, "Simultaneous composition

and thickness measurement of paper using terahertz time-domain spectroscopy," *Appl. Opt.,* vol. 48, pp. 6541-6546, 2009.

[57] D. Banerjee, W. von Spiegel, M. D. Thomson, S. Schabel, and H. G. Roskos, "Diagnosing water content in paper by terahertz radiation," *Opt. Express,* vol. 16, pp. 9060-9066, 2008.

[58] J. Federici and L. Moeller, "Review of terahertz and subterahertz wireless communications," *Journal of Applied Physics,* vol. 107, p. 111101, 2010.

[59] D. Saeedkia, *Handbook of terahertz technology for imaging, sensing and communications*. Cambridge , UK: Woodhead, 2013.

[60] T. Kleine-Ostmann, K. Pierz, G. Hein, P. Dawson, and M. Koch, "Audio signal transmission over THz communication channel using semiconductor modulator," *Electronics Letters,* vol. 40, pp. 124-126, 2004.

[61] T. Liu, G. Lin, Y. Chang, and C. Pan, "Wireless audio and burst communication link with directly modulated THz photoconductive antenna," *Opt. Express,* vol. 13, pp. 10416-10423, 2005.

[62] T. M. Korter and D. F. Plusquellic, "Continuous-wave terahertz spectroscopy of biotin: vibrational anharmonicity in the far-infrared," *Chemical Physics Letters,* vol. 385, pp. 45-51, 2004.

[63] W. Zhang, E. R. Brown, M. Rahman, and M. L. Norton, "Observation of terahertz absorption signatures in microliter DNA solutions," *Applied Physics Letters*, vol. 102, p. 023701, 2013.

[64] F. Hindle, A. Cuisset, R. Bocquet, and G. Mouret, "Continuous-wave terahertz by photomixing: applications to gas phase pollutant detection and quantification," *Comptes Rendus Physique,* vol. 9, pp. 262-275, 2008.

[65] I. S. Gregory, W. R. Tribe, C. Baker, B. E. Cole, M. J. Evans, L. Spencer, M. Pepper, and M. Missous, "Continuous-wave terahertz system with a 60 dB dynamic range," *Applied*

Physics Letters, vol. 86, p. 204104, 2005.

[66] J. Karsten, H. Quast, R. Leonhardt, T. Loffler, M. Thomson, T. Bauer, H. G. Roskos, and S. Czasch, "Continuous-wave all-optoelectronic terahertz imaging," *Applied Physics Letters,* vol. 80, pp. 3003-3005, 2002.

[67] R. Wilk, F. Breitfeld, M. Mikulics, and M. Koch, "Continuous wave terahertz spectrometer as a noncontact thickness measuring device," *Appl. Opt.,* vol. 47, pp. 3023-3026, 2008.

[68] D. H. Auston, K. P. Cheung, and P. R. Smith, "Picosecond photoconducting Hertzian dipoles," *Applied Physics Letters,* vol. 45, pp. 284-286, 1984.

[69] M. Tani, S. Matsuura, K. Sakai, and S.-i. Nakashima, "Emission characteristics of photoconductive antennas based on low-temperature-grown GaAs and semi-insulating GaAs," *Appl. Opt.,* vol. 36, pp. 7853-7859, 1997.

[70] http://www.synopsys.com.

[71] R. Huber, A. Brodschelm, F. Tauser, and A. Leitenstorfer, "Generation and field-resolved detection of femtosecond electromagnetic pulses tunable up to 41 THz," *Applied Physics Letters,* vol. 76, pp. 3191-3193, 2000.

[72] Y. C. Shen, P. C. Upadhya, H. E. Beere, E. H. Linfield, A. G. Davies, I. S. Gregory, C. Baker, W. R. Tribe, and M. J. Evans, "Generation and detection of ultrabroadband terahertz radiation using photoconductive emitters and receivers," *Applied Physics Letters,* vol. 85, pp. 164-166, 2004.

[73] E. R. Brown, "THz Generation by Photomixing in Ultrafast Photoconductors," *International Journal of High Speed Electronics and Systems,* vol. 13, pp. 497-545, 2003.

[74] D. H. Auston, "Picosecond optoelectronic switching and gating in silicon," *Applied Physics Letters,* vol. 26, pp. 101-103, 1975.

[75] J. T. Darrow, Z. Xi-Cheng, D. H. Auston, and J. D. Morse, "Saturation properties of large-aperture photoconducting antennas," *IEEE Journal of Quantum Electronics,,* vol.

28, pp. 1607-1616, 1992.

[76] M. R. Stone, M. Naftaly, R. E. Miles, J. R. Fletcher, and D. P. Steenson, "Electrical and radiation characteristics of semilarge photoconductive terahertz emitters," *IEEE Transactions on Microwave Theory and Techniques,* , vol. 52, pp. 2420-2429, 2004.

[77] G. Zhao, R. N. Schouten, N. v. d. Valk, W. T. Wenckebach, and P. C. M. Planken, "Design and performance of a THz emission and detection setup based on a semi-insulating GaAs emitter," *Review of Scientific Instruments,* vol. 73, pp. 1715-1719, 2002.

[78] P. U. Jepsen, R. H. Jacobsen, and S. R. Keiding, "Generation and detection of terahertz pulses from biased semiconductor antennas," *J. Opt. Soc. Am. B,* vol. 13, pp. 2424-2436, 1996.

[79] Y. Cai, I. Brener, J. Lopata, J. Wynn, L. Pfeiffer, and J. Federici, "Design and performance of singular electric field terahertz photoconducting antennas," *Applied Physics Letters,* vol. 71, pp. 2076-2078, 1997.

[80] K. Sakai, *Terahertz optoelectronics*, 1st ed. Berlin: Springer 2005.

[81] J. Colinge and C. A. Colinge, *Physics of semiconductor devices*. Boston: Kluwer Academic Publishers, 2002.

[82] Z. Piao, M. Tani, and K. Sakai, "Carrier Dynamics and Terahertz Radiation in Photoconductive Antennas," *Jpn. J. Appl. Phys.*, vol. 39, pp. 96-100, 2000.

[83] S. D. Brorson, J. Zhang, and S. R. Keiding, "Ultrafast carrier trapping and slow recombination in ion-bombarded silicon on sapphire measured via THz spectroscopy," *Applied Physics Letters*, vol. 64, pp. 2385-2387, 1994.

[84] P. K. Benicewicz, J. P. Roberts, and A. J. Taylor, "Scaling of terahertz radiation from large-aperture biased photoconductors," *J. Opt. Soc. Am. B,* vol. 11, pp. 2533-2546, 1994.

[85] L. Duvillaret, F. Garet, J. F. Roux, and J. L. Coutaz, "Analytical modeling and optimization of terahertz time-domain spectroscopy experiments, using photoswitches as antennas," *IEEE Journal of Selected Topics in Quantum Electronics,* vol. 7, pp. 615-623,

2001.

[86] S. Kono, M. Tani, P. Gu, and K. Sakai, "Detection of up to 20 THz with a low-temperature-grown GaAs photoconductive antenna gated with 15 fs light pulses," *Applied Physics Letters,* vol. 77, pp. 4104-4106, 2000.

[87] F. W. Smith, H. Q. Le, V. Diadiuk, M. A. Hollis, A. R. Calawa, S. Gupta, M. Frankel, D. R. Dykaar, G. A. Mourou, and T. Y. Hsiang, "Picosecond GaAs-based photoconductive optoelectronic detectors," *Applied Physics Letters,* vol. 54, pp. 890-892, 1989.

[88] S. Park, M. R. Melloch, and A. M. Weiner, "Analysis of terahertz waveforms measured by photoconductive and electrooptic sampling," *IEEE Journal of Quantum Electronics, ,* vol. 35, pp. 810-819, 1999.

[89] Y. Cai, I. Brener, J. Lopata, J. Wynn, L. Pfeiffer, J. B. Stark, Q. Wu, X. C. Zhang, and J. F. Federici, "Coherent terahertz radiation detection: Direct comparison between free-space electro-optic sampling and antenna detection," *Applied Physics Letters,* vol. 73, pp. 444-446, 1998.

[90] Y. Gao, M. Chen, S. Yin, P. Ruffin, C. Brantley, and E. Edwards, "Terahertz enhancement from terahertz-radiation-assisted large aperture photoconductive antenna," *Journal of Applied Physics,* vol. 109, p. 033108, 2011.

[91] N. Khiabani, Y. Huang, and Y. C. Shen, "Comparison of ultra-wideband THz generation and detection systems," in *Proceedings of the 5th European Conference on Antennas and Propagation (EUCAP), ,* 2011, pp. 457-461.

[92] Q. Wu and X. C. Zhang, "Free-space electro-optics sampling of mid-infrared pulses," *Applied Physics Letters,* vol. 71, pp. 1285-1286, 1997.

[93] Y. C. Shen, P. C. Upadhya, E. H. Linfield, H. E. Beere, and A. G. Davies, "Ultrabroadband terahertz radiation from low-temperature-grown GaAs photoconductive emitters," *Applied Physics Letters,* vol. 83, pp. 3117-3119, 2003.

[94] S. Kono, M. Tani, and K. Sakai, "Ultrabroadband photoconductive detection:

Comparison with free-space electro-optic sampling," *Applied Physics Letters*, vol. 79, pp. 898-900, 2001.

[95] M. Tani, M. Nakajima, S. Kono, and K. Sakai, "Generation of ultrabroadband terahertz radiation with a photoconductive emitter," in *The 15th Annual Meeting of the IEEE Lasers and Electro-Optics Society, 2002. LEOS 2002.* , 2002, pp. 532-533 vol.2.

[96] T. Liu, M. Tani, M. Nakajima, M. Hangyo, and C. Pan, "Ultrabroadband terahertz field detection by photoconductive antennas based on multi-energy arsenic-ion-implanted GaAs and semi-insulating GaAs," *Applied Physics Letters*, vol. 83, pp. 1322-1324, 2003.

[97] M. Scheller and M. Koch, "Terahertz quasi time domain spectroscopy," *Opt. Express*, vol. 17, pp. 17723-17733, 2009.

[98] S. Verghese, K. A. McIntosh, S. Calawa, W. F. Dinatale, E. K. Duerr, and K. A. Molvar, "Generation and detection of coherent terahertz waves using two photomixers," *Applied Physics Letters*, vol. 73, pp. 3824-3826, 1998.

[99] S. Matsuura, M. Tani, and K. Sakai, "Generation of coherent terahertz radiation by photomixing in dipole photoconductive antennas," *Applied Physics Letters*, vol. 70, pp. 559-561, 1997.

[100] R. Mendis, C. Sydlo, J. Sigmund, M. Feiginov, P. Meissner, and H. L. Hartnagel, "Tunable CW-THz system with a log-periodic photoconductive emitter," *Solid-State Electronics*, vol. 48, pp. 2041-2045, 2004.

[101] G. Mouret, S. Matton, R. Bocquet, F. Hindle, E. Peytavit, J. F. Lampin, and D. Lippens, "Far-infrared cw difference-frequency generation using vertically integrated and planar low temperature grown GaAs photomixers: application to H2S rotational spectrum up to 3THz," *Applied Physics B*, vol. 79, pp. 725-729, 2004.

[102] http://www.toptica.com/uploads/media/toptica_BR_SC_TDL_04.pdf.

[103] K. Nicholas, Z. Hua, X. Jingzhou, I. L. Kuang, H. Jenn-Shyong, and X. C. Zhang, "Comparison between pulsed terahertz time-domain imaging and continuous wave

terahertz imaging," *Semiconductor Science and Technology*, vol. 20, p. S293, 2005.

[104] http://www.newport.com/.

[105] http://www.femtolasers.com/.

[106] http://www.tme.eu/en/.

[107] X. C. Zhang, B. B. Hu, J. T. Darrow, and D. H. Auston, "Generation of femtosecond electromagnetic pulses from semiconductor surfaces," *Applied Physics Letters,* vol. 56, pp. 1011-1013, 1990.

[108] M. Johnston, D. Whittaker, A. Corchia, A. Davies, and E. Linfield, "Simulation of terahertz generation at semiconductor surfaces," *Physical Review B,* vol. 65, 2002.

[109] C. Weiss, R. Wallenstein, and R. Beigang, "Magnetic-field-enhanced generation of terahertz radiation in semiconductor surfaces," *Applied Physics Letters,* vol. 77, pp. 4160-4162, 2000.

[110] M. B. Johnston, D. M. Whittaker, A. Corchia, A. G. Davies, and E. H. Linfield, "Theory of magnetic-field enhancement of surface-field terahertz emission," *Journal of Applied Physics,* vol. 91, pp. 2104-2106, 2002.

[111] I. S. Gregory, C. Baker, W. R. Tribe, I. V. Bradley, M. J. Evans, E. H. Linfield, A. G. Davies, and M. Missous, "Optimization of photomixers and antennas for continuous-wave terahertz emission," *IEEE Journal of Quantum Electronics,*, vol. 41, pp. 717-728, 2005.

[112] http://www.menlosystems.com/products/?families=77.

[113] http://www.tetechs.com/.

[114] http://www.toptica.com/products/terahertz_generation/fs_packages/photoconductive_switches.html.

[115] http://www.thorlabs.co.uk/newgrouppage9.cfm?objectgroup_id=4716.

[116] Y. Huang, N. Khiabani, S. Shen, and L. Di, "Terahertz photoconductive antenna

efficiency," in *2011 International Workshop on Antenna Technology (iWAT),* , 2011, pp. 152-156.

[117] N. Khiabani, Y. Huang, Y. Shen, and S. Boyes, "Theoretical Modeling of a Photoconductive Antenna in a Terahertz Pulsed System," *IEEE Transactions on Antennas and Propagation,* , vol. PP, pp. 1-1, 2013.

[118] F. Ellrich, T. Weinland, D. Molter, J. Jonuscheit, and R. Beigang, "Compact fiber-coupled terahertz spectroscopy system pumped at 800 nm wavelength," *Review of Scientific Instruments,* vol. 82, p. 053102, 2011.

[119] B. Sartorius, H. Roehle, H. Künzel, J. Böttcher, M. Schlak, D. Stanze, H. Venghaus, and M. Schell, "All-fiber terahertz time-domain spectrometer operating at 1.5 um telecom wavelengths," *Opt. Express,* vol. 16, pp. 9565-9570, 2008.

[120] S. Han, H. Ko, N. Kim, H. Ryu, C. Wook Lee, Y. Ahn Leem, D. Lee, M. Yong Jeon, S. Kyu Noh, H. Sook Chun, and K. Hyun Park, "Optical fiber-coupled InGaAs-based terahertz time-domain spectroscopy system," *Opt. Lett.,* vol. 36, pp. 3094-3096, 2011.

[121] D. Singh, C. Kalialakis, P. Gardner, and P. S. Hall, "Small H-shaped antennas for MMIC applications," *IEEE Transactions on Antennas and Propagation,* , vol. 48, pp. 1134-1141, 2000.

[122] S. Gupta, J. F. Whitaker, and G. A. Mourou, "Ultrafast carrier dynamics in III-V semiconductors grown by molecular-beam epitaxy at very low substrate temperatures," *IEEE Journal of Quantum Electronics,* , vol. 28, pp. 2464-2472, 1992.

[123] S. Gupta, M. Y. Frankel, J. A. Valdmanis, J. F. Whitaker, G. A. Mourou, F. W. Smith, and A. R. Calawa, "Subpicosecond carrier lifetime in GaAs grown by molecular beam epitaxy at low temperatures," *Applied Physics Letters,* vol. 59, pp. 3276-3278, 1991.

[124] M. Martin and E. R. Brown, "Critical comparison of GaAs and InGaAs THz photoconductors," *Proc. of SPIE,* vol. 8261, pp. 826102-826102, 2012.

[125] I. Kostakis, D. Saeedkia, and M. Missous, "Characterization of low temperature InGaAs-

InAlAs semiconductor photo mixers at 1.55 mu wavelength illumination for terahertz generation and detection," *Journal of Applied Physics,* vol. 111, p. 103105, 2012.

[126] C. Baker, I. S. Gregory, W. R. Tribe, I. V. Bradley, M. J. Evans, E. H. Linfield, and M. Missous, "Highly resistive annealed low-temperature-grown InGaAs with sub-500 fs carrier lifetimes," *Applied Physics Letters,* vol. 85, pp. 4965-4967, 2004.

[127] S. M. Sze and K. K. Ng, *Physics of semiconductor devices,* 3rd ed. Hoboken, N.J.: Wiley-Interscience, 2007.

[128] Z. D. Taylor, E. R. Brown, J. E. Bjarnason, M. P. Hanson, and A. C. Gossard, "Resonant-optical-cavity photoconductive switch with 0.5% conversion efficiency and 1.0W peak power," *Opt. Lett.,* vol. 31, pp. 1729-1731, 2006.

[129] L. Hrivank, "Semi-insulating GaAs," *Czech. J. Phys. B,* vol. 34, pp. 436-444, 1984.

[130] A. W. Jackson, J. P. Ibbetson, A. C. Gossard, and U. K. Mishra, "Reduced thermal conductivity in low-temperature-grown GaAs," *Applied Physics Letters,* vol. 74, pp. 2325-2327, 1999.

[131] I. S. Gregory, C. Baker, W. R. Tribe, M. J. Evans, H. E. Beere, E. H. Linfield, A. G. Davies, and M. Missous, "High resistivity annealed low-temperature GaAs with 100 fs lifetimes," *Applied Physics Letters,* vol. 83, pp. 4199-4201, 2003.

[132] J. K. Luo, H. Thomas, D. V. Morgan, D. Westwood, and R. H. Williams, "The electrical breakdown properties of GaAs layers grown by molecular beam epitaxy at low temperature," *Semiconductor Science and Technology,* vol. 9, p. 2199, 1994.

[133] R. Yano, Y. Hirayama, S. Miyashita, H. Sasabu, N. Uesugi, and S. Uehara, "Pump–probe spectroscopy of low-temperature grown GaAs for carrier lifetime estimation: arsenic pressure dependence of carrier lifetime during MBE crystal growth," *Physics Letters A,* vol. 289, pp. 93-98, 2001.

[134] M. Missous, "Stoichiometric low temperature (SLT) GaAs and AlGaAs grown by molecular beam epitaxy," *Microelectronics Journal,* vol. 27, pp. 393-409, 1996.

[135] H. Nemec, A. Pashkin, P. Kuzel, M. Khazan, S. Schnull, and I. Wilke, "Carrier dynamics in low-temperature grown GaAs studied by terahertz emission spectroscopy," *Journal of Applied Physics,* vol. 90, pp. 1303-1306, 2001.

[136] A. Krotkus, R. Viselga, K. Bertulis, V. Jasutis, S. Marcinkevicius, and U. Olin, "Subpicosecond carrier lifetimes in GaAs grown by molecular beam epitaxy at low substrate temperature," *Applied Physics Letters,* vol. 66, pp. 1939-1941, 1995.

[137] M. Tani and e. al, "Spectroscopic characterization of Low-temperature- Grown GaAs epitaxial films," *Jpn. J. Appl. Phys.,* vol. 33, pp. 4807-4811, 1994.

[138] P. A. Loukakos, C. Kalpouzos, I. E. Perakis, Z. Hatzopoulos, M. Logaki, and C. Fotakis, "Ultrafast electron trapping times in low-temperature-grown gallium arsenide: The effect of the arsenic precipitate spacing and size," *Applied Physics Letters,* vol. 79, pp. 2883-2885, 2001.

[139] J. E. Bjarnason, T. L. J. Chan, A. W. M. Lee, E. R. Brown, D. C. Driscoll, M. Hanson, A. C. Gossard, and R. E. Muller, "ErAs:GaAs photomixer with two-decade tunability and 12 mu W peak output power," *Applied Physics Letters,* vol. 85, pp. 3983-3985, 2004.

[140] C. Kadowa and e. al, "Self-assembled ErAs islands in GaAs for THz applications," *Physica E* vol. 7, pp. 97-100, 2000.

[141] C. Berry and M. Jarrahi, "Terahertz generation using plasmonic photoconductive gratings," *New Journal of Physics,* vol. 14, p. 105029, 2012.

[142] M. Suzuki and M. Tonouchi, "Fe-implanted InGaAs photoconductive terahertz detectors triggered by 1.56 mu m femtosecond optical pulses," *Applied Physics Letters,* vol. 86, p. 163504, 2005.

[143] C. D. Wood, O. Hatem, J. E. Cunningham, E. H. Linfield, A. G. Davies, P. J. Cannard, M. J. Robertson, and D. G. Moodie, "Terahertz emission from metal-organic chemical vapor deposition grown Fe:InGaAs using 830 nm to 1.55 mu m excitation," *Applied Physics Letters,* vol. 96, p. 194104, 2010.

[144] M. Sukhotin, E. R. Brown, D. Driscoll, M. Hanson, and A. C. Gossard, "Picosecond photocarrier-lifetime in ErAs:InGaAs at 1.55 mu " *Applied Physics Letters,* vol. 83, pp. 3921-3923, 2003.

[145] J. Mangeney and P. Crozat, "Ion-irradiated In0.53Ga0.47As photoconductive antennas for THz generation and detection at 1.55 μm wavelength," *Comptes Rendus Physique,* vol. 9, pp. 142-152, 2008.

[146] A. Takazato, M. Kamakura, T. Matsui, J. Kitagawa, and Y. Kadoya, "Terahertz wave emission and detection using photoconductive antennas made on low-temperature-grown InGaAs with 1.56 mu m pulse excitation," *Applied Physics Letters,* vol. 91, p. 011102, 2007.

[147] R. Stibal, J. Windscheif, and W. Jantz, "Contactless evaluation of semi-insulating GaAs wafer resistivity using the time-dependent charge measurement," *Semiconductor Science and Technology,* vol. 6, p. 995, 1991.

[148] M. C. Beard, G. M. Turner, and C. A. Schmuttenmaer, "Subpicosecond carrier dynamics in low-temperature grown GaAs as measured by time-resolved terahertz spectroscopy," *Journal of Applied Physics,* vol. 90, pp. 5915-5923, 2001.

[149] S. J. Jo and e. al, "Carrier dynamics of low-temperature-grown In0.53Ga0.47As on GaAs using an InGaAlAs metamorphic buffer," *Applied Phyasics Letter,* vol. 86, p. 111903, 2005.

[150] N. Vieweg, M. Mikulics, M. Scheller, K. Ezdi, R. Wilk, H. W. Hübers, and M. Koch, "Impact of the contact metallization on the performance of photoconductive THz antennas," *Opt. Express,* vol. 16, pp. 19695-19705, 2008.

[151] M. Tamagnone, J. S. Gomez-Diaz, J. R. Mosig, and J. Perruisseau-Carrier, "Analysis and design of terahertz antennas based on plasmonic resonant graphene sheets," *Journal of Applied Physics,* vol. 112, p. 114915, 2012.

[152] I. Llatser, C. Kremers, A. Cabellos-Aparicio, J. M. Jornet, E. Alarcón, and D. N. Chigrin,

"Graphene-based nano-patch antenna for terahertz radiation," *Photonics and Nanostructures - Fundamentals and Applications*, vol. 10, pp. 353-358, 2012.

[153] A. K. Geim and K. S. Novoselov, "The rise of graphene," *Nat Mater*, vol. 6, pp. 183-191, 2007.

[154] M. Dragoman, A. A. Muller, D. Dragoman, F. Coccetti, and R. Plana, "Terahertz antenna based on graphene," *Journal of Applied Physics*, vol. 107, p. 104313, 2010.

[155] B. Heshmat, H. Pahlevaninezhad, T. E. Darcie, and C. Papadopoulos, "Evaluation of carbon nanotubes for THz photomixing," in *2010 IEEE Radar Conference*, , 2010, pp. 1176-1179.

[156] M. Tamagnone, J. S. Gómez-Díaz, J. R. Mosig, and J. Perruisseau-Carrier, "Reconfigurable terahertz plasmonic antenna concept using a graphene stack," *Applied Physics Letters*, vol. 101, p. 214102, 2012.

[157] B. B. Hu, A. S. Weling, D. H. Auston, A. V. Kuznetsov, and C. J. Stanton, "dc-electric-field dependence of THz radiation induced by femtosecond optical excitation of bulk GaAs," *Physical Review B*, vol. 49, pp. 2234-2237, 1994.

[158] J. Klier, S. Wohnsiedler, W. Zouaghi, E. Peytavit, J. Lampin, J. Jonuscheit, and R. Beigang, "Far-field THz radiation pattern from photoconductive emitters on different substrates," in *36th International Conference on Infrared, Millimeter and Terahertz Waves (IRMMW-THz), 2011* 2011, pp. 1-2.

[159] J. Van Rudd and D. M. Mittleman, "Influence of substrate-lens design in terahertz time-domain spectroscopy," *J. Opt. Soc. Am. B*, vol. 19, pp. 319-329, 2002.

[160] C. W. Berry, N. Wang, M. R. Hashemi, M. Unlu, and M. Jarrahi, "Significant performance enhancement in photoconductive terahertz optoelectronics by incorporating plasmonic contact electrodes," *Nat Commun*, vol. 4, p. 1622, 2013.

[161] P. N. Butcher and D. Cotter, *The elements of nonlinear optics*. Cambridge ; New York: Cambridge University Press, 1990.

[162] E. Peytavit, S. Lepilliet, F. Hindle, C. Coinon, T. Akalin, G. Ducournau, G. Mouret, and J.-F. Lampin, "Milliwatt-level output power in the sub-terahertz range generated by photomixing in a GaAs photoconductor," *Applied Physics Letters,* vol. 99, p. 223508, 2011.

[163] V. Pacebutas, A. Biciunas, S. Balakauskas, A. Krotkus, G. Andriukaitis, D. Lorenc, A. Pugzlys, and A. Baltuska, "Terahertz time-domain-spectroscopy system based on femtosecond Yb:fiber laser and GaBiAs photoconducting components," *Applied Physics Letters,* vol. 97, p. 031111, 2010.

[164] G. Matthaus, S. Nolte, R. Hohmuth, M. Voitsch, W. Richter, B. Pradarutti, S. Riehemann, G. Notni, and A. Tunnermann, "Microlens coupled interdigital photoconductive switch," *Applied Physics Letters,* vol. 93, p. 091110, 2008.

[165] H. Roehle, R. J. B. Dietz, H. J. Hensel, J. Böttcher, H. Künzel, D. Stanze, M. Schell, and B. Sartorius, "Next generation 1.5 µm terahertz antennas: mesa-structuring of InGaAs/InAlAs photoconductive layers," *Opt. Express,* vol. 18, pp. 2296-2301, 2010.

[166] S. Preu, G. H. Döhler, S. Malzer, L. J. Wang, and A. C. Gossard, "Tunable, continuous-wave Terahertz photomixer sources and applications," *Journal of Applied Physics,* vol. 109, p. 061301, 2011.

[167] M. Beck, H. Schäfer, G. Klatt, J. Demsar, S. Winnerl, M. Helm, and T. Dekorsy, "Impulsive terahertz radiation with high electric fields from an amplifier-driven large-area photoconductive antenna," *Opt. Express,* vol. 18, pp. 9251-9257, 2010.

[168] M. Jarrahi and T. H. Lee, "High-power tunable terahertz generation based on photoconductive antenna arrays," in *IEEE MTT-S International Microwave Symposium Digest,* , 2008, pp. 391-394.

[169] E. A. Michael, B. Vowinkel, R. Schieder, M. Mikulics, M. Marso, and P. Kordos, "Large-area traveling-wave photonic mixers for increased continuous terahertz power," *Applied Physics Letters,* vol. 86, p. 111120, 2005.

[170] A. Eshaghi, M. Shahabadi, and L. Chrostowski, "Radiation characteristics of large-area photomixer used for generation of CW THz radiation," *J. Opt. Soc. Am. B,* vol. 29, pp. 813-817, 2012.

[171] M. Mikulics, M. Marso, M. Lepsa, D. Grutzmacher, and P. Kordos, "Output Power Improvement in MSM Photomixers by Modified Finger Contacts Configuration," *IEEE Photonics Technology Letters,,* vol. 21, pp. 146-148, 2009.

[172] P. Kordoš, M. Marso, and M. Mikulics, "Performance optimization of GaAs-based photomixers as sources of THz radiation," *Applied Physics A,* vol. 87, pp. 563-567, 2007.

[173] E. Peytavit, A. Beck, T. Akalin, J.-F. Lampin, F. Hindle, C. Yang, and G. Mouret, "Continuous terahertz-wave generation using a monolithically integrated horn antenna," *Applied Physics Letters,* vol. 93, p. 111108, 2008.

[174] C. e. Zah, R. C. Compton, and D. B. Rutledge, "Efficiencies of Elementary Integrated-Circuit Feed Antennas," *Electromagnetics,* vol. 3, pp. 239-254, 1983.

[175] K. Ezdi, M. N. Islam, Y. A. N. Reddy, C. Jördens, A. Enders, and M. Koch, "A numerical study of photoconductive dipole antennas: the real emission frequency and an improved antenna design," *Proceeding of SPIE,* vol. 6194, pp. 61940G-61940G, 2006.

[176] D. Mittleman, *Sensing with terahertz radiation*. Berlin ; New York: Springer, 2003.

[177] R. H. Kingston, *Detection of optical and infrared radiation*. Berlin ; New York: Springer-Verlag, 1978.

[178] N. Khiabani, Y. Huang, and Y.-C. Shen, "Discussions on the main parameters of THz photoconductive antennas as emitters," in *Proceedings of the 5th European Conference on Antennas and Propagation (EUCAP),* , 2011, pp. 462-466.

[179] S. B. Qadri, D. H. Wu, B. D. Graber, N. A. Mahadik, and A. Garzarella, "Failure mechanism of THz GaAs photoconductive antenna," *Applied Physics Letters,* vol. 101, p. 011910, 2012.

[180] D. S. Kim and D. S. Citrin, "Enhancement of terahertz radiation from photoconductors by

elliptically focused excitation," *Applied Physics Letters,* vol. 87, p. 061108, 2005.

[181] J. H. Kim, A. Polley, and S. E. Ralph, "Efficient photoconductive terahertz source using line excitation," *Opt. Lett.,* vol. 30, pp. 2490-2492, 2005.

[182] T. Ackemann, M. Alduraibi, S. Campbell, S. Keatings, P. L. Sam, H. Fraser, A. S. Arnold, E. Riis, and M. Missous, "Diamond heat sinking of terahertz antennas for continuous-wave photomixing," *Journal of Applied Physics,* vol. 112, p. 123109, 2012.

[183] W. Shi, L. Hou, Z. Liu, and T. Tongue, "THz generation from SI-GaAs stripline antenna with different structural parameters," *J. Opt. Soc. Am. B,* vol. 26, pp. 107-112, 2009.

[184] I. Brener, D. Dykaar, A. Frommer, L. N. Pfeiffer, J. Lopata, J. Wynn, K. West, and M. C. Nuss, "Terahertz emission from electric field singularities in biased semiconductors," *Opt. Lett.,* vol. 21, pp. 1924-1926, 1996.

[185] S. E. Ralph and D. Grischkowsky, "Trap-enhanced electric fields in semi-insulators: The role of electrical and optical carrier injection," *Applied Physics Letters,* vol. 59, pp. 1972-1974, 1991.

[186] P. C. Upadhya, W. Fan, A. Burnett, J. Cunningham, A. G. Davies, E. H. Linfield, J. Lloyd-Hughes, E. Castro-Camus, M. B. Johnston, and H. Beere, "Excitation-density-dependent generation of broadband terahertz radiation in an asymmetrically excited photoconductive antenna," *Opt. Lett.,* vol. 32, pp. 2297-2299, 2007.

[187] W. Shi, L. Hou, and X. Wang, "High effective terahertz radiation from semi-insulating-GaAs photoconductive antennas with ohmic contact electrodes," *Journal of Applied Physics,* vol. 110, p. 023111, 2011.

[188] A. Dreyhaupt, S. Winnerl, T. Dekorsy, and M. Helm, "High-intensity terahertz radiation from a microstructured large-area photoconductor," *Applied Physics Letters,* vol. 86, p. 121114, 2005.

[189] M. Awad, M. Nagel, H. Kurz, J. Herfort, and K. Ploog, "Characterization of low temperature GaAs antenna array terahertz emitters," *Applied Physics Letters,* vol. 91, p.

181124, 2007.

[190] X. Ropagnol, R. Morandotti, T. Ozaki, and M. Reid, "THz pulse shaping and improved optical-to-THz conversion efficiency using a binary phase mask," *Opt. Lett.,* vol. 36, pp. 2662-2664, 2011.

[191] H. Tanoto, J. H. Teng, Q. Y. Wu, M. Sun, Z. N. Chen, S. A. Maier, WangB, C. C. Chum, G. Y. Si, A. J. Danner, and S. J. Chua, "Greatly enhanced continuous-wave terahertz emission by nano-electrodes in a photoconductive photomixer," *Nat Photon,* vol. 6, pp. 121-126, 2012.

[192] F. Miyamaru, Y. Saito, K. Yamamoto, T. Furuya, S. Nishizawa, and M. Tani, "Dependence of emission of terahertz radiation on geometrical parameters of dipole photoconductive antennas," *Applied Physics Letters,* vol. 96, p. 211104, 2010.

[193] R. Faulks, M. Evans, H. Page, S. Malik, I. Gregory, I. Farrer, D. Ritchie, and M. Pepper, "Enhanced Terahertz Receiver Using a Distributed Bragg Reflector Coupled to a Photoconductive Antenna," *IEEE Photonics Technology Letters, ,* vol. 21, pp. 1603-1605, 2009.

[194] S. Park, K. H. Jin, M. Yi, J. C. Ye, J. Ahn, and K. Jeong, "Enhancement of Terahertz Pulse Emission by Optical Nanoantenna," *ACS Nano,* vol. 6, pp. 2026-2031, 2012/03/27 2012.

[195] S. Park, Y. Choi, Y. Oh, and K. Jeong, "Terahertz photoconductive antenna with metal nanoislands," *Opt. Express*, vol. 20, pp. 25530-25535, 2012.

[196] J. Požela and A. Reklaitis, "Electron transport properties in GaAs at high electric fields," *Solid-State Electronics*, vol. 23, pp. 927-933, 1980.

[197] T. W. Ebbesen, H. J. Lezec, H. F. Ghaemi, T. Thio, and P. A. Wolff, "Extraordinary optical transmission through sub-wavelength hole arrays," *Nature*, vol. 391, pp. 667-669, 1998.

[198] W. L. Barnes, A. Dereux, and T. W. Ebbesen, "Surface plasmon subwavelength optics,"

Nature, vol. 424, pp. 824-830, 2003.

[199] B. Heshmat, H. Pahlevaninezhad, Y. Pang, M. Masnadi-Shirazi, R. Burton Lewis, T. Tiedje, R. Gordon, and T. E. Darcie, "Nanoplasmonic Terahertz Photoconductive Switch on GaAs," *Nano Letters,* vol. 12, pp. 6255-6259, 2012.

[200] S. M. Duffy, S. Verghese, A. McIntosh, A. Jackson, A. C. Gossard, and S. Matsuura, "Accurate modeling of dual dipole and slot elements used with photomixers for coherent terahertz output power," *IEEE Transactions on Microwave Theory and Techniques,* , vol. 49, pp. 1032-1038, 2001.

[201] I. Woo, T. K. Nguyen, H. Han, H. Lim, and I. Park, "Four-leaf-clover-shaped antenna for a THz photomixer," *Opt. Express,* vol. 18, pp. 18532-18542, 2010.

[202] K. Han, T. K. Nguyen, I. Park, and H. Han, "Terahertz Yagi-Uda Antenna for High Input Resistance," *Journal of Infrared, Millimeter, and Terahertz Waves,* 2009.

[203] D. B. Rutledge, D. P. Niekirk, and D. P. Kasilingam, "Integrated circuit antennas," *Infrared and Millimeter-Waves Series,* vol. 11, New York: Academic, 1983.

[204] P. U. Jepsen and S. R. Keiding, "Radiation patterns from lens-coupled terahertz antennas," *Opt. Lett.,* vol. 20, pp. 807-809, 1995.

[205] E. Peytavit, J. F. Lampin, T. Akalin, and L. Desplanque, "Integrated terahertz TEM horn antenna," *Electronics Letters,* vol. 43, pp. 73-75, 2007.

[206] S. Liu, X. Shou, and A. Nahata, "Coherent Detection of Multiband Terahertz Radiation Using a Surface Plasmon-Polariton Based Photoconductive Antenna," *IEEE Transactions on Terahertz Science and Technology,* , vol. 1, pp. 412-415, 2011.

[207] P. Maraghechi and A. Y. Elezzabi, "Enhanced THz radiation emission from plasmonic complementary Sierpinski fractal emitters," *Opt. Express,* vol. 18, pp. 27336-27345, 2010.

[208] P. Maraghechi and A. Y. Elezzabi, "Fractal Structures for THz Radiation Emitters," *EEE Journal of Selected Topics in Quantum Electronics, I,* vol. 19, pp. 8400310-8400310,

2013.

[209] J. B. Pendry, L. Martín-Moreno, and F. J. Garcia-Vidal, "Mimicking Surface Plasmons with Structured Surfaces," *Science*, vol. 305, pp. 847-848, August 6, 2004 2004.

[210] E. Castro-Camus, J. Lloyd-Hughes, M. B. Johnston, M. D. Fraser, H. H. Tan, and C. Jagadish, "Polarization-sensitive terahertz detection by multicontact photoconductive receivers," *Applied Physics Letters,* vol. 86, p. 254102, 2005.

[211] M. Tani, Y. Hirota, C. Que, S. Tanaka, R. Hattori, M. Yamaguchi, S. Nishizawa, and M. Hangyo, "Novel Terahertz Photoconductive Antennas," *International Journal of Infrared and Millimeter Waves,* vol. 27, pp. 531-546, 2006/04/01 2006.

[212] F. Miyamaru, Y. Saito, M. W. Takeda, L. Liu, B. Hou, W. Wen, and P. Sheng, "Emission of terahertz radiations from fractal antennas," *Applied Physics Letters,* vol. 95, p. 221111, 2009.

[213] P. F. Goldsmith, *Quasioptical systems : Gaussian beam quasioptical propagation and applications*. Piscataway, NJ: IEEE Press, 1998.

[214] S. Hughes, M. Tani, and K. Sakai, "Vector analysis of terahertz transients generated by photoconductive antennas in near- and far-field regimes," *Journal of Applied Physics*, vol. 93, p. 4880, 2003.

[215] N. Khiabani, Y. Huang, Y. Shen, and S. Boyes, "Time variant source resistance in the THz photoconductive antenna," in *Antennas and Propagation Conference (LAPC), 2011 Loughborough*, 2011, pp. 1-3.

[216] R. Wilk, K. Ezdi, M. Mikulics, and M. Koch, "Emission Spectra of Photoconductive Dipole Antennas: Pulsed vs. Photomixing Operation," in *Joint 31st International Conference on Infrared Millimeter Waves and 14th International Conference on Teraherz Electronics, 2006. IRMMW-THz 2006.* , 2006, pp. 380-380.

[217] N. Khiabani, Y. Huang, Y. Shen, and S. Boyes, "THz photoconductive antennas in pulsed systems and CW systems," in *Antenna Technology (iWAT), 2012 IEEE International*

Workshop on, 2012, pp. 181-184.

[218] J. Y. Suen, W. Li, Z. D. Taylor, and E. R. Brown, "Characterization and modeling of a terahertz photoconductive switch," *Applied Physics Letters,* vol. 96, p. 141103, 2010.

[219] G. C. Loata, M. D. Thomson, T. Loffler, and H. G. Roskos, "Radiation field screening in photoconductive antennae studied via pulsed terahertz emission spectroscopy," *Applied Physics Letters,* vol. 91, p. 232506, 2007.

[220] S. Rihani, R. Faulks, H. Beere, H. Page, I. Gregory, M. Evans, D. A. Ritchie, and M. Pepper, "Effect of defect saturation on terahertz emission and detection properties of low temperature GaAs photoconductive switches," *Applied Physics Letters,* vol. 95, p. 051106, 2009.

[221] D. S. Kim and D. S. Citrin, "Coulomb and radiation screening in photoconductive terahertz sources," *Applied Physics Letters,* vol. 88, p. 161117, 2006.

[222] D. H. Auston, "Impulse response of photoconductors in transmission lines," *IEEE Journal of Quantum Electronics, ,* vol. 19, pp. 639-648, 1983.

[223] J. F. Holzman, F. E. Vermeulen, and A. Y. Elezzabi, "Ultrafast photoconductive self-switching of subpicosecond electrical pulses," *IEEE Journal of Quantum Electronics, ,* vol. 36, pp. 130-136, 2000.

[224] B. Heshmat, H. Pahlevaninezhad, M. C. Beard, C. Papadopoulos, and T. E. Darcie, "Single-walled carbon nanotubes as base material for THz photoconductive switching: a theoretical study from input power to output THz emission," *Opt. Express*, vol. 19, pp. 15077-15089, 2011.

[225] G. C. Loata, "Investigation of low-temperature-grown GaAs photoconductive antennae for continuous-wave and pulsed terahertz generation," PhD thesis, Goethe-University, Frankfurt am Main, 2007.

[226] N. Engheta, C. H. Papas, and C. Elachi, "Radiation patterns of interfacial dipole antennas," *Radio Science,* vol. 17, pp. 1557-1566, 1982.

[227] N. G. Alexopoulos, P. B. Katehi, and D. B. Rutledge, "Substrate Optimization for Integrated Circuit Antennas," *IEEE Transactions on Microwave Theory and Techniques,* , vol. 31, pp. 550-557, 1983.

[228] D. M. Pozar, "Considerations for millimeter wave printed antennas," *IEEE Transactions on Antennas and Propagation,* , vol. 31, pp. 740-747, 1983.

[229] C. A. Balanis, *Advanced engineering electromagnetics*. New York: Wiley, 1989.

[230] H. Kogelnik, *Theory of dielectric waveguide*. New York: in Integrated optics, T. Tamir, ed., Springer-Verlag,, 1975.

[231] A. Shahvarpour, A. Alvarez Melcon, and C. Caloz, "Radiation Efficiency Issues in Planar Antennas on Electrically Thick Substrates and Solutions," *IEEE Transactions on Antennas and Propagation,,* vol. 61, pp. 4013-4025, 2013.

[232] http://www.cst.com/.

[233] S. Hughes, M. Tani, and K. Sakai, "Vector analysis of terahertz transients generated by photoconductive antennas in near- and far-field regimes," *Journal of Applied Physics,* vol. 93, pp. 4880-4884, 2003.

[234] P. U. Jepsen, R. H. Jacobsen, and S. R. Keiding, "Generation and detection of terahertz pulses from biased semiconductor antennas," *J. Opt. Soc. Am. B,* vol. 13, pp. 2424-2436, 1996.

[235] K. Ezdi, B. Heinen, C. Jordens, N. Vieweg, N. Krumbholz, R. Wilk, M. Mikulics, and M. Koch, "A hybrid time-domain model for pulsed terahertz dipole antennas," *Journal of the European Optical Society*, vol. 4, p. 09001, 2009.

[236] N. Khiabani, Y. Huang, Y. Shen, S. Boyes, and Q. Xu, "A novel simulation method for THz photoconductive antenna characterization," in *Antennas and Propagation (EuCAP), 2013 7th European Conference on,* 2013, pp. 751-754.

[237] M. Tani, K. Yamamoto, E. Estacio, C. Que, H. Nakajima, M. Hibi, F. Miyamaru, S. Nishizawa, and M. Hangyo, "Photoconductive Emission and Detection of Terahertz

Pulsed Radiation Using Semiconductors and Semiconductor Devices," *Journal of Infrared, Millimeter and Terahertz Waves,* vol. 33, pp. 393-404, 2012.

[238] K. Gan, J. Shi, Y. Chen, C. Sun, Y. Chiu, and J. E. Bowers, "Ultrahigh power-bandwidth-product performance of low-temperature-grown-GaAs based metal-semiconductor-metal traveling-wave photodetectors," *Applied Physics Letters,* vol. 80, pp. 4054-4056, 2002.

[239] E. Peytavit and e. al, "Terahertz frequency difference from vertically integrated low-temperature-grown GaAs photodetector," *Applied Physics Letters,* vol. 81, pp. 1174-1176, 2002.

[240] M. Mikulics and e. al, "Traveling-wave photomixer with recessed interdigitated contacts on low-temperature-grown GaAs," *Applied Physics Letters,* vol. 88, p. 041118, 2006.

[241] M. A. Seo and e. al, "Terahertz field enhancement by a metallic nano slit operating beyond the skin-depth limit," *Nat Photon,* vol. 3, pp. 152-156, 2009.

[242] E. R. Brown, "A photoconductive model for superior GaAs THz photomixers," *Applied Physics Letters,* vol. 75, pp. 769-771, 1999.

[243] E. R. Brown, K. A. McIntosh, K. B. Nichols, and C. L. Dennis, "Photomixing up to 3.8 THz in low-temperature-grown GaAs," *Applied Physics Letters,* vol. 66, pp. 285-287, 1995.

[244] I. S. Gregory, W. R. Tribe, B. E. Cole, M. J. Evans, E. H. Linfield, A. G. Davies, and M. Missous, "Resonant dipole antennas for continuous-wave terahertz photomixers," *Applied Physics Letters,* vol. 85, pp. 1622-1624, 2004.

[245] K. A. McIntosh, E. R. Brown, K. B. Nichols, O. B. McMahon, W. F. DiNatale, and T. M. Lyszczarz, "Terahertz measurements of resonant planar antennas coupled to low-temperature-grown GaAs photomixers," *Applied Physics Letters,* vol. 69, pp. 3632-3634, 1996.

[246] J. S. Hong and M. J. Lancaster, *Microstrip Filters for RF/Microwave Applications*: John Wiley & Sons, Inc, 2001.

[247] R. E. Collin, *Antennas and radiowave propagation*. New York: McGraw-Hill, 1985.

[248] G. M. Rebeiz, "Millimeter-wave and terahertz integrated circuit antennas," *Proceedings of the IEEE*, vol. 80, pp. 1748-1770, 1992.

[249] D. Li, Y. Huang, Y. Shen, A. Boland-Thoms, and A. Vickers, "Development of a THz photoconductive horn antenna," in *Proceedings of the Fourth European Conference on Antennas and Propagation (EuCAP)*, 2010, pp. 1-4.

[250] C. A. Balanis, *Modern antenna handbook*. Hoboken, NJ: Wiley, 2008.

[251] C. Ching-Wei, L. Yen-Cheng, C. Chia-Hua, Y. Peichen, S. Jia-Min, and P. Ci-Ling, "Frequency-Dependent Complex Conductivities and Dielectric Responses of Indium Tin Oxide Thin Films From the Visible to the Far-Infrared," *IEEE Journal of Quantum Electronics,*, vol. 46, pp. 1746-1754, 2010.

[252] S. H. Brewer and S. Franzen, "Calculation of the electronic and optical properties of indium tin oxide by density functional theory," *Chemical Physics*, vol. 300, pp. 285-293, 2004.

[253] B. Andres-Garcia, L. Garcia-Munoz, D. Segovia-Vargas, S. Bauerschmidt, G. Dohler, S. Preu, S. Malzer, L. Hong, and A. C. Gossard, "High power terahertz photomixer arrays," in *6th European Conference on Antennas and Propagation (EUCAP)*, 2012, pp. 1007-1010.

Appendix A E-field of THz Small and Large Gap Antennas

A.1. Small Gap THz Antennas

Hertzian dipole is an antenna with infinitesimal length dl ($dl<<\lambda$). Since the antenna length is very small, the current of the Hertzian antenna can be assumed to have constant amplitude of I_{pc} with a constant phase; hence antenna is equivalent to a constant current source of $I_{pc}dl$. It is good to state that $I_{pc}dl=J_{pc}dV$, where J_{pc} is the current density and dV is the source volume. The Hertzian dipole antenna geometry is illustrated in Fig. A.1.

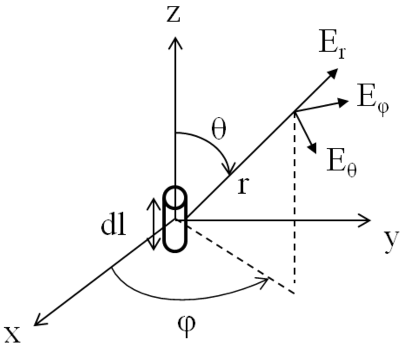

Fig. A.1 Geometry of a Hertzian dipole with its associated electric field components in the spherical coordinate

To derive the radiated electromagnetic fields using Maxwell's equations, first, the vector potential, A_z, needs to be calculated through equation (A.1) and then it is transformed to spherical coordinate as shown in equation (A.2) [1].

$$A_z = \frac{\mu I_{pc} dl}{4\pi r} e^{-jkr} \tag{A.1}$$

$$A_\theta = -A_z \sin\theta = -\frac{\mu I_{pc} dl}{4\pi r} e^{-jkr} \sin\theta \tag{A.2a}$$

$$A_r = A_z \cos\theta = \frac{\mu I_{pc} dl}{4\pi r} e^{-jkr} \cos\theta \tag{A.2b}$$

$$A_\varphi = 0 \tag{A.2c}$$

where $k = \frac{2\pi}{\lambda}$ is the wave number.

Considering the relations of electric and magnetic fields with the vector potential according to equation (A.3),

$$\vec{H} = \frac{1}{\mu} \nabla \times A \tag{A.3a}$$

$$\nabla \times \vec{E} = -j\omega\mu\vec{H} \tag{A.3b}$$

Electric, *E*, and magnetic, *H*, fields can be calculated as presented in (A.4):

$$H_\varphi = \frac{kI_{pc} dl}{4\pi r} \sin\theta \left[j + \frac{1}{kr} \right] e^{-jkr} \tag{A.4a}$$

$$E_\theta = \eta \frac{kI_{pc} dl}{4\pi r} \sin\theta \left[j + \frac{1}{kr} - \frac{j}{(kr)^2} \right] e^{-jkr} \tag{A.4b}$$

$$E_r = \eta \frac{kI_{pc} dl}{2\pi r^2} \cos\theta \left[1 + \frac{1}{jkr} \right] e^{-jkr} \tag{A.4c}$$

$$H_r = 0,\ H_\theta = 0,\ E_\varphi = 0 \tag{A.4d}$$

where $\eta = \sqrt{\frac{\mu}{\varepsilon}}$ is the intrinsic impedance and ε is the permittivity.

In THz photoconductive antennas, time domain behaviour of fields are used. Therefore, by multiplying field components of equation (A.4) with $e^{j\omega t}$, getting the real part of fields and considering the time difference between the observation point and source point as $t_d = t - \frac{r}{c}$ (*c* is the light velocity), time domain equations of the fields of equation (A.4) can be obtained by (A.5).

$$\tilde{H}_\varphi = \frac{I_{pc}dl}{4\pi}\sin\theta\left[\frac{-\omega\sin\omega t_d}{rc} + \frac{\cos\omega t_d}{r^2}\right] \tag{A.5a}$$

$$\tilde{E}_\theta = \frac{I_{pc}dl}{4\pi\varepsilon}\sin\theta\left[\frac{-\omega\sin\omega t_d}{rc^2} + \frac{\cos\omega t_d}{r^2 c} + \frac{\sin\omega t_d}{\omega r^3}\right] \tag{A.5b}$$

$$\tilde{E}_r = \frac{I_{pc}dl}{2\pi\varepsilon}\cos\theta\left[\frac{\cos\omega t_d}{r^2 c} + \frac{\sin\omega t_d}{\omega r^3}\right] \tag{A.5c}$$

From equation (A.5) it can be interpreted that $\tilde{E}_\theta$ and $\tilde{H}_\varphi$ are radiative components in far field (*kr*>>1) since they have the factor of *1/r*. Assuming that $I_{pc}(t_d) = I_{pc}\cos\omega t_d$ and considering the relation between charge and current, $I_{pc}(t) = \frac{\partial q}{\partial t}$, equations (A.5a) and (A.5b) can be rewritten as (A.6a) and (A.6b) respectively:

$$\tilde{H}_\varphi = \frac{dl}{4\pi rc}\sin\theta\frac{\partial I_{pc}(t_d)}{\partial t_d} + \frac{dl}{4\pi r^2}\sin\theta I_{pc}(t_d) \tag{A.6a}$$

$$\tilde{E}_\theta = \frac{dl}{4\pi\varepsilon rc^2}\sin\theta\frac{\partial I_{pc}(t_d)}{\partial t_d} + \frac{dl}{4\pi\varepsilon r^2 c}\sin\theta I_{pc}(t_d) + \frac{dl}{4\pi\varepsilon r^3}\sin\theta\frac{\partial q}{\partial t_d} \tag{A.6b}$$

Thus, the radiated electric field is proportional to the time derivative of the current (or equivalently it is proportional to the current density).

It is good to mention that in previous work in the literature, the relation of radiated THz power to the current was explained through Hertz vector potential of a time-varying dipole moment [34, 68] which is a popular method in areas like quantum electronics and solid-state physics. However, here this relation was explained through the usage of vector potential and considering the time-varying behaviour of the Hertzian dipole as an antenna.

A.2. Large-Aperture THz Antennas

Geometry of a large-aperture THz antenna is shown in Fig. A.2. Spectral and temporal format of emission of THz radiation from this antenna according to the Maxwell's equations can be written as [84]:

$$\vec{E}_{THz} = -j\omega\vec{A} \tag{A.7a}$$

$$\vec{E}_{THz}(r,t) = -\frac{\mu}{4\pi}\int\frac{\partial\vec{J}_s(t)}{\partial t}\frac{dS}{r} = -\frac{\mu S}{4\pi z}\frac{d\vec{J}_s(t)}{dt} \tag{A.7b}$$

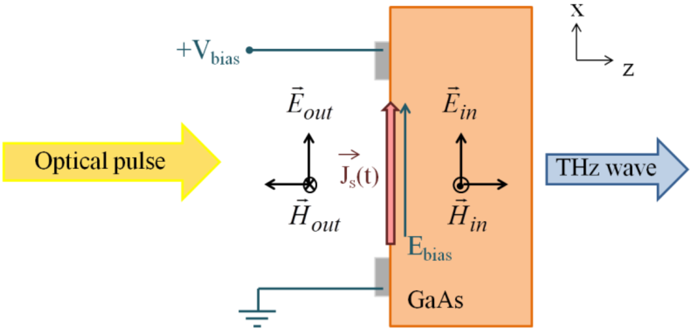

Fig. A.2 Geometry of a large-aperture THz antenna

In large-aperture THz antennas, the size of the excitation area by the laser on the photoconductive gap is greater than the wavelength of the emitted THz wave. Therefore, the fields from this type of antenna can be assumed as plane waves and be modelled by considering boundary conditions [75]. Thus, according to Fig. A.2 and based on the basics of electromagnetic fields, the boundary conditions for electric and magnetic fields at air-substrate interface can be written as:

$$\vec{E}_{in}(t) = \vec{E}_{out}(t) \tag{A.8a}$$

$$\vec{H}_{in}(t) - \vec{H}_{out}(t) = \vec{J}_s(t) \tag{A.8b}$$

The relation of E-field to H-field in two regions of air and substrate are:

$$\vec{H}_{in}(t) = -\frac{\sqrt{\varepsilon_r}}{\eta_0}\vec{E}_{in}(t) \tag{A.9a}$$

$$\vec{H}_{out}(t) = \frac{1}{\eta_0}\vec{E}_{out}(t) \tag{A.9b}$$

where η_0 is the intrinsic impedance of air and ε_r is the relative permittivity of the substrate. Thus, using equations (A.8) and (A.9) and considering Ohm's law that surface current density can be expressed as $\vec{J}_s(t) = \sigma_s(t)(\vec{E}_{in}(t) + \vec{E}_{bias}(t))$, and the surface current in a large-aperture antenna is derived as:

$$\vec{J}_s(t) = \frac{\sigma_s(t)\vec{E}_{bias}(t)}{\frac{\sigma_s(t)\eta_0}{1+\sqrt{\varepsilon_r}} + 1} \tag{A.10}$$

where $\sigma_s(t) = e \cdot \mu_e \cdot n(t)$ is the surface conductivity of the photoconductive substrate and μ_e is the electron mobility and related to photoconductive material characteristics as $\mu_e = e\tau_s / m^*$.

By considering (A.7b) and (A.10) the radiated THz field can be obtained as:

$$\vec{E}_{THz}(z,t) = -\frac{\mu S}{4\pi z}\frac{\frac{d\sigma_s(t)}{dt}}{(\frac{\sigma_s(t)\eta_0}{1+\sqrt{\varepsilon_r}} + 1)^2}\vec{E}_{bias} = -\frac{\mu S}{4\pi z}\frac{e\mu_e\frac{dn(t)}{dt}}{(\frac{e\mu_e n(t)\eta_0}{1+\sqrt{\varepsilon_r}} + 1)^2}\vec{E}_{bias} \tag{A.11}$$